

REPORT DOCUMENTATION PAGE		Form Approved OMB NO. 0704-0188	
Public Reporting Burden for this collection of information is estimated to average 1 hour per response, including the time for reviewing instructions, searching existing data sources, gathering and maintaining the data needed, and completing and reviewing the collection of information. Send comment regarding this burden estimate or any other aspect of this collection of information, including suggestions for reducing this burden, to Washington Headquarters Services, Directorate for Information Operations and Reports, 1215 Jefferson Davis Highway, Suite 1204, Arlington VA, 22202-4302, and to the Office of Management and Budget, Paperwork Reduction Project (0704-0188), Washington DC 20503			
1. AGENCY USE ONLY (Leave Blank)		2. REPORT DATE:	
		3. REPORT TYPE AND DATES COVERED Final Report 1-Aug-2002 - 31-Jul-2006	
4. TITLE AND SUBTITLE Simulation of Supersonic Base Flows: Numerical Investigations Using DNS, LES, and URANS		5. FUNDING NUMBERS DAAD190210361	
6. AUTHORS Hermann F. Fasel and Richard D. Sandberg		8. PERFORMING ORGANIZATION REPORT NUMBER	
7. PERFORMING ORGANIZATION NAMES AND ADDRESSES University of Arizona Sponsored Project Services 888 N. Euclid, #510 Tucson, AZ 85722 -			
9. SPONSORING/MONITORING AGENCY NAME(S) AND ADDRESS(ES) U.S. Army Research Office P.O. Box 12211 Research Triangle Park, NC 27709-2211		10. SPONSORING / MONITORING AGENCY REPORT NUMBER 42637-EG.1	
11. SUPPLEMENTARY NOTES The views, opinions and/or findings contained in this report are those of the author(s) and should not be construed as an official Department of the Army position, policy or decision, unless so designated by other documentation.			
12. DISTRIBUTION AVAILABILITY STATEMENT Approved for Public Release; Distribution Unlimited		12b. DISTRIBUTION CODE	
13. ABSTRACT (Maximum 200 words) The abstract is below since many authors do not follow the 200 word limit			
14. SUBJECT TERMS Axisymmetric Supersonic Base Flows, Axisymmetric Supersonic Wakes, Hydrodynamic Stability of Supersonic Base Flows		15. NUMBER OF PAGES Unknown due to possible attachments	
		16. PRICE CODE	
17. SECURITY CLASSIFICATION OF REPORT UNCLASSIFIED	18. SECURITY CLASSIFICATION ON THIS PAGE UNCLASSIFIED	19. SECURITY CLASSIFICATION OF ABSTRACT UNCLASSIFIED	20. LIMITATION OF ABSTRACT UL

Report Title

Simulation of Supersonic Base Flows: Numerical Investigations Using DNS, LES, and URANS

ABSTRACT

Transitional and turbulent supersonic axisymmetric wakes were investigated by conducting various numerical experiments. The main objective was to identify hydrodynamic instability mechanisms in the flow at Mach number $M = 2.46$ for several Reynolds numbers, and relating these to coherent structures that are found from various visualization techniques. The premise for this approach is the assumption that flow instabilities lead to the formation of coherent structures. The effect of these structures on the mean flow is of particular interest, as they strongly affect the base drag. Three high-order accurate compressible codes were developed in cylindrical coordinates for this research: A spatial Navier-Stokes (N-S) code to conduct Direct Numerical Simulations (DNS), a linearized N-S code for linear stability investigations using two-dimensional basic states, and a temporal N-S code for performing local stability analyses. The ability of numerical simulations to deliberately exclude physical effects is exploited. This includes intentionally eliminating certain azimuthal/helical modes by employing DNS for various circumferential domain-sizes. With this approach, the impact of structures associated with certain modes on the global wake-behavior can be scrutinized. It is concluded that azimuthal modes with low wavenumbers are responsible for a flat mean base-pressure distribution and that $k=2$ and $k=4$ are the dominant modes in the trailing wake, producing a four-lobe wake pattern. Complementary spatial and temporal calculations are carried out to investigate whether instabilities are of local or global nature. Circumstantial evidence is presented that absolutely unstable global modes within the recirculation region coexist with convectively unstable shear-layer modes. The flow is found to be absolutely unstable with respect to modes $k>0$ for $Re_D > 5,000$ and with respect to the axisymmetric mode for $Re_D > 100,000$. Furthermore, it is investigated whether flow control measures designed to weaken the naturally most significant modes can decrease the base drag. Finally, the novel Flow Simulation Methodology (FSM), using state-of-the-art turbulence closures, was shown to reproduce DNS results at a fraction of the computational cost.

List of papers submitted or published that acknowledge ARO support during this reporting period. List the papers, including journal references, in the following categories:

(a) Papers published in peer-reviewed journals (N/A for none)

R. D. Sandberg and H. F. Fasel, 2006; "Numerical Investigation of Transitional Supersonic Axisymmetric Wakes", Vol. 563, Page 1-41, Journal of Fluid Mechanics.

R. D. Sandberg and H. F. Fasel, 2006; "Investigation of Supersonic Wakes using Conventional and Hybrid Turbulence Models", Vol. 44, No. 9, September, AIAA Journal

R. D. Sandberg and H. F. Fasel, 2006; "Direct Numerical Simulations of Transitional Supersonic Base Flows", Vol. 44, No.4, April, AIAA Journal.

H. F. Fasel, D. A. von Terzi and R. D. Sandberg, 2006; "A Methodology for Simulating Compressible Turbulent Flows", Vol. 73, Page 405-412, Journal of Applied Mechanics.

Number of Papers published in peer-reviewed journals: 4.00

(b) Papers published in non-peer-reviewed journals or in conference proceedings (N/A for none)

Number of Papers published in non peer-reviewed journals: 0.00

(c) Presentations

Number of Presentations: 0.00

Non Peer-Reviewed Conference Proceeding publications (other than abstracts):

Number of Non Peer-Reviewed Conference Proceeding publications (other than abstracts): 0

Peer-Reviewed Conference Proceeding publications (other than abstracts):

J. Sivasubramanian and H.F. Fasel, 2006, “LES and DES of high Reynolds number, supersonic base flows with control of the near wake”, IEEE Proc. of DoD UGC 2006, DoD High Performance Computing Modernization Program Users Group Conference, 26-29 June 2006 / Denver, CO

J. Sivasubramanian, R. D. Sandberg, D. A. von Terzi and H. F. Fasel, 2006; "Numerical investigation of flow control mechanisms for drag reduction in supersonic base-flows", AIAA paper 2006-902, 44th AIAA Aerospace Sciences Meeting and Exhibit, 9-12 January 2006, Reno, NV

J. Sivasubramanian, R. D. Sandberg, D. A. von Terzi and H. F. Fasel, 2006; "Numerical investigation of transitional supersonic base flows with flow control", AIAA paper 2006-479, 44th AIAA Aerospace Sciences Meeting and Exhibit, 9-12 January 2006, Reno, NV

D. A. von Terzi, R. D. Sandberg, J. Sivasubramanian and H. F. Fasel, 2005; "High accuracy DNS and LES of high Reynolds number, supersonic base flows and passive control of the near wake", 2005 DoD HPC Users Group Conference, Nashville, TN,27-30 June 2005, published in IEEE Proceedings of the HPCMP Users Group Conference 2005 - ISBN 0-7695-2496-6

R. D. Sandberg and H. F. Fasel, 2005; "Direct Numerical Simulations of Transitional Supersonic Base Flows", AIAA Paper 2005-0098, 43rd AIAA Aerospace Sciences Meeting and Exhibit, 10-13 January 2005, Reno, NV

R. D. Sandberg and H. F. Fasel, 2004; "High-Accuracy DNS of Supersonic Base Flows and Control of the Near Wake", 2004 DoD HPC Users Group Conference, Williamsburg, Virginia, 7-11 June 2004, published in IEEE Proceedings of the Users Group Conference 2004 - ISBN 0-7695-2259-9

R. D. Sandberg and H. F. Fasel, 2004; "Application of a new Flow Simulation Methodology for Supersonic Axisymmetric Wakes", AIAA Paper 2004-0067, AIAA 42nd Aerospace Sciences Meeting and Exhibit, 5-8 January 2004, Reno, NV

R. D. Sandberg and H. F. Fasel, 2004; "Instability Mechanisms in Supersonic Base Flows", AIAA Paper 2004-0593, AIAA 42nd Aerospace Sciences Meeting and Exhibit, 5-8 January 2004, Reno, NV

R. D. Sandberg and H. F. Fasel, 2003; "A Flow Simulation Methodology for Compressible Turbulent Axisymmetric Wakes", AIAA Paper 2003-0267, AIAA 41st Aerospace Sciences Meeting and Exhibit, 6-9 January 2003, Reno, NV

Number of Peer-Reviewed Conference Proceeding publications (other than abstracts): 9

(d) Manuscripts

D. A. von Terzi, R. D. Sandberg and H. F. Fasel, 2006; “ Identification of large coherent structures in compressible wake flows”, submitted to Journal of Fluid Mechanics

Number of Manuscripts: 1.00

Number of Inventions:

Graduate Students

<u>NAME</u>	<u>PERCENT SUPPORTED</u>	
Jayahar Sivasubramanian	0.50	No
Richard D Sandberg	0.50	No
FTE Equivalent:	1.00	
Total Number:	2	

Names of Post Doctorates

<u>NAME</u>	<u>PERCENT SUPPORTED</u>
FTE Equivalent:	
Total Number:	

Names of Faculty Supported

<u>NAME</u>	<u>PERCENT SUPPORTED</u>	National Academy Member
Hermann F Fasel	0.04	No
FTE Equivalent:	0.04	
Total Number:	1	

Names of Under Graduate students supported

<u>NAME</u>	<u>PERCENT SUPPORTED</u>
FTE Equivalent:	
Total Number:	

Names of Personnel receiving masters degrees

<u>NAME</u>
Total Number:

Names of personnel receiving PHDs

<u>NAME</u>	
Richard D. Sandberg	No
Total Number:	1

Names of other research staff

<u>NAME</u>	<u>PERCENT SUPPORTED</u>
FTE Equivalent:	
Total Number:	

Sub Contractors (DD882)

Inventions (DD882)

FINAL REPORT

ARO Grant No. DAAD190210361

SIMULATION OF SUPERSONIC BASE FLOWS:
NUMERICAL INVESTIGATIONS USING DNS,
LES AND URANS

by

Hermann F Fasel

Richard D Sandberg

Department of Aerospace and Mechanical Engineering

The university of Arizona

Tucson, AZ 85721

Submitted to

Dr. Thomas L. Doligalski, chief

Fluid Dynamics Branch

Engineering Sciences Division

U.S. Army Research Office

O c t o b e r 2 0 0 6

Table of Contents

List of Figures	7
List of Tables	17
Nomenclature	19
Abstract	23
1. INTRODUCTION	24
1.1 Physical Problem	24
1.1.1 Mean Flow	25
1.1.2 Coherent Structures	27
1.2 Numerical Simulations	31
1.2.1 Hydrodynamic Stability Investigations	31
1.2.2 Turbulence Modelling	34
1.3 Present Research	38
2. GOVERNING EQUATIONS	43
2.1 Navier-Stokes Equations	43
2.2 Turbulence Models	45
2.2.1 Turbulent Stress-Tensor	45
2.2.2 Turbulent Transport Equations	48
2.2.3 Subgrid Heat-Flux Vector	49
2.2.4 Source Terms	49
2.2.5 Extensions to Wall-Bounded Flows	50
2.3 Flow Simulation Methodology (FSM)	52
2.4 Scaling Laws	53
2.5 Linearized Navier-Stokes (LNS) Equations	54

Table of Contents—Continued

3. NUMERICAL METHOD	56
3.1 Boundary and Initial Conditions	57
3.2 Axis Treatment	60
3.3 Spatial and Temporal Discretization	61
3.4 Grid Stretching	63
3.5 Filtering	63
3.6 Parallelization	64
3.7 Disturbance Generation	65
3.8 Linearized Code	66
3.9 Temporal Code	67
4. CODE VALIDATION	69
4.1 Tollmien-Schlichting Waves ($M = 0.25$)	69
4.2 Tollmien-Schlichting Waves ($M = 1.6$)	72
4.3 Oblique Tollmien-Schlichting Waves ($M = 3.0$)	74
4.4 Subsonic Wake Flows	78
4.4.1 Axisymmetric Calculations	78
4.4.2 3-D Calculations	80
4.5 Turbulence Models	85
4.5.1 Incompressible Turbulent Boundary Layer	86
4.5.2 Compressible Turbulent Boundary Layer	94
4.6 Summary	96
5. RESULTS - LINEAR STABILITY ANALYSIS	98
5.1 Basic State	98
5.2 Spatial Results	100
5.3 Temporal Results	111

Table of Contents—Continued

5.4	Convective Instability	116
5.5	Summary	119
6.	RESULTS - DIRECT NUMERICAL SIMULATIONS	120
6.1	DNS for $Re_D = 30,000$	123
6.1.1	Time-Dependent Results	124
6.1.2	Coherent Structures	131
6.1.3	Mean Flow	143
6.1.4	Turbulent Statistics	160
6.1.5	Flow Control	165
6.1.6	Summary	177
6.2	DNS for $Re_D = 60,000$	179
6.2.1	Time-Dependent Results	179
6.2.2	Coherent Structures	185
6.2.3	Mean Flow and Turbulent Statistics	189
6.2.4	Summary	201
6.3	DNS for $Re_D = 100,000$	202
6.3.1	Time-Dependent Results	202
6.3.2	Coherent Structures	206
6.3.3	Mean Flow and Turbulent Statistics	214
6.3.4	Summary	222
7.	RESULTS - FLOW SIMULATION METHODOLOGY	223
7.1	Transitional Wake at $Re_D = 30,000$	224
7.1.1	Axisymmetric RANS Calculations	224
7.1.2	3-D FSM Calculations	228
7.2	Transitional Wake at $Re_D = 60,000$	234

Table of Contents—*Continued*

7.2.1	Axisymmetric RANS Calculations	234
7.2.2	3-D FSM Calculations	236
7.3	Transitional Wake at $Re_D = 100,000$	245
7.3.1	Flow Control	246
7.4	High Reynolds Number UIUC Case	252
7.4.1	Axisymmetric RANS Calculations	253
7.4.2	3-D FSM Calculations	262
7.5	Summary	267
8.	SUMMARY OF THE MOST IMPORTANT RESULTS	270
Appendix A	EQUATIONS IN CYLINDRICAL COORDINATES	277
A.1	Resolved Navier-Stokes Equations	277
A.2	Derivation of Turbulent Kinetic Energy Equation	280
A.3	Derivation of Linearized Navier-Stokes Equations	282
A.3.1	High Reynolds Number Extension	286
A.4	Equations in Fourier Space	286
A.4.1	Azimuthal Fourier Transforms	286
A.4.2	Streamwise Fourier Transforms for Temporal Simulations	289
Appendix B	SYMMETRY CONDITIONS	292
Appendix C	NUMERICAL DETAILS	293
C.1	Runge-Kutta Time Integration	293
C.2	Finite Difference Stencils	293
C.3	Derivation of Parity Conditions	297
C.3.1	Scalars	298
C.3.2	Vectors	299

Table of Contents—*Continued*

C.4	Stability of the Numerical Method	300
C.4.1	Low-Order Discretization	300
C.4.2	High-Order Discretization	303
C.5	Filtering	307
C.5.1	Derivation	307
C.5.2	Validation and Observations	311
C.6	Parallelization	317
C.6.1	Domain Decomposition	317
C.6.2	Performance Study	320
Appendix D FLOW PARAMETERS		325
References		331

List of Figures

1.1	Schematic of the mean flow-field of a supersonic base flow.	26
3.1	Computational domain for spatial calculations.	58
3.2	Computational domains for temporal calculations.	67
4.1	Amplitude distributions and amplification rate obtained from LNS simulations and DNS; $M = 0.25$, $Re = 100,000$, $F = 1.4 \cdot 10^{-4}$	71
4.2	Amplitude distributions and amplification rate obtained from LNS simulations and DNS; $Re = 100,000$, $M = 1.6$, $F = 5.0025 \cdot 10^{-5}$	73
4.3	Amplitude and phase distributions from TDNS; $Re_x = 700$, $M = 3.0$. .	75
4.4	Amplitude and phase distributions from LNS simulations; $Re_x = 700$, $M = 3.0$	76
4.5	Growth rate α_i and normalized amplification rates from LNS simulations; $\psi = 60^\circ$, $Re = 1,578,102$, $M = 3.0$, $F = 5 \cdot 10^{-5}$	77
4.6	Centerline streamwise velocity for different Reynolds numbers at $M = 0.25$, compared with incompressible reference code	79
4.7	Centerline streamwise velocity for different Reynolds numbers at $M = 0.25$, keeping the approach boundary-layer thickness constant.	80
4.8	Temporal development of higher azimuthal modes at the disturbance location for subsonic wake calculations.	81
4.9	Contours of total vorticity; $Re_D = 1,000$, $M = 0.25$	82
4.10	Sideview of contours of total vorticity and perspective view of iso-surfaces of $Q = 0.2$; $Re_D = 2,000$, $M = 0.25$	83
4.11	Amplitude distributions of mode $k = 1$ for subsonic wake calculations . .	84
4.12	Temporal RANS calculations of a turbulent boundary layer for different values of α_i ; $Re_\delta \approx 1700$, $M = 0.25$	88
4.13	Temporal RANS calculations of a turbulent boundary layer using different grids; $Re_\delta \approx 1,700$, $M = 0.25$	91

List of Figures—*Continued*

4.14	Temporal RANS calculations of a turbulent boundary layer using values for c_T ; $Re_\delta \approx 50,000$, $M = 0.25$	93
4.15	Streamwise velocity profiles in wall-coordinates from temporal boundary layer calculations using EASM $_\alpha$; $Re_\delta = 165,000$, $M = 2.46$	96
5.1	Centerline streamwise velocity obtained from axisymmetric N-S calculations for different Reynolds numbers; $\delta_c = 0.1$, $M = 2.46$	99
5.2	Temporal development of azimuthal Fourier modes of streamwise velocity obtained from LNS calculations for various Reynolds numbers	101
5.3	Two-dimensional mode-shape obtained from LNS calculations; $k = 3$, $Re_D = 30,000$, $M = 2.46$	104
5.4	Radial mode-shapes of Fourier modes of u , obtained from LNS calculations for various Reynolds numbers	106
5.5	Radial mode-shapes of Fourier modes of v , obtained from LNS calculations for various Reynolds numbers	107
5.6	Radial mode-shapes of Fourier modes of w , obtained from LNS calculations for various Reynolds numbers	108
5.7	Radial mode-shapes of Fourier modes of u , obtained from LNS calculations at $z = 0.5$	110
5.8	Temporal development of Fourier modes of ρ obtained from TDNS for various Reynolds numbers	113
5.9	Radial mode-shapes of Fourier modes of u , obtained from TDNS at $z = 0.5$	115
5.10	Instantaneous azimuthal Fourier modes of ρ ; $z = 2.5$, $r = 0.5$, $Re_D = 5,000$, $M = 2.46$	117
5.11	Temporal development of azimuthal Fourier modes obtained from an LNS calculation employing periodic forcing.	119
6.1	Schematic of wake patterns generated by various azimuthal modes. . . .	122

List of Figures—*Continued*

6.2	Temporal development of Fourier modes of (ρu) at start-up for half-cylinder calculation; $Re_D = 30,000$, $M = 2.46$	124
6.3	Sideviews of instantaneous total vorticity; $Re_D = 30,000$, $M = 2.46$. . .	125
6.4	Temporal development of Fourier modes of in a region of high activity; $z = 4.82$, $r = 0.238$, $Re_D = 30,000$, $M = 2.46$	126
6.5	Fourier decomposition in time of higher density modes in a region of high activity; $Re_D = 30,000$, $M = 2.46$	129
6.6	Instantaneous iso-contours of $Q = 0.1$ for half-cylinder case; $Re_D = 30,000$, $M = 2.46$	132
6.7	Instantaneous iso-contours of $Q = 0.1$ for quarter-cylinder case; $Re_D = 30,000$, $M = 2.46$	135
6.8	Instantaneous iso-contours of $Q = 0.1$ for $1/6^{th}$ - and $1/8^{th}$ -cylinder cases; $Re_D = 30,000$, $M = 2.46$	136
6.9	Instantaneous iso-contours of $Q = 0.4$ for initial transient of $1/8^{th}$ -cylinder case; $Re_D = 30,000$, $M = 2.46$	138
6.10	Temporal development of Fourier modes of (ρu) from TDNS for half-cylinder case; $Re_D = 30,000$, $M = 2.46$	139
6.11	Perspective views of iso-contours of $Q = 0.1$ from temporal calculations of half-cylinder case; $Re_D = 30,000$, $M = 2.46$	140
6.12	Instantaneous iso-contours of magnitude of baroclinic torque for half-cylinder case; $Re_D = 30,000$, $M = 2.46$	141
6.13	Time-averaged radial mode-shapes of $(\rho u)^k$ obtained from DNS; $Re_D = 30,000$, $M = 2.46$	145
6.14	Time-averaged radial mode-shapes of $(\rho v)^k$ obtained from DNS; $Re_D = 30,000$, $M = 2.46$	146

List of Figures—*Continued*

6.15	Time-averaged radial mode-shapes of $(\rho w)^k$ obtained from DNS; $Re_D = 30,000$, $M = 2.46$	147
6.16	Endviews of time-averaged quantities upstream of the recompression region; $Re_D = 30,000$, $M = 2.46$	151
6.17	Endviews of time-averaged quantities downstream of the recompression region; $Re_D = 30,000$, $M = 2.46$	154
6.18	Time-averaged iso-contours of $Q = 0.05$ for all circumferential domain-sizes	156
6.19	Averaged pressure coefficient and streamwise axis-velocity for all circumferential domain-sizes; $Re_D = 30,000$, $M = 2.46$	157
6.20	Pressure coefficient on the base obtained from axisymmetric DNS calculations for various Reynolds numbers; $M = 2.46$	159
6.21	Side- and endviews of averaged turbulent statistics for half-cylinder case; $Re_D = 30,000$, $M = 2.46$	161
6.22	Radial maxima of various averaged turbulent statistics over streamwise coordinate; $Re_D = 30,000$, $M = 2.46$	163
6.23	Endviews of time-averaged streamwise vorticity in the initial shear-layer at $z=1$ for cases using flow control; $Re_D = 30,000$, $M = 2.46$	166
6.24	Temporal development of Fourier modes of ρ in a region of high activity for volume-forced cases; $z = 10.13$, $r = 0.45$, $Re_D = 30,000$, $M = 2.46$. .	168
6.25	Fourier decomposition in time of Fourier modes of ρ in a region of high activity for forced cases	169
6.26	Instantaneous iso-contours of $Q = 0.1$ for cases employing forcing of $k = 0$ and $k = 4$; $Re_D = 30,000$, $M = 2.46$	170
6.27	Instantaneous iso-contours of $Q = 0.1$ for cases employing forcing of $k = 8$ and $k = 16$; $Re_D = 30,000$, $M = 2.46$	171

List of Figures—*Continued*

6.28	Time-averaged radial profiles of azimuthal Fourier modes of (ρu) obtained from calculations employing forcing; $Re_D = 30,000$, $M = 2.46$	172
6.29	Endviews of time-averaged contours of total vorticity in the trailing wake at $z = 9$ for forced cases; $Re_D = 30,000$, $M = 2.46$	174
6.30	Pressure coefficient and streamwise axis-velocity from simulations using flow control; $Re_D = 30,000$, $M = 2.46$	175
6.31	Temporal development of Fourier modes of (ρu) at start-up for half-cylinder calculation; $Re_D = 60,000$, $M = 2.46$	180
6.32	Sideviews of instantaneous total vorticity; $Re_D = 60,000$, $M = 2.46$. . .	181
6.33	Temporal development of higher Fourier modes of ρ in a region of high activity; $z = 7.85$, $r = 0.465$, $Re_D = 60,000$, $M = 2.46$	182
6.34	Fourier decomposition in time of higher Fourier modes of ρ in a region of high activity; $Re_D = 60,000$, $M = 2.46$	183
6.35	Instantaneous iso-contours of $Q = 0.1$ for half-cylinder case; $Re_D = 60,000$, $M = 2.46$	186
6.36	Instantaneous iso-contours of $Q = 0.1$ for $1/6^{th}$ - and $1/8^{th}$ -cylinder cases; $Re_D = 60,000$, $M = 2.46$	187
6.37	Instantaneous iso-contours of $Q = 0.1$ for $1/16^{th}$ -cylinder case; $Re_D = 60,000$, $M = 2.46$	188
6.38	Time-averaged radial profiles of azimuthal Fourier modes of (ρu) ; $Re_D = 60,000$, $M = 2.46$	190
6.39	Time-averaged radial profiles of azimuthal Fourier modes of (ρv) ; $Re_D = 60,000$, $M = 2.46$	191
6.40	Time-averaged radial profiles of azimuthal Fourier modes of (ρw) ; $Re_D = 60,000$, $M = 2.46$	192

List of Figures—*Continued*

6.41	Endviews of time-averaged quantities upstream of the recompression region; $Re_D = 60,000$, $M = 2.46$	195
6.42	Endviews of time-averaged quantities downstream of the recompression region; $Re_D = 60,000$, $M = 2.46$	197
6.43	Time-averaged pressure coefficient and streamwise axis-velocity for all circumferential domain-sizes; $Re_D = 60,000$, $M = 2.46$	198
6.44	Sideviews of averaged turbulent statistics for half-cylinder case; $Re_D = 60,000$, $M = 2.46$	199
6.45	Sideviews of instantaneous total vorticity; $Re_D = 100,000$, $M = 2.46$. .	203
6.46	Temporal development of Fourier modes of ρ in a region of high activity; $z = 8.27$, $r = 0.336$, $Re_D = 100,000$, $M = 2.46$	204
6.47	Fourier decomposition in time of Fourier modes of ρ in a region of high activity; $Re_D = 100,000$, $M = 2.46$	205
6.48	Instantaneous streamwise density gradient; $Re_D = 100,000$, $M = 2.46$. .	206
6.49	Endviews of contours of instantaneous local Mach number compared with visualizations from UIUC experiments; $Re_D = 100,000$, $M = 2.46$	208
6.50	Instantaneous perspective views for half-cylinder case; $Re_D = 100,000$, $M = 2.46$	209
6.51	Instantaneous iso-contours of $Q = 0.1$ for half-cylinder case; $Re_D = 100,000$, $M = 2.46$	210
6.52	Instantaneous iso-contours of $Q = 0.1$ for $1/16^{th}$ -cylinder case; $Re_D = 100,000$, $M = 2.46$	212
6.53	Time-averaged radial profiles of azimuthal Fourier modes of (ρu) ; $Re_D = 100,000$, $M = 2.46$	214
6.54	Time-averaged radial profiles of azimuthal Fourier modes of (ρv) ; $Re_D = 100,000$, $M = 2.46$	215

List of Figures—*Continued*

6.55	Time-averaged radial profiles of azimuthal Fourier modes of (ρw) ; $Re_D = 100,000$, $M = 2.46$	216
6.56	Endviews of time-averaged quantities; $Re_D = 100,000$, $M = 2.46$	218
6.57	Time-averaged pressure coefficient and streamwise axis-velocity for all circumferential domain-sizes; $Re_D = 100,000$, $M = 2.46$	219
6.58	Radial maxima of various averaged turbulent statistics over streamwise coordinate; $Re_D = 100,000$, $M = 2.46$	220
7.1	Pressure coefficient and streamwise axis-velocity from axisymmetric RANS calculations; $Re_D = 30,000$, $M = 2.46$	226
7.2	Distribution of TKE obtained from axisymmetric RANS calculations; $Re_D = 30,000$ and $M = 2.46$	227
7.3	Mean contribution function $f(\Delta/L_K)$ from FSM calculations using EASM $_{\alpha}$; $Re_D = 30,000$ and $M = 2.46$	229
7.4	Time-averaged pressure coefficient and streamwise axis-velocity from FSM calculations; $Re_D = 30,000$, $M = 2.46$	230
7.5	Time-averaged radial velocity and pressure field for DNS and FSM; $Re_D = 30,000$ and $M = 2.46$	231
7.6	Time-averaged mode-shapes of $(\rho u)^k$ obtained from FSM calculations; $Re_D = 30,000$, $M = 2.46$	232
7.7	Pressure coefficient and streamwise axis-velocity from axisymmetric RANS calculations; $Re_D = 60,000$, $M = 2.46$	235
7.8	Sideviews of instantaneous total vorticity; $Re_D = 60,000$, $M = 2.46$. . .	237
7.9	Time-averaged contribution function $f(\Delta/L_K)$ for FSM; $Re_D = 60,000$, $M = 2.46$	238
7.10	Time-averaged pressure coefficient and streamwise axis-velocity from FSM calculations on coarse grid; $Re_D = 60,000$, $M = 2.46$	239

List of Figures—*Continued*

7.11	Time-averaged mode-shapes of $(\rho u)^k$ obtained from FSM calculation on coarse grid with 4 Fourier modes and $\beta = 2 \cdot 10^{-4}$; $Re_D = 60,000$, $M = 2.46$	240
7.12	Time-averaged pressure coefficient and streamwise axis-velocity from FSM calculations on fine grid; $Re_D = 60,000$, $M = 2.46$	241
7.13	Time-averaged mode-shapes of $(\rho u)^k$ obtained from FSM calculation on fine grid with $\beta = 1 \cdot 10^{-3}$; $Re_D = 60,000$, $M = 2.46$	242
7.14	Instantaneous iso-contours of $Q = 0.1$ from FSM calculation; $Re_D = 60,000$, $M = 2.46$	243
7.15	Time-averaged pressure coefficient and streamwise axis-velocity from FSM calculations on fine grid; $Re_D = 100,000$, $M = 2.46$	245
7.16	Instantaneous iso-contours of $Q = 0.05$ for the unforced case; FSM for $Re_D = 100,000$ and $M = 2.46$	247
7.17	Endviews of time-averaged streamwise vorticity in the initial shear-layer at $z=1$ for cases using flow control; FSM for $Re_D = 100,000$ and $M = 2.46$	247
7.18	Instantaneous iso-contours of $Q = 0.05$ for steady forcing cases with $A_{dist} = 1.0$, perspective topview with flow from left to right; FSM for $Re_D = 100,000$.	248
7.19	Instantaneous iso-contours of $Q = 0.05$ for periodic forcing cases with $A_{dist} = 1.0$, perspective topview with flow from left to right; FSM for $Re_D = 100,000$.	249
7.20	Pressure coefficient and streamwise axis-velocity from FSM simulations using steady forcing of higher azimuthal modes; $Re_D = 100,000$, $M = 2.46$	250
7.21	Pressure coefficient and streamwise axis-velocity from FSM simulations using periodic forcing of axisymmetric mode; $Re_D = 100,000$, $M = 2.46$	251
7.22	Pressure coefficient and streamwise axis-velocity from axisymmetric RANS calculations; $Re_D = 3,300,000$, $M = 2.46$	254

List of Figures—Continued

7.23	Comparison of radial profiles of u , v , K and $\overline{u'v'}$ from axisymmetric RANS calculations with UIUC experiments; $Re_D = 3,300,000$, $M = 2.46$	256
7.24	Pressure coefficient and streamwise axis-velocity from axisymmetric RANS calculations with modified inflow; $Re_D = 3,300,000$, $M = 2.46$	257
7.25	Comparison of radial profiles from RANS calculations with modified inflow with UIUC experiments; $Re_D = 3,300,000$, $M = 2.46$	259
7.26	Estimate of the Kolmogorov length-scale; $Re_D = 3,300,000$ and $M = 2.46$	260
7.27	Instantaneous iso-contours of $Q = 0.5$ for FSM calculation; $Re_D = 3,300,000$, $M = 2.46$	263
7.28	Time-averaged pressure coefficient and streamwise axis-velocity from FSM calculations; $Re_D = 3,300,000$, $M = 2.46$	264
7.29	Time-averaged mode-shapes obtained from FSM calculation on fine grid with $\beta = 1 \cdot 10^{-4}$; $Re_D = 3,300,000$, $M = 2.46$	266
C.1	Typical grids for base flow calculations	295
C.2	Cartesian coordinate system rotated by angle κ in the $r - \theta$ plane. . . .	297
C.3	Amplification factor and phase shift for linearized wave equation using 2^{nd} -order split differences with 2^{nd} -order Runge-Kutta time integration .	302
C.4	Amplification factor and phase shift for linearized wave equation using 4^{th} -order central differences with 4^{th} -order Runge-Kutta time integration	304
C.5	Amplification factor and phase shift for linearized wave equation using 4^{th} -order split differences with 4^{th} -order Runge-Kutta time integration .	305
C.6	Propagation of a discontinuity using the inviscid Burger's equation; 4^{th} -order central differences with 4^{th} -order Runge-Kutta time integration . .	306
C.7	Propagation of a discontinuity using the inviscid Burger's equation; 4^{th} -order split differences with 4^{th} -order Runge-Kutta time integration . . .	307
C.8	Transfer functions for explicit and compact filters over wavenumber Θ .	309

List of Figures—*Continued*

C.9	Errors for explicit filters on stretched grids	313
C.10	Converged streamwise velocity field employing different filters; axisymmetric “DNS” on stretched grid; $M = 2.46$ and $Re_D = 10,000$	315
C.11	Domain decomposition for base flow simulations with 4 processors.	317
C.12	Domain decomposition for base flow simulations with 8 processors.	318
C.13	Flow chart of parallel loops and implicit synchronization contained in one Runge-Kutta cycle for a boundary-layer calculation.	319
C.14	Speed-up and efficiency over number of CPUs for calculations with different problem-sizes on an <i>SGI Origin 3800</i>	322
C.15	Speed-up and efficiency over number of CPUs for a calculation with large memory size	323

List of Tables

4.1	Comparison of integral quantities from RANS calculations with UIUC data for turbulent approach-flow; $Re_\delta = 165,000$, $M = 2.46$	95
7.1	Comparison of computational cost per flow-through-time for FSM and DNS calculations; $Re_D = 30,000$, $M = 2.46$	233
7.2	Comparison of computational cost per flow-through-time of FSM calculations with DNS ; $Re_D = 60,000$, $M = 2.46$	244
A.1	Symmetries for FFTs in the streamwise (z) and the azimuthal (θ) directions for all variables and equations.	288
B.1	Symmetries of computational azimuthal Fourier modes at the axis for all variables and equations for different azimuthal domain-sizes	292
B.2	Boundary conditions of computational azimuthal Fourier modes at the axis for all variables for different circumferential domain-sizes.	292
C.1	Coefficients of 4 th - and 6 th -order accurate filter-stencils for an equidistant grid	312
C.2	Parameters for computational grids employed for testing accuracy of filter-operations on stretched grids	312
C.3	Parameters of test-cases conducted for illustration of importance of cache-effects for parallel calculations	321
C.4	Time in seconds per step, $MFLOPS$ -rate, speed up Sp and efficiency η_p for large wake-computation	324
D.1	Parameters for 2-D TS wave validation calculations with the DNS, TDNS and the LNS code	325
D.2	Parameters for supersonic TS wave validation calculations with the DNS, TDNS and the LNS code	326
D.3	Parameters for stability investigations using the temporal code	327

List of Tables—*Continued*

D.4	Parameters used for DNS and LNS code validation calculations of subsonic axisymmetric and 3-D wake	327
D.5	Parameters for validation calculations of turbulent boundary layers . . .	328
D.6	Parameters used for DNS and LNS calculations of supersonic base flows	328
D.7	Parameters used for DNS of supersonic base flows	329
D.8	Parameters used for RANS/FSM calculations of transitional supersonic base flows	329
D.9	Parameters used for RANS/FSM calculations of UIUC case	330

Nomenclature

Tensors

δ_{ik}	Kronecker operator
\hat{F}_{VF}^k	forcing vector
q_k, Q_k	heat-flux vector, turbulent heat-flux vector
σ_{ik}	Reynolds stress tensor
S_{ik}	strain-rate tensor
τ_{ik}	stress tensor
u_i	velocity vector
W_{ik}	vorticity tensor

Scalars

α_i	coefficients for EASM
β	parameter in contribution function
$\alpha_\theta^k / \alpha_z^l$	azimuthal / streamwise wavenumber
Δ	computational grid-size
δ	boundary layer thickness (Schlichting, 1979)
δ_1	displacement thickness
δ_2	momentum thickness (Schlichting, 1979)
ε	turbulent dissipation rate, error
η	irrotational strain-rate invariant, similarity variable
η_P	parallel efficiency
$\ddot{\gamma}$	coefficients for EASM $_\alpha$
κ	thermal conductivity, rotation angle
K	turbulent kinetic energy
$\lambda_\theta / \lambda_z$	fundamental azimuthal / streamwise wavelength
μ, μ_T	molecular kinematic viscosity, turbulent kinematic viscosity
ν, ν_T	molecular dynamic viscosity, turbulent dynamic viscosity
Π	source terms
ϕ	arbitrary function
Ψ	test function, oblique angle
ρ	density
$\sigma_\varepsilon, \sigma_K, \sigma_\rho$	constants for turbulent transport equations
θ	azimuthal angle
Θ	wavenumber
τ_T	turbulent time-scale
ξ	rotational strain-rate invariant

Nomenclature—*Continued*

A^+	van Driest factor
a^*	speed of sound
a, c	constants
c_p	specific heat coefficient
dt	time step
E	total energy
Ec	Eckert number
$f_{\varepsilon 2}, f_\mu$	wall-damping functions
H	total enthalpy
h	grid spacing
\mathbf{i}	complex number $\mathbf{i} = \sqrt{-1}$
k	physical azimuthal mode
k_N	numerical/computational azimuthal mode
kh, lh	number of azimuthal and streamwise modes
ls, la	number of symmetric and anti-symmetric azimuthal modes
(l, k)	combined Fourier mode for temporal simulations (l : streamwise mode, k : azimuthal mode)
L_K	Kolmogorov length-scale
M, M_T	Mach number, turbulent Mach number
$mr1$	number of radial points in boundary layer region
$mr2$	number of radial points in wake region
N	wall-distance
nd	number of currently computed sub-domain
$ndom1$	number of sub-domains in boundary layer region
$ndom2$	number of sub-domains in wake region
$nz1tot$	number of streamwise points in boundary layer region
$nz2tot$	number of streamwise points in wake region
$nz1$	number of streamwise points in each sub-domain in boundary layer region
$nz2$	number of streamwise points in each sub-domain in wake region
P	turbulent production
Pr, Pr_T	Prandtl number, turbulent Prandtl number
p	pressure
p, q, r	coefficients for EASM $_\alpha$
\mathcal{R}_{Su}	Sutherland temperature
\mathcal{R}	gas constant
Re, Re_T	global Reynolds number, turbulent Reynolds number
Re_{δ_1}	local Reynolds number, based on the displacement thickness

Nomenclature—*Continued*

Sp	speed-up
T	temperature
$T(\Theta)$	transfer function
t	time
u, v, w	streamwise, radial, and azimuthal velocity components
U^+	streamwise velocity component in wall-coordinates
r_{max}	height of integration domain in the radial direction
W	rotational strain rate invariant
y^+	wall normal direction in wall coordinates
z_a	length of approach flow
z_{max}	length of domain from base in the streamwise direction

Subscripts

ax	axis
c	base-corner
b	begin
D	diameter
$dist$	disturbance
ε	transport equation for turbulent dissipation rate
e	end
i, j, k, l, m	indices for cartesian tensor notation
∞	reference point values
K	transport equation for turbulent kinetic energy
max	maximum of referring quantity
T	turbulent
z, r, θ	streamwise, radial, and azimuthal coordinate

Superscripts

$-$	backward splitting / downwinding
$+$	wall coordinates, forward splitting / upwinding
n	time-level
R	RANS model

Modifiers

\star	dimensional number
$-$	Reynolds-/time-average
$'$	fluctuation quantities for Reynolds-/time-average

Nomenclature—*Continued*

\sim	Favre average, filtered variable
$''$	fluctuation quantities for Favre average
$..$	quantity for EASM $_{\alpha}$
\smile	basic state variable
$'$	disturbance quantities for linearization
\wedge	Fourier coefficient

Abbreviations

BC, B.C.	Boundary Condition
c.e.	compressible extensions
CPU	Central Processing Unit
CFL	Courant-Friedrichs-Levy ($\frac{c\Delta x}{\Delta t}$)
DNS	Direct Numerical Simulation
EASM	Explicit Algebraic Stress Model
EASM $_{\alpha}$	Explicit Algebraic Stress Model with variable ratio of $\frac{P}{\varepsilon}$
EOS	Equation Of State
FFT	Fast Fourier Transformation
FLOPS	Floating-Point Operation per Second
FSM	Flow Simulation Methodology
I.C.	Initial Condition
LDV	Laser Doppler Velocimetry
LES	Large-Eddy Simulation
LNS	Linearized Navier-Stokes
LST	Linear Stability Theory (Orr-Sommerfeld equation)
N-S	Navier-Stokes
OMP	Open Multi Processing
RANS	Reynolds Averaged Navier-Stokes
RHS	Right-Hand-Side terms of transport equation
RK	Runge-Kutta
STKE	Standard K - ε Model
TDNS	Temporal Direct Numerical Simulation
TKE	Turbulent Kinetic Energy
TS	Tollmien-Schlichting
UIUC	University of Illinois at Urbana-Champaign

Style

\mathcal{O}	order of
---------------	----------

Abstract

With funding from ARO Grant No. DAAD190210361 transitional and turbulent supersonic axisymmetric wakes were investigated by conducting various numerical experiments. The main objective was to identify hydrodynamic instability mechanisms in the flow at $M = 2.46$ for several Reynolds numbers, and relating these to coherent structures that are found from various visualization techniques. The premise for this approach is the assumption that flow instabilities lead to the formation of coherent structures. Three high-order accurate compressible codes were developed in cylindrical coordinates for this research: A spatial Navier-Stokes (N-S) code to conduct Direct Numerical Simulations (DNS), a linearized N-S code for linear stability investigations using two-dimensional basic states, and a temporal N-S code for performing local stability analyses. The ability of numerical simulations to deliberately exclude physical effects is exploited. This includes intentionally eliminating certain azimuthal/helical modes by employing DNS for various circumferential domain-sizes. With this approach, the impact of structures associated with certain modes on the global wake-behavior can be scrutinized. It is concluded that azimuthal modes with low wavenumbers are responsible for a flat mean base-pressure distribution and that $k = 2$ and $k = 4$ are the dominant modes in the trailing wake, producing a four-lobe wake pattern. Complementary spatial and temporal calculations are carried out to investigate whether instabilities are of local or global nature. Circumstantial evidence is presented that absolutely unstable global modes within the recirculation region coexist with convectively unstable shear-layer modes. The flow is found to be absolutely unstable with respect to modes $k > 0$ for $Re_D > 5,000$ and with respect to the axisymmetric mode for $Re_D > 100,000$. Furthermore, it is investigated whether flow control measures designed to weaken the naturally most significant modes can decrease the base drag. Finally, the novel Flow Simulation Methodology (FSM), using state-of-the-art turbulence closures, was shown to reproduce DNS results at a fraction of the computational cost.

1. INTRODUCTION

Flight vehicles at supersonic speed ideally are fitted with a streamlined afterbody to avoid a large drag force. In many practical applications, ranging from projectiles to missiles, however, it is not possible to implement such an aerodynamic improvement. For example, most tactical and defense missiles spend a considerable time of their flight coasting, where the burnt out rocket motor presents a blunt base to the flow. A recirculation region forms behind the base of the body that is responsible for a low base-pressure, thus causing aerodynamic drag (base-drag). Flight tests with projectiles (U.S. Army 549 projectile) conducted by Rollstin (1987) have shown that the base-drag may account for up to 35% of the total drag. Simulations performed by Sahu *et al.* (1985) for artillery shells at $M = 0.9$ showed that the base-drag can even account for up to 50% of the total aerodynamic drag. The total drag determines the range, terminal velocity or the payload of the object, thus playing a crucial role in the design process.

Due to the large contribution of the base-drag to the overall drag, modifying the near-wake region such that the base-pressure would increase could be highly rewarding with respect to drag-reduction and, as a consequence, increasing the performance characteristics of flight vehicles or projectiles. However, in order to modify the near-wake flow effectively, a detailed understanding of the underlying physical mechanisms that are responsible for the flow behavior is required. For this reason, in the past, numerous research efforts, experimental, theoretical, and computational, have focused on understanding the physics of the near-wake region, also referred to as *base flow*.

1.1 Physical Problem

Due to the complexity of the physical problem and limitations of experimental and numerical techniques, discussed below, early studies have focused almost exclusively

on the mean flow behavior. Only recently, the attention has shifted to identifying coherent structures. A review of investigations concerned with the mean flow and coherent structures is given in following.

1.1.1 Mean Flow

Historically, the fundamentals of supersonic base flows were mainly investigated experimentally. However, wind tunnel experiments suffered from the difficulty of properly supporting the (axisymmetric) base model so as not to cause undue effects on the flow field behind the base. In experimental investigations, different methods of model support have been proposed; for example, Chapman (1951) used side mounted struts, Donaldson (1955) employed a rear sting support and Dayman (1963) constructed upstream wire mounts. However, all of these techniques showed non-negligible effects on the near-wake behavior and, in particular, on the base-pressure. Other factors that can compromise experimentally obtained data include the use of intrusive probes (such as Pitot pressure tubes, hot wire probes, etc.) and wind tunnel interference, i.e., vibrations, upstream sound, noise radiated from turbulent boundary layers of the wind tunnel walls and blockage, to name a few. The strong sensitivity of the flow to perturbations (in form of sound, solid surfaces, such as probes, etc.) most likely is due to a global instability that may be present in the recirculation region (see discussion in section 1.2). It is, therefore, paramount to understand and minimize the effects of external disturbances, in particular if the objective is to investigate the role of instabilities and large coherent structures (c.f. section 1.1.2).

One remedy to most above mentioned difficulties are free-flight experiments. However, in addition to the much greater cost, free-flight experiments also suffer from major disadvantages. For example, it is not possible to map out details of the flow field as is possible with wind tunnel experiments. Also, the reliability of flight-test data is often in question because of the considerable difficulties in controlling conditions and

parameters in the free-flight tests.

A series of very carefully designed experiments of supersonic axisymmetric wakes have been performed at the University of Illinois at Urbana Champaign (UIUC) in a specifically constructed supersonic blowdown-type wind tunnel (see, e.g., Herrin & Dutton, 1989, 1994, 1995; Mathur & Dutton, 1996*a,b*). Dutton and co-workers used a forward sting support which appears to be superior to other methods with regard to minimizing flow interference. Results were obtained by non-intrusive Laser Doppler Velocimetry (LDV). The published data include the mean velocity, turbulent kinetic energy (TKE) and Reynolds stress components. Additionally, data were released for the pressure distribution on the base, obtained by pressure tabs distributed radially across the base.

The mean flow topology of the near-wake region downstream of an axisymmetric cylinder with a blunt base is depicted schematically in figure 1.1. Already the mean

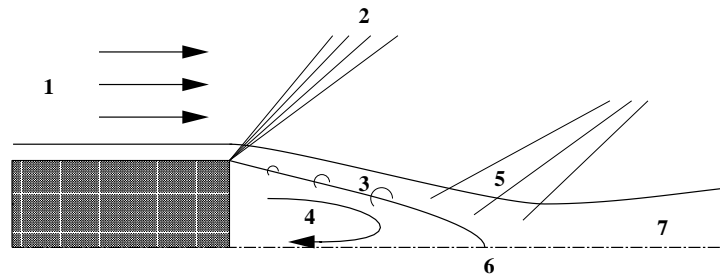


Figure 1.1 Schematic of the mean flow-field of a supersonic base flow.

flow field is highly complex: A uniform supersonic flow aligned with a cylindrical body produces an approach boundary layer (1) that separates at the body corner. The flow undergoes an expansion (2) with a large turning angle that causes a strong reduction in pressure. A thin, yet very energetic free shear-layer forms (3), separating the outer inviscid fluid from a large recirculation region (4) downstream of the base. The effect of the rapid expansion on the shear layer was investigated by Herrin & Dutton (1995). They found that the shear layer could essentially be divided

into an outer region where the turbulent fluctuations are quenched due to compressibility effects, and an inner region where the turbulent activity is magnified by the interaction of organized large-scale structures in the shear layer with low-speed fluid entrained from the recirculation region. As the free shear-layer approaches the axis of symmetry, a recompression (5) process occurs that realigns the flow with the axis and subjects the shear layer to a strong adverse pressure gradient. The location at which the mean streamwise axis-velocity is zero is defined as the reattachment point (6). Herrin & Dutton (1997) found that in this region, “extra” strain rates, such as bulk compression (due to the adverse pressure gradient), the concave streamline curvature and the lateral streamline convergence are important. It was shown that out of these additional strain rates the lateral streamline convergence is the dominant effect, reducing the Reynolds stress throughout the reattachment region. Finally, farther downstream, a trailing wake (7) develops.

The sharp radial gradients in the shear layer and the rapid spatial changes make the flow field highly complex, and therefore very difficult to investigate both experimentally and computationally, even if the flow field were “steady.” However, the mean flow topology of figure 1.1 is misleading and disguises the fact that, in reality, the flow is highly unsteady. Herrin & Dutton (1994) found that even in the “low-speed” recirculation region, a significant dynamical behavior can be observed with reverse velocities of up to $100\frac{\text{m}}{\text{s}}$.

1.1.2 Coherent Structures

It is well known that for subsonic (incompressible) wakes, the dynamics of the large (coherent) structures play a dominant role in the local and global behavior of the flow. This evidence was found from both experimental investigations and numerical simulations and was confirmed by theoretical studies. For example, in experiments of the flow around a sphere, Aschenbach (1974) detected large structures and identified

two different modes of vortex shedding: A shear-layer mode for moderate Reynolds numbers with a Strouhal number increasing with Reynolds number, and a second mode of shedding that has an approximately constant Strouhal number. He showed that the shedding from the second mode was in the form of two counter-rotating helices.

For supersonic flows, on the other hand, little is known yet about the dynamical behavior of turbulent flows. Early measurements of turbulence in an axisymmetric compressible wake include the work by Demetriades (1968*a,b*, 1976). By using an intrusive probe, his research was restricted to the far-wake and focused on the effect of compressibility on turbulent structures. Nevertheless, some quantitative evidence of the existence of dominant large structures in supersonic axisymmetric wake flows was provided: Amplitude spectra (see figures 11 to 14 in Demetriades, 1968*b*) displayed distinct peaks at relatively low frequencies, thus indicating the presence of dominant modes (structures). In addition, the amplitude distribution for the velocity fluctuations (figures 2 and 3, respectively, of Demetriades, 1968*b*) resembled that of an incompressible axisymmetric wake, where it is known that the resulting profile is due to the presence of dominant, large coherent structures (see, e.g., Cannon & Champagne, 1991). Morkovin (1968) suggested that when normalized properly, the distribution of fluctuations (as caused by large structures) has a universal character and that compressibility effects can be accounted for by the mean density variations alone. Gaviglio *et al.* (1977) decomposed different terms in the TKE equation, focusing on the production term and showing the effects of compressibility and streamline curvature on turbulence production. Their analysis showed that Morkovin's hypothesis is fully valid in self-preserving flows. For rapid expansions or compressions, on the other hand, higher order approximations might be needed.

For increasing Mach numbers, it was observed that shear layers and jets have a reduced spreading rate which was commonly attributed to density effects alone. Brown & Roshko (1974), after studying incompressible shear layers with large density

ratios, concluded that it was the intrinsic compressibility that affects the development of the supersonic shear layer. In their experiments they were also among the first to identify what we today call coherent turbulent structures. Hussain (1986) defines these structures as “a connected turbulent fluid mass with instantaneously phase-correlated vorticity over its spatial extent.”¹ Large coherent structures were also observed in experiments of supersonic jets by Oertel (1979).

Bogdanoff (1983) introduced the convective Mach number² as a parameter for the compressibility of the flow. His work was extended by Papamoschou & Roshko (1988) who did an extensive study of turbulent shear-layers that clearly revealed the presence of dominant large-scale structures for various Mach numbers and density ratios. Further work on turbulent mixing-layers was done by Elliott *et al.* (1995) who used single and double pulsed visualizations to track the evolution of the large-scale structures. In their work, Papamoschou & Bunyajitradulya (1996) addressed the following observations: For increasing convective Mach number, not only does the growth rate of the shear layer decline but the turbulence becomes less organized (shows less 2-D coherence) and 3-D disturbances become more amplified. Some analytical work, validated with numerical simulations, was done by Sarkar *et al.* (1991) who focused on the effect of the dilatational terms on compressible turbulence. They identified another measure for compressibility, namely the turbulent Mach number which relates the speed of the turbulent fluctuations with the local speed of sound. A comprehensive review of compressibility effects on turbulence is given by Lele (1994).

In more recent experimental investigations, Bourdon & Dutton (1998); Bourdon *et al.* (1998); Bourdon & Dutton (2001) were able to clearly show the presence of large coherent structures in the axisymmetric base flow by employing planar visualizations

¹Crow & Champagne (1971) had also observed coherent structures in their experiments of jet turbulence but called them “orderly structures.”

²This is the Mach number in a coordinate system travelling with the velocity of the dominant waves.

to complement their earlier LDV measurements.³ The observed structures appeared to be of significant size relative to the shear layer thickness.

Thus, sufficient evidence exists that large coherent structures are present in supersonic axisymmetric wakes and may indeed play an important role. Furthermore, it is of great interest to understand how these structures are altered by passive control mechanisms, such as “boat-tailing” (see Bowman & Clayden, 1968; Bourdon & Dutton, 2000), “base bleed” (c.f. Cortwright & Schroeder, 1951; Reid & Hastings, 1959; Clayden & Bowman, 1968; Valentine & Przirembel, 1970; Sahu *et al.*, 1985; Sahu & Heavey, 1995; Mathur & Dutton, 1996*a,b*), “base burning” (Hubbartt *et al.*, 1981; Ding *et al.*, 1992), etc. Such techniques were shown to modify the mean base flow and, as a consequence, the base-drag. However, the underlying mechanisms responsible for the changes are not understood. In order to optimize such techniques for practical applications, it is essential that the fundamental mechanisms that are responsible for these changes be brought to light. The key to uncovering these essential mechanisms is in first understanding the role of the coherent turbulent flow structures and, in particular, how the dynamics of these structures might be influenced by techniques for drag reduction. Questions that thereby arise are: How are these structures generated, i.e., are they a consequence of a convective instability of the shear layer or are they generated by global modes originating in the recirculation region? Finally, how significant is the influence of these structures on the mean flow, and in particular on the base-pressure that determines the base-drag?

Although the existence of large-scale structures could be verified in experiments, the high speeds of the flows under investigation make an accurate observation of the generation and evolution of these structures very difficult. So far, it has been virtually impossible to obtain time-accurate three-dimensional visualizations of these structures. In light of the difficulties, uncertainties and high costs associated with experiments, numerical simulations have been considered as attractive alternatives

³LDV is a pointwise technique that is incapable of directly investigating large scale structures.

and/or complements to experimental investigations.

1.2 Numerical Simulations

There is considerable evidence that the formation of large-scale structures is due to hydrodynamic instabilities of the (time-averaged) mean flow and that the development of these structures can be captured by stability theory (see, e.g., Gaster *et al.*, 1985; Oertel, 1990; Theofilis, 2003). In fact, certain aspects of the development can be captured with linear stability theory, although intensities (amplitudes) of the structures are often too large for the linear stability theory to be valid. Experimental results for incompressible turbulent mixing layers, two-dimensional turbulent wakes, and axisymmetric wakes with a blunt base have shown that certain key features, such as dominant frequencies, mode shapes (amplitude distributions), and streamwise spacing (streamwise wavelengths) of the structures can be well predicted by linear stability theory (Wyganski *et al.*, 1986; Marasli *et al.*, 1989). These investigations support the notion that hydrodynamic instabilities give rise to the generation of large-scale structures and affect their spatial and temporal development.

1.2.1 Hydrodynamic Stability Investigations

There are several approaches to investigate the stability behavior of a given flow. Standard linear stability theory (LST) deals with instabilities of infinitesimally small amplitudes that develop in a parallel flow, containing only one inhomogeneous spatial direction. Mathematically, the problem can be formulated as an eigenvalue problem (EVP) that requires the solution of the Orr-Sommerfeld equation. Theofilis (2003) demonstrated that, once the parallel assumption is not invoked and the EVP is extended to multiple dimensions, this method becomes prohibitively expensive in terms of computational cost. In spite of (or because of) the restrictions of parallel theory, LST has been applied by many researchers. For example, Huerre & Monkewitz

(1985) presented the distinction between convective and absolute instabilities in parallel shear flows, a terminology that originated from plasma physics. According to their definition, a flow is convectively unstable if a pulse disturbance decays to zero in time at all locations in the flow. On the other hand, an absolute instability is present if a disturbance leads to exponential growth in the entire field. Monkewitz (1988) found analytically that the first helical mode is absolutely unstable in the near wake behind a bluff body for Reynolds numbers in excess of 3,300 (based on wake-diameter and freestream velocity). Monkewitz also found that large-scale structures co-exist with a recirculation region, which was later confirmed experimentally by Cannon & Champagne (1991). The experiments also revealed that these large-scale structures are predominantly helical with a dominant first azimuthal mode.

In an extensive review on different classes of instabilities for spatially growing flows, Huerre & Monkewitz (1990) introduced the concept of global instability in the context of slow variations of the basic flow in the streamwise direction. Using numerical simulations in conjunction with LST, absolute/global instabilities were found for a two-dimensional bluff body with a blunt base by Hannemann & Oertel (1989). Oertel (1990) found that the development of the von Kármán vortex street can be suppressed using passive control mechanisms such as base-bleed or suction in order to avoid the absolutely unstable region. Numerical simulations for an axisymmetric body with a blunt base conducted by Schwarz *et al.* (1994) also revealed the existence of absolutely/globally unstable modes that are of helical nature.

An approach for solving the stability equations where the basic state features a weak dependence of the streamwise coordinate was accomplished by the derivation of the parabolized stability equations (Herbert, 1997). If, however, the basic state is truly non-parallel, another approach is required. The numerical integration of the linearized Navier-Stokes (LNS) equations appears to be an efficient method for conducting linear stability investigations of a non-parallel, steady or time-periodic state. A recent summary of insights gained into three-dimensional linear stability

investigations was given by Theofilis (2003). Here, a multidimensional eigenvalue problem is solved with the underlying basic state being a fully two-dimensional, steady or time-periodic non-parallel flow. The term *BiGlobal* instability was introduced, to distinguish this kind of analysis from the previous, above mentioned, absolute or global instability work, that assumes a parallel or weakly non-parallel basic state, respectively.

However, once the nonlinear behavior becomes of interest, which is the case when investigating the effect of nonlinear disturbances (such as coherent structures) on the mean flow, the full Navier-Stokes equations need to be solved, i.e., Direct Numerical Simulations (DNS) need to be conducted. Supported by the dramatic increase of available computing power of supercomputers over the last decades, numerous attempts have been made to calculate the flow field around and behind axisymmetric bodies aligned with the free stream. In addition to the potential of providing further understanding of the relevant physics involved, these calculations were also motivated by the considerable challenge that this complex flow field represents for the area of computational fluid dynamics. As mentioned above, the flow contains a large variety of difficulties such as the combination of shock waves, thin free shear-layers, boundary layers, and recirculating regions that have to be captured correctly in a numerical simulation. In addition, high Reynolds number flows exhibit a very broad spectrum of time- and length-scales that, in the case of DNS, need to be fully resolved by the computational grid. For that reason, DNS of wakes at Reynolds numbers in the order of $\mathcal{O}(10^6)$, as investigated by Dutton and co-workers, with sufficient resolution in all three dimensions and in time, are out of reach even with present supercomputers and probably will be for a considerable time. For that reason, other approaches for computing such flows have been considered that require turbulence models, such as Reynolds Averaged Navier-Stokes equations (RANS) and Large Eddy Simulation (LES).

1.2.2 Turbulence Modelling

A filter can be applied to the governing equations (see section 2) of the underlying problem. The averaged equations then nearly take the form of the original equations (which would be used for DNS), except for turbulence closure terms which have to be modelled. Traditionally, the modelling of the closure terms was separated into two categories: LES and RANS.

For LES, the filter applied to the governing equations is of a spatial nature and only the large-scale motion is computed directly. The sub-grid scale structures, which are assumed to be isotropic, are modelled. This method was initially proposed by Smagorinsky (1963) who based his model on the Boussinesq assumption (Boussinesq, 1877) which states that the turbulent stresses can be related linearly to the mean velocity gradients by an eddy-viscosity. For RANS, where typically a temporal filter or ensemble averages are used, the entire spectrum of turbulent fluctuations is modelled and only a steady mean flow is solved for. In the case of non-turbulent temporal fluctuations of the mean flow this class of turbulence models has been extended to unsteady RANS (URANS).

In terms of resolution requirements, typical grids used for LES are coarser than those employed by DNS. Nevertheless, the large scales need to be resolved in a three-dimensional and time-dependent fashion. Also, for wall-bounded flows, the gradient of the viscous sublayer has to be captured which, for large Reynolds numbers, can be prohibitively expensive – even for LES. RANS simulations, in contrast, can often be carried out in two dimensions and only require resolving the mean flow gradients. They are, therefore, the least expensive method even though additional transport equations⁴ have to be solved to obtain an estimate of the turbulent length- and time-scales (it has been argued by Speziale, 1995, that two-equation models constitute the minimum level of closure that is physically acceptable).

⁴The number of additional equations determines the type of model: zero, one- or two-equation model.

Owing to the least restricting resolution requirements, the RANS approach was the first to be considered for simulating supersonic base flows. Early RANS calculations include thin-layer Navier-Stokes simulations employing an algebraic eddy-viscosity (zero equation) model by Sahu *et al.* (1985) or by Petrie & Walker (1985). The calculations were able to capture the qualitative features of the experimentally obtained flow field. However, relevant quantities, such as turbulent shear-stresses and, in particular, such fundamental aspects as the all important base-pressure or the size of the separation bubble (recirculation region), were often not predicted well. Childs & Caruso (1987) surveyed existing computational Navier-Stokes methods for calculating turbulent compressible wake flows. They concluded that inadequate numerical resolution of the large gradients and, in particular, the turbulence modelling were the major culprits for not being able to reliably and accurately calculate the flow field.

RANS calculations were also employed for investigating different means of drag-reduction, such as the effects of base bleed (see, e.g., Danberg & Nietubicz, 1992; Sahu & Heavey, 1995) and base burning (Nietubicz & Gibeling, 1993). The simulations showed a correct trend for the drag reduction when compared with experimental results but, in some cases, even global flow field characteristics such as the center-line velocity were not in good agreement with experiments. Two facts suggested that some relevant physical mechanisms were not captured by the computational approach: First, using different turbulence models but otherwise identical codes yielded inconsistent (and often contradictory) results. Second, the predicted pressure distribution on the base consistently deviated from experimental results.

Considerable efforts were made to determine the influence of the dilatational terms on compressible turbulence in the hope that this had been the reason for failure of earlier computations. Sarkar *et al.* (1991) and Sarkar (1995) showed that these terms can be responsible for up to 20% of the TKE budget. Sarkar (1992) introduced a simplified model, that algebraically relates the pressure-dilatation to quantities

obtained in incompressible closures.

Tucker & Shyy (1993) and, more recently, Krishnamurty & Shyy (1997) made an assessment of $K - \varepsilon$ model RANS calculations of the UIUC flow using the full Navier-Stokes equations. They incorporated the above mentioned as well as additional compressibility extensions and showed some improvement over previous results. However, Tucker & Shyy (1993) found that the eddy viscosity in the recirculation region and the K -level in the shear layer were overpredicted and mentioned that the model did not account for baroclinic torque, which is an important factor in the TKE budget. Furthermore, a strong (unphysical) radial variation of the base-pressure was observed. The shortcomings of steady RANS calculations in combination with the presented evidence of the existence of energetic, large scale structures that may have a profound effect on the mean flow, as discussed above, suggest that unsteady calculations need to be carried out in order to achieve better agreement with experiments.

Therefore, it appears that LES would be the method of choice because of the ability to capture three-dimensional and unsteady effects. However, several shortcomings of the “standard” Smagorinsky LES model might make this model ill-suited for the current research. Some of the deficiencies include the failure to account for the normal stress components (which are important in the recirculation region, for example), an ad-hoc constant that is only valid for a certain flow region and “damping functions that are needed at the walls which are empirical in nature and do not apply to general wall bounded turbulent flows” (Speziale, 1997). Further shortcomings of this widely used model can also be found in Jiménez & Moser (1998).

Fureby (1999) used LES to compute the supersonic base flow, employing different subgrid models. For modelling the subgrid scales, a standard Smagorinsky model, a one-equation eddy-viscosity model and a Monotone Integrated LES model were used. The results were shown to not depend noticeably on the underlying SGS model, which suggests that, in his calculations, the resolved scales were fairly independent

of the details of the subgrid scales. The calculations overpredicted the base-pressure and underpredicted the recirculation length which was attributed to the effect of a different approach boundary layer thickness in the calculations when compared to experiments. In order to achieve a better prediction of the approach boundary layer, a considerably better resolution would be required in that region, increasing the overall computational cost drastically.

In order to reduce computational costs while still computing unsteady flows with large coherent structures, hybrid RANS/LES approaches have been proposed. The underlying principle is to conduct a RANS-type simulation close to a wall and perform an LES away from the wall to capture the unsteadiness. One way of implementing this method has been proposed by Spalart *et al.* (1997) and is known as Detached Eddy Simulation (DES). In principle, the method compares the distance to the closest wall with the product of the local grid spacing and an empirical constant. For small distances, the eddy viscosity is computed according to a one-equation RANS model, otherwise a Smagorinsky type LES is employed.

This approach was applied to the UIUC experiments by Forsythe & Hoffmann (2000) who reported results agreeing reasonably well with the experimental data for values of the empirical constant smaller than originally suggested. The mean flow quantities in the recirculation region were found to deviate from the experiments and were dependent on the utilized grid, even though they reported very good agreement of the mean base pressure distribution. Later work by Forsythe *et al.* (2002) included the testing of DES based on both the originally used Spalart-Allmaras model and a Shear Stress Transport model Menter (1994) while also incorporating the compressible shear-layer corrections into the turbulent transport equations.

Another approach, that smoothly blends DNS, LES and RANS has been suggested by Speziale (1998*a,b*) and was named the Flow Simulation Methodology (FSM) (for details, see review papers by Fasel *et al.*, 2002, 2006). The centerpiece of FSM is

a strategy to provide a proper amount of modelling of the subgrid scales based on the “local and time-instantaneous physical resolution” of the calculation. This is accomplished by employing a so-called “contribution function” which locally and instantaneously compares the smallest relevant turbulent flow scales to the local computational grid size. The contribution function has to be designed such that it provides no modelling if the computation is locally well resolved so that the simulation approaches a DNS in the fine-grid limit. The contribution function needs to provide modelling of all scales in the coarse-grid limit and thus RANS or URANS calculations are conducted. In between these resolution limits, the contribution function adjusts the necessary modelling for the unresolved scales while the larger (resolved) scales are computed as in “traditional” LES. However, in contrast to “traditional” LES, the subgrid scales are now modelled using a sophisticated two-equation turbulence model. Furthermore, due to the ability of FSM to locally and instantaneously adjust for the required contribution of turbulence modelling, regions away from the wall that lack sufficient grid-resolution can be computed in the URANS limit. This is in contrast to the DES approach, where the method is restricted to switching to RANS close to walls only. Therefore, the FSM approach appears to be a promising strategy for the calculation of high Reynolds number supersonic wakes. For that reason, this methodology will be employed in the current investigation. The same idea of using a contribution function to scale the closure terms was similarly incorporated in the “limited numerical scales” approach by Batten *et al.* (2000, 2002).

1.3 Present Research

The objective of this work is to contribute towards the understanding of the origin and the dynamics of coherent structures in supersonic, axisymmetric wakes behind bluff bodies. The premise for this study is the underlying assumption that flow instabilities lead to the formation of coherent structures and determine their evolution.

As mentioned before, it is not yet clear whether the structures that have been detected in supersonic base flows are a consequence of a convective instability of the shear layer or of global modes that might be present in the recirculation region. Furthermore, the effect of large coherent structures, associated with specific instabilities, on the mean flow is of particular interest, as they presumably strongly affect the base-pressure and, consequently, determine the base-drag.

To that end, a high-order accurate compressible Navier-Stokes (N-S) solver in cylindrical coordinates was developed for numerical experiments of transitional and turbulent supersonic base flows. In addition, a linearized version of the full N-S code was developed for linear stability investigations using a two-dimensional basic state. Furthermore, a temporal N-S code was implemented for performing local stability calculations (for a detailed discussion of the spatial versus temporal approach see Fasel, 1990). In order to pursue the above named objectives, numerical experiments are conducted exploiting the ability of numerical simulations to deliberately exclude physical effects and, therefore assess their importance. For example, by employing DNS for various circumferential domain-sizes, certain azimuthal modes can be intentionally eliminated. Thereby, their impact on the global wake-behavior can be scrutinized. In addition, when using the temporal code, it is sought to exploit the fact, that the effects caused by streamline curvature, pressure gradients, shocks and expansion waves, etc. are eliminated by this model. This is in contrast to many previous investigations that have employed the temporal model. There, the objective oftentimes was to extend the approach by including additional terms that model non-parallel effects etc., such that temporal results could be compared directly with data obtained from spatial calculations (see, e.g., Guo *et al.*, 1996). Here, by comparing with results from spatial calculations, the importance of the omitted physical mechanisms can be evaluated. In particular, by conducting spatial and temporal simulations in a complementary fashion, instabilities can be identified as local or global modes. In the following, a brief outline of the report is given:

In chapter 2, the governing equations are presented. The filtered Navier-Stokes equations are given in index notation in section 2.1. All turbulence closures and transport equations, including the extension to wall-bounded flows, are described in section 2.2. A more detailed description of the FSM is given in section 2.3, followed by the introduction of the linearized N-S approach including a high Reynolds number extension in section 2.5. The full form of all equations and the derivation of the LNS equations are compiled in Appendix A.

Chapter 3 contains information about the numerical method for all codes developed for the present research. This includes the spatial and temporal discretization, the boundary and initial conditions, the axis treatment and a brief overview of grid stretching, filtering and parallelization. The chapter is completed by presenting the differences in the numerical method between the full N-S and the TDNS and LNS codes. Further details about the numerical method, such as the finite-difference stencils, a stability analysis of the numerical method and the derivation of filters for non-equidistant grids are presented in Appendix C. Details of the parallelization by domain decomposition and a performance study of the algorithms are given in Appendix C.6.

Chapter 4 is concerned with establishing that the developed codes are suitable for the investigation of hydrodynamic instabilities. To that end, simulations of Tollmien-Schlichting (TS) waves and oblique disturbances in subsonic and supersonic boundary layers are discussed in sections 4.1–4.3. The capability of capturing the formation and evolution of coherent structures is demonstrated with reproducing results by Schwarz (1996) of the flow field behind an axisymmetric afterbody. In addition, the LNS code is employed for this case to determine whether the flow is absolutely unstable with respect to more than one helical mode. Finally, wall-distance independent versions

of the explicit algebraic stress model (EASM) of Gatski & Speziale (1993) and the generalized EASM (EASM _{α}) by Rumsey *et al.* (2000), including compressibility extensions, are validated for incompressible, flat-plate turbulent boundary layers and the axisymmetric approach flow of UIUC in section 4.5. A 1-D variant of the temporal code is also used in order to achieve a high turn-around-time for resolution and parameter studies.

The linear stability behavior of axisymmetric wakes at $M = 2.46$ is investigated in chapter 5 for various Reynolds numbers. The main focus is on establishing whether the flow is absolutely or convectively unstable with respect to two- or three-dimensional disturbances. Furthermore, it is investigated if the instabilities are of local or global nature, and whether helical modes are present as for subsonic wakes. To accomplish these objectives, complementary spatial calculations, employing the LNS code, and local TDNS simulations are carried out.

In chapter 6, DNS results are presented for base flows at $M = 2.46$ and three different Reynolds numbers. For each Reynolds number, simulations were conducted for various circumferential domain-sizes, thereby deliberately eliminating azimuthal/helical modes. Thus, the effect of large-scale structures associated with particular azimuthal/helical modes on the global flow behavior, in particular the base-pressure, can be evaluated. In order to determine which modes are most important, several figures of merit are scrutinized. These include temporal spectra for the detection of dominant frequencies connected with certain azimuthal modes, endviews and radial mode-shapes in order to determine which modes are responsible for the resulting wake-pattern, time-averaged base-pressure distributions and streamwise axis velocity profiles. A vortex-identification criterion is employed, along with visualizations of contours of total vorticity, instantaneous local Mach number and the magnitude of baroclinic torque, to identify the relevant structures in the flow. An effort is made

to relate the observed structures to instability mechanisms that might be present for the mean or the instantaneous flow-field. Once it has been established which modes dominate the global flow behavior for various Reynolds numbers, an attempt is made to exploit the identified hydrodynamic instabilities for influencing the near-wake. The effects of flow-control on the resulting wake-patterns and the mean base-pressure are investigated.

Axisymmetric RANS and three-dimensional FSM calculations are discussed in chapter 7. The performance of different turbulence models for RANS and FSM calculations are evaluated for transitional base flows by comparing the results with the DNS data of chapter 6. The turbulence closures include the state-of-the-art EASM _{α} , the original EASM and the standard $K - \varepsilon$ model (STKE) by Launder *et al.* (1975), for comparison. In addition, the applicability of compressibility extensions, coefficient modifications as suggested by Papp *et al.* (2002), and the influence of the inflow conditions on the global solution are investigated. Finally, both the RANS and the novel FSM approach are applied to the UIUC case. The results are discussed and compared to the experimental data in section 7.4.

To conclude, the most important results are summarized in chapter 8, followed by a compilation of relevant parameters for all calculations conducted (Appendix D) and the list of references.

2. GOVERNING EQUATIONS

2.1 Navier-Stokes Equations

The compressible Navier-Stokes equations, consisting of conservation of mass, momentum and total energy govern the physical problem under consideration. The flow is assumed to be an ideal gas with constant specific heat coefficients. For simplicity, all equations in this section are presented in tensor notation. The governing equations in cylindrical coordinates are given in Appendix A.1.

All quantities are made dimensionless using the flow quantities at a reference location in the flow; here the free-stream/inflow location is used. The radius of the body was chosen as the reference length. The non-dimensionalization results in the following dimensionless parameters:

$$Re = \frac{\rho_{\infty}^* u_{\infty}^* r^*}{\mu_{\infty}^*} \quad , \quad M_{\infty} = \frac{u_{\infty}^*}{a_{\infty}^*} \quad , \quad Pr = \frac{\mu_{\infty}^* c_p^*}{\kappa_{\infty}^*} \quad , \quad Ec = \frac{u_{\infty}^{*2}}{c_p^* T_{\infty}^*} \quad . \quad (2.1)$$

When using any kind of turbulence model, the governing equations need to be known in filtered form. For LES-type calculations, a spatial filter is used whereas for RANS-type calculations, filtering is mostly associated with a temporal average. However, the filtered equations take the same form, regardless of whether a temporal or spatial average is considered; only the method of obtaining the sub-grid quantities is different. Therefore, the overbars that appear in the averaged equations can either represent a spatial or temporal average (i.e., for this research, the implicit filter inherent to the discretization scheme with a filter width related to the grid size or time-step). A tilde denotes a Favre-average defined as

$$\tilde{f} = \frac{\overline{\rho f}}{\bar{\rho}} \quad . \quad (2.2)$$

The velocity vector u_i and the temperature T are decomposed into a Favre-average and a fluctuating part (denoted by $''$) and the pressure p and the density ρ are split

into the Reynolds-average (denoted by $\bar{}$) and a fluctuating part (denoted by $\tilde{}$). The non-dimensional resolved continuity, momentum and the energy equations are:

$$\frac{\partial \bar{\rho}}{\partial t} + \frac{\partial}{\partial x_k} (\bar{\rho} \tilde{u}_k) = 0 \quad , \quad (2.3)$$

$$\frac{\partial}{\partial t} (\bar{\rho} \tilde{u}_i) + \frac{\partial}{\partial x_k} [\bar{\rho} \tilde{u}_i \tilde{u}_k + \bar{p} \delta_{ik} - (\bar{\tau}_{ik} - \bar{\rho} \sigma_{ik})] = 0 \quad , \quad (2.4)$$

$$\frac{\partial}{\partial t} (\bar{\rho} E_R) + \frac{\partial}{\partial x_k} [\bar{\rho} \tilde{u}_k H + \bar{q}_k + Q_k - \tilde{u}_i (\bar{\tau}_{ik} - \bar{\rho} \sigma_{ik})] = \Pi \quad , \quad (2.5)$$

where the resolved stress-tensor is computed as

$$\bar{\tau}_{ik} = \frac{2}{Re} \bar{\mu} \left(\tilde{S}_{ik} - \frac{1}{3} \tilde{S}_{jj} \delta_{ik} \right) \quad , \quad (2.6)$$

with the resolved strain rates

$$\tilde{S}_{ik} = \frac{1}{2} \left(\frac{\partial \tilde{u}_i}{\partial x_k} + \frac{\partial \tilde{u}_k}{\partial x_i} \right) \quad . \quad (2.7)$$

The resolved total enthalpy and total energy are defined as

$$H = E + \frac{\bar{p}}{\bar{\rho}} \quad , \quad E = c_v \tilde{T} + \frac{1}{2} \tilde{u}_i \tilde{u}_i \quad , \quad (2.8)$$

respectively. The resolved pressure is obtained from the equation of state

$$\bar{p} = \frac{\bar{\rho} \tilde{T}}{\gamma M^2} \quad , \quad (2.9)$$

with $\gamma = 1.4$. The resolved heat flux is computed from

$$\bar{q}_k = - \frac{\kappa}{Pr Ec Re} \frac{\partial \tilde{T}}{\partial x_k} \quad , \quad (2.10)$$

with $Pr = 0.70$ and the Eckert number being $Ec = (\gamma - 1) M^2$. Finally, the resolved molecular viscosity $\bar{\mu}$ and the resolved thermal conductivity are computed according to Sutherland's law (see White, 1991)

$$\bar{\mu}(\tilde{T}) = \bar{\kappa}(\tilde{T}) = \tilde{T}^{\frac{3}{2}} \left(\frac{1 + \mathcal{R}_{Su}}{\tilde{T} + \mathcal{R}_{Su}} \right) \quad , \quad \text{with} \quad \mathcal{R}_{Su} = \frac{110.6 K}{T_{\infty}^*} \quad . \quad (2.11)$$

The above equations contain three terms that do not occur in the unfiltered equations: the subgrid-tensor $\bar{\rho}\sigma_{ik}$, the subgrid heat-flux vector Q_k and the source term Π in the energy equation. These terms have to be modelled (see section 2.2). For a DNS, where it is assumed that all relevant time- and length-scales are resolved by the computational grid and a sufficiently small time-step, the model terms are set to zero, implying that $\phi = \bar{\phi} = \tilde{\phi}$. In the other limit, where the filter-width is so large that all fluctuations are filtered out, a traditional RANS is recovered.

2.2 Turbulence Models

If the numerical simulations are not performed in the DNS limit, a closure is needed for equations (2.4) - (2.5). In the following section, several models for the subgrid-stress tensor, $\bar{\rho}\sigma_{ik}$, the subgrid heat-flux vector, Q_k , and the source term, Π , are introduced.

2.2.1 Turbulent Stress-Tensor

Three different closures are employed for representing the turbulent stress-tensor: a “standard” K - ε model (c.f. Wilcox, 1998), the explicit algebraic Reynolds Stress model (EASM) of Gatski & Speziale (1993) and the generalized version of the EASM (EASM $_{\alpha}$, Rumsey & Gatski, 2001).

Standard $K - \varepsilon$ Model (STKE)

The subgrid stress-tensor is computed from

$$\bar{\rho}\sigma_{ik}^R = \frac{2}{3}\bar{\rho}K\delta_{ik} - 2\mu_T \left(\tilde{S}_{ik} - \frac{1}{3}S_{jj}\delta_{ik} \right), \quad (2.12)$$

where the eddy viscosity is given as

$$\mu_T = c_{\mu}f_{\mu}\tau_T K, \quad (2.13)$$

with $c_\mu = 0.09$. The turbulent time-scale is given as the ratio between the turbulent kinetic energy and the turbulent dissipation rate $\tau_T = \frac{K}{\varepsilon}$. This model is widely used in commercial and research codes where, for wall-bounded flows, an empirical wall-damping function, f_μ , is frequently employed to enforce the logarithmic law of the wall. A more detailed discussion of wall-damping functions is given in section 2.2.5.

Explicit Algebraic Stress Model (EASM)

The EASM was derived from the explicit solution of the equilibrium form of the modelled Reynolds stress transport equation for incompressible flows in Gatski & Speziale (1993) and extended to compressible flows by Speziale (1997). The model is of the form of an anisotropic eddy viscosity model with strain-dependent coefficients:

$$\begin{aligned} \bar{\rho}\sigma_{ik}^R = & \frac{2}{3}\bar{\rho}K\delta_{ik} - \bar{\rho}K\tau_T f(\eta, \xi) \left[\alpha_1 \left(\tilde{S}_{ik} - \frac{1}{3}\tilde{S}_{jj}\delta_{ik} \right) \right. \\ & - \alpha_2 \tau_T \left(\tilde{S}_{ij}\tilde{W}_{jk} + \tilde{S}_{kj}\tilde{W}_{ji} \right) \\ & \left. + \alpha_3 \tau_T \left(\tilde{S}_{ij}\tilde{S}_{jk} - \frac{1}{3}\tilde{S}_{lm}\tilde{S}_{lm}\delta_{ik} \right) \right]. \end{aligned} \quad (2.14)$$

with $\tilde{W}_{ik} = \frac{1}{2} \left(\frac{\partial \tilde{u}_i}{\partial x_k} - \frac{\partial \tilde{u}_k}{\partial x_i} \right)$.

To remove the possibility of singularities, a regularized version for $f(\eta, \xi)$ is used:

$$f(\eta, \xi) = \frac{3}{3 - 2\eta^2 + 6\xi^2} \approx \frac{3(1 + \eta^2)}{3 + \eta^2 + 6\eta^2\xi^2 + 6\xi^2}. \quad (2.15)$$

The terms η and ξ are related to the irrotational and the rotational strain rate invariants according to

$$\xi = \frac{\alpha_2}{\alpha_1} \frac{K}{\varepsilon} \left(\tilde{W}_{lm}\tilde{W}_{lm} \right)^{\frac{1}{2}}, \quad \eta = \frac{1}{2} \frac{\alpha_3}{\alpha_1} \frac{K}{\varepsilon} \left(\tilde{S}_{lm}\tilde{S}_{lm} \right)^{\frac{1}{2}}. \quad (2.16)$$

The values of the coefficients appearing in equations (2.14) and (2.16) depend on the flow region. In the approach boundary layer, the ratio of production over dissipation rate is assumed to be unity, whereas in the separated flow regime, $\frac{P}{\varepsilon} = \frac{c_{\varepsilon 2}-1}{c_{\varepsilon 1}-1}$, resulting in different values of α_i (c.f. Sandberg & Fasel, 2003).

Generalized Version of EASM ($EASM_\alpha$)

As mentioned above, the flow under investigation features physically very disparate regions such as a boundary layer, a free shear layer subject to pressure gradients and a recirculation region. It is safe to say, that assuming the production to dissipation ratio to be a constant cannot hold for all regions. For that reason, the generalized EASM, where the production over dissipation ratio is *not* fixed to a constant but computed locally and instantaneously as presented in Rumsey *et al.* (2000) was also chosen. In order to locally determine the ratio of turbulent production over dissipation, the roots of a cubic equation have to be solved. The turbulent stress-tensor is computed from

$$\begin{aligned} \bar{\rho}\sigma_{ik}^R = \frac{2}{3}\bar{\rho}K\delta_{ik} & - 2\ddot{\mu}_T \left[\left(\tilde{S}_{ik} - \frac{1}{3}S_{jj}\delta_{ik} \right) \right. \\ & \left. + a_2a_4 \left(\tilde{S}_{ij}\tilde{W}_{jk} + \tilde{S}_{kj}\tilde{W}_{ji} \right) - 2a_3a_4 \left(\tilde{S}_{ij}\tilde{S}_{jk} - \frac{1}{3}\tilde{S}_{lm}\tilde{S}_{lm}\delta_{ik} \right) \right]. \end{aligned} \quad (2.17)$$

The eddy viscosity is given by

$$\ddot{\mu}_T = \bar{\rho}\ddot{\nu}_T = \ddot{C}_\mu\bar{\rho}K\tau_T = -\bar{\rho}K\tau_T \left(\frac{\alpha_1}{\tau_T} \right). \quad (2.18)$$

Note, that the eddy viscosity used by the $EASM_\alpha$ is not the same as used for the turbulent heat-flux (see equation 2.25) and the transport equations for K and ε (equations 2.23 and 2.24).

The value of α_1/τ_T is obtained by locally and instantaneously solving the following cubic equation:

$$\left(\frac{\alpha_1}{\tau_T} \right)^3 + p \left(\frac{\alpha_1}{\tau_T} \right)^2 + q \left(\frac{\alpha_1}{\tau_T} \right) + r = 0, \quad (2.19)$$

where

$$\begin{aligned} p &= -\frac{\ddot{\gamma}_1}{\phi\ddot{\gamma}_0}, \\ q &= \frac{1}{(2\phi\ddot{\gamma}_0)^2} \left(\ddot{\gamma}_1^2 - 2\phi\ddot{\gamma}_0a_1 - \frac{2}{3}\phi a_3^2 - 2W^2\tau_T^2a_2^2 \right), \\ r &= \frac{\ddot{\gamma}_1a_1}{(2\phi\ddot{\gamma}_0)^2}. \end{aligned} \quad (2.20)$$

The needed parameters are assembled as follows:

$$\begin{aligned}\phi &= \tilde{S}_{ik}\tilde{S}_{ik}\tau_T^2 \quad , \quad W = -\widetilde{W}_{ik}\widetilde{W}_{ik} \quad , \\ a_4 &= \frac{\tau_T}{\ddot{\gamma}_1 - 2\ddot{\gamma}_0\left(\frac{\alpha_1}{\tau_T}\right)\phi} \quad , \\ \ddot{\gamma}_0 &= \frac{C_1^1}{2} \quad , \quad \ddot{\gamma}_1 = \frac{C_1^0}{2} + \left(\frac{C_{\epsilon 2} - C_{\epsilon 1}}{C_{\epsilon 1} - 1}\right) .\end{aligned}\tag{2.21}$$

The constants are given as $C_{\epsilon 1} = 1.44$, $C_{\epsilon 2} = 1.83$, $C_1^0 = 3.4$, $C_1^1 = 1.8$, $a_1 = 0.4866$, $a_2 = 0.8$ and $a_3 = 0.375$. An algorithm to solve the cubic equation is given in detail in Rumsey & Gatski (2001). Hence, the turbulent viscosity for the most recent EASM $_{\alpha}$ is computed without having to assume a constant ratio of turbulent production over turbulent dissipation rate, in contrast to the original EASM of Gatski & Speziale (1993). Comparing the turbulent viscosity of the two models gives

$$2\dot{\mu}_T = \alpha_1 \bar{\rho} \frac{K^2}{\varepsilon} f(\eta, \xi) ,\tag{2.22}$$

where $f(\eta, \xi)$ in the old EASM is a function of the irrotational and rotational strain-rate invariants that also include α_1 . In this approach, α_1 is computed by assuming a constant value for $\frac{P}{\varepsilon}$ which can be different for separate flow regions (c.f. Sandberg & Fasel, 2003).

2.2.2 Turbulent Transport Equations

The Reynolds stress models require the turbulent kinetic energy, K , and the turbulent dissipation rate, ε . They are computed solving two additional transport equations

$$\frac{\partial}{\partial t}(\bar{\rho}K) + \frac{\partial}{\partial x_k} \left[\bar{\rho} \tilde{u}_k K - \left(\frac{\bar{\mu}}{Re} + \frac{\mu_T}{\sigma_K} \right) \frac{\partial K}{\partial x_k} \right] = \Pi_K ,\tag{2.23}$$

$$\frac{\partial}{\partial t}(\bar{\rho}\varepsilon) + \frac{\partial}{\partial x_k} \left[\bar{\rho} \tilde{u}_k \varepsilon - \left(\frac{\bar{\mu}}{Re} + \frac{\mu_T}{\sigma_{\varepsilon}} \right) \frac{\partial \varepsilon}{\partial x_k} \right] = \Pi_{\varepsilon} .\tag{2.24}$$

The turbulent viscosity μ_T can either be determined using equation (2.13) or using equation (2.18). The constants for the turbulent diffusion terms are $\sigma_K = 1.0$ and $\sigma_{\varepsilon} = 1.3$.

2.2.3 Subgrid Heat-Flux Vector

The subgrid heat-flux vector is modelled by assuming similarity in the gradient transport of heat and momentum, thus relating the thermal eddy diffusivity κ_T to the eddy diffusivity μ_T (equation 2.13) by a constant turbulent Prandtl number Pr_T as described in Speziale & So (1996)

$$Q_k = -\frac{1}{\gamma Ec} \frac{\mu_T}{Pr_T} \frac{\partial \tilde{T}}{\partial x_k}. \quad (2.25)$$

Speziale & So (1996) suggest that, for most engineering applications, a turbulent Prandtl number of $Pr_T = 0.9$ is adequate. Note that, for a turbulent Prandtl number of unity, complete similarity is assumed which is the well known Reynolds analogy for turbulent heat transfer.

2.2.4 Source Terms

The source terms Π and Π_K in the energy and K -equations include a pressure dilatation term, terms involving the turbulent dissipation rate and the subgrid mass-flux. It was shown by Sarkar *et al.* (1991) that both pressure dilatation and compressible dissipation are important in compressible turbulence. Therefore, both effects are modelled according to Sarkar *et al.* (1991), Sarkar (1992) and Speziale (1996)

$$\overline{p' \frac{\partial u_j''}{\partial x_j}} = a_2 \bar{\rho} \sigma_{ik} \tilde{S}_{ik} M_T + a_3 \bar{\rho} \varepsilon M_T^2, \quad (2.26)$$

with the turbulent Mach number (a measure of influence of compressibility on turbulence)

$$M_T = \sqrt{\frac{2K}{\tilde{T}}} M. \quad (2.27)$$

The turbulent dissipation rate is defined and the subgrid mass-flux is modelled according to Speziale (1996) as

$$\overline{\tau_{ik}'' \frac{\partial u_i''}{\partial x_k}} = \bar{\rho} \varepsilon, \quad \overline{u_k''} = \frac{1}{\bar{\rho} \sigma_\rho} \mu_T \frac{\partial \bar{\rho}}{\partial x_k}, \quad (2.28)$$

respectively. Using these model terms results in the source terms for the energy equation and the transport equation for turbulent kinetic energy K

$$\begin{aligned}\Pi &= (1 - a_2 M_T) \bar{\rho} \sigma_{ik} \tilde{S}_{ik} + (1 - a_3 M_T^2) \bar{\rho} \varepsilon - (\bar{\tau}_{ik} - \bar{p} \delta_{ik}) \frac{\partial}{\partial x_k} \left[\frac{\mu_T}{\sigma_\rho} \frac{\partial}{\partial x_i} \left(\frac{1}{\bar{\rho}} \right) \right], \\ \Pi_K &= -(1 - a_2 M_T) \bar{\rho} \sigma_{ik} \tilde{S}_{ik} - (1 - a_3 M_T^2) \bar{\rho} \varepsilon - \left(\frac{\partial p}{\partial x_i} - \frac{\partial \tau_{ik}}{\partial x_k} \right) \frac{C_\mu}{\bar{\rho} \sigma_\rho} \tau_T K \frac{\partial \bar{\rho}}{\partial x_i},\end{aligned}\quad (2.29)$$

respectively, with the constants $\sigma_\rho = 0.5$, $a_2 = 0.15$ and $a_3 = 0.2$. In absence of turbulent mass fluctuations, the source term in transport equation for K needs to be the negative value of the source term in the energy equation because any production of turbulent kinetic energy must be equal to the dissipation of the averaged energy. The source term of the transport equation for the turbulent dissipation rate is

$$\Pi_\varepsilon = -C_{\varepsilon 1} \bar{\rho} \frac{1}{\tau_T} \sigma_{ik} \left(\frac{\partial \tilde{u}_i}{\partial x_k} - \frac{1}{3} \tilde{S}_{jj} \delta_{ik} \right) - C_{\varepsilon 2} f_{\varepsilon 2} \bar{\rho} \frac{\varepsilon}{\tau_T} + C_{\varepsilon 3} \bar{\rho} Re_T^{\frac{1}{2}} \frac{\varepsilon}{\tau_T} - \frac{4}{3} \bar{\rho} \varepsilon \tilde{S}_{jj}, \quad (2.30)$$

where $f_{\varepsilon 2}$ is a wall-damping function discussed in section 2.2.5, $C_{\varepsilon 1} = 1.44$, $C_{\varepsilon 2} = 1.83$, $C_{\varepsilon 3} = 0.001$ and Re_T being the turbulent Reynolds number

$$Re_T = \frac{\bar{\rho} K}{\bar{\mu}} \tau_T. \quad (2.31)$$

All terms in the above equations, for which summation of repeated indices applies, are fully expanded for cylindrical coordinates in Appendix A.1.

2.2.5 Extensions to Wall-Bounded Flows

For the present research, one has to distinguish between two walls with inherently different properties: The approach flow wall and the base-wall. The approach boundary layer does not experience significant pressure gradients or streamline curvature until very close to the corner. It is therefore safe to assume that non-equilibrium effects are not present and standard wall-damping functions derived for equilibrium boundary layers can be utilized. This is, of course, only necessary for the Reynolds number regime where the approach flow is turbulent, as in the UIUC experiments

($Re_\theta = 13,700$). For the transitional cases investigated, the approach boundary layer is laminar and the turbulence model is switched off entirely in the approach region.

The flow along the base-wall, on the other hand, reaches much lower velocities and does not exceed $Re_\theta \approx 500$, even for the highest Reynolds number under investigation (UIUC case). Moreover, both for axisymmetric RANS and for three-dimensional calculations, the flow along the base-wall at best can be described as a stagnation-point flow,¹ exhibiting strong acceleration away from the stagnation point and a significant deceleration and flow-separation when approaching the corner. Additionally, for unsteady calculations, large structures impinge on the base, hence describing the flow over the base as an equilibrium flow does not appear to be an adequate assessment. Not only are most wall-damping functions derived for equilibrium boundary layers, but they oftentimes rely on the wall-distance in wall-coordinates, an ill-defined quantity when encountering regions of zero wall-shear as found at a stagnation point.

One example of a commonly used wall-damping function used for the STKE model (equation 2.13) is the *van Driest damping function*

$$f_\mu = 1 - \exp\left(-\frac{N^+}{A^+}\right), \quad (2.32)$$

where N^+ is the wall-normal distance in wall coordinates and $A^+ = 25$. If utilized, however, the damping function was only employed for the turbulent approach boundary layer but not for the base-wall due to the above mentioned reasons.

To remove singularities at walls in the destruction term of the ε -equation, i.e., $K = 0$, a damping function $f_{\varepsilon 2}$ is used. Traditionally, this wall-damping function takes the form

$$f_{\varepsilon 2}(N) = 1 - \exp\left(-Re\sqrt{0.1KN}\right), \quad (2.33)$$

where N is the wall-normal distance. For both EASM models, $f_{\varepsilon 2}(N)$ is the only term containing a wall-distance; the Reynolds stress model automatically accounts

¹In the case of an axisymmetric calculation, the stagnation point is fixed at the axis, whereas for 3-D calculations it can move freely.

for near-wall effects through the computation of $f(\eta, \xi)$ (equation 2.15) or $\frac{\alpha_1}{\tau}$ (equation 2.19).

To be completely independent of the wall-distance, another approach is used for computing $f_{\varepsilon 2}$ which is based on a suggestion by Durbin (1993). It relies on the assumption that the smallest physical time-scale in a turbulent flow is the Kolmogorov time-scale. Therefore, by computing $f_{\varepsilon 2}$ as

$$f_{\varepsilon 2} = \frac{1}{\max \left[1, \frac{C_T}{\sqrt{Re_T}} \right]} , \quad (2.34)$$

a completely wall-distance independent model is obtained. This function contains an additional constant that requires calibration. The effects of wall-damping functions and the limiter in turbulent boundary layers are evaluated in section 4.5. An alternative approach of obtaining an entirely wall-distance independent turbulence model that is more closely related to Durbin's original suggestion was used for results presented in Sandberg & Fasel (2003). There, the turbulent time-scale was limited utilizing the Kolmogorov time-scale

$$\tau = \frac{K}{\varepsilon} = \max \left[\frac{K}{\varepsilon}, C_T \sqrt{\frac{\bar{\mu}}{Re \bar{\rho} \varepsilon}} \right] . \quad (2.35)$$

This limited value was used in all instances where a turbulent time-scale appears in the transport equations for resolved energy, K and ε , and the calculation of the eddy viscosity.

2.3 Flow Simulation Methodology (FSM)

The fundamental concept of the methodology was already introduced in section 1.2.2. The details of the implementation are given in the following. For the Flow Simulation Methodology, the turbulent stress tensor is multiplied with the contribution function $f(\Delta/L)$

$$\sigma_{ik} = f(\Delta/L) \sigma_{ik}^R . \quad (2.36)$$

For the compressible extension, the source term in the energy equation and the turbulent heat-flux vector also have to be rescaled with the contribution function:

$$Q_k = f(\Delta/L) Q_k^R \quad \text{and} \quad \Pi = f(\Delta/L) \Pi^R. \quad (2.37)$$

The term $\Delta = [(\Delta z^2 + \Delta r^2 + (r\Delta\theta)^2)/3]^{1/2}$ is the representative computational grid size and L is the relevant length-scale. In the present calculations, a contribution function in a form proposed by Speziale (1998a) was used

$$f(\Delta/L_k) = \left(1 - e^{-\beta \frac{\Delta}{L_k}} \right)^n, \quad (2.38)$$

where L_K is the Kolmogorov length-scale $L_K = \left(\frac{\mu}{\rho Re} \right)^{3/4} / \epsilon^{1/4}$ and where β and n are adjustable parameters. Currently n is set to unity and β is set to a small value on the order of $\mathcal{O}(10^{-3})$. Other forms of the contribution function and different choices of the length-scale are possible (see, e.g. Fasel *et al.*, 2002).

As the ratio $\frac{\beta\Delta}{L_k}$ becomes small (grid resolution sufficient to resolve the relevant scales), $f(\Delta/L_k)$ approaches zero and the computation will approach the DNS-limit. For insufficient resolution, $f(\Delta/L_k)$ approaches unity, the RANS-limit is approached. For all intermediate values of the contribution function, a LES based on a state-of-the-art Reynolds Stress model is performed.

2.4 Scaling Laws

For base flow calculations, the most common scaling of quantities employs the diameter or radius of the base, D or R , and the maximum velocity of the approach flow, U . This *outer scaling* is used for the non-dimensionalization of the governing equations in the present work.

For emphasis of the near-wall behavior and better comparison with theory, the *wall-scaling*, or *inner scaling* for incompressible turbulent boundary layer flows is

introduced (see, e.g., Schlichting, 1979). The velocity, the wall-normal coordinate and the Reynolds number are scaled with the friction velocity $u_\tau = \sqrt{\frac{\bar{\tau}_w}{\rho_w}}$ as follows:

$$\begin{aligned} U^+ &= \frac{\tilde{u}_z}{u_\tau} , \\ x_i^+ &= x_i u_\tau \frac{\bar{\rho} Re}{\bar{\mu}} . \end{aligned} \quad (2.39)$$

In the limit of $Re \rightarrow \infty$, a turbulent boundary layer has an overlap region between the wall-layer and an outer layer, called the *logarithmic law of the wall*

$$U^+ = \kappa \ln(y^+) + C , \quad (2.40)$$

with $\kappa \approx 0.4$ and $C \approx 5.24$ in the absence of a streamwise pressure gradient. The wall-layer, or *viscous sublayer*, can be shown to satisfy

$$U^+ = y^+ . \quad (2.41)$$

In order to obtain several turbulent quantities in wall-coordinates, the following scalings are used

$$K^+ = \frac{K}{u_\tau^2} , \quad \varepsilon^+ = \frac{\bar{\mu}}{\bar{\rho} Re} \frac{\varepsilon}{u_\tau^4} , \quad R_{rz}^+ = \frac{R_{rz}}{u_\tau^2} . \quad (2.42)$$

2.5 Linearized Navier-Stokes (LNS) Equations

The compressible Navier-Stokes equations in cylindrical coordinates, as described in section A.1 are used as the basis for obtaining the linearized Navier-Stokes (LNS) equations. All variables are decomposed into a steady, two-dimensional basic-state component and disturbance quantities:

$$\phi = \check{\phi} + \acute{\phi} . \quad (2.43)$$

Terms that contain products of basic state variables only can be subtracted because they satisfy the Navier-Stokes equations for the basic state. All products containing

more than one disturbance variable are neglected as they are considered small compared to products of disturbance variables and basic state variables. Because only two-dimensional basic states will be considered for the present research ($\check{w} = 0$), all azimuthal derivatives of basic-state terms vanish. The set of equations that needs to be solved is derived in detail in Appendix A.3.

One of the objectives of this research is to investigate the hydrodynamic stability behavior of supersonic axisymmetric wakes for high Reynolds numbers, as in the experiments at UIUC. If a two-dimensional basic state is available for such a flow, from either an axisymmetric RANS solution or an averaged LES solution, a linear stability analysis can be conducted with the linearized code. However, the additional viscosity caused by the turbulent fluctuations (eddy viscosity) needs to be accounted for. Otherwise the amplification rates of the disturbances might be significantly over-predicted, or, in the worst case, modes that should not be amplified at the “effective Reynolds number”² might grow if the eddy viscosity is neglected.

The simplest approach to include the effects of the additional viscosity is to simply estimate the eddy viscosity and reduce the Reynolds number accordingly. For this approach, however, no information about the distribution of the eddy viscosity is included and the resulting deficiencies in the solution are expected to be unacceptably large. The most complete methodology would be to linearize the transport equations for the turbulent quantities K and ε in order to provide an accurate eddy viscosity. This approach, however, was beyond the scope of this work. An intermediate approach was chosen by assuming that the fluctuations of the eddy viscosity are small compared to the basic state values. Wernz (2001) found this to be a good approximation for turbulent wall-jets. The derivation of this high Reynolds number extension to the linearized equations can be found in Appendix A.3.1.

²Typically the eddy viscosity is significantly larger than the molecular viscosity, hence if the Reynolds number is based on the eddy viscosity it becomes considerably smaller than when based on the molecular viscosity.

3. NUMERICAL METHOD

All transport equations given in section 2 can be written in the form of an advection and a diffusion term on the left-hand-side and a source term on the right-hand-side. In cylindrical coordinates, this results in the following system of partial differential equations (PDE)

$$\frac{\partial U}{\partial t} + \frac{\partial A}{\partial z} + \frac{\partial B}{\partial r} + \frac{1}{r} \frac{\partial C}{\partial \theta} + \frac{1}{r} D = S^1. \quad (3.1)$$

The complete contents of the vectors are given in Appendix A.1. The system of equations (3.1) and all closures are solved numerically at discrete points. For spatial calculations, derivatives in time and in the $r - z$ plane are discretized using high-order accurate finite differences. The azimuthal direction is discretized employing a spectral method. For temporal calculations, derivatives in the streamwise direction are also approximated with a spectral method (see section 3.9). Note that the transport equations for the turbulent quantities K and ε were manipulated to the compact vector form, i.e., they represent the 6th and 7th equation of the system 3.1.

Unlike in previous investigations, where the transport equations of the turbulent quantities are solved in 2-D² with a lower-order accurate, separate solver, such as an ADI-method (e.g. Seidel, 2000) or the MacCormack method (e.g. Terzi, 2004), the same algorithm is used as for the Navier-Stokes equations. Several factors make this approach attractive: Implementation is facilitated and no additional numerical solver needs to be validated. Furthermore, the turbulent quantities are solved fully three-dimensionally. This is of particular importance when assuming that turbulent, helical structures are present and generate strong azimuthal variations in the

¹Note that for DNS, the right-hand-side of equations (3.1) vanishes and a system of homogeneous PDEs is recovered.

²The assumption of homogeneous statistics in the spanwise direction is commonly invoked.

turbulent quantities.³ Finally, the turbulent quantities are also solved to high-order accuracy, facilitating the separation of the contribution of the turbulence model and excessive discretization errors of a low-order accurate algorithm.

As already mentioned in the introduction, the flows under investigation, even for the lowest Reynolds number of interest, contain turbulent regions and, therefore, require a large number of grid points to resolve all relevant scales. The restriction of the *CFL* number, essential for conducting a time-accurate simulation, and the simultaneous requirement to compute several flow-through-times in order to be able to obtain time-averages and statistics also necessitates a very large number of time-steps, hence making the desired calculations very costly. It is therefore paramount to reduce the computational time as much as possible. To that end, significant savings in computational time are achieved by grid-stretching and symmetric Fourier transforms which drastically decrease the number of required grid-points. Further, employing a domain-decomposition technique, combined with parallel computing, enables the reduction of wall-time required for a given calculation. These three elements, along with other details of the numerical procedure are discussed in the following sections.

3.1 Boundary and Initial Conditions

The computational domain is shown in figure 3.1. As in the simulations by Tourbier (1996), only the last part of the approach flow is computed (region 1), i.e., the inflow boundary layer represents another parameter in the simulation. The code was written such that region 1 alone can be computed, allowing for boundary layer calculations, a feature that was essential for validation of the turbulence models. Both region 1 and 2 can be decomposed into sub-domains in order to compute efficiently on multiple CPUs. The domain-decomposition is described in section 3.6.

³That this is indeed the case is shown in section 6.1.4.

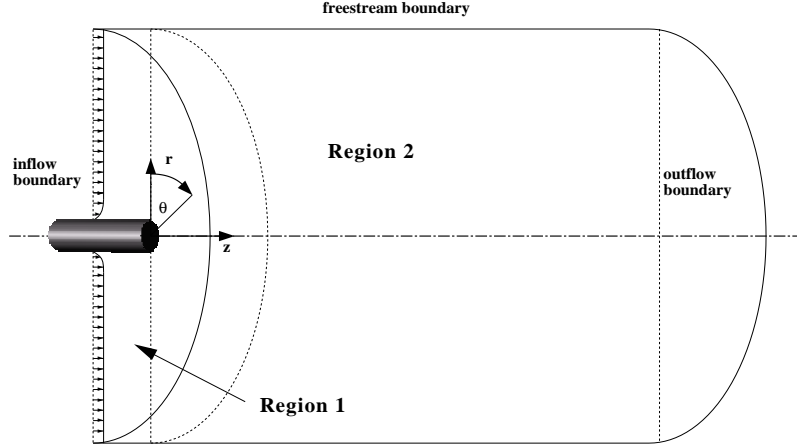


Figure 3.1 Computational domain for spatial calculations.

At the inflow boundary, the axial and azimuthal velocity and the temperature are set to a constant value. In subsonic calculations, either Dirichlet or Neumann conditions can be imposed on pressure, K and ε . For supersonic simulations, the pressure is fixed in the supersonic region and a Neumann condition is used in the subsonic part of the approach boundary layer. The outflow boundary is computed via one-sided stencils, setting the second derivative to zero. For subsonic cases, the pressure can be set to a constant value at the outflow. The freestream boundary is represented by Neumann conditions on all variables for subsonic cases and by simplified characteristic boundary conditions according to Harris (1997) for supersonic cases.

At the walls, no-slip and no-penetration are enforced for all velocity components and the turbulent kinetic energy is set to zero. The pressure at the wall can be either computed from the applicable momentum equation, i.e., the radial momentum at the approach flow wall, and the axial momentum for the base wall. Alternatively, a Neumann condition can be applied. Temperature can be set to a constant value or computed through a high-order extrapolation, i.e., either isothermal or adiabatic walls are specified. For all boundaries mentioned above, the density is computed through the equation of state for a perfect gas.

The initial condition for flat-plate boundary layer calculations is generated by interpolating a compressible similarity solution onto the utilized grid. For axisymmetric wake calculations, the initial condition is constructed by extending the above mentioned similarity solution downstream of the base in the region $1 \leq r \leq r_{max}$. Behind the base ($0 \leq r < 1$), all variables are set to the value of the corner-point, except the u -velocity, which is prescribed by a hyperbolic tangent function, ranging from 0 at the base to a value smaller than unity at the outflow. This measure is taken to avoid reverse flow at the outflow during start-up of the calculation. Because this initial condition deviates strongly from the expected axisymmetric base flow solution, very strong transients occur during start-up, generating large disturbances. For higher Reynolds numbers, at start-up, smaller time-steps or higher spatial resolution are required than for the converged case. To alleviate this problem, the flow is initially converged out for a moderate Reynolds number and then continued and converged (in some cases using multiple iterations) for the desired Reynolds number. Typically, several flow-through times are necessary to obtain axisymmetric steady-state solutions.

For all three-dimensional calculations, a converged axisymmetric flow field is used as initial condition for the 0^{th} Fourier mode and the higher modes are set to zero. A density-pulse in the higher Fourier modes is then utilized to accelerate the growth of the higher Fourier modes (see, e.g., chapter 6.1).

When performing RANS calculations, a laminar flow field is read in and the turbulent quantities K and ε are set to constants within the field, typically on the order of $\mathcal{O}(10^{-2})$ and $\mathcal{O}(10^{-3})$ for K and ε , respectively. Note that K must be zero at the walls. It was found that the time-step could be significantly enlarged when the initial condition of K was filtered multiple times in the wall-normal direction to mitigate excessively large gradients close to the wall.

3.2 Axis Treatment

Due to a pseudospectral approach in the azimuthal direction, the flow field is represented in Fourier modes, with the zeroth mode being the spatial mean flow and the higher modes being higher azimuthal modes. A state-of-the-art axis treatment is implemented, exploiting parity conditions. Even parity implies that the even azimuthal modes of a variable have an even symmetry and, conversely, the odd modes have an odd symmetry at the axis. On the other hand, for odd parity, the even azimuthal modes of the variable have an odd symmetry and the odd modes have an even symmetry at the axis. The derivation of which variables have which parity in the case of a half-cylinder calculation is given in Appendix C.3. The resulting boundary conditions at the axis are as follows: The zeroth azimuthal mode (mean flow) of all quantities evolves according to the governing equations, except for the radial and the azimuthal velocity components, which are set to zero. The first mode of the radial and azimuthal velocity components are permitted to be non-zero at the axis, however, all other higher modes are set to zero at the axis.

A modification of this axis treatment had to be implemented to allow for calculations of domain-sizes with an azimuthal extent of less than π . In the case of a quarter-cylinder, the numerical modes $k_N = 0, 1, 2, 3, \dots$ correspond to the physical modes $k = 2, 4, 6, \dots$ in the half-cylinder case, hence *all* higher modes in azimuthal have to be set to zero at the axis. Also, for the quarter-cylinder case, the parity conditions have to be changed, because all corresponding physical modes are even. For the option of computing $1/8^{th}$ or $1/16^{th}$ of a cylinder, only the azimuthal modes $k = 4, 8, 12, \dots$ or $k = 8, 16, 24, \dots$ are computed, respectively. They require the same axis treatment as for the quarter cylinder case.

An investigation of $1/6^{th}$ of a cylinder only contains the physical modes $k = 3, 6, 9, \dots$ and therefore, as above, all higher modes are set to zero for this case. However, as opposed to the quarter-, $1/8^{th}$ - or $1/16^{th}$ -cylinder cases, the odd numer-

ical azimuthal modes correspond to odd physical modes (e.g., $k_N = 1 \rightarrow k = 3$) and the even numerical azimuthal modes correspond to even physical modes (e.g., $k_N = 2 \rightarrow k = 6$). Hence, the same parity conditions as in the half-cylinder case can be utilized. A compilation of all symmetry and boundary conditions at the axis is given in Appendix B.

3.3 Spatial and Temporal Discretization

In radial direction, sixth-order accurate split compact finite differences are employed. As described in Burke (2001), compact finite-difference stencils are derived that are valid on a non-equidistant grid in contrast to mapping the computational domain to a uniform grid. Burke (2001) chose this method because it results in greater flexibility of the choice of grids and because Meitz & Fasel (2000) showed that it leads to a lower truncation error. In streamwise direction, fourth-order accurate standard split differences are utilized to facilitate the domain-decomposition described in section 3.6. The fourth-order accurate standard split differences are described in Tourbier (1996) or Harris (1997) for equidistant grids. In the current implementation, however, the difference stencils are derived for stretched grids in the same way and for the same reasons as the radial compact differences, see Appendix C.2. The sub-grid mass fluxes, however, are computed differently. Derivatives of density, pressure and the viscous stress-tensor are computed to second-order accuracy in the $r - z$ plane to introduce additional dissipation for enhanced numerical stability in regions where expansion fans and shocks are present.

The axisymmetric wake is a natural application for the use of Fourier transforms in the azimuthal direction due to the periodicity of the physical problem. For a plane geometry, on the other hand, domain-width studies need to be conducted to determine which spanwise wavelengths are most amplified because, using Fourier transforms,

only integer multiples of the fundamental wavenumber can be captured. For example, when using a domain width of $L_z = 3$, not only waves with wavelengths larger than $\lambda_z > 3$ are omitted, but also a disturbance with a wavelength of $\lambda_z = 2$ would be excluded. In the cylindrical coordinate system, these studies are not necessary because the geometry requires the wavelength of the disturbance wave to be an integer fraction of the fundamental wave ($\lambda_\theta = 2\pi$).

Water tunnel results of incompressible, low Reynolds number wakes conducted by Siegel (1999) show that the flow selects a symmetry plane that moves on a time-scale much slower than that of interest for the unsteady structures. Experimental work by Bourdon & Dutton (1998) shows that compressible wakes also exhibit a degree of symmetry in the azimuthal direction. A more recent paper by Bourdon & Dutton (2001) shows a clear symmetry of the flow in circumferential direction when using delta-shaped tabs on the body. Employing symmetric transforms enforces a symmetry plane similar to that caused by the surface disturbances (tabs) in the experiment. Assuming a perfectly axisymmetric base flow, the only additional information that could be obtained by employing full Fourier transforms is the azimuthal variation of the position of helical structures which most likely won't affect mean flow results and statistics. Therefore, as in previous work on this topic by Tourbier (1996), symmetric Fourier transforms can be justified in the azimuthal direction that lead to a significant reduction in computing time. The derivation of the equations in Fourier space is given in Appendix A.4.1.

For time advancement, a four-stage Runge-Kutta scheme is employed which is described in more detail in Appendix C.1. Details of the derivative stencils and the splitting are given in Appendix C.2. The benefits of using split finite-differences are illustrated using a von Neumann stability analysis for a model problem in Appendix C.4.

3.4 Grid Stretching

Grid stretching for the radial and the streamwise directions is employed to enable clustering of points in regions of high gradients, e.g., in the approach flow boundary layer, the shear layer, and the corner of the after-body. Utilizing coarse grids in regions of benign gradients such as the free-stream, saves a large amount of grid-points. This leads to a significant reduction of computational time, in particular for 3-D calculations. In the azimuthal direction, the grid is necessarily equidistant, as a spectral method is used in this direction. The grids for the downstream and the radial directions are generated with separate tools before runtime and saved in separate files. The values of the grid-points are read at initialization and the weighted derivative and filter stencils can then be computed. For the current investigation, the grids were chiefly generated using polynomial functions. A detailed discussion of various options of grid stretching can be found in Appendix C.2.

Chung & Tucker (2003) show that the accuracy of high-order finite difference schemes suffers significantly once the grid is very strongly stretched. Therefore, for the DNS calculations, in radial direction the grid is equidistant behind the base ($0 \leq r \leq 1$) to achieve the highest possible accuracy and a large amount of grid-points is used in the streamwise direction in order to achieve a very benign stretching with ratios of $\frac{\Delta z_{max}}{\Delta z_{min}} \leq 20$. The authors also showed that strong stretching in combination with coarse grids can cause compact schemes to exhibit negative numerical dissipation, which can quickly lead to divergence of the solution. For that reason, coarse FSM calculations that feature strong grid-stretching are always conducted employing filtering (see discussion in section 3.5).

3.5 Filtering

It was demonstrated by Chung & Tucker (2003) that using high-order compact differences on stretched grids leads to an amplification of high-wavenumber oscillations.

Low-pass filters need to be employed in order to prevent a contamination of lower wavenumbers by these high-frequency artifacts of the numerical method and, more importantly, to ensure numerical stability of the numerical method. Burke (2001) implemented a 4th-order accurate compact filter, that was designed to have its cut-off at the wavenumber $\Theta = 2$ (c.f. Lele, 1992). This filter, however, is derived for an equidistant grid and will, therefore, not exhibit the designed transfer function if applied to a stretched grid. At this point, it is unclear how to define a transfer function which removes a given frequency on a stretched grid. Thus, an analytic evaluation of the performance of filters on stretched grids is not attempted in the present work.

Another downside of employing the compact filter in streamwise direction was the incompatibility with the domain-decomposition because a matrix needs to be solved for, that requires knowledge of the full streamwise extent which cannot be accomplished in parallel. For that reason, explicit filters (6th- and 4th-order accurate) were derived for non-equidistant grids and employed in the streamwise direction. The derivation is given in appendix C.5.1 and the accuracy is discussed for different resolutions and types of grid-stretching. A further discussion of issues regarding filtering can be found in Appendix C.5.1.

3.6 Parallelization

In recent years, the number of CPUs that have become available on shared memory computers or distributed memory clusters has increased drastically. To exploit this trend, a domain decomposition was implemented in the streamwise direction. The streamwise direction was chosen for several reasons: This direction typically requires a significantly larger amount of points than the radial direction because of the larger downstream extent of the computational domain (typically, $-1 < z < 12$ versus $0 \leq r < 6$). Further, in the radial direction, high resolution is only required in the region $0 \leq r < 1.5$ because the free-stream is not of interest and does not contain

large gradients. In contrast, in the streamwise direction, high resolution is required from the base to the highly turbulent recompression region and the trailing wake, i.e., the grid-stretching in the streamwise direction is required to be moderate to avoid overly coarse grids far downstream of the base.

The implementation of the domain decomposition employs *Open MP* for the assignment of sub-domains to CPUs, limiting parallel simulations to shared-memory computers. The maximum number of processors that can be used depends on the number of streamwise points and the largest stencil-size of the streamwise derivatives or filters, respectively. A detailed description of how the domain-decomposition is implemented, e.g., when synchronization is required, etc. are given in Appendix C.6, together with a performance study of the code on parallel computers.

3.7 Disturbance Generation

Pulse disturbances are introduced using the following procedure: Higher Fourier modes ($k > 0$) initialized with zero are added to the converged or averaged axisymmetric flow field ($k = 0$). Within the recirculation region, a top-hat function with an extent of six gridpoints in the streamwise and the radial directions is specified in all Fourier modes of density with a small amplitude (typically of order 10^{-4}). This distribution serves as initial condition and, thus, constitutes a pulse disturbance in both space and time.

Controlled disturbances are introduced using a volume force. The forcing function is added in Fourier space to the right-hand-side of either the streamwise or the radial momentum equations (2.4) in a steady or periodic fashion. The disturbances are described by half a wavelength of a cosine in both the radial and the streamwise directions with a frequency ω ($\omega = 0$ for steady forcing) and an amplitude A_{dist} :

$$\hat{F}_{VF}^k = A_{dist} \sin(2\pi\omega t) \left[1 - \cos\left(\frac{(r - r_b)\pi}{r_e - r_b}\right) \right] \left[1 - \cos\left(\frac{(z - z_b)\pi}{z_e - z_b}\right) \right], \quad (3.2)$$

with k denoting which azimuthal mode is forced, and r_b , r_e , z_b and z_e being the starting and end points of the forcing in the radial and the streamwise directions, respectively. A monopole disturbance was chosen to keep the spatial extent of the volume force sufficiently compact to be fully immersed within the shear or boundary layer.

3.8 Linearized Code

The linearized code is based on the full Navier-Stokes code. The same numerical method was used, keeping close to all subroutines unchanged. Only the transport equations were substituted with the linearized equations derived in Appendix A.3. The main difference between the original N-S code and the linearized code is that, in the absence of nonlinear terms, the linearized equations can be solved entirely in Fourier space. As a consequence, the Fourier transform routines were omitted. Without having to conduct Fourier transforms and allocate additional collocation points to avoid aliasing errors, the computational cost is significantly reduced.

The initial condition for the linearized calculations always consisted of a two-dimensional basic-state that was either a similarity solution (if available) or a converged axisymmetric solution from the full Navier-Stokes code. As only the disturbance quantities are solved for, several modifications were required for the boundary conditions. At walls, in addition to setting the fluctuations of the velocity components to zero, temperature fluctuations are also prohibited, even when an adiabatic boundary condition is used for the basic state. At the free-stream, a decay condition was implemented for the validation calculations described in sections 4.1 - 4.3. For supersonic flow, all fluctuations are set to zero at the inflow and, for subsonic flow, a Neumann condition was specified for the disturbance density. All other boundary conditions were treated as in the full N-S code.

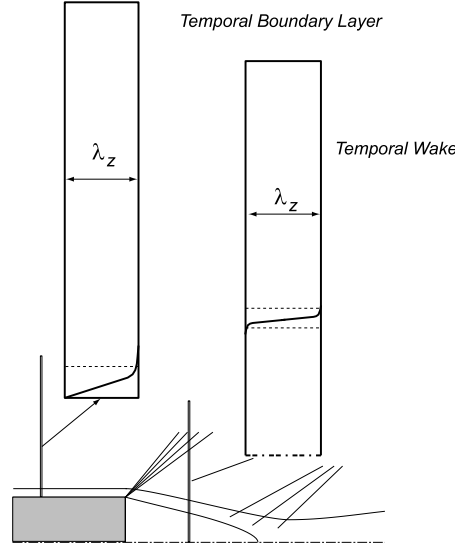


Figure 3.2 Computational domains for temporal calculations.

3.9 Temporal Code

The temporal code was derived from the full N-S code. Depending on whether it is desired to conduct temporal simulations of a boundary layer or a wake, the temporal code is based on the subroutines of the spatial code for a sub-domain of region 1 or a sub-domain of region 2, respectively (see figure 3.1). Figure 3.2 shows the computational domains for both temporal boundary layer and wake calculations. For temporal simulations, the streamwise extent of the domain is small to justify the assumption of locally parallel flow. The measure for the domain-length thereby is the wavelength of the fundamental instability wave. Hence, periodic boundary conditions can be employed for the inflow and outflow and, therefore, Fourier transforms can also be used for the streamwise direction. In the streamwise direction, however, full Fourier transforms need to be utilized to allow for flow *through* the domain.

High commonality between the spatial and the temporal code was desired to accelerate validation and to facilitate the implementation of new elements, such as modified/new turbulence models. Additionally, the temporal code was designed to conduct

calculations in order to, e.g., establish resolution requirements for high Reynolds number cases or design an appropriate contribution function for FSM. In order for the temporal results to be applicable in the spatial case, the numerical method of both codes needs to be as similar as possible. Therefore, the use of a spectral method in the downstream direction and abandoning the domain decomposition are the only significant differences between the temporal and the spatial code. In spite of the different approaches, the same system of equations (3.1) and all closures as for the spatial code are solved numerically at discrete points in the temporal approach. The governing equations in double-spectral space are presented in Appendix A.4.1. One-dimensional calculations can be conducted with the temporal code by setting the number of azimuthal and streamwise Fourier modes to zero, hence only the $(k, l) = (0, 0)$ mode is computed, where the indices denote the streamwise and azimuthal mode-number, respectively. This was of interest for testing the turbulence models for a flat plate boundary layer because, for temporal RANS calculations, no streamwise or azimuthal gradients would occur. Considerable savings in computational time were achieved by evaluating the turbulence models with 1-D temporal RANS calculations because they typically only required a few minutes on a single CPU. The results of these validation calculations are discussed in section 4.5.

4. CODE VALIDATION

For the research presented in this work, three separate codes were employed, namely a full Navier-Stokes code, a linearized Navier-Stokes (LNS) code and a temporal code. As described in section 3, both the LNS code and the temporal code are based on the full Navier-Stokes code and share most of its key numerical features. However, before applying any of the codes to turbulent simulations at high Reynolds numbers and supersonic speeds, a thorough validation of each code was conducted.

As described in Appendix C.4, the combination of split finite differences with a Runge-Kutta time-integration method is suited for the current research. To verify, that the method is sufficiently accurate to investigate flow instabilities, Tollmien-Schlichting (TS) waves were computed with all three codes and compared to linear stability results and data presented in the literature. Then, incompressible wakes were simulated with the linearized and the full Navier-Stokes code. Finally, the turbulence models were tested for incompressible and compressible boundary layers using both the full Navier-Stokes and the temporal code.

4.1 Tollmien-Schlichting Waves ($M = 0.25$)

The computation of TS waves was chosen as a challenging test for the numerical method. A viscous hydrodynamic instability is responsible for the growth of small amplitude waves (TS waves) in a boundary layer. Therefore, an accurate representation of the physical mechanisms in the near-wall region is crucial for capturing the correct behavior of the waves, such as phase and amplitude distributions and, in particular, the growth rates.

The first validation case described here was the computation of two-dimensional TS waves in an incompressible, flat plate boundary-layer. In order to conduct simulations of a flat plate with the present codes in cylindrical coordinates, the boundary

layer thickness was chosen to satisfy $\delta \ll r_{wall}$. This was realized by adding a large cylinder radius r_{wall} , typically on the order of $\mathcal{O}(10^4)$ to the values of the radial grid, such that $r_{wall} \leq r \leq r_{wall} + r_{max}$ and therefore all $\frac{1}{r}$ terms become negligible. Computing at very low Mach numbers with a compressible code without specific modifications, such as preconditioning, is impractical due to the increasing stiffness of the energy equation when $M \rightarrow 0$, requiring unreasonably small time-steps. On the other hand, to reproduce the incompressible results, the Mach number needed to be small enough to not introduce compressibility effects. $M = 0.25$ was chosen as a good compromise, where Mach number effects are negligible and the time-step restriction was acceptable.

Most of the validation results are presented in Balzer (2003) and here only few key results are shown here in order to establish the validity of results obtained with the temporal code. Balzer found excellent agreement between the data obtained from temporal simulations and LST. In the process of conducting several parameter studies (domain height, cylinder radius, near-wall resolution), Balzer also investigated the influence of the Mach number on the results (i.e., growth rate, amplitude and phase distributions) and confirmed that $M = 0.25$ is suitable for reproducing incompressible results without requiring unreasonably small time-steps.

To validate the full Navier-Stokes and the linearized code, data were compared to DNS results from an incompressible code and another compressible code, both presented in Terzi & Fasel (2002). The set-up of the calculation follows case 1 from Fasel & Konzmann (1990) where a DNS code, albeit an incompressible one, was employed and, therefore, potential deviations from LST caused by non-parallel effects were accounted for. Fasel & Konzmann (1990) chose a global Reynolds number of $Re = 100,000$, and a non-dimensional frequency of the disturbance $F = 1.4 \cdot 10^{-4}$, defined as $F = \beta^* \nu^* / U_\infty^*$, where β^* denoted the dimensional frequency. Converting the frequency to the current non-dimensionalization, the non-dimensional frequency

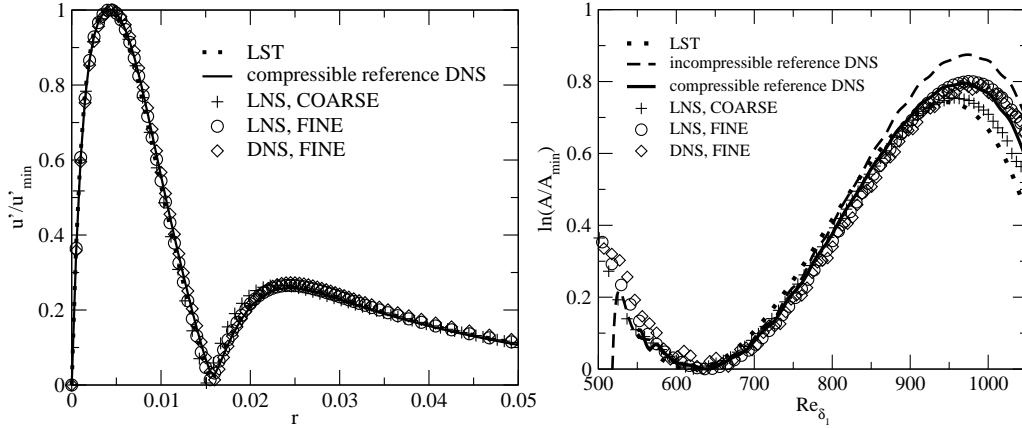


Figure 4.1 Amplitude distributions (left) of streamwise velocity component and amplification rate (right) of inner maximum of streamwise velocity at $Re_{\delta_1} = 800$; results from DNS and LNS calculations compared to LST and reference DNS; $M = 0.25$, $F = 1.4 \cdot 10^{-4}$.

is $\beta = F \cdot Re = 14$. Following the findings from above, the Mach number was set to $M = 0.25$. Two different grids were employed, a coarse and a fine corresponding to the grids utilized by Fasel & Konzelmann (1990) and Terzi & Fasel (2002), respectively. The disturbances were introduced into the flow by a volume forcing technique, as described in section 3.7. When varying the computational grids, the same grid points were used for the volume forcing, resulting in slightly different positions of the forcing. However, it was determined that this had no influence on the resulting wave as the forcing location for all cases was upstream of the amplified region. All other relevant parameters are listed in table D.1 in Appendix D.

The amplitude distribution of the streamwise velocity component at $Re_{\delta_1} = 800$ is shown in figure 4.1. The results obtained with both the full Navier Stokes code and the linearized code agree very well with LST and the reference DNS, in particular when the fine grid is used. For the coarse grid, the outer maximum is slightly shifted towards the wall, suggesting that the effective Reynolds number is slightly lower at this location, caused by a larger truncation error as the grid-spacing is larger.¹ Figure

¹It is shown in Appendix C.4 that the utilized numerical scheme produces mainly dissipation errors, increasing the effective viscosity and consequently decreasing the effective Reynolds number.

4.1 also shows the amplification rate of the inner maximum of the streamwise velocity component as a function of Re_{δ_1} . It is interesting to see, that the results obtained employing the finer grid with the present code agree very well with the data from the compressible reference DNS (that utilized the same grid). A calculation with an even finer grid was conducted (not shown) but displayed no visible difference in the solution, suggesting that the result was converged.

When using the coarse grid, the amplification rate is slightly decreased, consistent with the presumed lower effective Reynolds number caused by the larger grid-spacing. Nevertheless, the result computed on the coarse grid still shows a larger amplification rate than that predicted by LST and the maximum is shifted downstream, consistent with the findings of Fasel & Konzelmann (1990). The incompressible reference DNS, which matches the data by Fasel & Konzelmann (1990) produced an even larger amplification rate. None of the compressible calculations were able to reproduce this result. Since the reference compressible code uses a very similar numerical method as the codes used for this work, (split finite differences with a Runge Kutta method), it is conjectured that small phase errors caused by the numerical scheme when computing at small CFL numbers (due to the low Mach number) might be a cause for the discrepancy (see the discussion in Appendix C.4). However, the compressible code used by Terzi (2004) has been extensively tested and used for stability investigations of incompressible shear layers and supersonic boundary layers and was therefore considered as a good benchmark.

4.2 Tollmien-Schlichting Waves ($M = 1.6$)

The accurate computation of incompressible 2-D TS waves presented in the previous section gives considerable confidence in the codes utilized in this work. Nevertheless, the correct implementation of the energy equation could not yet be scrutinized as the effect of the temperature field on the velocity field (through viscosity and EOS)

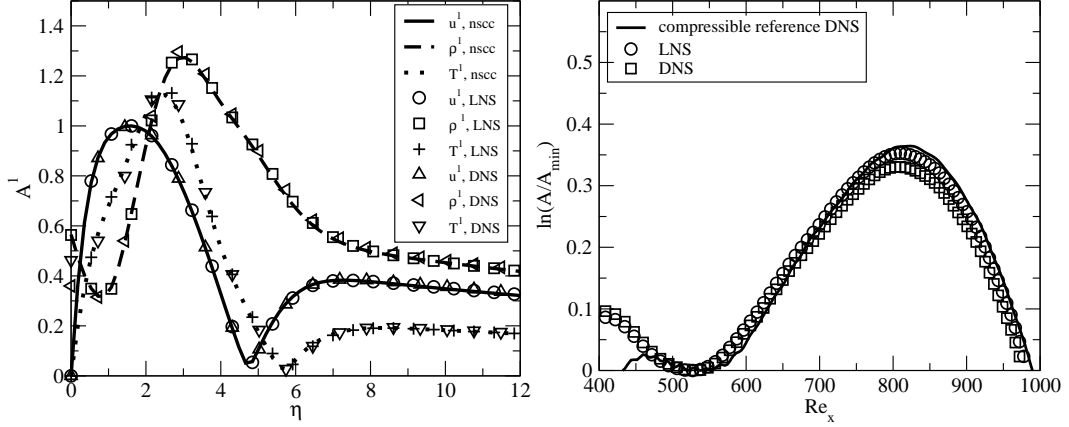


Figure 4.2 Amplitude distributions (left) of streamwise velocity component and thermodynamic variables ρ and T and amplification rate (right) of inner maximum of streamwise velocity at $Re_x = 800$; results from DNS and LNS simulations compared to reference DNS (nscc); $Re = 100,000$, $M = 1.6$, $F = 5.0025 \cdot 10^{-5}$.

is negligible at low Mach numbers. To that end, the growth of 2-D disturbances in a supersonic boundary layer at $M = 1.6$, as investigated by Thumm (1991), were computed and compared to a reference DNS. The Mach number $M = 1.6$ was chosen because for $M < 2.2$ only the viscous mode is unstable and no higher Modes (Mack modes) are present. This facilitates the investigation of the development of the disturbance. The global Reynolds number was chosen to be $Re = 100,000$ and the forcing frequency $F = 5.0025 \cdot 10^{-5}$. All further parameters are compiled in table D.2 in Appendix D.

The amplitude distributions of the streamwise velocity component and the thermodynamic variables ρ and T at $Re_x = 700$ are shown in figure 4.2 (left). All curves are scaled with the maximum of the respective streamwise velocity component. The results obtained with both the DNS and the LNS codes agree very well with the data from the compressible reference DNS. When scrutinizing the amplification rate (figure 4.2, right), it can be observed that the onset and the end of the unstable region for the frequency investigated is predicted correctly with both the LNS and the DNS codes. The DNS code shows a slightly smaller value of the maximum amplification

rate than the reference and the LNS simulations which might be attributed to the fact that the base flow (mode $k=0$) deviated slightly from the initial condition. The initial condition was obtained with the reference DNS using a characteristic boundary condition at the free-stream, whereas for the present DNS, only a Neumann condition was applied. In the LNS calculation, the base flow remains unchanged and, therefore, the agreement with the data from the reference calculation is superior.

4.3 Oblique Tollmien-Schlichting Waves ($M = 3.0$)

The previous sections have illustrated that the codes developed can accurately predict 2-D TS waves, both for subsonic and supersonic flow. Nevertheless, the above test cases were only two-dimensional and, therefore, the validity of the azimuthal discretization, in particular the Fourier transforms has not yet been established. To that end, the growth of oblique disturbances in a supersonic boundary layer at $M = 3.0$ were computed and compared to a reference DNS by Husmeier (2002).

In order to simulate a three-dimensional flat plate with the cylindrical codes developed for this research, only a circumferential fraction of a cylinder must be computed. As explained previously, the radius of the cylinder is specified to be $r_{wall} \gg 1$ so that $\delta \ll r_{wall}$. Thus, the curvature of the cylinder in azimuthal direction is very benign and $\lambda_\theta \ll r_{wall}$. The azimuthal wavenumber α_θ needs to be scaled with the desired azimuthal wavelength λ_θ and the specified cylinder radius r_{wall} as explained in detail in Appendix A.4.1.

For the temporal simulation, the Reynolds number, based on streamwise position, was specified as $Re_x = 700$ and the displacement thickness was fixed to be $\delta_1 = 0.002435$. The streamwise domain length was set to $\lambda_z = 0.05194$ and the azimuthal (spanwise) domain length to $\lambda_\theta = 0.02998$. When disturbing mode $(1, 1)$, this resulted in an oblique angle of $\psi = 60^\circ$, which according to LST is the most amplified

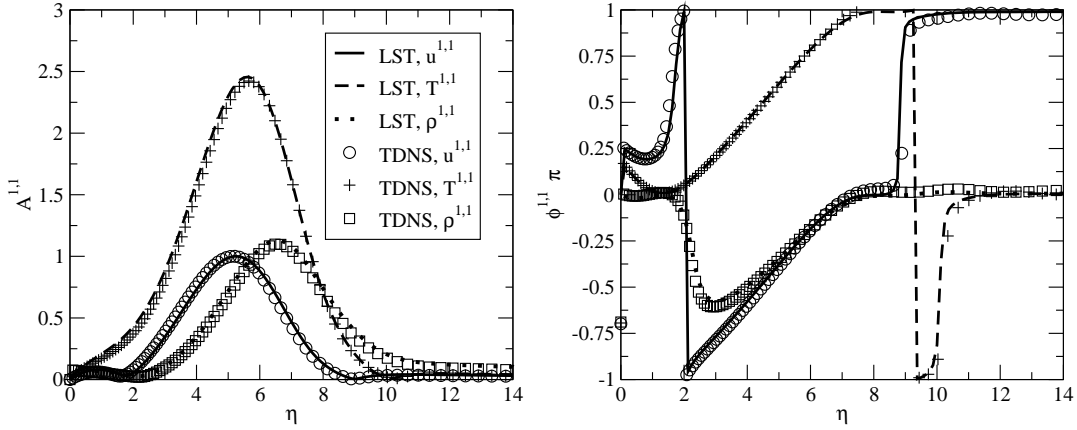


Figure 4.3 Amplitude (left) and phase (right) distributions for the streamwise velocity component, the temperature and density of the first streamwise and azimuthal Fourier mode (1,1) obtained from TDNS compared to LST; $Re_x = 700$, $M = 3.0$ and $\psi = 60^\circ$; data by Balzer (2003).

angle. Note, that for three-dimensional temporal calculations, combined modes (l, k) are used, where l denotes the streamwise mode-number and k denotes the azimuthal wavenumber. Further parameters for the calculation can again be found in table D.2 in Appendix D. The amplitude and phase distributions of the first streamwise and azimuthal mode (1,1) for the streamwise velocity component and the thermodynamic variables ρ and T are shown in figure 4.3. The results obtained with TDNS correspond very well with the data from LST. Balzer also compared the temporal growth rate obtained from TDNS with the spatial growth rate from LST, which he related through the phase speed, and found a deviation between the two results of merely 10%. This is acceptable, considering that the Gaster transformation was employed at this higher Mach number.

The reference DNS by Husmeier (2002) was conducted with 328 points in the wall-normal direction. However, based on the good agreement of the results from the temporal code with LST using only 120 wall-normal points, the validation calculations for the full Navier-Stokes and the linearized codes were conducted with 130 points

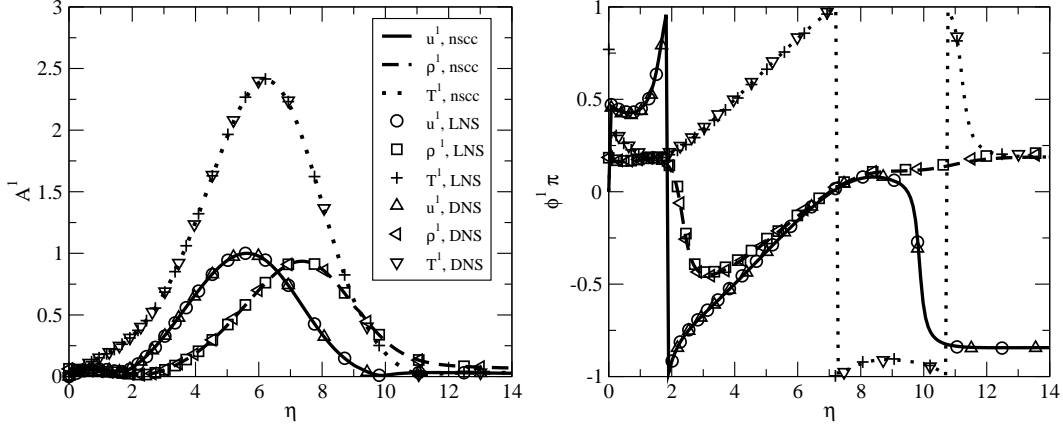


Figure 4.4 Amplitude (left) and phase (right) distributions for the streamwise velocity component, the temperature and density of the first azimuthal Fourier mode at $Re_x = 700$, obtained from LNS simulations compared to reference DNS (nscc); $\psi = 60^\circ$, $Re = 1,578,102$, $M = 3.0$, $F = 5 \cdot 10^{-5}$.

in the wall-normal direction. The global Reynolds number was specified as $Re = 1,578,102$, the inflow location was $z_0 = 1.5917 \cdot 10^{-3}$ and the azimuthal (spanwise) domain length was specified to be $\lambda_\theta = 0.02998$ in order to match the parameters given by Husmeier (2002). By introducing the periodic forcing into the first azimuthal mode, an oblique wave with $\psi = 60^\circ$ was generated. All other relevant parameters are listed in table D.2 in Appendix D. The amplitude (left) and phase (right) distributions of the streamwise velocity component and the thermodynamic variables ρ and T at $Re_x = 700$ are shown in figure 4.4. All amplitude distributions are scaled with the maximum of the respective streamwise velocity component. Very good agreement is achieved between the results obtained from both spatial codes and the data from the compressible reference DNS. The accurate representation of the phase relations is of particular interest for the current research as phase errors can influence where and if vortices are generated and thereby affect global results.

The growth rates α_i (figure 4.5, left) obtained from both the DNS and LNS code correspond very well with the data of the reference. When scrutinizing the amplification rate (figure 4.5, right), it can be observed that the DNS and the LNS codes

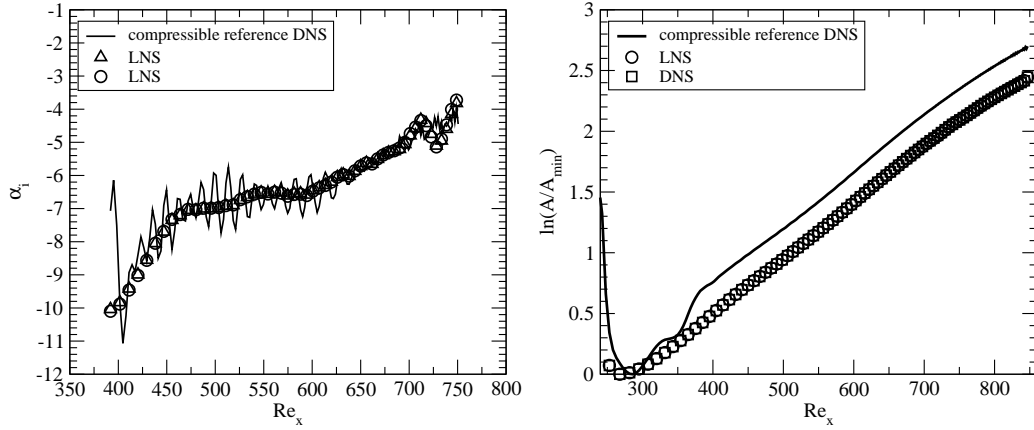


Figure 4.5 Growth rate α_i (left) and normalized amplification rates (right) of inner maximum of streamwise velocity component of at $Re_x = 700$; results from DNS and LNS simulations compared to reference DNS; $\psi = 60^\circ$, $Re = 1,578,102$, $M = 3.0$, $F = 5 \cdot 10^{-5}$.

produce the same results. The agreement with the reference DNS is excellent except for in the region $325 < Re_x < 375$. This deviation most likely arises due to the use of different forcing mechanisms. Husmeier (2002) used wall blowing and suction, whereas the codes developed here employed volume forcing with the largest amplitude of the forcing function in wall-normal direction at approximately half the boundary layer thickness. The strong oscillations in α_i in the data from the reference DNS in this Re_x region are an indication that the disturbance wave is not fully established yet, as opposed to the case where the volume forcing is used. Once the receptivity region is overcome, the slopes obtained from all calculations are identical.

In conclusion, the validation cases conducted so far demonstrate that the codes developed for this research are capable of accurately representing the development of hydrodynamic instabilities. Even weak viscous instabilities leading to TS waves are captured correctly in 2-D and 3-D, for both subsonic and supersonic flows.

4.4 Subsonic Wake Flows

In order to ascertain the correct implementation of the axis-treatment (see section 3.2) and the interface between regions 1 and 2 (see section 3.1), several calculations were conducted for low Mach number, axisymmetric wakes at various Reynolds numbers. These cases were chosen as they could be conducted at reasonable computational cost and because comparison data of Schwarz (1996) was available. Schwarz investigated incompressible, axisymmetric wakes for several Reynolds numbers, comparing and validating his results with water tunnel experiments. The radial velocity was set to $v = 0$ at the inflow to match the B.C.s incorporated in the incompressible formulation by Schwarz.

First, axisymmetric calculations were conducted for various Reynolds numbers and then fully 3-D calculations were performed for three cases, using the axisymmetric results as initial condition. All relevant data for the calculations presented in the following are specified in table D.4 of Appendix D.

4.4.1 Axisymmetric Calculations

In the calculations conducted by Schwarz, for increasing Reynolds numbers the approach boundary layer thickness was decreased accordingly. This is equivalent to keeping the size of the cylinder and the kinematic viscosity constant in an experiment and only augmenting the free-stream velocity.

Figure 4.6 shows the axial velocity distribution along the centerline for $M = 0.25$ and Reynolds numbers ranging between 500 and 8,000 for axisymmetric calculations. The lines denote the results obtained with the compressible N-S code, the open symbols indicate the results by Schwarz (1996). Up to $Re_D = 4,000$, very good agreement is achieved. For the $Re_D = 8,000$ case, the discrepancy is accepted as Schwarz suggests that his higher Reynolds number calculations were not fully converged. For the Reynolds numbers 1,000 and 2,000, the calculations were repeated with a different

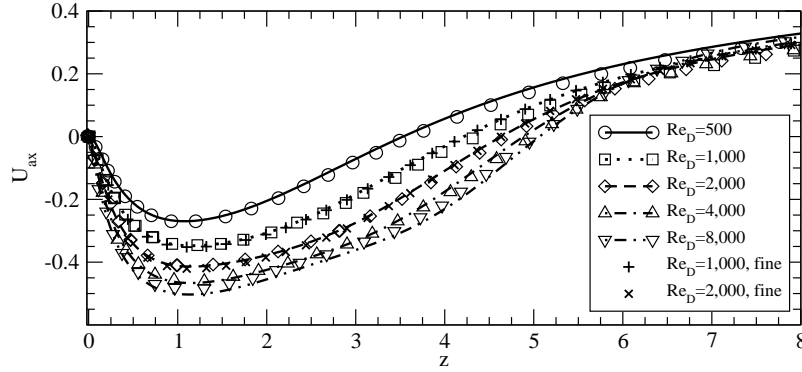


Figure 4.6 Centerline streamwise velocity for different Reynolds numbers at $M = 0.25$; open symbols represent data by Schwarz (1996), lines and symbols denote results obtained with current compressible code with coarse and fine resolution, respectively.

grid. The grid spacing at the base corner was slightly coarser as for the above cases, however, a significantly larger number of points was used in both the streamwise and the radial direction. The grid-stretching was, therefore, much more benign and the resolution several radii away from the body was significantly finer. As seen in figure 4.6, the solution obtained on the finer grid does not differ from the results computed on the coarser grid. This shows that the numerical method converges and that the accuracy of the finite differences and the filtering does not deteriorate with relatively strong stretching factors as used for the coarse grid case.

While conducting the validation calculations, the following interesting behavior was recognized. At different Reynolds numbers, not only the recirculation length changes, but also the maximum reverse velocity is drastically altered. When fixing the approach boundary layer thickness to a constant value for varying Reynolds numbers, which corresponds to increasing the size of the body while keeping the velocity and the viscosity of the flow constant, the results differ noticeable. Only the recirculation length increases with increasing Reynolds numbers, however, the maximum reverse velocity is nearly constant at $u \approx -0.33$ and the peak is located about one radius from the base for all cases. Clearly, this implies that the thickness of the

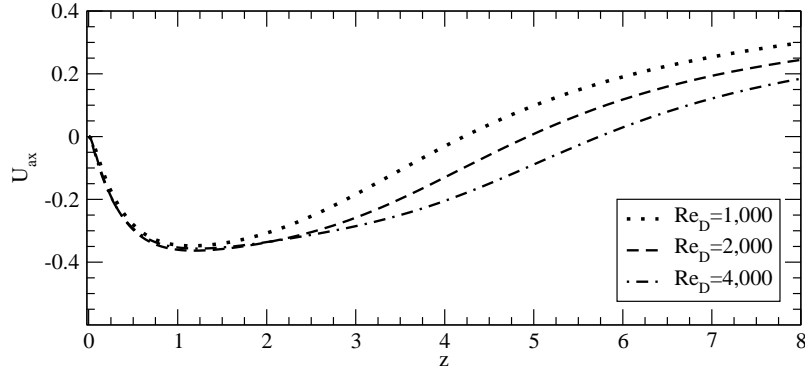


Figure 4.7 Centerline streamwise velocity for different Reynolds numbers at $M = 0.25$, keeping the approach boundary-layer thickness constant.

separating boundary layer has a pronounced effect on the global behavior, even for the axisymmetric case that converges to a steady-state solution. For a fully three-dimensional flow, this would be expected as a steeper gradient at separation would lead to faster growth of instabilities and more entrainment of high-speed fluid would result, altering the global wake-behavior.

4.4.2 3-D Calculations

Fully three-dimensional calculations were conducted for three different Reynolds numbers with both the linearized and the full N-S code. At $t = 0$, a pulse disturbance was introduced in all azimuthal modes of density at $z = r = 1$ with the same amplitude to accelerate the growth of the amplitudes of the higher modes.²

The temporal development of the higher azimuthal Fourier modes (u^k for the LNS simulations and (ρu^k) for the DNS) at the disturbance location was monitored to evaluate whether they are amplified or whether they decay in time. The results of the calculations with $500 \leq Re_D \leq 2,000$ obtained with LNS simulations and DNS are shown in figure 4.8 left and right, respectively. When looking at the results from

²Due to an absolute instability of the flow at the investigated Reynolds and Mach numbers, round-off errors would suffice to generate a contribution of the higher modes, however, this would require considerably longer computation times.

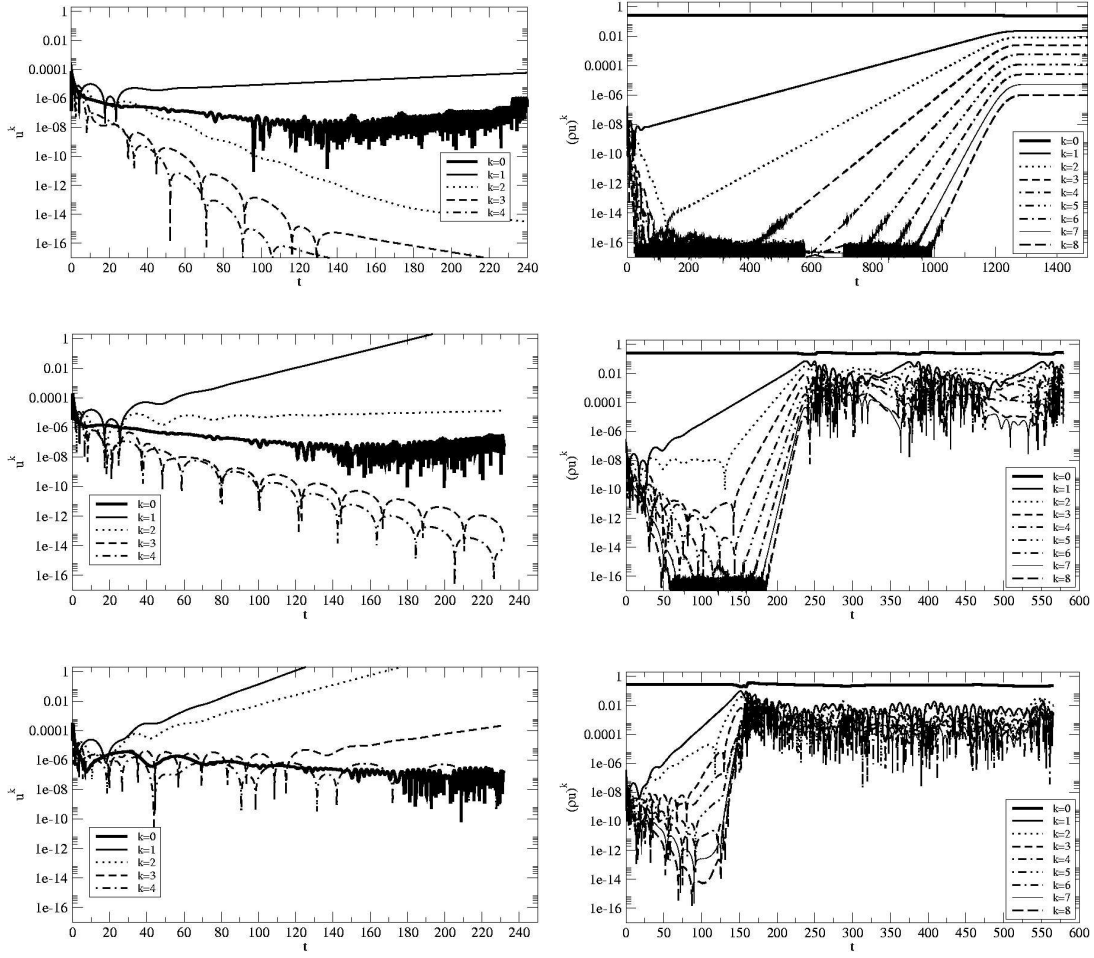


Figure 4.8 Temporal development of higher azimuthal modes at the disturbance location $(z, r) = (1, 1)$ obtained with LNS calculations (left) and full Navier-Stokes codes (right) for Reynolds numbers 500, 1,000 and 2,000 from top to bottom; $M = 0.25$.

the LNS calculations, at $Re_D = 500$ it appears as if only mode $k = 1$ is amplified and all other modes decay. Increasing the Reynolds number to 1,000, the amplification rate of mode $k = 1$ increases and mode $k = 2$ appears to be neutrally stable. At $Re_D = 2,000$, modes $k = 1, 2, 3$ are amplified, with the first azimuthal mode $k = 1$ having an even higher amplification rate. When scrutinizing the results obtained from DNS, the same observations can be made. For $Re_D = 500$, only the first azimuthal mode exhibits exponential growth initially and all other modes decay. At $t \approx 150$, the first mode has reached an amplitude large enough so that nonlinear interaction

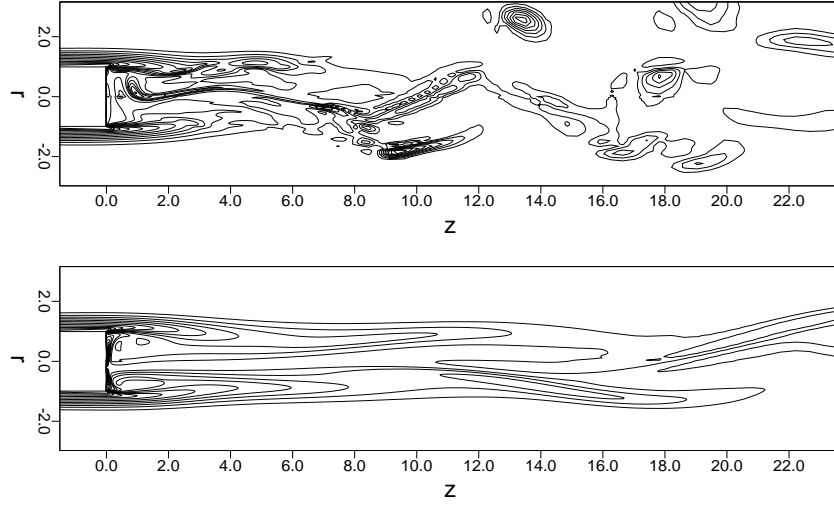


Figure 4.9 Contours of total vorticity at $t = 180$ (top) and $t = 229$ (bottom); $Re_D = 1,000$, $M = 0.25$.

with itself leads to growth of the second azimuthal mode $k = 2$. One higher mode after the other is generated and they grow until a steady saturation state is reached at $t \approx 1200$. However, no deviation in mode $k = 0$ from the axisymmetric solution is observed because the nonlinear saturation amplitudes are too small.

At $Re_D = 1,000$, the results from the DNS also show the increased growth rate of the first azimuthal mode and a neutrally stable second mode ($k = 2$). At $t \approx 130$, nonlinear interaction causes all modes to be amplified until they reach a saturation state. However, at this higher Reynolds number, the amplitude levels at saturation are large enough to result in a significant alteration of the azimuthal mean flow ($k = 0$). This nonlinear interaction in the region $240 < t < 320$ manifests itself in vortex shedding, as can be seen in the sideviews of instantaneous total vorticity, shown in figure 4.9. That is followed by a quieter interval $320 < t < 370$, also shown in figure 4.9, again succeeded by shedding of several structures. This intermittent behavior was also observed by Schwarz (1996). The Strouhal number for the vortex shedding was found to be $St = 0.155$ which compares exactly to that found by Schwarz (1996).

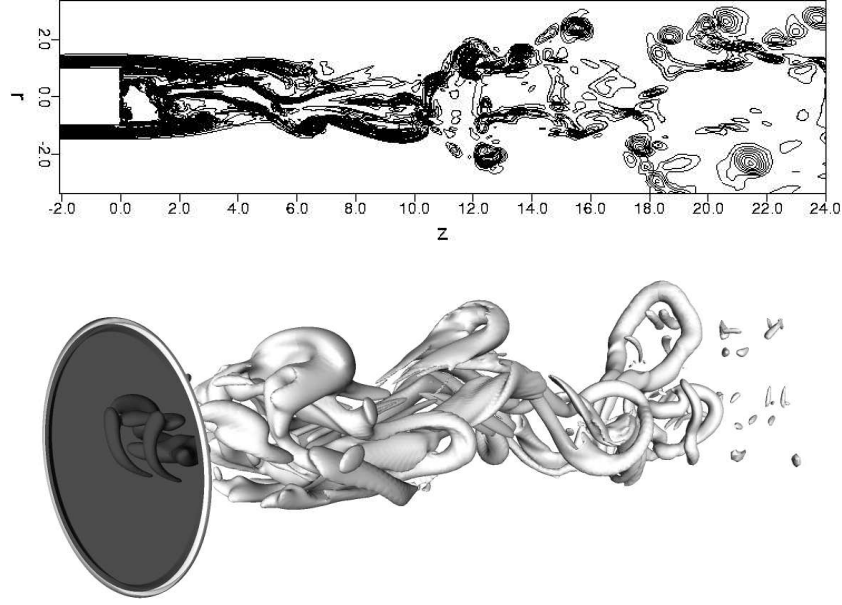


Figure 4.10 Sideview of total vorticity at $t = 180$ (top) and perspective view of iso-surfaces of $Q = 0.2$ at $t = 191.2$ (bottom); $Re_D = 2,000$, $M = 0.25$.

The Strouhal number for the intermittency was $St_I \approx 0.015$.

At $Re_D = 2,000$, as in the results obtained with LNS calculations, the first two azimuthal mode are amplified in the linear stage before nonlinear effects lead to exponential growth of all higher Fourier modes. The saturation level is again large enough to cause a strong interaction with the axisymmetric Fourier mode and no intermittency is observed, which is in agreement with the calculations by Schwarz (1996). The Strouhal number of the vortex shedding is $St = 0.0946$. Figure 4.10 shows a sideview of contours of instantaneous total vorticity (top), clearly highlighting the vortex shedding and the presence of smaller scale structures. The visualization of a perspective view of iso-contours of $Q = 0.2$ ³ (figure 4.10) illustrates the structure of the vortices generated in this flow. For clarity, the base is marked by the dark-grey surface. The formation of vortex loops can be observed and is in very good agreement

³The vortex-identification criterion Q will be introduced in detail in section 6.1.2.

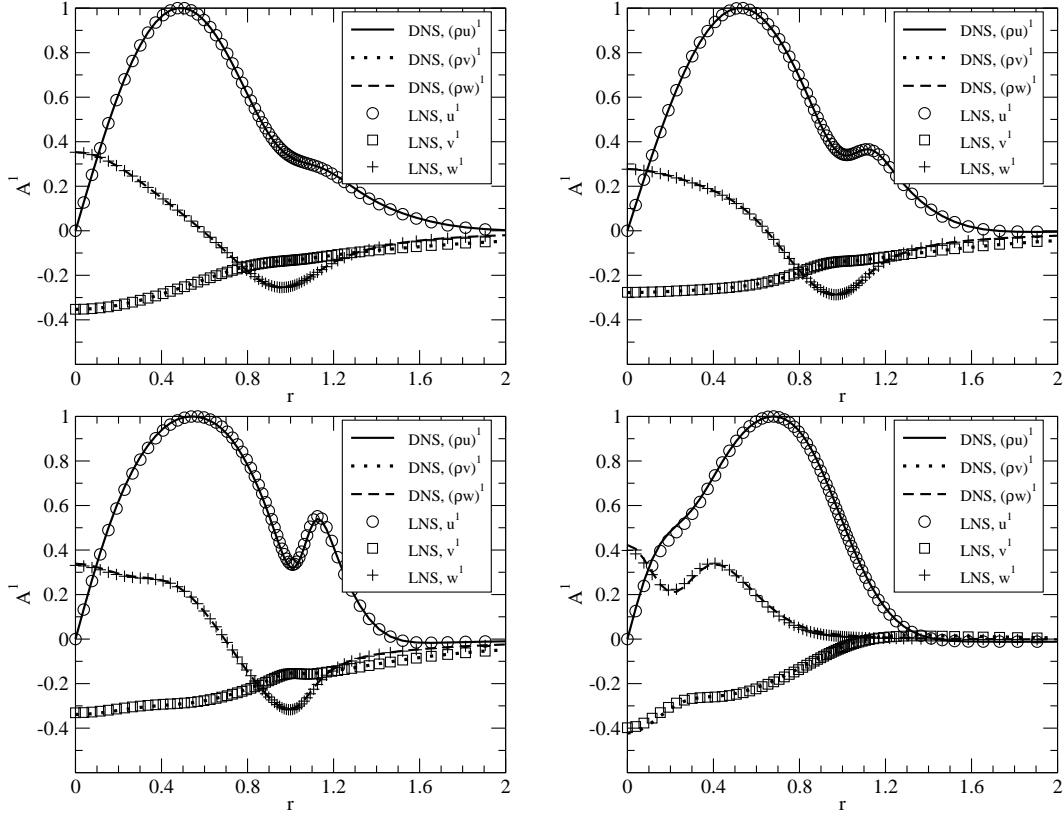


Figure 4.11 Amplitude distributions of the first azimuthal mode for all three velocity components obtained with DNS and LNS simulations; $Re_D = 500$ at $z = 1$ for $t = 231.7$ (top left), $Re_D = 1,000$ at $z = 1$ for $t = 115.9$ (top right), $Re_D = 2,000$ at $z = 1$ for $t = 57.9$ (bottom left), $Re_D = 2,000$ at $z = 4$ for $t = 57.9$ (bottom right); $M = 0.25$.

with the data of Schwarz (1996).

Being able to obtain the same three-dimensional flow field as Schwarz (1996) with the DNS code gives confidence in the correct implementation of the axis and the interface between regions 1 and 2. In order to verify that the LNS code also works properly for a full wake calculation, the amplitude distribution of the first azimuthal mode for all three velocity components obtained from both the DNS and the LNS calculations are compared in figure 4.11. The radial profiles obtained in the recirculation region at $z = 1$ are shown for all three Reynolds numbers. The most significant

difference in the radial profiles for increasing Reynolds number is the appearance and growing importance of a secondary maximum in the streamwise velocity component at $r = 1.1$. The amplitude distributions are also shown for $Re_D = 2,000$ at a location further downstream, still inside the recirculation region at $z = 4$. At this location, the secondary maximum in the streamwise component is no longer present. However, a distortion in all three profiles is visible close to the axis at $r = 0.2$. The data obtained from LNS simulations virtually match the DNS results for all velocity components, Reynolds numbers and streamwise locations at a significantly lower computational cost (see table D.4 in Appendix D).

This section concludes the validation of the tools that were developed for the investigation of physical flow instabilities in supersonic axisymmetric wakes. It was demonstrated that the three-dimensional flow field behind an axisymmetric afterbody can be accurately captured, quantitatively reproducing the data obtained from incompressible reference DNS that were validated with water tunnel results. Furthermore, data from LNS calculations indicated that, at $Re_D = 2,000$, the flow is absolutely unstable with respect to both the first *and* the second helical mode.

4.5 Turbulence Models

The turbulence models described in section 2.2 are validated with calculations of turbulent boundary layers, both on a flat plate in the incompressible limit, and for a supersonic flow over a cylinder. Furthermore, an additional constant that is introduced in order to make the turbulence models wall-distance independent (see section 2.2.5) was calibrated with these calculations. All turbulence models are implemented in the same codes (spatial and temporal Navier-Stokes codes) that are employed for stability investigations and the solution of the filtered N-S equations. Any variation in the flow solution can therefore entirely be attributed to the contribution of the

turbulence models. This allows for evaluating the performance of different closures. The temporal code was employed for the validation calculations of the incompressible boundary layers. In order to achieve the fastest possible turn-around times for parameter studies, 1-D calculations were conducted, i.e., the number of streamwise and azimuthal modes was set to zero and only the radial (wall-normal) direction was solved for. The calculations could typically be conducted in less than three minutes on a desktop PC. Once the appropriate constants were found, the results from the temporal calculations were verified with the spatial code.

4.5.1 Incompressible Turbulent Boundary Layer

Initially, a flat plate, zero pressure gradient turbulent boundary layer was computed at $M = 0.25$ and $Re_\delta \approx 1,700$. As for the calculations of TS-waves (section 4.1), the radius of the body was set to $r_{wall} \gg 1$ to prevent lateral curvature effects from having an impact on the solution. As initial condition, a laminar boundary layer profile was chosen for the velocity field and both turbulent quantities K and ε were set to a constant (typically on the order of 10^{-3}) throughout the domain. All further parameters are listed in table D.5 in Appendix D.

In figure 4.12, the influence of the choice of α_i (see section 2.2.1) on the numerical solution is illustrated by means of several quantities in wall coordinates to emphasize the near-wall behavior. The EASM calculations are conducted using either the wall-distance dependent damping function $f_{\varepsilon 2}(N)$ (equation 2.33), or employing the fully wall-distance independent EASM (equation 2.14 and 2.35), varying the constant c_T of equation 2.35. For this approach, the turbulent time-scale limiter is applied to every occurrence of a turbulent time-scale, τ_T . The results are compared with each other and to theoretical curves (laminar sublayer with $U^+ = y^+$ and logarithmic law region with $U^+ = 2.5 \ln(y^+) + 5.24$). For all quantities shown, it appears as if, when using the wall-damping function $f_{\varepsilon 2}(N)$, the choice of α_i does not influence the solution.

This was expected, as the wall-damping function overrides the turbulence model close to the wall. However, once the wall-distance independent variant is used, the solution becomes highly dependent of which coefficients α_i are used. It is noteworthy that virtually the same solution is obtained when using either $c_T = 10$ in combination with using values of α_i , obtained by assuming $P/\varepsilon = 1.88$, or when specifying $c_T = 12$ and employing the “incompressible” values of α_i . For the flow currently considered, the latter appears to be the better choice.

Looking at the streamwise velocity component in wall-coordinates, the slope in the region $10 < y^+ < 300$ is slightly too high when using the wall-damping function $f_{\varepsilon 2}(N)$, which might be attributed to the low Reynolds number. However, when using the limiter with $c_T = 12$, the slope corresponds slightly better to the theoretical values. It was therefore determined that this was the appropriate value for c_T when using this particular approach of limiting the turbulent time-scale (equation 2.35). For values of $0 < c_T < 6$, the calculations produced the same results as without any limiter and $f_{\varepsilon 2}(N) = 1$, significantly undershooting the logarithmic-law curve. In contrast, when choosing $c_T > 12$, the departure from the viscous sub-layer curve was delayed to approximately $y^+ \approx c_T$, thereby overshooting the theoretical curve.

Comparing the results obtained for the turbulent quantities K^+ and ε^+ when using the turbulent time-scale limiter versus using the wall-damping function also reveals qualitative differences. When employing the limiter, the decay of K towards the wall is not as rapid as when using the wall-damping function. Furthermore, ε at the wall reaches values close to the global maximum, in agreement with the recently empirically suggested absolute maximum at the wall (Speziale & So, 1996, specify $0.1 < \varepsilon_{wall}^+ < 0.2$, and $\frac{\partial \varepsilon^+}{\partial y^+} \Big|_{wall} = 0$). In contrast, when using $f_{\varepsilon 2}(N)$, the wall value of ε^+ is considerably smaller than the absolute maximum at $y^+ \approx 7$. Most importantly was, however, that good agreement with theory was obtained using a wall-distance independent turbulence model, so that the more complex base flow geometry could be investigated. Results for supersonic base flow calculations using this approach are

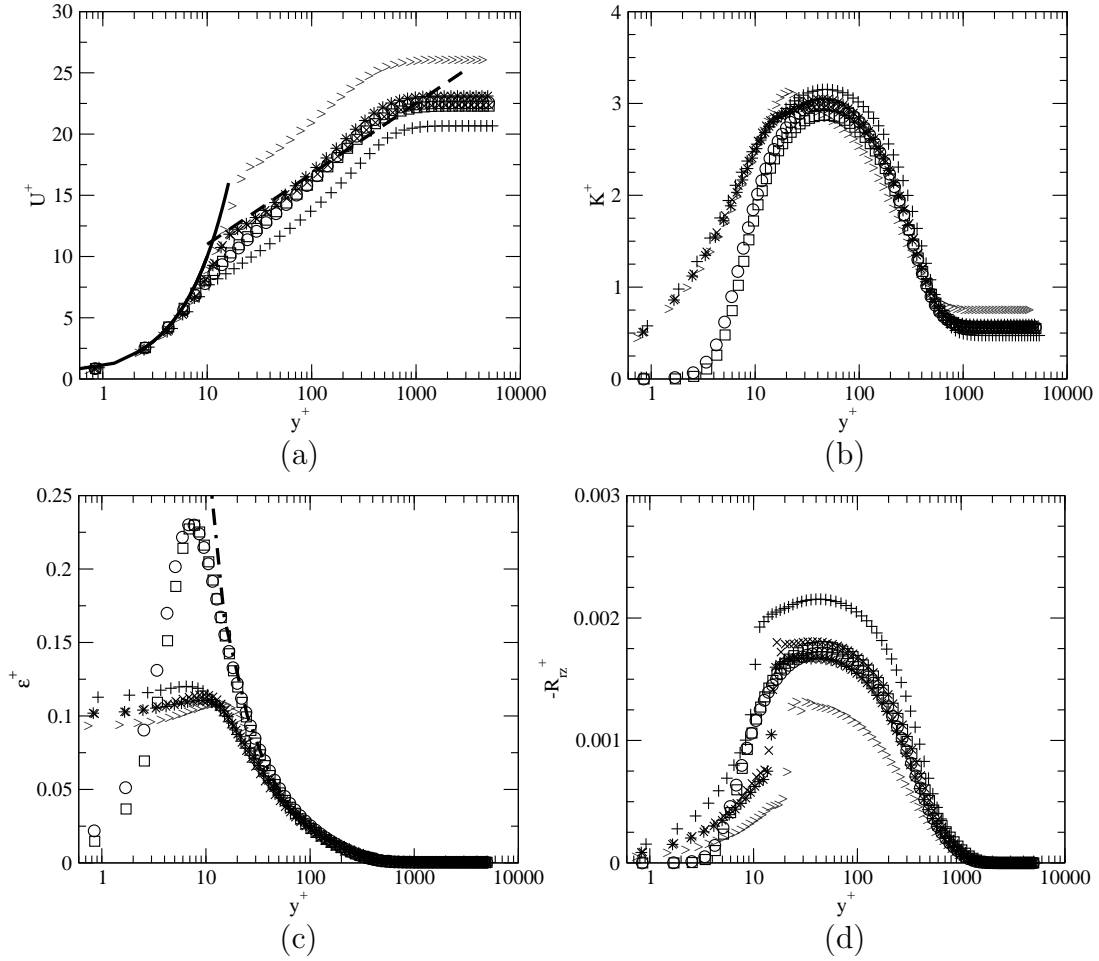


Figure 4.12 One-dimensional temporal RANS calculations of a turbulent boundary layer employing the EASM for different values of α_i and utilizing $f_{\varepsilon 2}(N)$ (equation 2.33) or the limiter for the turbulent time scale (equation 2.35); shown are streamwise velocity (a), turbulent kinetic energy (b), turbulent dissipation rate (c) and the rz -component of the Reynolds stress (d) in wall-coordinates: $u^+ = y^+$ (—), $u^+ = 2.5 \ln(y^+) + 5.24$ (---); $\varepsilon^+ = 2.5/y^+$ (- · -); using $f_{\varepsilon 2}(N)$ with incomp. α_i (○); $f_{\varepsilon 2}(N)$ with $P/\varepsilon = 1.88$ (□); $c_T = 10$ with incomp. α_i (+); $c_T = 10$ with $P/\varepsilon = 1.88$ (×); $c_T = 12$ with incomp. α_i (★); $c_T = 12$ with $P/\varepsilon = 1.88$ (>); $Re_\delta \approx 1700$, $M = 0.25$.

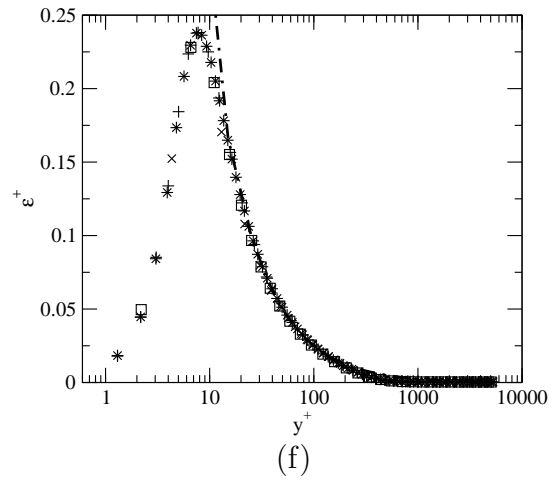
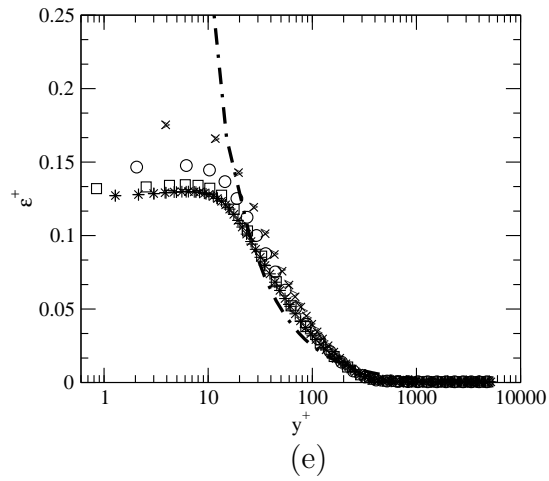
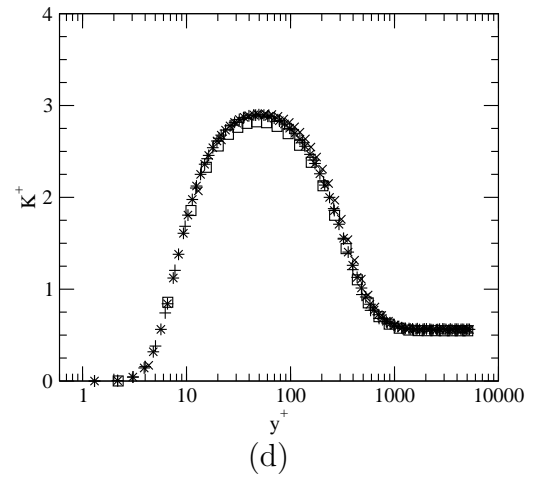
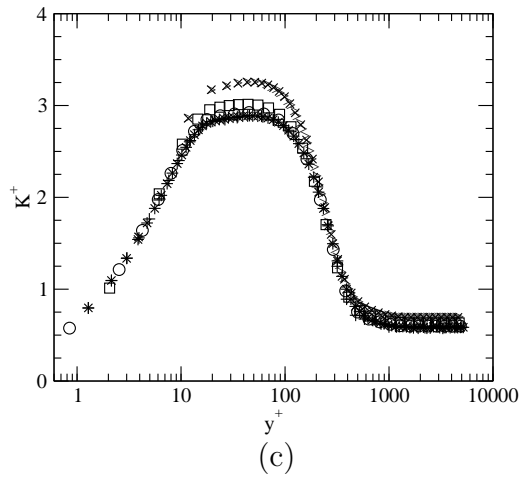
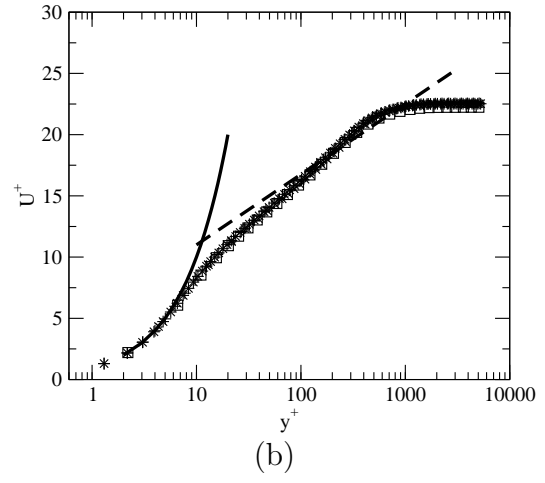
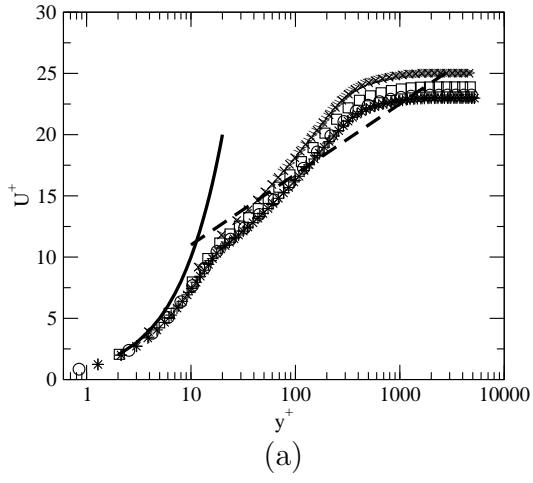
presented in Sandberg & Fasel (2003).

However, for the flow under investigation in this research which features very disparate flow-regions, assuming a constant ratio of production over dissipation rate most likely will deteriorate the solution. Finding in addition the strong dependence

of the solution on the values of the coefficients α_i when utilizing the turbulent time-scale limiter led to the decision of abandoning this particular turbulence model for the current work. The generalized version of the EASM, where P/ε is locally and instantaneously computed (see section 2.2.1) was considered instead and needed to be validated as well.

The same case as above was considered for the validation of the EASM $_{\alpha}$, namely a turbulent flat plate boundary layer with zero pressure gradient at $M = 0.25$ and $Re_{\delta} \approx 1,700$. The new turbulence closure was also implemented into the temporal code, therefore, the same kind of 1-D calculations as described above were conducted with the new model. The main difference between the new EASM $_{\alpha}$ and the EASM was found to be a different optimum value for c_T , implying that the limiter value is dependent on the turbulence model used. The best agreement with the theoretical curves was obtained when using $c_T = 18$. Most likely, the change in the value of c_T is caused by an increase in \check{c}_{μ} near the wall when using the EASM $_{\alpha}$. With this value of c_T established as the best choice for the EASM $_{\alpha}$ closure, a grid study was conducted using both the limiter and the traditional $f_{\varepsilon 2}(N)$ wall-damping function, shown in figure 4.13 left and right, respectively. Both the number of points in wall-normal direction, determining the degree of stretching employed, and the finest spacing at the wall were varied. All parameters for these cases are compiled in table D.5 in Appendix D.

The results from the calculations where the wall-damping function $f_{\varepsilon 2}(N)$ was employed can easily be summarized as not showing any significant differences, regardless of which grid was used. When using the turbulent time-scale limiter, however, the picture changes and the solution varies for different grids. This was expected, as the wall-damping function $f_{\varepsilon 2}(N)$ basically determines the near wall behavior, whereas the near-wall region needs to be fully resolved when using the wall-distance independent version of the turbulence model. Once the near-wall spacing becomes too coarse



For caption, see next page

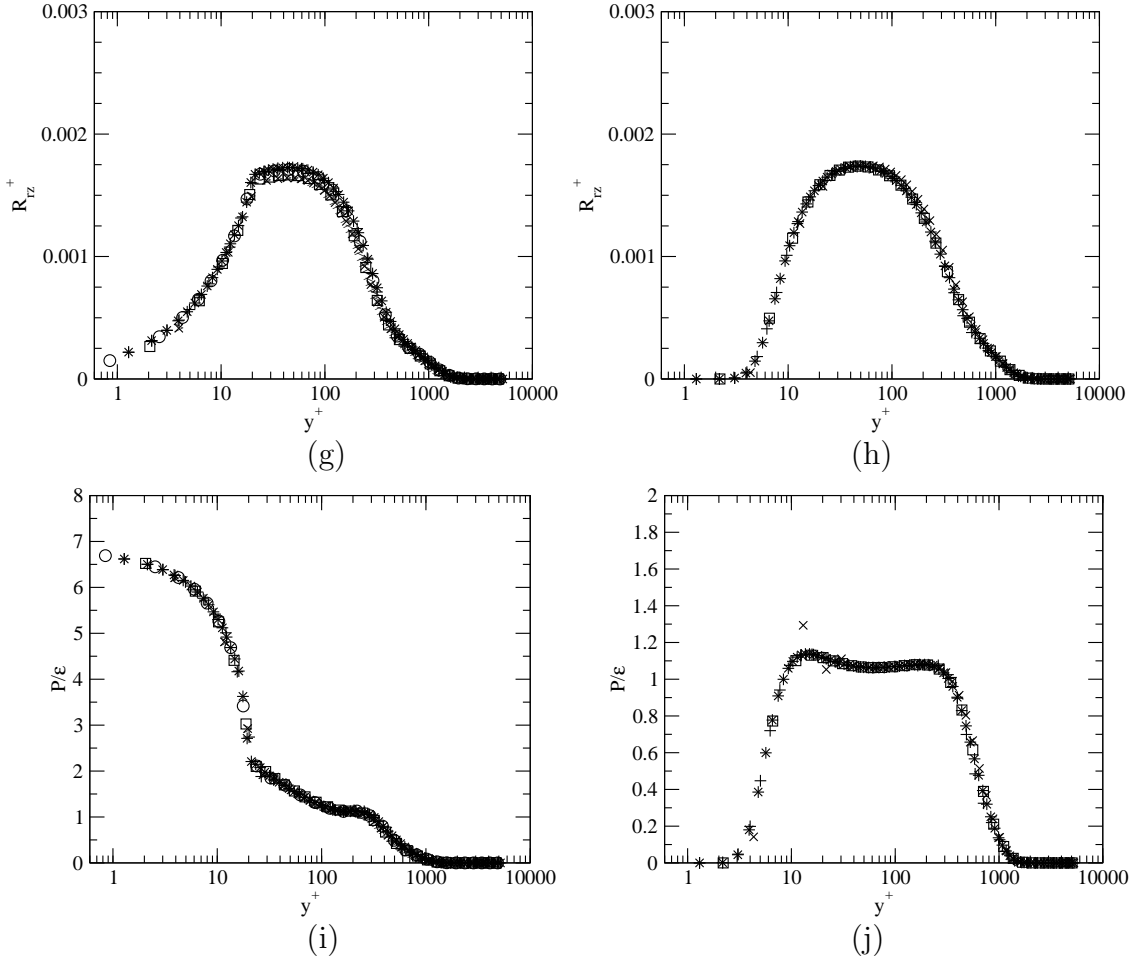


Figure 4.13 One-dimensional temporal RANS calculations of a turbulent boundary layer employing the $EASM_\alpha$ for different computational grids utilizing either the turbulent time-scale limiter (equation 2.35) with $c_T = 18$ (left) or $f_{\epsilon 2}(N)$ (equation 2.33) (right); shown are streamwise velocity in (a) and (b), turbulent kinetic energy in (c) and (d), turbulent dissipation rate in (e) and (f), the rz -component of the Reynolds stress in (g) and (h) and production over dissipation in (i) and (j), all in wall-coordinates; $u^+ = y^+$ (—); $u^+ = 2.5\ln(y^+) + 5.24$ (---); $\epsilon^+ = 2.5/y^+$ (· · ·); $mr2 = 60$, $\Delta r_{wall} = 0.0004$ (\circ); $mr2 = 60$, $\Delta r_{wall} = 0.001$ (\square); $mr2 = 80$, $\Delta r_{wall} = 0.0002$ ($+$); $mr2 = 80$, $\Delta r_{wall} = 0.002$ (\times); $mr2 = 160$, $\Delta r_{wall} = 0.0002$ (\star); $mr2 = 160$, $\Delta r_{wall} = 0.002$ ($>$); $Re_\delta \approx 1,700$, $M = 0.25$.

in calculations using the turbulent time-scale limiter, the solution deteriorates, as can be seen for the cases employing $\Delta r_{wall} = 0.002$, denoted by the symbols (\times) and ($>$). Here, the streamwise velocity profiles in wall coordinates deviate from the theoretical

curves. The turbulent kinetic energy is overpredicted, as is the value of the turbulent dissipation rate. Only the rz -component of the Reynolds stress tensor seems to be unaffected by which grid is used. Note that, as for the case when using the original EASM, the maximum value of ε^+ is located at the wall when using the turbulent time-scale limiter as opposed to ε^+ being far from its maximum value at the wall when using the wall-damping function $f_{\varepsilon 2}(N)$. It appears as if the number of points (the amount of stretching) has a negligible effect on the solution.

As already mentioned, in contrast to assuming a specific ratio of turbulent production over the dissipation rate, the EASM $_{\alpha}$ computes P/ε locally and instantaneously. The value of P/ε is shown in plots (i) and (j). When using the wall-damping function, P/ε approaches zero at the wall and varies between $1.05 < P/\varepsilon < 1.15$ in the logarithmic law region, suggesting that the assumption of setting $P/\varepsilon = 1$ for this kind of flow is a valid assumption. When using the limiter, however, the values of P/ε rise to significantly larger levels in the viscous sub-layer. This appears to be inconsistent as the Reynolds stresses should be zero at the wall and P/ε therefore also should approach zero, because $P = \rho \sigma_{ik} S_{ik}$.

In light of this inconsistency, another approach was considered to make the turbulence model entirely wall-distance independent (see section 2.2.5). Instead of limiting every occurrence of a turbulent time-scale, only τ_T in the destruction term of the transport equation for ε (equation 2.24) is multiplied by a wall-damping function that is constructed using a turbulent time-scale limiter, as shown in equation (2.34). This approach was again tested with the calculation of a turbulent, flat plate boundary layer with zero pressure gradient, so that the temporal code could be employed. For this case, the flow parameters were $M = 0.25$ and $Re_{\delta} \approx 50,000$ and the EASM $_{\alpha}$ was used. The results for the calculations are shown in figure 4.14. Scrutinizing the streamwise velocity component in wall-normal coordinates, it becomes obvious that the solution is quite sensitive with respect to the value of c_T . For $c_T = 4.65$, very

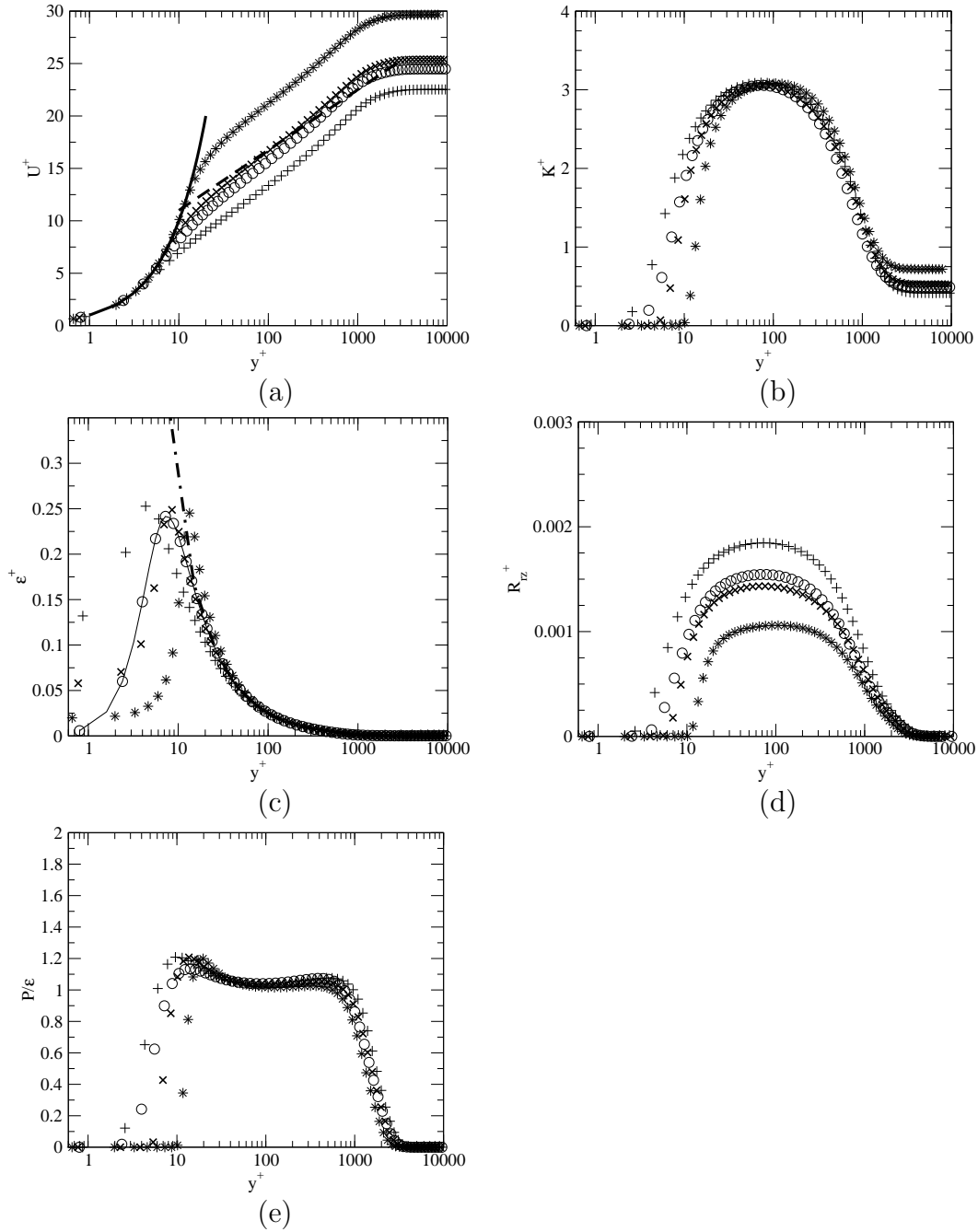


Figure 4.14 One-dimensional temporal RANS calculations of a turbulent boundary layer employing the $EASM_\alpha$ with different values of c_T ; shown are streamwise velocity (a), turbulent kinetic energy (b), turbulent dissipation rate (c) production over dissipation rate $\frac{P}{\varepsilon}$, (d) and the rz -component of the Reynolds stress (e), all in wall-coordinates; $u^+ = y^+$ (—); $u^+ = 2.5\ln(y^+) + 5.24$ (---); $\varepsilon^+ = 2.5/y^+$ (- · -); $f_{\varepsilon 2}(N)$ (○); $c_T = 4.60$ (+); $c_T = 4.65$ (×); $c_T = 4.70$ (★); $Re_\delta \approx 50,000$, $M = 0.25$.

good agreement with the theoretical curves is achieved. For this value of the constant, all quantities but the turbulent dissipation rate are predicted very similar to when the traditional wall-damping function is used. Most importantly, the deficiency of the above method is overcome, the production over dissipation ratio approaches zero at the wall when using the wall-distance independent wall-damping function $f_{\varepsilon 2}$. In spite of the sensitivity towards the value of c_T , it was decided to use this approach for the investigation of turbulent axisymmetric wakes, because this approach constituted a fully wall-distance independent turbulence model without apparent inconsistencies.

In conclusion, the results from calculations of turbulent boundary layers demonstrated that theoretical results could be reproduced, in particular for the streamwise velocity component in wall-coordinates. Wall-distance independent versions of both the EASM and EASM $_{\alpha}$ were successfully validated. The constants required in the limiters were calibrated to reproduce the correct slope and offset of the law of the wall for turbulent boundary layers with zero pressure gradient over flat plates. The near-wall behavior of ε and the slope U^+ over y^+ was found to correspond more accurately to theoretical and empirical references when using the wall-distance independent versions of the turbulence models than when using a standard wall-damping function.

4.5.2 Compressible Turbulent Boundary Layer

To validate the compressible extensions to the turbulence model, an axisymmetric supersonic turbulent boundary layer simulation was calculated with the spatial code. The flow parameters were chosen as $M = 2.46$ and $Re_{\delta} = 165,000$ at the outflow in order to match the approach boundary layer in the experiments by Herrin & Dutton (1991). 52×80 points were used in the streamwise and the radial directions, respectively. Further parameters for the simulations can be found in table D.5 in

Appendix D. An additional objective of these computations was to obtain results that could serve as inflow conditions for calculations of the entire base flow geometry, using both RANS and FSM. Several calculations were conducted with the original EASM, using both the wall-damping function $f_{\varepsilon 2}(N)$ and the turbulent time-scale limiter with different values for c_T . The results were presented in Sandberg & Fasel (2003) and in summary, good agreement between the calculations using $f_{\varepsilon 2}(N)$ or when using the limiter with $c_T = 12$ and the experiments was found. Several integral quantities such as the compressible displacement thickness, δ_1 , momentum thickness, θ , and Re_θ , calculated for an axisymmetric boundary layer are compared to the experimental values in table 4.1.

Employing the $EASM_\alpha$, the calculations were repeated with the wall-distance independent wall-damping function $f_{\varepsilon 2}$ in order to calibrate the constant c_T for later RANS and FSM calculations of the UIUC flow. Figure 4.15 shows the computed streamwise velocity profiles in comparison to the experimental data and theory. The best agreement with the theoretical curves was achieved using $c_T = 4.45$. Using the friction velocity obtained from that case to rescale the data of Herrin and Dutton, the agreement between experiment and RANS calculation is found to be very good. For smaller values of c_T , the velocity profiles undershoot the theoretical log-layer solution. For larger values of c_T , the opposite is the case and the velocity profile departs from the laminar sub-layer too far away from the wall. Several integral quantities, calculated for an axisymmetric boundary layer are again compared to the experiments and to

UIUC		EASM		EASM $_\alpha$		
		$f_{\varepsilon 2}$	$c_T = 12$	$c_T = 4.40$	$c_T = 4.45$	$c_T = 4.50$
δ_1	0.031	0.0349	0.0333	0.0343	0.0341	0.0332
θ	0.0083	0.00833	0.00814	0.00837	0.00831	0.00813
Re_θ	13,700	13,744	13,431	13,810	13,711	13,414

Table 4.1 Comparison of integral quantities from RANS calculations with UIUC-experimental data for turbulent approach-flow; $Re_\delta = 165,000$, $M = 2.46$.

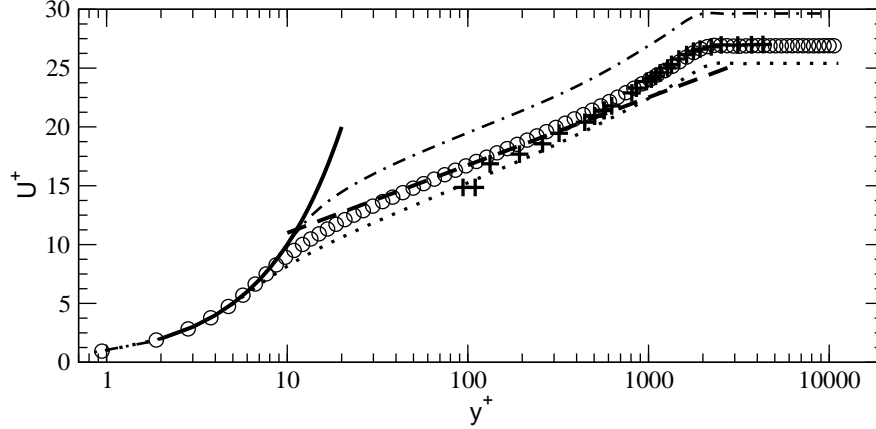


Figure 4.15 Streamwise velocity profiles in wall-coordinates from temporal boundary layer calculations using $EASM_\alpha$; $u^+ = y^+$ (—), $u^+ = 2.5\ln(y^+) + 5.24$ (---), experiments by Herrin & Dutton (1991) (+), $c_T = 4.40$ (- · -), $c_T = 4.45$ (○), $c_T = 4.50$ (- · · -); $Re_\delta = 165,000$, $M = 2.46$.

the previous calculations employing the original EASM. All results are compiled in table 4.1. Overall, the best agreement with the experimental data is found when using the $EASM_\alpha$ with $c_T = 4.45$. Therefore, the result obtained with that calculation was chosen as inflow data for future calculations of the entire base flow at experimental flow conditions.

In summary, the compressible extensions to the source terms of the transport equation for energy and turbulent kinetic energy K were shown to work properly. All turbulence models tested were able to reproduce the supersonic turbulent approach boundary layer over an axisymmetric cylinder, measured in the experiments at UIUC.

4.6 Summary

It was demonstrated in the previous sections that all elements are in place for conducting numerical simulations of transitional and turbulent axisymmetric wakes. Numerous calculations verified that the codes developed for the present research can accurately capture the growth of disturbance waves due to hydrodynamic instabilities, both for incompressible and compressible flows in two and three dimensions.

Numerical codes are therefore available for the investigation of the development and evolution of coherent structures that are the consequence of physical flow instabilities.

The axisymmetric solution of subsonic wakes matched reference data and the three-dimensional, unsteady flow fields of incompressible reference calculations were reproduced. In addition, data from LNS calculations indicated that, at $Re_D = 2,000$, the flow becomes absolutely unstable with respect to both the first *and* the second helical mode.

Finally, it was shown that the implementation of several turbulence models was successful and that turbulent boundary layers, both for incompressible flow over a flat plate and for supersonic flow aligned with a cylinder, could be accurately computed. The results compared well with theory and experimental data. Wall-distance independent versions of the EASM and $EASM_\alpha$ were successfully validated and the additional constants appearing in the limiters were calibrated. A strong dependence of the solution on the values of the coefficients α_i when utilizing the turbulent time-scale limiter was observed for the EASM. For several cases, employing these versions yielded superior results over the standard approach using a traditional wall-damping function.

5. RESULTS - LINEAR STABILITY ANALYSIS

Linear stability calculations were conducted for supersonic axisymmetric wakes at Reynolds numbers between 5,000 and 3,300,000. For all cases, the Mach number was chosen to be $M = 2.46$ to match the flow parameters of the UIUC experiments when computing at the highest Reynolds number. The Mach number was kept constant to show whether certain trends could be established and different flow regimes could be identified as a function of Reynolds number only. Both spatial and temporal stability calculations were conducted in order to determine whether local and/or global instabilities are present in the flow. To investigate whether the flows are absolutely unstable with respect to azimuthal/helical perturbations, pulse disturbances were introduced into the azimuthal Fourier modes within the recirculation region. The amplitudes of the Fourier modes at the disturbance location were monitored over time to determine whether the disturbances grow or decay. For cases where the pulse response decayed in time, periodic forcing was applied to the shear layer and the spatial growth or decay of the perturbations was observed to identify whether the flow is subject to convective instabilities.

5.1 Basic State

In order to obtain a basic state for the linear stability calculations, axisymmetric calculations were conducted with the full N-S code for Reynolds numbers up to $Re_D = 400,000$. The basic state for the $Re_D = 3,300,000$ case was obtained from an axisymmetric RANS calculation (see chapter 7). The converged axisymmetric flow fields served as basic state for the three-dimensional spatial and temporal stability calculations. As shown in the validation chapter (section 4.4.1), the boundary layer thickness at separation has a pronounced effect on the global flow-field, even for axisymmetric calculations. To match the approach boundary layer thickness measured

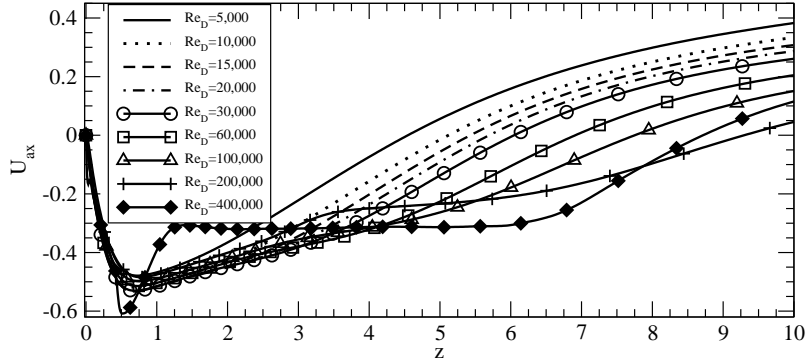


Figure 5.1 Centerline streamwise velocity obtained from axisymmetric N-S calculations for different Reynolds numbers; $\delta_c = 0.1$, $M = 2.46$.

in the experiments at UIUC, the approach boundary layer was designed such that $\delta_c = 0.1$ for all cases. The parameters used for the calculations are listed in the second column of table D.6 in Appendix D, except that $kh = 0$, $dt = 7 \cdot 10^{-3}$ and the computational cost per flow-through-time was 0.428 CPU hours on an *HP Alpha* computer. Several calculations were repeated on different computational grids to verify that the grid-resolution was sufficient. The axisymmetric calculations converged to a steady-state solution for all Reynolds numbers $Re_D \leq 100,000$, implying that no absolute instability with respect to axisymmetric disturbances is present. However, for $Re_D \geq 200,000$, the flow became unsteady, suggesting that the flow may be absolutely unstable with respect to the axisymmetric mode.

The streamwise velocity component at the axis obtained from the axisymmetric N-S calculations is shown in figure 5.1. As for the subsonic case, the maximum reverse velocity is fairly constant for all Reynolds numbers investigated when keeping the approach boundary layer thickness constant. However, the recirculation length varies considerably and increases for larger Reynolds numbers. The streamwise axis-velocity at the outflow ($z = 15.9$) is supersonic for $Re_D < 20,000$. For larger Reynolds number, the flow becomes marginally subsonic close to the axis. Due to the fact that the cases with $Re_D \geq 200,000$ become unsteady, averaged solutions are shown. For a further discussion of the $Re_D = 400,000$ case, see section 6.1.3.

5.2 Spatial Results

In contrast to standard LST, when using spatial simulations, the basic state can be two-dimensional and allow for strong gradients in the streamwise direction. Thereby, calculations are not restricted to local analysis and can account for non-parallel and other global effects. In the LNS code, all azimuthal modes are decoupled and a linear analysis for each individual mode can be accomplished simultaneously. In addition, it was shown in the validation chapter (chapter 4) that results obtained with the linearized N-S code reproduced the data obtained from the full N-S code for small disturbances. As the LNS calculations can be conducted entirely in Fourier space without having to utilize Fourier transforms and allocate additional collocation points to avoid aliasing errors, the computational costs are significantly reduced. For these reasons the linearized code was employed for all spatial linear stability calculations.

Pulse disturbances were introduced into the azimuthal modes behind the base within the recirculation region at $r = 0.5$ and $z = 2.5$. For all other relevant parameters of the stability calculations conducted with the linearized code, see table D.6 in Appendix D. As opposed to the temporal calculations that will be presented later, for each azimuthal mode the most amplified streamwise wavelengths are included in the calculations and cannot be excluded by an unfortunate choice of the streamwise domain-length. Note that the temporal behavior of each azimuthal mode can be composed of multiple unstable streamwise wavelengths. The temporal development of the azimuthal Fourier modes of the streamwise velocity component was monitored at the disturbance point and is shown in figure 5.2 for several Reynolds numbers.

In contrast to the subsonic cases investigated in the validation chapter (section 4.4.2), at $Re_D = 5,000$, all azimuthal modes decay rapidly, implying that, at this Reynolds number, the supersonic flow is linearly stable with respect to axisymmetric and helical modes. This fact illustrates the strong damping effect of compressibility, in particular considering that the approach boundary layer for the supersonic cases

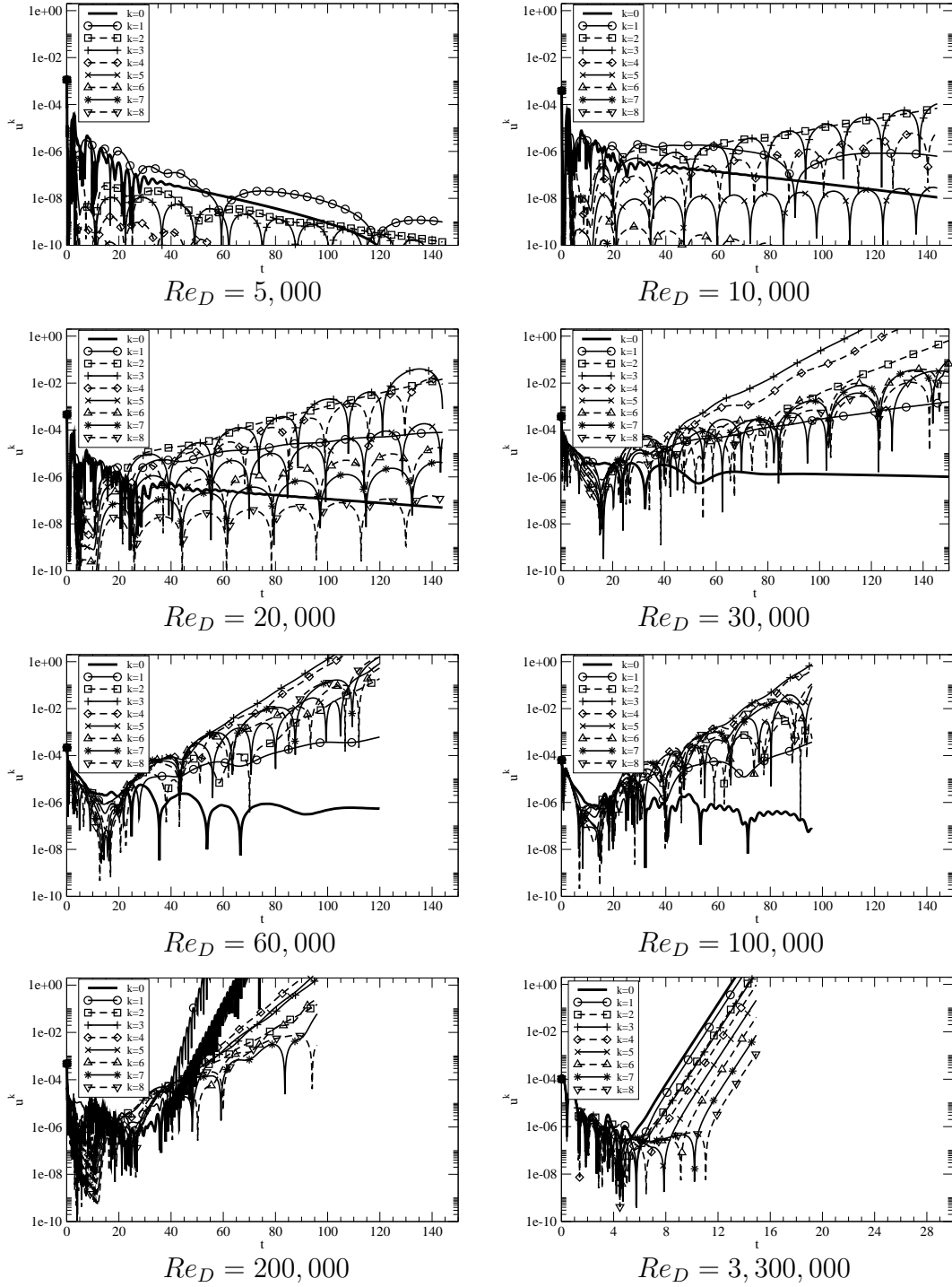


Figure 5.2 Temporal development of azimuthal Fourier modes of streamwise velocity obtained from LNS calculations for various Reynolds numbers; $M = 2.46$.

was chosen to be significantly thinner than for the subsonic cases. A steeper gradient in the separated shear-layer is, therefore, enforced and should lead to even larger growth rates of the disturbances than in the subsonic case. Even though modes $k = 0$ and $k = 1$ are the least damped ones at $Re_D = 5,000$, when increasing the Reynolds number to 10,000, these two modes do not grow but the azimuthal Fourier modes $k = 2$ and $k = 3$ are the only modes to become amplified. It should be noted that mode $k = 2$ grows monotonically, while mode $k = 3$ and several higher modes exhibit an oscillatory behavior in time with a regular period of $F \approx 12$.¹ Further increasing the Reynolds number to $Re_D = 20,000$, the first azimuthal mode also becomes unstable, showing the same regular growth as $k = 2$. At this Reynolds number, all higher Fourier modes included in the calculation are amplified. For $Re_D = 30,000$, the amplification rates of all unstable modes are increased and modes $k = 1 - 4$ all exhibit monotone growth with modes $k = 3$ and $k = 4$ featuring the largest growth rates. At this point it would be of interest to solve the multi-dimensional eigenvalue problem for the basic states under consideration according to Theofilis (2003). This could determine whether the modes exhibiting monotonous growth possess a purely imaginary complex frequency, i.e., are non-oscillatory.

The main difference that can be observed for both the $Re_D = 60,000$ and $Re_D = 100,000$ cases (besides the increased amplification rates) is that modes $k = 7$ and $k = 8$ possess growth rates exceeding those of most other modes, except for $k = 3$ and $k = 4$. Only when increasing the Reynolds number to 200,000, a qualitative change can be noticed. For this case, mode $k = 1$ is the most amplified Fourier mode and the axisymmetric mode exhibits a larger growth rate than all remaining modes. This confirms the suspicion, that, at this Reynolds number, an absolute instability of the axisymmetric mode could be present for the flow conditions under investigation. At $Re_D = 3,300,000$, the linear stability calculation was conducted with the high

¹The absolute value of the data is shown in order to display the results on a logarithmic scale, therefore, sign changes appear as local minima.

Reynolds number version of the LNS code, as presented in Appendix A.3.1. Note that, for this case, a much shorter time-interval is selected, illustrating the considerably increased growth-rate for all Fourier modes, in spite of the additional eddy viscosity which was included in the calculation. In contrast to all previous cases, the amplification rate of all modes, including the axisymmetric mode, is similar.

Tourbier (1996) found no absolute instability with respect to helical modes for $Re_D < 30,000$. However, judging from results obtained from the LNS simulations, it appears to be more likely that the lower limit for an absolute instability with respect to helical modes lies between 5,000 and 10,000. It can only be speculated about the reasons of the discrepancy between the current results and those by Tourbier (1996). At $Re_D = 20,000$, the first growth of the higher modes was not detected before $t \sim 30$, which corresponds to approximately two full flow-through times. In light of considerably less available computer power at the time of the previous investigation, it seems likely that Tourbier (1996) terminated the calculations at an earlier time, where the amplitudes of the azimuthal modes were still decaying.

To exclude the possibility that reflections from the domain boundaries introduced non-physical perturbations in the region of interest and continuously excited convective instabilities, the calculation for $Re_D = 20,000$ was repeated with a larger domain size. As stated in section 5.1, for $Re_D \leq 20,000$, the flow is subsonic in the vicinity of the axis at the outflow when $z_{max} = 15.9$. For a domain with $z_{max} = 26$, on the other hand, the streamwise axis-velocity at the outflow becomes $U_{ax} = 0.46$, which corresponds to $M_{ax} = 1.12$. Therefore upstream travelling reflections from the outflow were eliminated. The inflow of the computational domain was also moved to 2 radii upstream of the base. Furthermore, no perturbations from the free-stream were anticipated for the radial domain-size chosen. The Mach angle at $M = 2.46$ is $\sim 24^\circ$, therefore, for a domain height of $r = 6$, the expansion wave emanating from the base corner reaches the freestream at approximately $z = 11$. Hence, potential

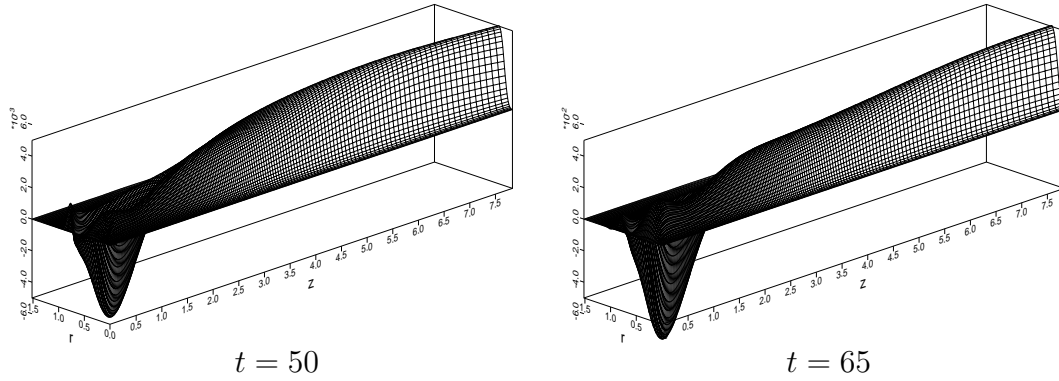


Figure 5.3 Two dimensional mode-shape of Fourier mode $k = 3$ of the streamwise velocity component obtained from LNS calculations for two instances; $Re_D = 30,000$, $M = 2.46$.

reflections from the free-stream boundary will not interfere with the wake before approximately 22 radii downstream of the base. The calculation with a different domain size showed no significant difference from the original computation, giving confidence in the results discussed above.

So far, only the pulse response in time for a single location was discussed. When observing the entire flow field, it appears as if the unstable modes are of two-dimensional nature. Representative for all other cases, the third azimuthal Fourier mode of the $Re_D = 30,000$ case is shown in figure 5.3 for two time-instants. Even though the amplitude increases one order of magnitude from $t = 50$ to $t = 65$, the shape of the mode changes only marginally, in particular close to the base at $z \approx 0.5$. Farther downstream, several azimuthal modes oscillate in time while growing, as was observed in figure 5.2, however, the shape of the modes also is preserved. The local maximum close to the base grows monotonically for all unstable modes, irrespective of the Reynolds number, also maintaining a “frozen” two-dimensional distribution. It is suggested, that this is an indication for the presence of a global mode. In order to verify that this might be the case, temporal calculations were conducted, which, due to the parallel assumption of the basic state inherently exclude the presence of global modes. The temporal results are presented in section 5.3.

The radial profiles of azimuthal Fourier modes for all three velocity components, obtained from LNS calculations, are shown in figures 5.4 – 5.6 in order to establish the effect of the Reynolds number on the amplitude distributions. A streamwise location within the recirculation region, $z = 2.5$, was selected. For all data-sets, the azimuthal modes of all velocity components were scaled with the global maximum of the first azimuthal Fourier mode of the streamwise component. This procedure was chosen to ensure that, for each azimuthal Fourier mode, the amplitudes of the three velocity components could be compared to each other. The amplitudes among separate Fourier modes were not considered crucial, as all modes are decoupled in the linearized calculations and, therefore, do not interact with each other.

For all Reynolds numbers investigated, the radial profiles of the axisymmetric mode $k = 0$ possess their maximum in the vicinity of the shear layer. In contrast, for Reynolds numbers up to $Re_D = 100,000$, the amplitude distribution of the first azimuthal mode exhibits a global maximum at $r \approx 0.2$ for the streamwise component, and a maximum at the axis for the radial and the azimuthal components. The mode-shapes, therefore, strongly resemble those found for the subsonic wake calculations at $Re_D = 1,000$ (see section 4.4.2). For $Re_D \geq 200,000$, however, the radial profiles exhibit an entirely different behavior, with the global maximum of the first mode of all velocity components located in the shear layer. The above observations lead to the conclusion, that, in spite of being damped up to $Re_D = 10,000$ and amplified for $Re_D \geq 20,000$, the mode-shape of the first azimuthal mode is fairly independent of Reynolds numbers up to $Re_D = 100,000$ at $M = 2.46$. The Mach number appears to determine the threshold value of the Reynolds number at which a significant change in shape occurs, as evidenced by the development of global maxima in the mode-shapes in the shear layer for $Re_D \geq 2,000$ at $M = 0.25$ (see figure 4.11).

For the higher azimuthal modes, a similar behavior can be observed as for the first mode, i.e., for lower Reynolds numbers, the global maxima are located within

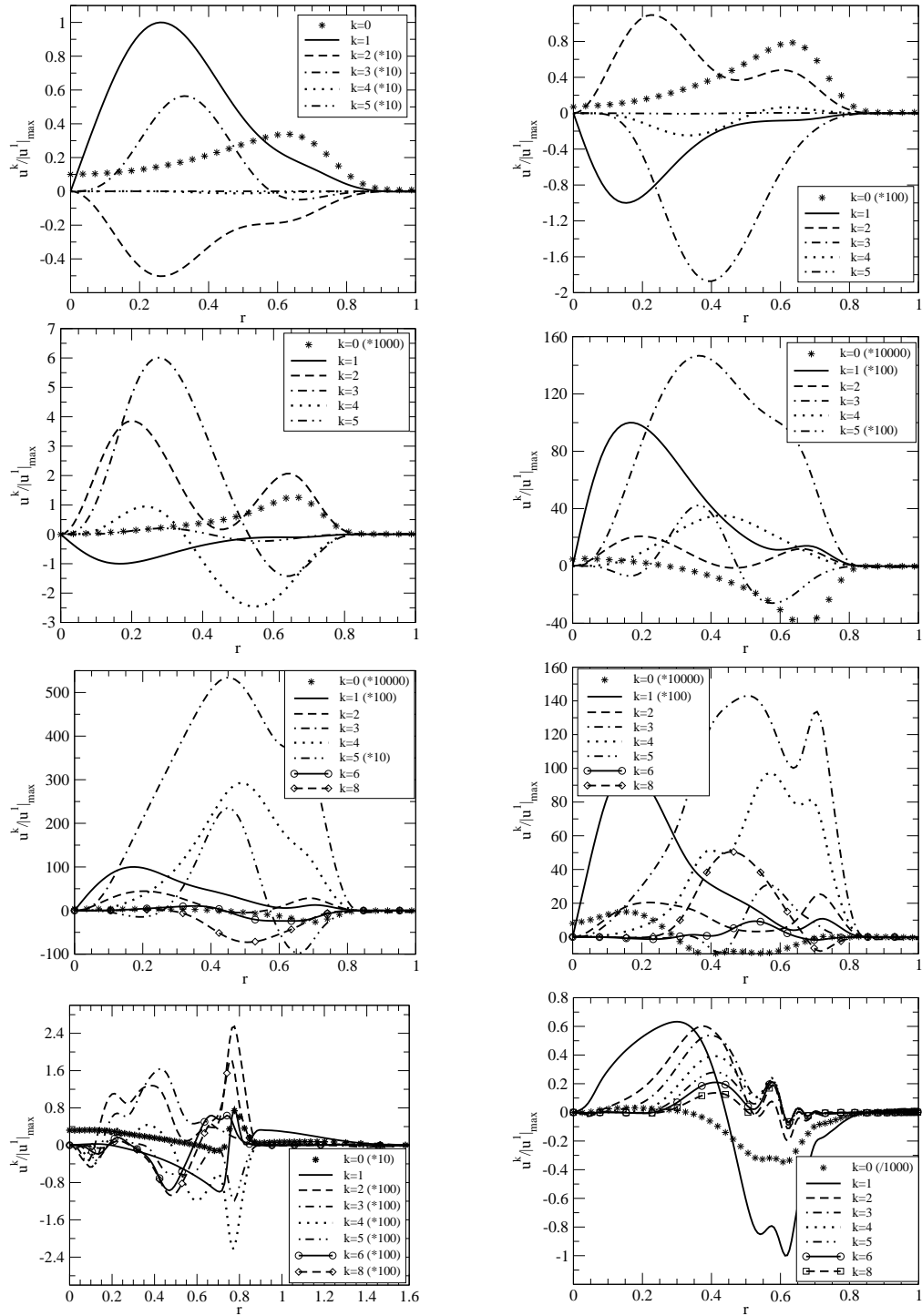


Figure 5.4 Radial mode-shapes of Fourier modes of the streamwise velocity component, obtained from LNS calculations for Reynolds numbers: 5,000, 10,000, 20,000, 30,000, 60,000, 100,000, 200,000 and 3,300,000, from top left to bottom right; $z = 2.5$, $M = 2.46$.

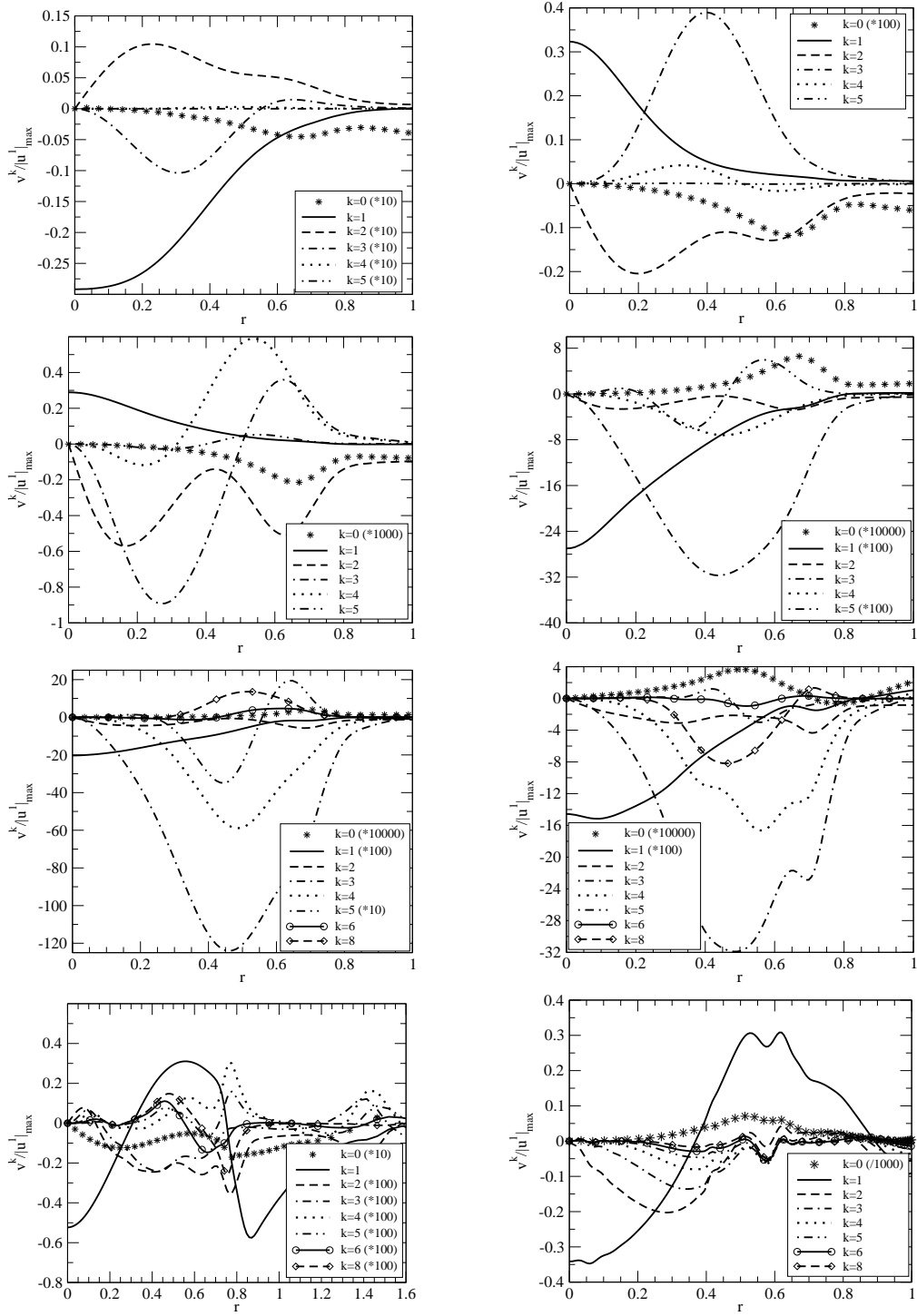


Figure 5.5 Radial mode-shapes of Fourier modes of the radial velocity component, obtained from LNS calculations for Reynolds numbers: 5,000, 10,000, 20,000, 30,000, 60,000, 100,000, 200,000 and 3,300,000, from top left to bottom right; $z = 2.5$, $M = 2.46$.

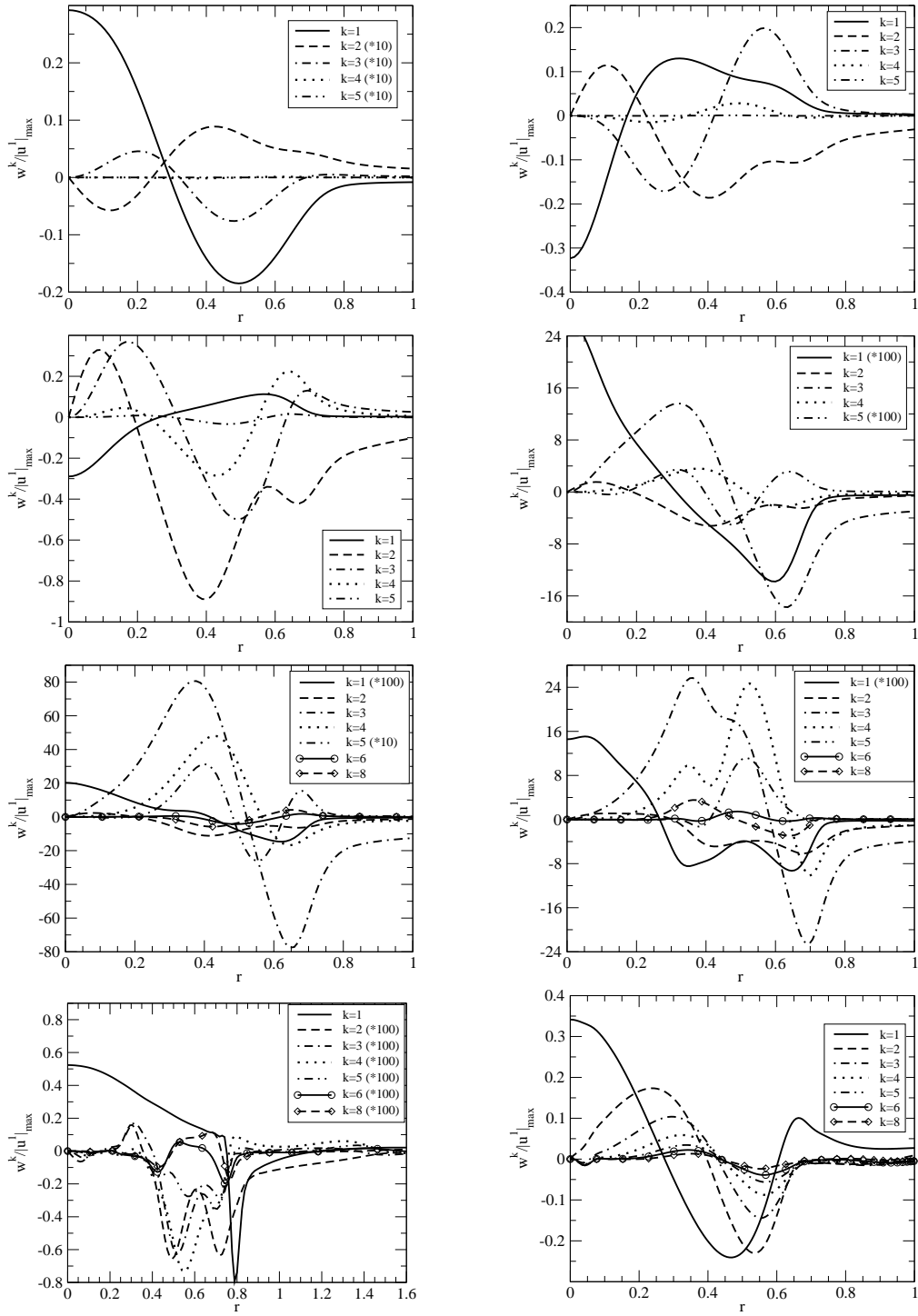


Figure 5.6 Radial mode-shapes of Fourier modes of the azimuthal velocity component, obtained from LNS calculations for Reynolds numbers: 5,000, 10,000, 20,000, 30,000, 60,000, 100,000, 200,000 and 3,300,000, from top left to bottom right; $z = 2.5$, $M = 2.46$.

the recirculation region and for increasing Reynolds numbers, an additional local maximum develops in the shear layer, becoming the absolute maxima for $Re_D \geq 200,000$. As opposed to the first azimuthal mode, for higher modes the presence of a local maximum in the shear layer region occurs for considerably smaller Reynolds numbers, starting at $Re_D = 10,000$.

This behavior leads to the suggestion that two distinct instability mechanisms for the higher azimuthal modes might be present in the flow: A *global mode* within the recirculation region, and a *shear-layer mode*. The fact that the shear-layer mode becomes visible in the radial profiles only for higher Reynolds numbers is expected. The shear-layer mode is subject to strong damping in high compressibility environments. A measure for the compressibility of the flow is the convective Mach number M_c , introduced by Bogdanoff (1983). When using the isentropic definition of M_c , the largest convective Mach number is reached at the streamwise location where the maximum reverse velocity can be found,² i.e., in the initial shear-layer. Therefore, large Reynolds numbers are required in order to enable the shear-layer instability to be amplified. Several azimuthal modes with $k > 1$ display a strong contribution of the shear-layer mode at lower Reynolds numbers. This can be attributed to the fact that oblique disturbances possess larger amplification rates under high compressibility conditions.

The location $z = 2.5$ was selected for the above discussion because it is representative of a large part of the recirculation region. However, the two-dimensional mode-shape shown in figure 5.3 exhibited a local maximum at $z = 0.5$, growing monotonically for all Reynolds numbers. Therefore, mode-shapes of the streamwise velocity component are also shown for two Reynolds numbers in figure 5.7. In contrast to the location $z = 2.5$, the global mode appears to be dominant for both Reynolds numbers. Merely the first azimuthal mode shows a significant contribution of the shear-layer

²In fact, due to the rapid expansion at the base, the free-stream velocity also possesses its largest value at the same streamwise location.

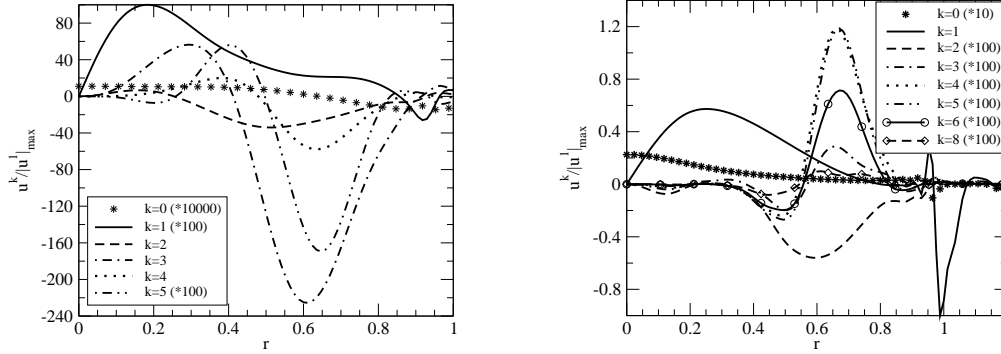


Figure 5.7 Radial mode-shapes of Fourier modes of the streamwise velocity component, obtained from LNS calculations; $Re_D = 30,000$ (left) and $Re_D = 200,000$ (right); $z = 0.5$, $M = 2.46$.

mode in the $Re_D = 200,000$ case. The decreased contribution of the shear-layer mode at the location $z = 0.5$ compared to the location $z = 2.5$ suggests that this instability is of convective nature, i.e., grows in the downstream direction.

The radial profiles of the azimuthal modes at a streamwise location downstream of the recompression region (not shown here), were also scrutinized. All mode-shapes only exhibited one maximum, contracted to a smaller radial extent due to the lesser circumference of the wake at the location further downstream. In the absence of a recirculation region, only the shear-layer mode is present at the location within the trailing wake.

In conclusion, evidence for an absolute instability with respect to higher azimuthal modes, $k > 0$, was found at $M = 2.46$ for $Re_D > 5,000$. For $Re_D > 100,000$, the flow appears to be absolutely unstable with respect to the axisymmetric mode, $k = 0$. For the Reynolds number range $10,000 \leq Re_D \leq 100,000$, the linearly most amplified modes are $k = 2, 3, 4$. It is suggested that, for higher azimuthal modes, a global mode and a shear-layer mode coexist. For increasing Reynolds numbers, the shear-layer mode gains in importance and, eventually, becomes dominant.

5.3 Temporal Results

In order to determine whether the flow is locally or globally unstable with respect to axisymmetric, azimuthal or helical modes, stability investigations at several characteristic streamwise positions were conducted with the temporal code. Using the temporal approach for small disturbances can be compared to performing standard linear stability analysis. The primary benefit of conducting temporal calculations complementary to spatial calculations is that it can be determined whether disturbances are locally unstable or if they only become unstable in the presence of global effects, such as streamwise pressure gradients, streamline curvature, etc.

To obtain the local profiles required for the stability investigations, axisymmetric DNS calculations were conducted for all Reynolds numbers of interest. The one-dimensional profiles of the desired streamwise location were then extracted from the converged spatial solutions and the radial velocity component was set to zero in order to be consistent with the temporal assumption of parallel flow. The profiles were read into the temporal calculations at initialization and constituted the basic state, i.e., the mode $(l, k) = (0, 0)$. With the radial velocity set to zero and the lack of streamwise gradients of the basic state, for the mode $(0, 0)$, the governing equations reduce to a pure diffusion equation. A forcing term needs to be added to the RHS of the governing equations in order to avoid a significant change of the basic state over time. For a detailed discussion of applying forcing terms in order to maintain the basic state, see, e.g., Laurien & Kleiser (1989); Sandberg (1999); Balzer (2003). Three characteristic positions were chosen for the stability calculations: Firstly, a location fairly close to the base, at $z = 0.5$. Here, the highest reverse velocity is reached for all Reynolds numbers investigated (see figure 5.1) and the shear layer features a large radial gradient just after separation. In the spatial calculations, the maximum of the global mode was found at this position. Secondly, a position farther downstream, at $z = 2.5$, where the shear layer has grown and the gradient is reduced. This location

is representative of a large area within the recirculation region. Finally, downstream of the reattachment point, at $z = 7$ or $z = 9$, within the trailing wake. No reverse flow is present, however a significant velocity deficit occurs.

The same numerical grid in the radial direction was used in the temporal case as for the spatial calculations. The azimuthal extent of the domain was $0 \leq \theta \leq \pi$ for all cases. However, which streamwise length of the domain to chose was not obvious. Therefore, a calculation of a representative case, here $Re_D = 30,000$ at $z = 2.5$, was conducted for a fairly long streamwise extent ($\lambda_z = 4 \cdot \pi$) with a large number of streamwise Fourier modes ($lh = 32$). The calculation revealed that no modes with $l \leq 2$ or $l \geq 12$ were strongly amplified. Thus, all stability computations were done with 8 streamwise modes for a domain length of $\lambda_z = 2 \cdot \pi$. For further relevant parameters, see table D.3 in Appendix D. A pulse was introduced at the inflection point of the respective profile when the calculation is initialized and the development of the streamwise and azimuthal Fourier modes was monitored at the forcing location.

The results are shown for Reynolds numbers $5,000 \leq Re_D \leq 200,000$ in figure 5.8. For clarity, only the most amplified Fourier modes are shown. Recall that the mode numbers are given in the format (l, k) , where l denotes the streamwise mode-number and k denotes the azimuthal wavenumber. Each azimuthal mode is assigned one symbol and the streamwise modes are distinguished through separate line-styles. In general, it can be observed that the growth rates of the most amplified modes increase with increasing Reynolds numbers. Also, the closer the location of the profile under investigation is to the base, the higher the growth rates appear to be and the more modes experience strong amplification. The graphs also reveal that the most unstable modes are always helical (oblique) modes, i.e., $k, l \neq 0$. In fact, unstable axisymmetric modes ($k = 0$) are only found for the two upstream locations, and no unstable streamwise modes ($l = 0$) were found at all in the linear regime.

For the lowest Reynolds number investigated (5,000), at $z = 0.5$, modes with

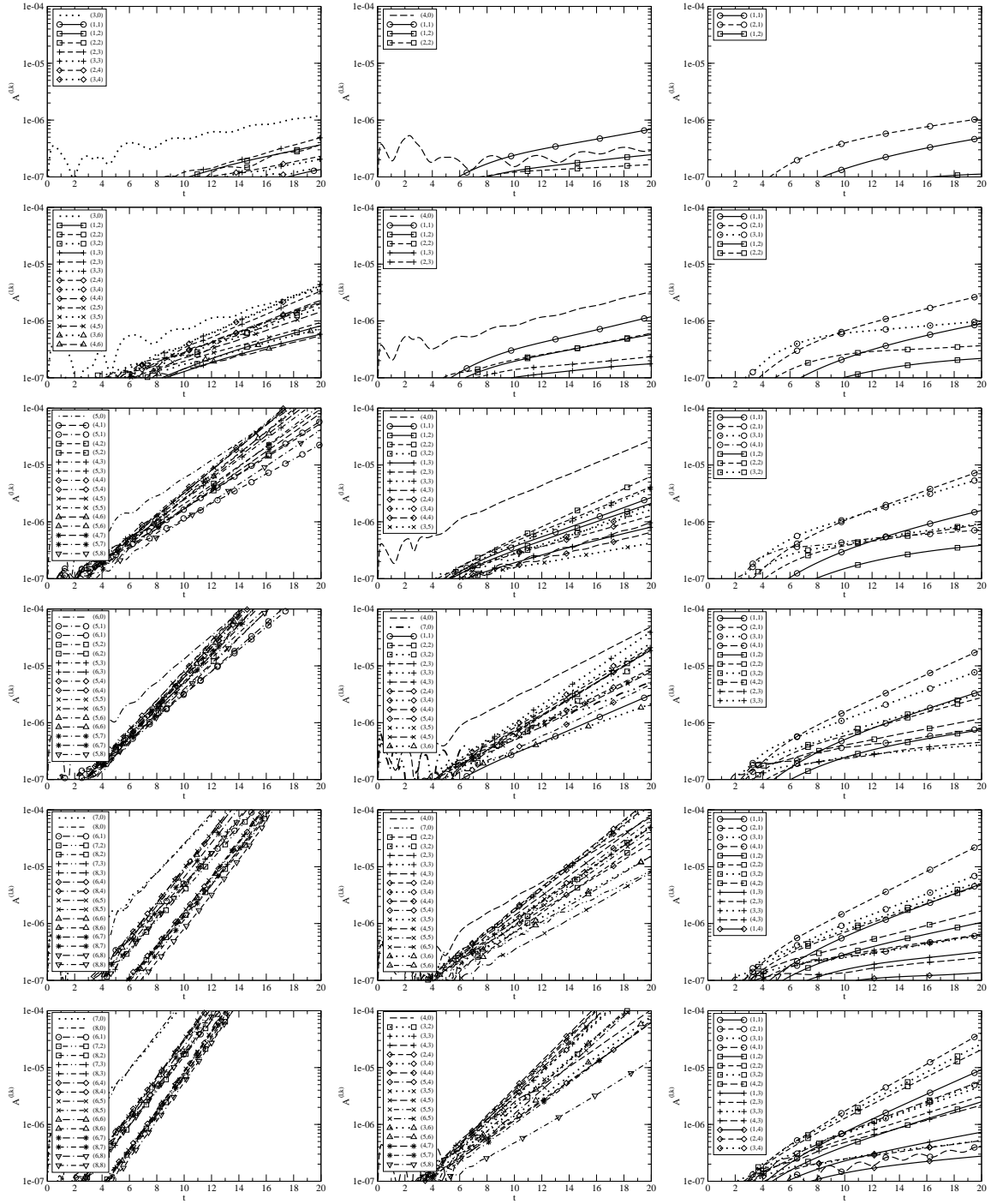


Figure 5.8 Temporal development of Fourier modes of density obtained from TDNS for $Re_D = 5,000$, $Re_D = 10,000$, $Re_D = 30,000$, $Re_D = 60,000$, $Re_D = 100,000$ and $Re_D = 200,000$ from top to bottom; left: $z = 0.5$, center: $z = 2.5$ and right: $z = 9$ (top two), $z = 7$ (remaining); $M = 2.46$.

$k = 2, 3, 4$ are most amplified with the streamwise mode numbers being $l \leq 3$. Further downstream, at $z = 2.5$, where the reverse velocity is reduced and the radial shear-layer gradient is diminished, only the first two azimuthal modes are amplified for long streamwise wavelengths. Within the trailing wake, the local analysis shows that only the first azimuthal mode is unstable for $l = 1, 2$.

Increasing the Reynolds number to 10,000, a larger amount of Fourier modes becomes unstable. At the location close to the base, azimuthal modes up to $k = 6$ are strongly amplified. At $z = 2.5$, as opposed to the lower Reynolds number, modes with $k = 3$ also are amplified and in the trailing wake modes with $k = 2$ start to grow, albeit at a considerably smaller rate than modes with $k = 1$.

Further increasing the Reynolds number, the trend, that larger azimuthal mode-numbers also become strongly amplified, continues. However, a significant difference can be observed when comparing the three streamwise locations. For the location within the trailing wake, the streamwise mode-number of the most unstable modes does not increase considerably, i.e., $l = 2, 3$ for all k . In contrast, at $z = 0.5$, the streamwise wavenumber of the most amplified Fourier modes increases steadily with Reynolds number such that, at $Re_D = 200,000$, modes with $l \geq 4$ are most amplified for all k . The location at $z = 2.5$ shows a similar behavior, however, the shift towards higher streamwise wavenumbers is not as pronounced. In order to assert that no streamwise modes higher than $l = 8$ are significant, the calculations at $z = 0.5$ for the higher Reynolds numbers were repeated with a streamwise domain length eight times smaller, i.e., $\lambda_z = 0.25 \cdot \pi$. For these cases, $l = 1$ corresponds to $l = 8$ in the calculations with the longer domain-length. The additional calculations revealed that no modes with $l > 8$ (in the original case) were strongly amplified for the Reynolds numbers investigated.

Additional calculations were conducted by Balzer (2003) for a streamwise location close to the mean reattachment point. For all Reynolds numbers, the results were similar to those found here at $z = 7$ or $z = 9$, i.e., the azimuthal modes with $k = 1$

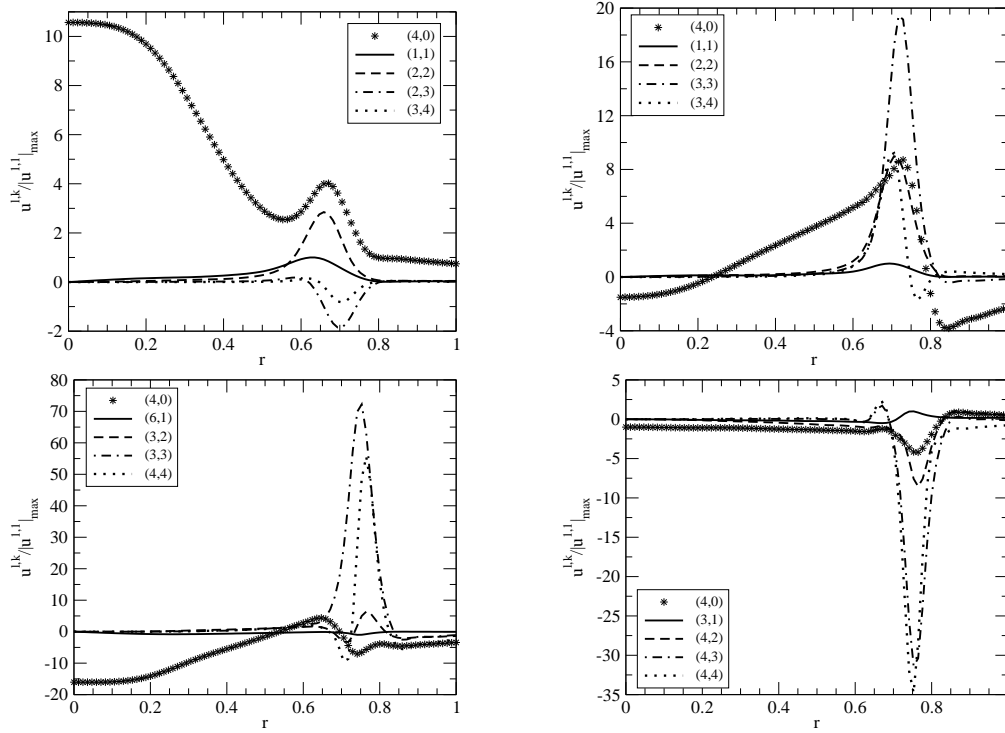


Figure 5.9 Radial mode-shapes of Fourier modes of the streamwise velocity component, obtained from TDNS; $Re_D = 30,000$ (top left), $Re_D = 60,000$ (top right), $Re_D = 100,000$ (bottom left) and $Re_D = 200,000$ (bottom right); $z = 2.5$, $M = 2.46$.

and $k = 2$ were most amplified. Recall that in the spatial calculations employing the linearized code, the azimuthal modes $k = 2, 3, 4$ were the most amplified modes for $10,000 \leq Re_D \leq 100,000$.

The radial mode-shapes obtained from temporal calculations are shown in figure 5.9. For all Reynolds numbers and locations $z \geq 2.5$ investigated with the temporal code, the mode-shapes exhibit a maximum exclusively in the shear layer region. Virtually no variation can be observed within the recirculation region, implying that, at this location the local analysis only captures the shear-layer mode. This leads to the hypothesis that the inner maximum found in the radial profiles obtained from spatial calculations might indeed be caused by global modes. The above results also confirm that the shear-layer instability is generated locally. Judging from the non-

zero phase speeds found for all unstable modes, the shear-layer mode appears to be a convective instability. Radial profiles obtained from local stability calculations using a profiles from the trailing wake (not shown here) showed a similar behavior to the spatial results. This supports the notion that the trailing wake region only contains the shear-layer mode.

In summary, for all Reynolds numbers and streamwise positions investigated here, unstable modes were found. The dominant unstable modes most likely can be classified as convective *shear-layer* modes and are of helical nature. For increasing Reynolds numbers, the growth rates increase and higher azimuthal modes gain importance. Depending on the streamwise location, the streamwise wavenumbers of the fastest growing modes also increase for larger Reynolds numbers. Comparing the results from the temporal calculations with the spatial results presented above constitutes circumstantial evidence that global modes are present in the spatial calculations. The (linearly) most unstable shear-layer modes appear to be generated locally. In order to determine, whether the instabilities found in the lowest Reynolds number case are of convective or absolute nature, additional spatial computations were conducted and are presented in the following section.

5.4 Convective Instability

It was determined in the spatial calculations, that supersonic axisymmetric wakes at $M = 2.46$ with an approach boundary layer thickness of $\delta = 0.1$ become absolutely unstable with regard to higher azimuthal modes for $Re_D > 5,000$. The temporal results presented in section 5.3, however, showed amplification of disturbances at $Re_D = 5,000$. Due to the periodic boundary conditions in the streamwise direction, the temporal approach converts every physical problem to a closed system, i.e., disturbances cannot leave the system. If the flow is convectively unstable, the disturbance

will, therefore, grow in time, which in the spatial case would be defined as an absolute instability.

In order to verify that the instabilities detected for $Re_D = 5,000$ in the temporal code are of convective nature, i.e., requiring continuous excitation in order to remain in the region of interest, an additional calculation was conducted. Here, a time-periodic volume forcing, see section 3.7, was introduced in the shear layer immediately after separation (center of disturbance at $r = 1.05$, $z = 0.04$). The fact that all azimuthal Fourier modes are decoupled in the linearized code was advantageous, as

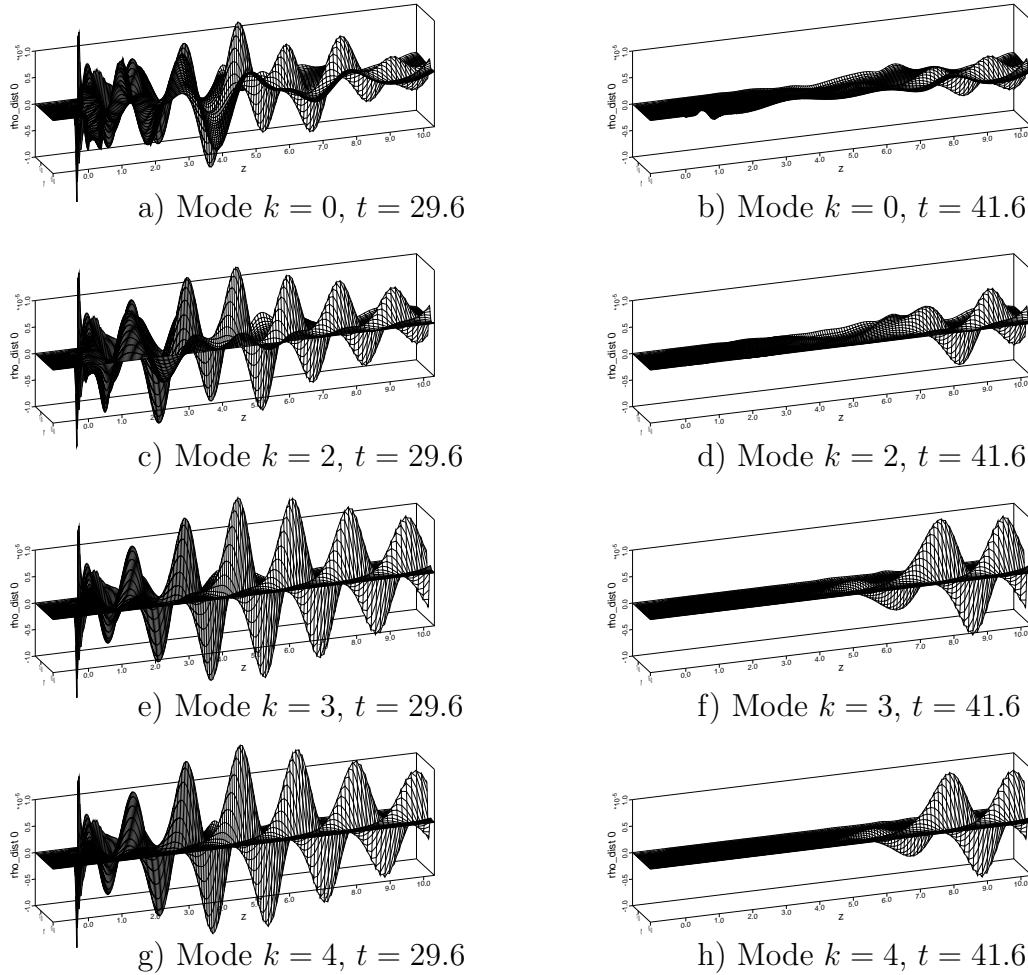


Figure 5.10 Instantaneous azimuthal Fourier modes of ρ ; periodic forcing active (left) and switched off (right) $z = 2.5$, $r = 0.5$, $Re_D = 5,000$, $M = 2.46$.

the stability behavior of several azimuthal modes could be investigated with a single calculation. Four higher azimuthal Fourier modes were used, and the forcing at low amplitude ($A_{dist} = 1 \cdot 10^{-5}$) was introduced into every mode. The periodic forcing at a frequency of $\omega = 0.5$, which appeared to be the most amplified one in the temporal calculations, was active for the time-interval $0 \leq t \leq 32$. The forcing was then switched off, in order to evaluate whether the disturbances were entirely convected out of the computational domain. Results for all azimuthal modes are shown in figures 5.10 (a) to (h).

At $t = 29.6$, while the forcing is still active, it can be observed for all modes that the disturbances grow in the streamwise direction up to the end of the recirculation region (the recirculation length of the basic state is $z = 4.4$) and then start to decay. It can also be seen that modes $k = 3$ and $k = 4$ exhibit the largest growth rates. The graphs on the right hand side of figure 5.10 show instantaneous results 4.8 forcing-periods after the forcing was switched off ($t = 41.6$). The disturbances have travelled downstream and the amplitudes of disturbances remaining in the recirculation region have become small. At a later time (not shown here), no disturbances remain in the region of interest, a clear indication that, for this Reynolds number, the flow is convectively unstable (and not absolutely unstable) with regard to all azimuthal modes.

In order to verify that the disturbances contained in the recirculation region truly decay once the forcing is switched off, the temporal development of all modes was again monitored at the same probe point as for all above cases. The temporal behavior of all modes is shown in figure 5.11. While the forcing is still active, no temporal growth (as opposed to the spatial growth seen in figure 5.10) can be observed at the probe point. All modes exhibit an oscillation with the forcing frequency and the amplitude being similar to the forcing amplitude. After switching off the periodic forcing, all modes start decaying ($t \approx 34$) once the last disturbance generated at the forcing location ($r = 1.05$, $z = 0.04$) has passed the probe point ($r = 0.5$, $z = 2.5$).

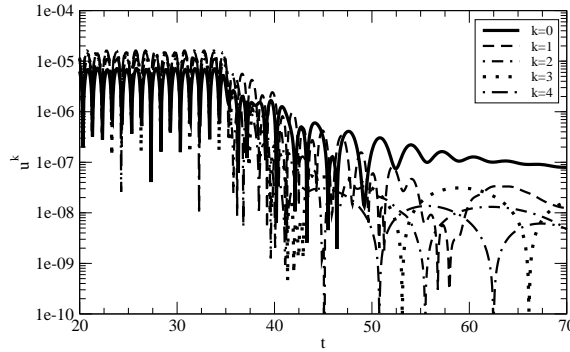


Figure 5.11 Temporal development of azimuthal Fourier modes of the streamwise velocity component obtained from an LNS calculation employing periodic forcing; $Re_D = 5,000$, $M = 2.46$.

5.5 Summary

Supersonic axisymmetric wakes with an approach boundary layer thickness of $\delta_c = 0.1$ were found to be convectively unstable with respect to all azimuthal modes at $Re_D = 5,000$. For larger Reynolds numbers, a pulse disturbance led to temporal amplification of higher azimuthal modes, implying that the flow is absolutely unstable with respect to higher azimuthal modes, $k > 0$, for $Re_D > 5,000$. It was conjectured that absolutely unstable *global modes* within the recirculation region coexist with convectively unstable *shear-layer modes*. The local stability simulations also revealed that the shear-layer modes possess a non-zero streamwise wavenumber, implying that the modes are of helical nature.

The third azimuthal mode $k = 3$ has the highest amplification rate for Reynolds numbers up to $Re_D = 100,000$. For $Re_D > 100,000$, the flow also becomes absolutely unstable with respect to the axisymmetric mode, $k = 0$. The mode-shapes obtained from spatial simulations illustrate that the global mode is dominant for low Reynolds numbers. For larger Re_D , the strong damping effect of compressibility is overcome and the global maxima of all azimuthal modes move from the interior of the recirculation region to the shear-layer region, i.e., the shear-layer mode gains in importance.

6. RESULTS - DIRECT NUMERICAL SIMULATIONS

The results presented in the previous chapter have given valuable insight into the linear stability characteristics of supersonic axisymmetric wakes at various Reynolds numbers. Nevertheless, by excluding nonlinear effects, the occurrence of coherent structures and the break-down to turbulence is not permitted. The main objective of this research is, however, the investigation of the formation and evolution of coherent structures that are a consequence of physical flow instabilities. The understanding of the physical mechanisms is essential as it is supposed that the structures have a significant impact on the mean flow and are responsible for a considerable amount of base-drag. To that end DNS were employed to investigate the near-wake region in supersonic axisymmetric wakes.

As mentioned in the introduction (section 1.2), DNS of supersonic wakes at flow conditions investigated at UIUC are currently, and will be in the near future, out of reach with present super-computers.¹ For that reason, here transitional supersonic base flows are investigated. Although the flow is not fully turbulent, it will be shown that many of the qualitative features found in the experiments by Dutton and co-workers can be captured. Moreover, transitional flows facilitate the investigation of the initial development of the large structures because the break-down to small-scale turbulence either does not fully occur or takes place on a relatively slow time-scale (or large length-scale), leading to a well-defined separation of scales.

Of particular interest was to determine the significance of certain modes and their effect on the mean flow. This was accomplished by exploiting one of the strengths of conducting numerical simulations: Deliberately simplifying the physical problem at hand. Here, simulations were conducted of various circumferential domain-sizes, thereby intentionally eliminating different azimuthal/helical modes. Thus, the effect

¹This will be illustrated later in section 7.4.1.

of large-scale structures associated with particular azimuthal/helical modes on the global flow behavior could be evaluated.

For all Reynolds numbers investigated in this work, initially a DNS for a half-cylinder (domain with $0 \leq \theta \leq \pi$) was conducted. Once it was verified that the grid-resolution was adequate, integration domains with an azimuthal extent of $\theta < \pi$ were also computed. Thus, various modes of the half-cylinder case were deliberately suppressed and their effect on the mean flow could be studied. For more details about which modes are excluded for different azimuthal domain-sizes, see the description of the axis treatment in section 3.2. Note that in the following, the mode numbers denoted by k refer to the corresponding mode in the half-cylinder case, not the computational mode of the respective calculation, i.e., mode $k = 2$ always has a wavelength of π , for example.

To judge what effect certain azimuthal Fourier modes have on the mean flow, one of the figures of merit will be the visualization of endviews at different downstream locations. In order to give an impression of what kind of wake patterns (when looking at an endview) are generated by various azimuthal modes, several examples were computed analytically, superimposing individual azimuthal Fourier modes with the axisymmetric mode. For calculations employing symmetric Fourier transforms, scalar quantities, such as total vorticity, are represented by a cosine-series (for a complete listing of symmetries, see table B.1 in Appendix B). The polar representation of the endview of the wake then becomes a function of the azimuthal mode-number, k , the mean radial extent of the shear layer, r_0 , chosen as unity here, and an amplitude, A , according to

$$r = r_0 + A \cos(k \cdot \theta) . \quad (6.1)$$

Two fundamentally different solutions can be generated depending on how the amplitude A is treated: The sign of A can be kept constant, here the choice was a

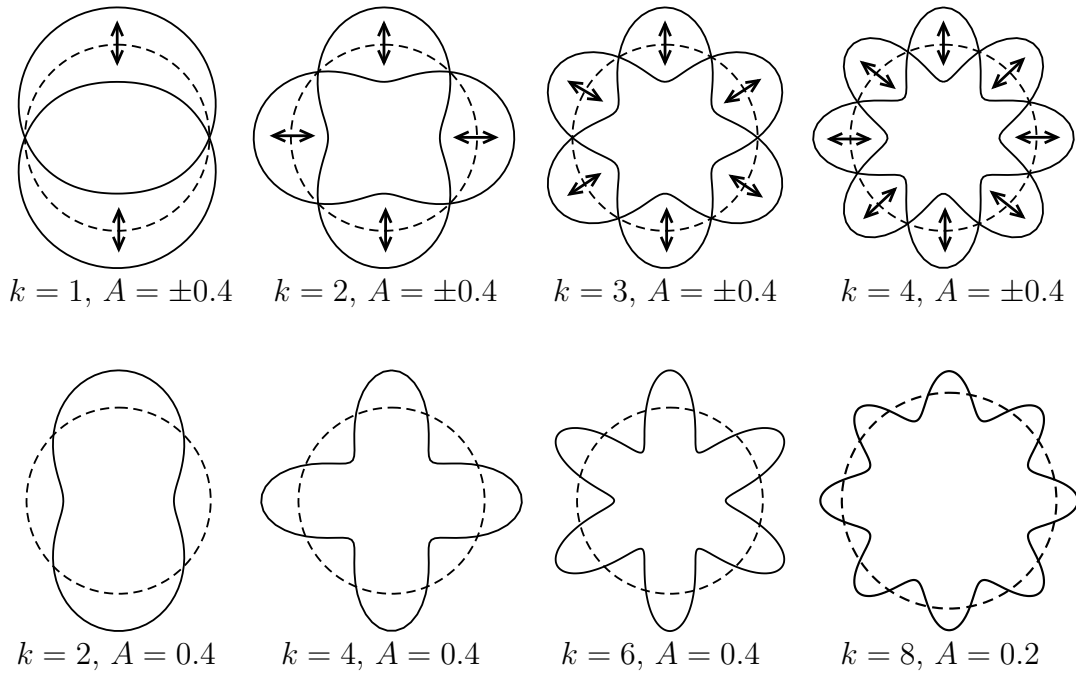


Figure 6.1 Schematic of wake patterns generated by various azimuthal modes.

positive sign; or the sign of the constant can alternate, which would be the case if the respective mode exhibits an oscillatory behavior in time. The resulting patterns are illustrated in figure 6.1 with the dashed line representing the undisturbed axisymmetric state. On top, the results for an oscillating constant A are shown, and on the bottom the solutions obtained when keeping the sign of A constant are displayed. It can clearly be seen, that the same qualitative wake pattern can be produced with different modes. In the top and bottom left figures, a similar shape of the wake can be generated either through a flapping of the wake in the lateral direction, caused by an oscillatory mode $k = 1$, or the presence of a steady mode $k = 2$. A “four-lobe” structure (second graph from left) is possible either through an oscillating mode $k = 2$ or a dominant steady fourth mode. A “six-lobe” pattern (third from left) would be the consequence of either an oscillating dominant mode $k = 3$ or a steady mode $k = 6$, and in case the fourth mode (oscillatory) or $k = 8$ (steady) would exhibit the largest amplitudes, an “eight-lobe” shape (bottom right) could occur. Naturally, any combi-

nation of the above patterns also could be generated if multiple azimuthal modes are significant in a particular case. In order to determine which mode is responsible for the resulting wake pattern, additional data, such as radial amplitude distributions of the azimuthal modes, need to be considered.

The DNS calculations at $M = 2.46$ were conducted for three different Reynolds numbers. The lowest Reynolds number investigated was $Re_D = 30,000$, for which preliminary results were discussed in Tourbier (1996). For the second series of calculations, the Reynolds number was doubled. Finally, the largest Reynolds number chosen was $Re_D = 100,000$, as this constituted the highest Reynolds number possible with the resources available at the time of this research. For all cases, the approach flow is laminar, and transition occurs downstream of the separation point.

6.1 DNS for $Re_D = 30,000$

All calculations were performed on the same streamwise/radial grid with 516×200 points in the streamwise and the radial direction, respectively, and with the smallest grid-spacing at the corner, where $\Delta z_c = \Delta r_c = 0.008$. In the azimuthal direction, the simulation of the half-cylinder was initially carried out with 16 symmetric spectral modes. The amplitudes of the azimuthal modes were scrutinized in the recompression region and here the magnitude of mode $k = 16$ was only one order of magnitude lower than that of the first Fourier mode. Therefore, the calculation was repeated (using the old calculation as three-dimensional initial condition) with 64 symmetrical azimuthal modes. The number of Fourier modes chosen for the calculations with smaller circumferential domain-sizes were chosen such that the azimuthal resolution remained constant, i.e., 32, 24, 16 and 8 modes were used for the quarter-cylinder, $1/6^{th}$ -cylinder, $1/8^{th}$ -cylinder and the $1/16^{th}$ -cylinder calculations, respectively. For all further parameters, see table D.7 in Appendix D.

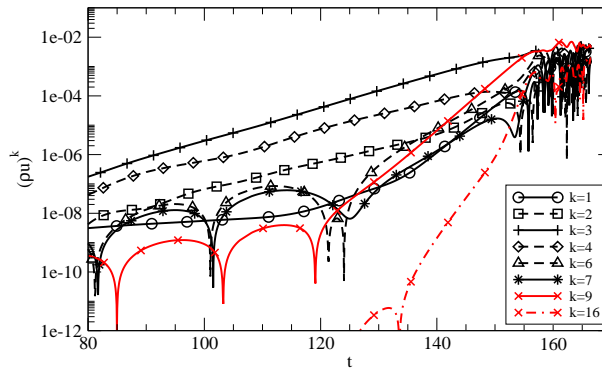


Figure 6.2 Temporal development of Fourier modes of (ρu) at disturbance location $z = 2.5$, $r = 0.5$ at start-up for half-cylinder calculation; $Re_D = 30,000$, $M = 2.46$.

6.1.1 Time-Dependent Results

The pulse response of the higher azimuthal density modes at the disturbance location was monitored for all cases investigated. Rapid growth was observed for all domain sizes, implying that the flow is absolutely unstable with respect to modes $k = 1$ through $k = 8$ for this Reynolds number.² Representative for all circumferential domain-sizes, the temporal development of the Fourier modes of (ρu) at the pulse location for the start-up transient of the half-cylinder case are shown in figure 6.2.

When comparing the temporal development of the Fourier modes with the results obtained from the linear calculations (shown in figure 5.2), the same behavior can be observed up to $t \approx 110$, e.g. the azimuthal Fourier modes $k = 2, 3, 4$ possess the largest growth rates. For $t > 110$, however, modes $k = 3$ and $k = 4$ reach sufficiently large amplitudes such that the nonlinear interaction between these two modes causes an increase in the growth rate of mode $k = 1$. In addition, the nonlinear interaction between modes $k = 3$ and $k = 4$ results in increased growth rates of $k = 6$ and $k = 7$. For $t > 125$ mode $k = 6$ reaches large amplitudes and the nonlinear interaction with $k = 3$ produces a strongly increased amplification rate of mode $k = 9$.

²In order to investigate whether the flow is absolutely unstable with respect to higher azimuthal modes, even smaller azimuthal domain-sizes would have to be computed. Alternatively, LNS simulations with a greater number of modes could be performed.

Eventually, all higher modes experience large growth rates, nonlinearly generated by low-wavenumber azimuthal modes. It is noteworthy that modes $k = 3$ and $k = 4$ continue growing linearly until reaching the nonlinear saturation state. This illustrates that the presence of several linearly (absolutely) unstable azimuthal modes leads to the generation of higher wavenumber modes through nonlinear interaction.

To get a qualitative impression of the dynamics of the flow for varying azimuthal domain-sizes, instantaneous vorticity for the plane with $\theta = 0^\circ$ and $\theta = \theta_{max}$ of the respective calculations are shown in figures 6.3 (a) to (e). Large structures develop in the inner part of the shear layer in agreement with the observations made in experiments by Herrin & Dutton (1995). These structures help to entrain a significant amount of low speed fluid from the recirculation zone and noticeably shorten

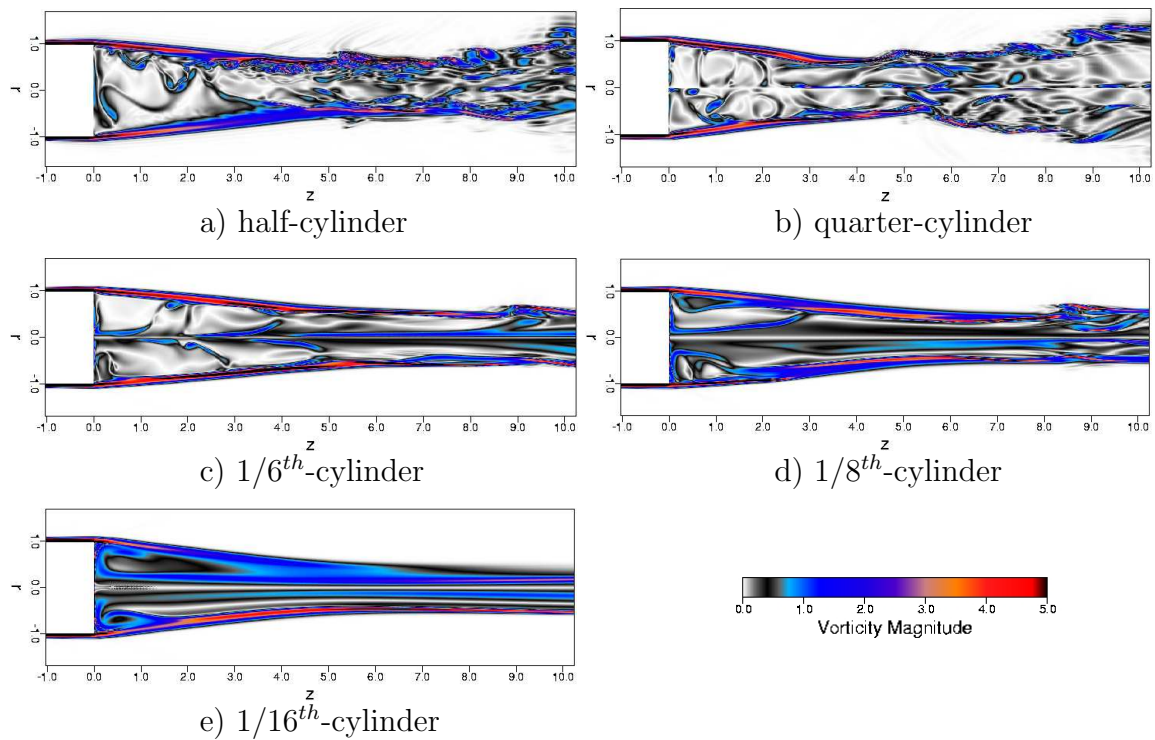


Figure 6.3 Sideviews of instantaneous contours of total vorticity; top half $\theta = 0^\circ$, bottom half a) $\theta = 180^\circ$, b) $\theta = 90^\circ$, c) $\theta = 60^\circ$, d) $\theta = 45^\circ$ and e) $\theta = 22.5^\circ$; $Re_D = 30,000$, $M = 2.46$.

the recirculation region compared to the axisymmetric solution of section 6.1.3. The quarter-cylinder case appears to contain a smaller amount of small-scale structures than the half-cylinder case. For the $1/6^{th}$ -, $1/8^{th}$ - and the $1/16^{th}$ -cylinder cases, the number of large-scale structures is reduced, leading to a significantly longer recirculation region due to the lack of entrainment of low-momentum fluid by large structures (also see figure 6.19), and even less small-scale structures can be observed.

An interval of the temporal development of the Fourier modes of density in a region of high activity, in this case the recompression region, is shown in figures 6.4 (a) – (e). The initial start-up transient is already overcome and a fully nonlinear saturation level has been reached. The decay in energy over the azimuthal modes

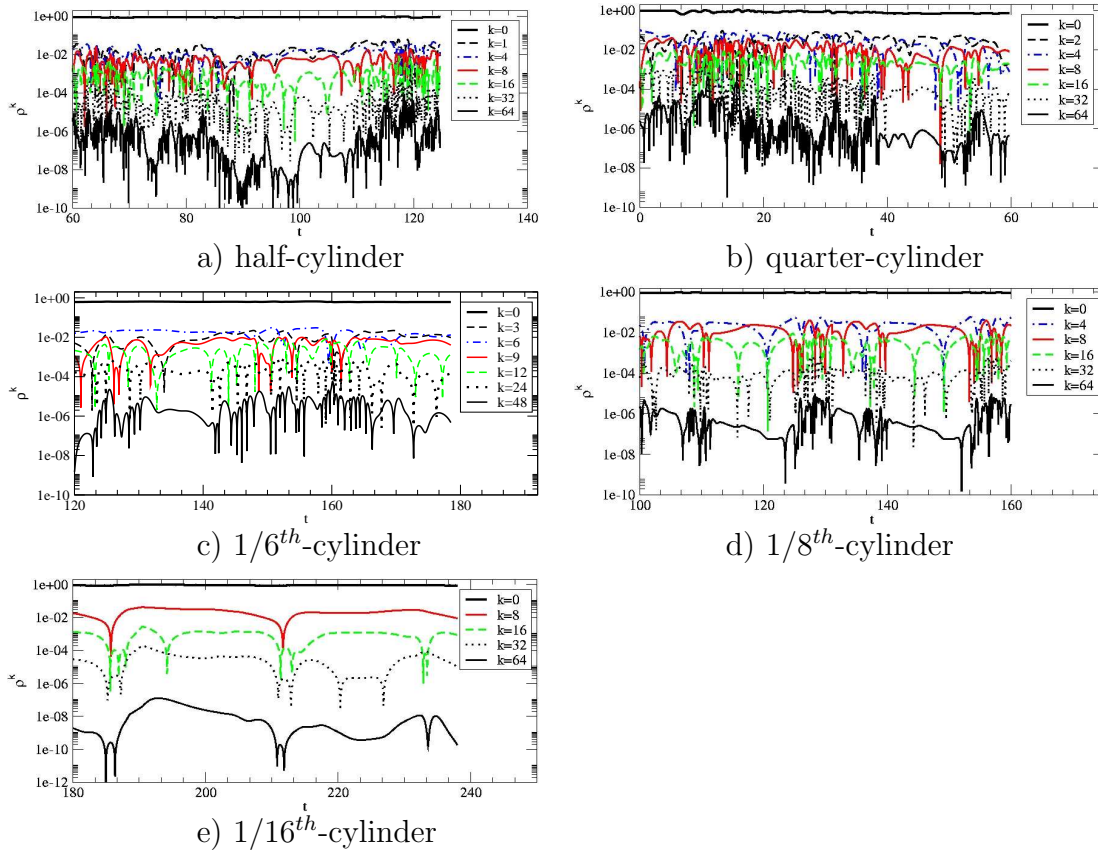


Figure 6.4 Temporal development of Fourier modes of in a region of high activity; $z = 4.82$, $r = 0.238$, $Re_D = 30,000$, $M = 2.46$.

amounts to approximately five orders of magnitude for the four largest domain sizes and even more for the $1/16^{th}$ -cylinder, suggesting that the resolution in the azimuthal direction is sufficient.

For the half-cylinder (a) it can be observed that the magnitude of all modes decays between $80 < t < 100$, leading to a relatively quiet region in the interval $100 < t < 110$. This is an indication that the flow is intermittent. Note that this behavior was also found for the subsonic wake at $Re_D = 1,000$ investigated in section 4.4.2. The presence of intermittency for the current case at a significantly higher Reynolds number illustrates the damping effect of compressibility. It will be attempted to give an explanation for the occurrence of intermittency once a better understanding of the flow field has been established.

The same behavior is observed for the quarter-cylinder case (b) and the $1/6^{th}$ -cylinder case (c), i.e., the flow displays intermittency, particularly noticeable in the intervals $130 < t < 142$ and $40 < t < 50$, respectively. For the $1/8^{th}$ -cylinder (d), the picture changes drastically, showing far smaller amplitudes in the higher modes, and the fraction of quiet regions increases. This behavior is even more pronounced in the $1/16^{th}$ -cylinder case, where the flow fails to exhibit any high-frequency oscillations. Also, no distortion in the azimuthal mean flow $k = 0$ can be detected for the smallest domain size.

The data of the azimuthal Fourier modes of density in the recompression region (for a much larger time interval than shown in figure 6.4) were Fourier-decomposed in time. The obtained frequency spectra were scrutinized to identify dominant frequencies in the flow and to determine if the temporal resolution of the calculations was adequate. For all cases that were investigated, the amplitudes of the azimuthal Fourier modes showed a decay of approximately three decades over the Strouhal number based on diameter. This implies that the time-step chosen for the calculation was sufficiently small to resolve all relevant temporal scales. This was expected, as the

time-step limitation due to the explicit time-integration is fairly restrictive.

As shown in figures 6.4 (a) – (e), the flow exhibits an intermittent behavior for all cases. This complicated the Fourier analysis in time and a study of how the size of the sampling interval would affect the resulting frequency spectrum was conducted. In conclusion, post-processing only a smaller interval led to more distinguished peaks and facilitated the identification of dominant frequencies. However, when the entire data set was Fourier transformed, the same dominant frequencies (for $St_D > 0.1$) could still be detected, with the benefit of including additional information in the low-frequency range. Therefore, for all cases, the entire data was used for the temporal Fourier decomposition.

The amplitudes of selected azimuthal Fourier modes over the Strouhal number are shown for all circumferential domain-sizes, except the $1/6^{th}$ -cylinder, in figure 6.5. For the half-cylinder case, it can be observed that modes $k = 1, 2, 3, 4$ contain most of the energy. Modes $k = 1$ and $k = 4$ exhibit a very strong peak at $St_D = 0.031$. It can be argued that they interact nonlinearly with themselves, resulting in a peak with twice the frequency in the azimuthal mean flow $k = 0$. This can be validated by detecting that this peak in $k = 0$ does not exist in the cases where mode $k = 1$ was omitted. Further, the fact that modes $k = 1, 3$ and $k = 4$ exhibit a peak at the same frequency corroborates the notion that the first mode might be nonlinearly generated by $k = 3$ and $k = 4$ as discussed in the context of the temporal development of the Fourier modes at start-up. At $St_D = 0.08$, peaks in both $k = 1$ and $k = 2$ coincide. This value is similar to the frequency observed for the slow lateral motion (flapping) of the entire wake in the $r - z$ -plane at $\theta = 0, \pi$ which therefore can be attributed to these two modes. Furthermore, mode $k = 2$ exhibits multiple peaks at moderate frequencies, coinciding with mode $k = 4$ at $St_D = 0.22$, suggesting that these two modes are causing large structures in the recompression region. For higher St_D , the frequencies of the peaks for the mean flow $k = 0$ cannot be expressed in multiples of isolated higher modes, leading to the conclusion that the modification of the mean

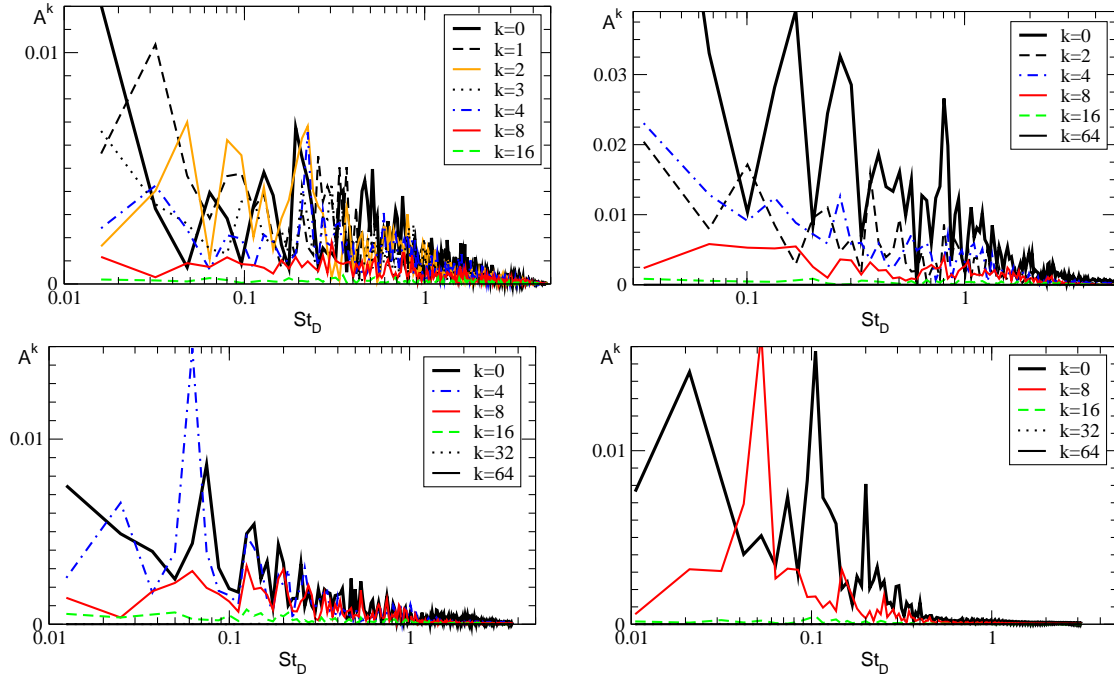


Figure 6.5 Fourier decomposition in time of higher density modes in a region of high activity, half-cylinder top left, quarter-cylinder top right, $1/8^{th}$ -cylinder bottom left, $1/16^{th}$ -cylinder bottom right; $z = 4.82$, $r = 0.238$, $Re_D = 30,000$, $M = 2.46$.

flow is caused by simultaneous nonlinear interaction of several higher modes.

In the quarter-cylinder case, it can again be concluded, that strong structures are present in the recompression region, considering the large amplitudes of the lower modes at low frequencies. Modes $k = 2$ and $k = 4$ exhibit the most prominent peaks. The azimuthal mean flow ($k = 0$) shows several prominent peaks at low frequencies but also exhibits a distinctive maximum at $St_D \approx 0.8$, nonlinearly generated by $k = 2$.

The $1/8^{th}$ -cylinder case reveals a peak of mode $k = 4$ at $St_D = 0.022$, which denotes the frequency of the vortex shedding. Also, a very prominent maximum can be seen at $St_D = 0.06$ for the same mode, possibly generating a peak in mode $k = 8$ for the same Strouhal number through a nonlinear interaction with itself. Both modes seem to produce a peak in the zeroth mode at twice the frequency, i.e., $St_D = 0.12$. For the $1/16^{th}$ -cylinder case, the picture simplifies drastically due to the fact, that

only one mode appears to interact with the circumferential mean flow. Mode $k = 8$ exhibits only one noticeable peak at $St_D = 0.05$, nonlinearly interacting with itself and producing a reaction of the mean flow $k = 0$ for twice ($St_D = 0.1$) the frequency. Mode $k = 0$ then nonlinearly interacts with itself to produce a peak at $St_D = 0.2$. The snapshot of instantaneous total vorticity for this case, shown in figure 6.3 (e), confirms the absence of structures with varying length-scales. The lack of small-scale structures for the small domain sizes most likely can be attributed to a viscous cut-off of the high-wavenumber modes, i.e., the highest modes are damped by viscous diffusion. For the larger domain sizes, modes with longer wavelengths are unstable and reach large amplitudes, *nonlinearly* generating higher mode numbers and thus producing small-scale structures.

In summary, at this Reynolds number, both the half-cylinder and quarter-cylinder cases appear to fully transition to turbulence downstream of the recompression region, exhibiting high-frequency fluctuations in higher azimuthal modes. An intermittent behavior is observed for all cases at the specified flow conditions. The bulk of the energy is contained in modes $k = 1, 2, 3, 4$. Peaks were found at low frequencies in the temporal spectra for the lower azimuthal modes that suggest the presence of large scale structures in the recompression region. Dominant maxima in the temporal spectrum of the zeroth azimuthal mode appear to be generated by nonlinear interaction of the most important helical modes with themselves or $k = 0$. For the small circumferential domain-sizes, a viscous cut-off of the high wavenumbers prevents the high azimuthal modes to grow linearly. In addition, because the long wavenumbers are eliminated in the small domain sizes, the large wavenumbers cannot be generated nonlinearly either. Consequently, no small-scale structures are generated for these cases.

6.1.2 Coherent Structures

In order to identify what kind of structures are generated in the flows under investigation and how those structures evolve, a vortex-identification method needs to be employed. Terzi, Sandberg & Fasel (2006) performed a study of various vortex education methods and concluded that the Q -criterion is an adequate choice as the desired information can be obtained from available data at low computational cost and the method can be implemented easily. The Q -criterion is named after the second invariant of the gradient of the velocity vector and for compressible flows can be computed as:

$$Q = \frac{1}{2} \left[\left(\frac{\partial u_i}{\partial x_i} \right)^2 + W_{ik} W_{ik} - S_{ik} S_{ik} \right], \quad (6.2)$$

with $S_{ik} = \frac{1}{2} \left(\frac{\partial u_i}{\partial x_k} + \frac{\partial u_k}{\partial x_i} \right)$ and $W_{ik} = \frac{1}{2} \left(\frac{\partial u_i}{\partial x_k} - \frac{\partial u_k}{\partial x_i} \right)$. For incompressible flows, $\frac{\partial u_i}{\partial x_i} = 0$ from continuity, and Q reduces to a balance between the total vorticity and the total strain magnitudes. For positive Q , rotation dominates strain and vortical structures can be visualized. For compressible flows, the dilatational term needs to be included for the sake of maintaining the invariant property of Q . This complicates the above intuitive interpretation of Q and it is not entirely clear whether positive values of Q educe pure vortical structures for compressible flows. To evaluate the influence of the dilatational term, the vortex-identification method was applied to the same data-field with and without the compressible extension. For both methods, very similar structures were observed in the visualizations of the resulting variables (see Terzi *et al.*, 2006), suggesting that the Q -criterion is also useful for the flows under investigation.

Figure 6.6 shows several views of instantaneous iso-contours of $Q = 0.1$ for the half-cylinder case for two time-levels. On the left side, top- and sideviews are shown and on the right side a perspective view, looking from the inflow towards the outflow, is visualized with the dark-grey surface marking the base. The difference between the

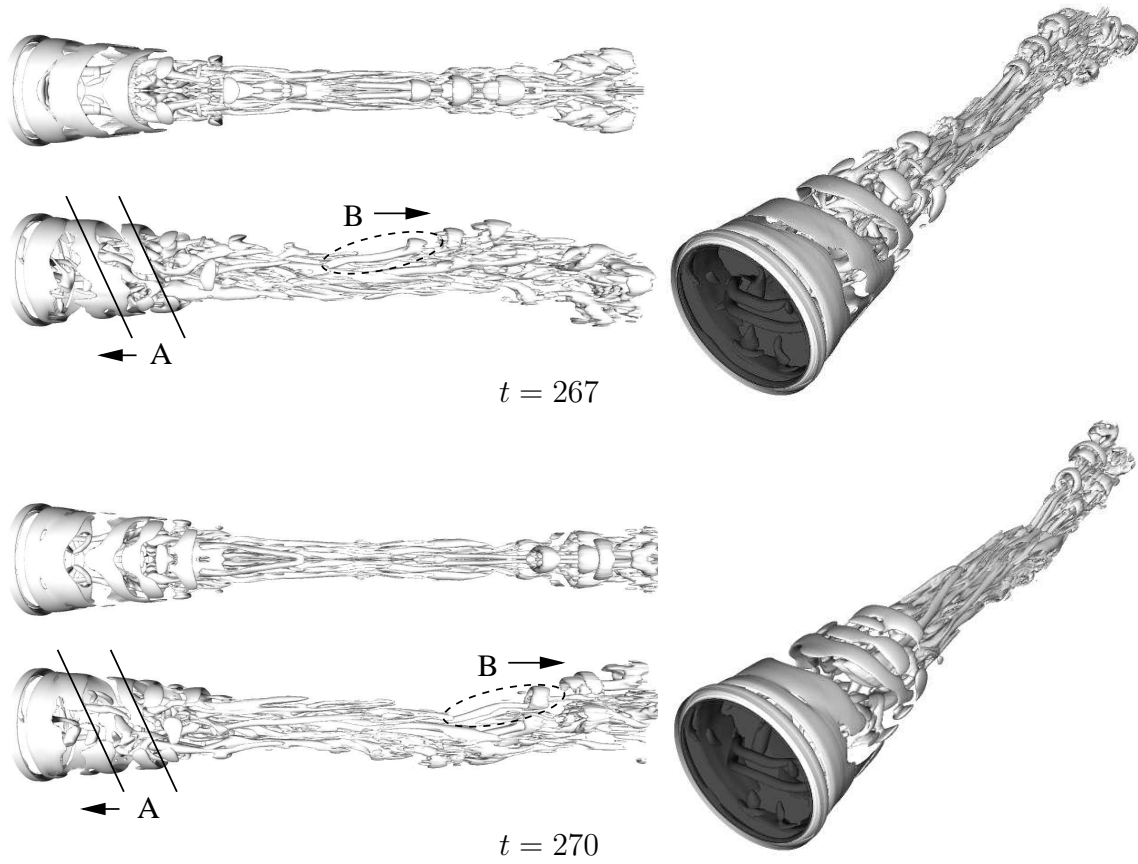


Figure 6.6 Instantaneous iso-contours of $Q = 0.1$ for half-cylinder case, top- and sideview (top and bottom, left) and perspective view from inflow towards outflow (right); $Re_D = 30,000$, $M = 2.46$.

two time-levels is $\Delta t = 3$, which corresponds to roughly one fourth of a flow-through-time, allowing free-stream fluid to travel three radii downstream.

Comparing the visualizations of Q for the supersonic case with the results obtained for the subsonic wake at $Re_D = 2,000$ (see section 4.4.2, figure 4.10), a fundamentally different flow behavior can be detected. Even though the Reynolds number in both cases is sufficiently large for the flow to transition to turbulence several diameters downstream of the base, the considerable difference in Mach number leads to a significant change in the flow field. For the subsonic case, large vortex-loops are shed alternately on the upper and lower side, highlighting the dominance of the first helical

mode. In contrast, in the supersonic case, close to the base, oblique, or helical, structures can be seen, denoted by “A”. In addition, longitudinal structures are present within the recirculation region that protrude into the trailing wake. This confirms the findings of the local analysis using temporal simulations, that the most unstable modes are always helical with $k, l \neq 0$. Therefore, it can be concluded that the helical structures are a consequence of the shear-layer mode.

Comparing the two time-intervals, the outer helical structures appear to move upstream on a slow time-scale, implying that they reside on the inner boundary of the shear layer, where the streamwise velocity component is negative. Typically, one would expect two-dimensional rollers to be located at the inflection point of the mean local profile. However, the inflection point of the mean profile is located where the mean streamwise velocity component is supersonic. As discussed in section 5.2, the convective Mach number M_c reaches large values in the initial shear layer, implying that considerable compressibility effects are present in this region. Therefore, the generation of oblique, or in this case, helical disturbances in this region can be expected. However, due to the considerably smaller compressibility in the low-velocity region (within the inner part of the shear layer), these disturbances seem to be more amplified there, such that they become large enough to be detected. It will be seen later, that for larger Reynolds numbers, where the amplification rates of the disturbances are increased, the helical structures also become visible close to the inflection point, i.e., they can be seen travelling downstream.

Farther downstream, the convective Mach number decreases (as the streamwise axis-velocity increases) and mainly longitudinal structures and several vortex loops appear. The structures observed within the trailing wake strongly resemble hairpin structures, commonly observed in boundary-layer transition (one of them marked with “B”). The “legs” of these structures can be seen to extend into the recirculation region and the “heads” of the hairpin vortices form vortex loops which travel downstream and move away from the axis. Similar to the boundary-layer transition

scenario, once the “heads” of the hairpin vortices are lifted, an instantaneous layer of high shear is developed, which is highly unstable and is the basis for tertiary instabilities that generate high-frequency oscillations. This process appears to be one of the mechanisms responsible for the generation of small-scale structures that can be observed in the trailing wake in the sideviews of the total vorticity in figure 6.3. These small structures possess a considerably larger value of Q and are, therefore, not visible in the figures currently discussed.

The helical structures appearing within the shear layer exhibit a sinusoidal modulation with a fairly large wavelength, implying that azimuthal modes with a small wavenumber are significant. In addition, the lateral motion (flapping) of the entire wake in the $r - z$ -plane at $\theta = 0, \pi$ can also be observed in figure 6.6, particularly in the sideviews, albeit by far not as pronounced as for the flow at $M = 0.25$. This supports the observation from the frequency spectra, that the first azimuthal mode plays a considerable role.

In figure 6.7, results are presented for the quarter-cylinder case. Qualitatively, the same flow features can be observed as for the half-cylinder case, i.e., helical structures within the shear layer and hairpin vortices with “legs” extending from the trailing wake into the recirculation region. For the sideviews, an extended time-sequence is shown in order to better demonstrate the dynamical behavior of the structures present in the flow. For the first time-step shown ($t = 132.08$), three streamwise structures are marked. The first structure (“A”) is located within the recompression region and protrudes into the recirculation region. Structures “B” and “C” are found downstream of the mean reattachment point, in the trailing wake. The spacing between the three structures is fairly constant, suggesting a dominant frequency in the (unforced) flow with a low value, as seen in the frequency spectrum of the quarter-cylinder case. At the second time-instant shown, structure A has not only travelled downstream but also has been stretched in the streamwise direction by the adverse pressure gradient within the recompression region. Further in time, the vortex A appears to have been

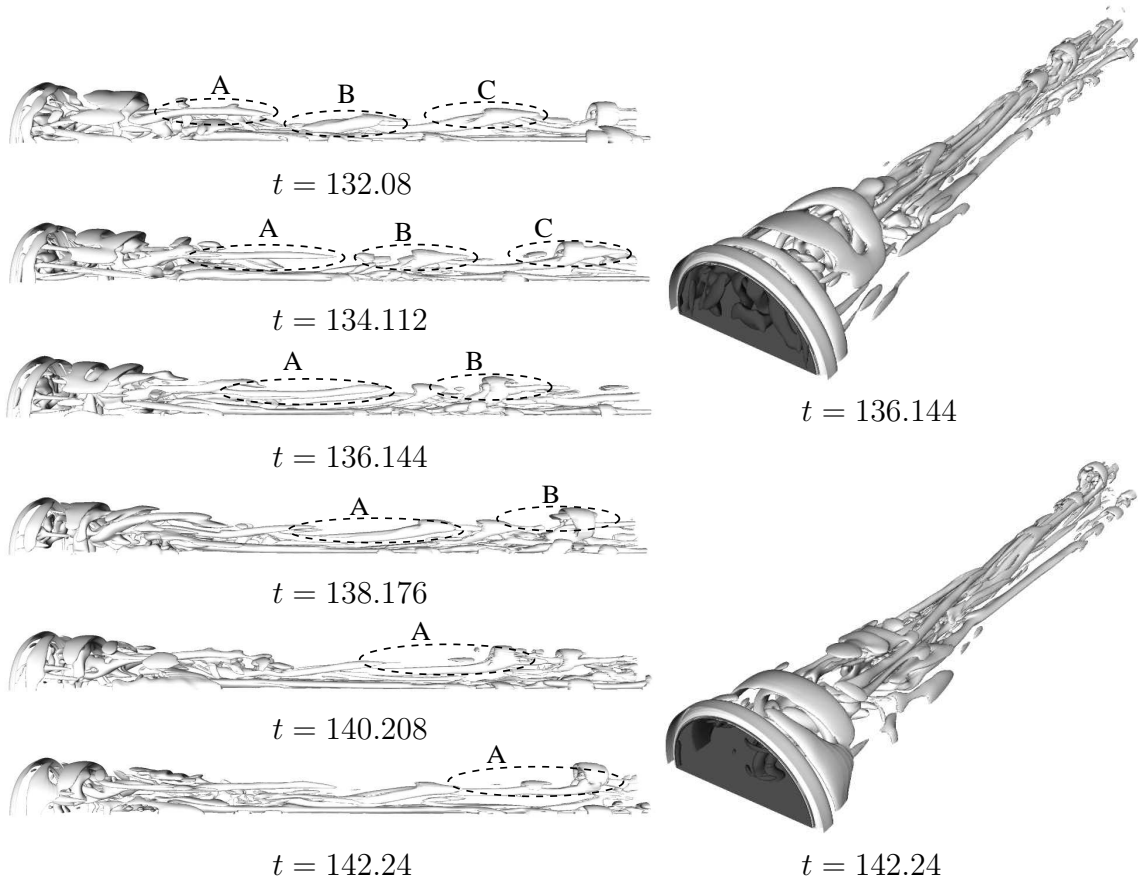


Figure 6.7 Instantaneous iso-contours of $Q = 0.1$ for quarter-cylinder case; time-sequence of sideviews (left) and perspective view from inflow towards outflow (right); $Re_D = 30,000$, $M = 2.46$.

stretched even further, still keeping its “legs” within the recirculation region. In the remaining pictures of the time-sequence, it can be observed how the structure finally detaches from the recirculation region and travels further downstream at a fairly constant convective speed. A vortex ring is eventually shed when the peak station is lifted up. Structures B and C can be seen undergoing the same dynamical behavior. The time-sequence also reveals that, as for the half-cylinder case, the helical structures in the shear layer slowly travel upstream. In addition, due to the exclusion of mode $k = 1$, no flapping of the entire wake is permitted, which is visible in the sideviews shown in figure 6.7.



Figure 6.8 Instantaneous iso-contours of $Q = 0.1$; perspective view from inflow towards outflow of $1/6^{th}$ -cylinder case (left) and $1/8^{th}$ -cylinder case (right); $Re_D = 30,000$, $M = 2.46$.

Perspective views of $Q = 0.1$ are shown for both the $1/6^{th}$ -cylinder and the $1/8^{th}$ -cylinder cases in figure 6.8. Again, hairpin vortices with “legs” extending from the trailing wake into the recirculation region can be observed. However, the structures within the shear layer appear to be of more axisymmetric than helical nature, in particular for the $1/8^{th}$ -cylinder case. In contrast to the results of larger domain sizes, the longitudinal structures that are visible in the trailing wake are aligned with the axis and mostly parallel to each other. When visualizing larger values of Q (not shown here), considerably less small-scale structures are visible than for the half-cylinder case. This is an indication that the modes with low wavenumbers are partly responsible for the creation of small-scale structures, either directly or through the generation of secondary instabilities leading to tertiary instabilities. In the visualizations of the smaller circumferential domain-sizes, a considerably smaller amount of the streamwise structures is observed. It is suggested that this, in combination with the absence of the azimuthal modes $k = 1$ to $k = 4$ for decreasing circumferential domain-sizes, leads to a reduced azimuthal and streamwise modulation of the longitudinal structures. This inhibits the occurrence of secondary and tertiary instabilities that might result in small-scale structures. Also, a reduced number of hairpin structures diminishes

the number of vortex loops, which would, if present, lead to an instantaneous layer of high shear. Thereby one basis for the formation of small-scale structures is revoked.

For all cases shown so far, a large number of longitudinal structures was not only seen in the trailing wake but also within the recirculation region. An effort is now made to unveil how these vortices are generated. One possible mechanism is proposed here: On the basis of linear stability calculations (see section 5) it was suggested that the flow is absolutely unstable with respect to global modes within the recirculation region. Once the amplitudes of these global modes reach sufficiently large values, chevron-like patterns are imposed onto the recirculating fluid. These patterns are similar to those illustrated in figure 6.1. It will be shown later in section 6.1.5, that longitudinal structures can be generated when flow in the streamwise direction passes through a region with a strong circumferential modulation. For a fully developed recirculation region, most likely multiple mechanisms compete, complicating the reconstruction of the most dominant events. For that reason, a time-sequence of the initial start-up of the $1/8^{th}$ -cylinder calculation is shown in figure 6.9 in order to isolate individual events. Iso-contours of $Q = 0.4$ are shown in a perspective view, looking from downstream towards the base.

Initially, the amplitudes of the higher azimuthal modes are small and the flow is fully axisymmetric, with an axisymmetric structure (“A”) generated by the stagnation point at the base (marked by a black surface). In the second figure of the time-sequence, a significant azimuthal modulation of the axisymmetric structure can be observed (“B”). The circumferential variation occurs within the recirculation region and not in the shear layer. Linear stability calculations at $Re_D = 30,000$ (figure 5.2) showed that mode $k = 4$, which is the fundamental azimuthal mode for the $1/8^{th}$ -cylinder case, possesses the largest amplitude at $r \approx 0.45$ and was, therefore, classified as global mode. Consequently, it can be speculated that global modes have reached large amplitudes and are responsible for the azimuthal modulation of

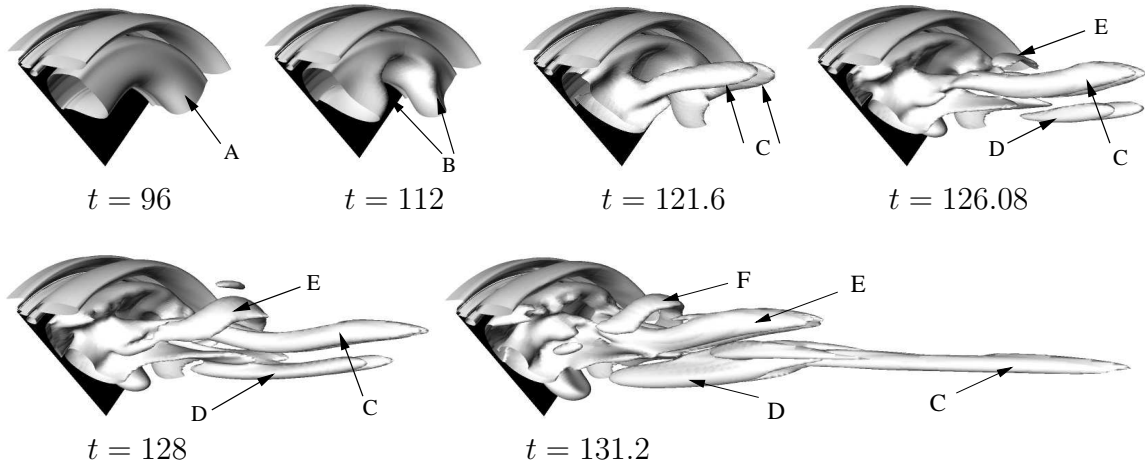


Figure 6.9 Time-sequence of instantaneous iso-contours of $Q = 0.4$ for initial transient of $1/8^{th}$ -cylinder case; perspective view from the trailing wake towards the base; $Re_D = 30,000$, $M = 2.46$.

structure A. This sinusoidal variation in the circumferential direction appears to be the cause for the occurrence of longitudinal structures, visible at the next time-instant $t = 121.6$ and marked with “C”. In the following graph, it can be seen that another streamwise structure has been generated (“D”), which pushes C toward the shear layer through induction of radial velocity. The structure C appears to reach the part of the shear layer where the streamwise velocity is positive and the outer part of C is convected downstream, thereby stretching the vortex. Another structure, similar to C, is present, albeit the iso-value at this time-instant is smaller than that of C and, therefore, only the outermost part can be seen, denoted by “E”. Going further in time, to $t = 128$, it can be observed that the outer parts of C and E have travelled downstream and the structures have been stretched in the streamwise direction. In the last time-instant shown, several observations can be made: The outer part of C appears to have overcome the adverse pressure gradient in the recompression region and has travelled a considerable distance downstream. D on the other hand fully remains within the recirculation region and actually slowly travels upstream again. The structure E follows C and the next structure, marked “F”, appears. Once the

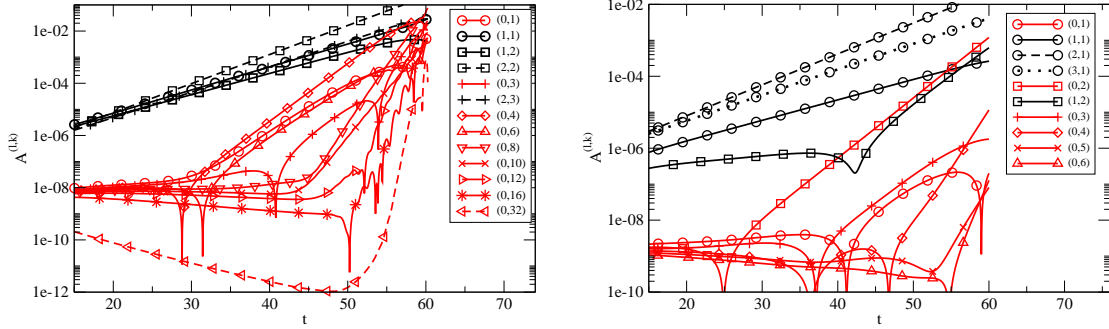


Figure 6.10 Temporal development of Fourier modes of (ρu) from temporal calculations for half-cylinder case; $z = 2.5$ (left) and $z = 9$ (right); $Re_D = 30,000$, $M = 2.46$.

initial transient is overcome, the recirculation region continuously contains several streamwise structures and, in addition, vortex loops can be observed (see, e.g., the structures at the base seen in the perspective view of the half-cylinder case in figure 6.6). These structures constantly impinge on the shear layer and thereby introduce disturbances. Because the shear layer was shown to be convectively unstable, the perturbations experience amplification in the streamwise direction which most likely results in the generation of additional structures.

To support that the longitudinal structures within the recirculation region are generated when global modes reach large amplitudes, additional temporal calculations were performed. The local stability calculations conducted with the temporal code, presented in section 5.3 were continued into the nonlinear regime. The Fourier decomposition in the streamwise direction allows for the distinction between helical and streamwise modes, i.e., all mode-pairs (l, k) with the streamwise component $l = 0$ represent longitudinal modes. The results obtained from the temporal calculations are shown in figure 6.10. Note that the initial pulse disturbance was introduced at the inflection point of the mean profiles and the time-response was monitored at the same location. For the location $z = 2.5$ (left), it can be seen that the longitudinal modes ($l = 0$) are damped or barely amplified in the linear regime. For $t > 30$, longitudinal modes with $k = 1, 4, 6$ become strongly amplified due to a secondary

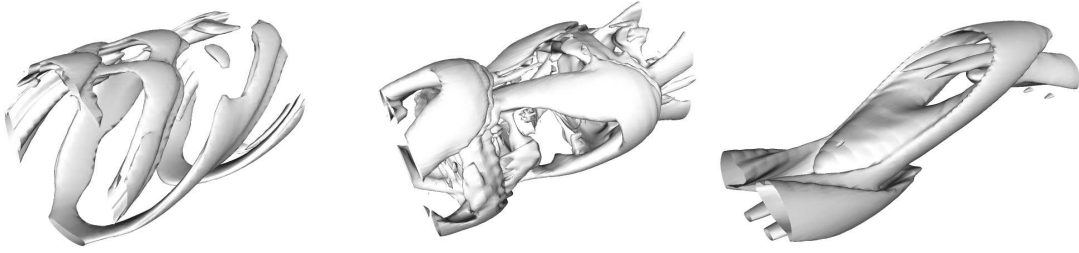


Figure 6.11 Perspective views of iso-contours of $Q = 0.1$ from temporal calculations of half-cylinder case; $z = 0.5$, $z = 2.5$ and $z = 9$ (from left to right); $Re_D = 30,000$, $M = 2.46$.

instability, and, at $t > 45$, higher azimuthal modes up to $k = 32$ become amplified. At the position further downstream at $z = 9$ (right), the mode-pair $(l, k) = (0, 2)$ is the first to become strongly amplified due to nonlinear interaction for $t > 25$, followed by higher azimuthal modes for $t > 35$. These observations imply that longitudinal structures develop in the shear layer.

The resulting flow fields obtained from the temporal simulations at separate streamwise locations are shown in figure 6.11. At the location close to the base, the occurrence of helical structures in the shear layer, as seen in the spatial calculations, is clearly visible. When the temporal calculation is conducted using the local profile at $z = 2.5$, several large vortex loops develop which are most likely a consequence of the nonlinearly strongly amplified modes $k = 4$ and $k = 6$. However, for both locations, no streamwise structures can be observed *within* the recirculation region. This reinforces the suggestion that the longitudinal structures are a consequence of additional instabilities occurring global modes within the recirculation region reach finite amplitudes. Looking at the flow field that is obtained from a temporal simulation using a profile from the trailing wake, large vortex loops, similar to those observed in the subsonic wake at $Re_D = 2,000$ (see figure 4.9), can be seen. These vortices are a consequence of modes $k = 2$ and $k = 4$ reaching a nonlinear saturation level. It can be speculated that in the presence of streamwise pressure gradients, significant stretching of these structures would occur which might lead to similar structures as

those observed in the spatial case. Therefore, it can be assumed that the hairpin vortices in the trailing wake might be partly generated locally.

The results obtained from the temporal simulations suggest, that the helical structures in the shear layer and the hairpin structures in the trailing wake, observed in the spatial calculations, are a consequence of local instabilities and are not caused by global effects. In contradistinction, because the longitudinal structures within the recirculation region could not be reproduced with local calculations, it is conjectured that these structures are most likely a consequence of a global instability.

In addition, compressibility itself also might be responsible for the generation of vortical structures. The vorticity equation for compressible flows distinguishes itself from the incompressible formulation through an additional term, the baroclinic torque. The misalignment of the density gradients with the pressure gradients can lead to vorticity generation and destruction. At the base-corner, for example, the rapid expansion produces strong density and pressure gradients. These two gradients are not aligned with each other and, therefore, the $r - z$, or axisymmetric, component of the baroclinic torque will be non-zero. As already stated above, axisymmetric

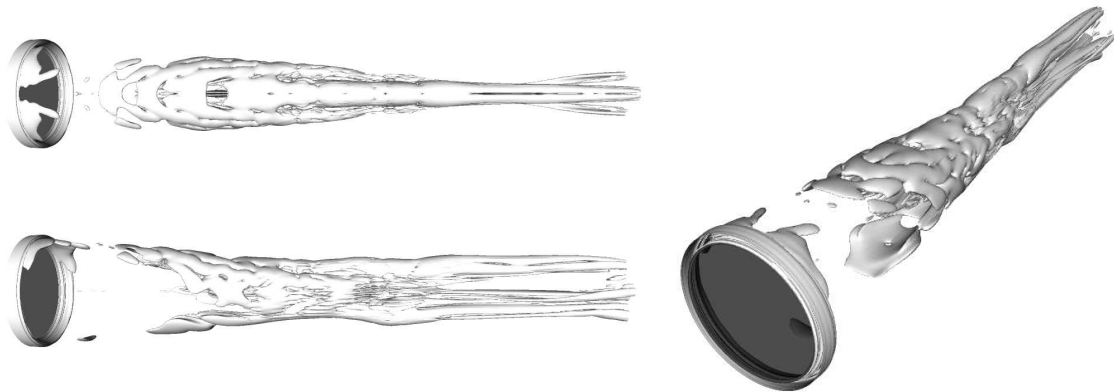


Figure 6.12 Instantaneous iso-contours of magnitude of baroclinic torque for half-cylinder case at $t = 270$; top- and sideview (top and bottom, left) and perspective view from inflow towards outflow (right); iso-level 0.2; $Re_D = 30,000$, $M = 2.46$.

disturbances are not significantly amplified in this region due to the compressibility of the flow. However, once structures are present within the flow-field, instantaneous density and pressure gradients will be present that move with the structures and produce all components of the baroclinic torque vector. Iso-contours of the magnitude of baroclinic torque ($\frac{1}{\rho^2} |\nabla \rho \times \nabla p| = 0.2$) are shown in figure 6.12 for the same time-instant as the iso-contours of Q presented in figure 6.6. The main contribution of vorticity production or destruction can be found in the outer shear-layer and the trailing wake, i.e., where the flow is supersonic and the density gradients are significantly larger than in low-speed regions. The axisymmetric distribution of the magnitude of baroclinic torque observed just downstream of the base can be attributed to the steady rapid expansion mentioned above, which results in a large contribution of the $r - z$ -component. Further downstream, the helical nature of the instantaneous structures can be observed with the degree of obliqueness decreasing in the downstream direction. This might be due to the diminishing convective Mach number, leading to a stronger axisymmetric organization of the structures.

From a large number of additional visualizations, which are omitted for brevity, other features were observed that suggest that additional instability mechanisms might be present. These additional mechanisms will be further discussed for the higher Reynolds number cases in sections 6.2.2 and 6.3.2.

With the knowledge gained from the results discussed above, a possible explanation for the occurrence of intermittency can now be proposed: The axisymmetric mean flow is unstable and gives rise to primary instabilities, which, in turn, lead to secondary and tertiary instabilities that cause the formation of large- and small-scale structures. The large-scale structures might interact with the mean flow to an extent that the resulting mean flow is no longer unstable, which, as a consequence, leads to a quiet region. Once the large structures are convected downstream and the mean flow becomes unstable again, disturbances can again be amplified, resulting in the

repeated generation of large- and small-scale structures.

In summary, it was demonstrated that helical structures are present within the initial shear-layer, confirming results from the linear local analysis with the temporal code. Higher azimuthal modes lead to a sinusoidal modulation of the helical structures, causing the generation of longitudinal structures within the shear layer. Circumstantial evidence was presented, showing that longitudinal structures within the recirculation region are generated as a consequence of global modes reaching large amplitudes. When the outer parts of these streamwise vortices are entrained by the shear layer, the structures are strongly stretched and, eventually, they detach from the recirculation region. In the trailing wake, the structures have strong resemblance with hairpin vortices, forming vortex loops. For smaller circumferential domain-sizes, the number of hairpin structures is strongly decreased. The exclusion of low wavenumber modes inhibits an energy cascade to higher wavenumbers, resulting in considerably fewer small-scale structures. Furthermore, it was shown that the baroclinic torque also might be an important vorticity-production mechanism. The main contribution of vorticity production or destruction through baroclinic torque was found in regions subject to high compressibility, i.e., the outer shear-layer and the trailing wake.

6.1.3 Mean Flow

In order to assess the impact of the large-scale structures, on the mean flow, averaged flow-quantities need to be evaluated. To obtain time-averages, the DNS were conducted until running averages were converged, which required approximately twelve flow-through times for all cases.

The time-averaged radial profiles of several azimuthal Fourier modes for all three velocity components are shown in figures 6.13 – 6.15. Two characteristic streamwise locations are chosen. One region of interest is upstream of the recompression region,

where the flow has not yet fully transitioned and considerable reverse-flow occurs. The second region chosen is within the far wake, as the question arises whether the mode shapes are affected by the strong adverse pressure gradient in the recompression region and by the highly unsteady flow behavior. In contrast to the radial distributions obtained from linear calculations, the amplitudes of the individual azimuthal modes obtained from DNS are relevant as they determine the degree of interaction between separate modes. Therefore, none of the modes is rescaled in the graphs to allow for a direct evaluation of the significance of individual modes.

When comparing the results obtained from the DNS of the half-cylinder calculation at $z = 2.5$ (figures 6.13 – 6.15 top left) with the results presented for the linear calculations in figures 5.4 – 5.6, the following differences can be found: For the first azimuthal mode, the maximum amplitudes of the radial and the azimuthal components amount to approximately 50% of the streamwise maximum, as opposed to roughly 30% in the linear case. The shape of the streamwise component is significantly changed versus the result obtained in the linear calculation, showing similarities to several higher modes (in terms of the locations of maxima, inflection points and slopes). Also, the overall values of the first mode are on the same order as those of the dominant modes, in spite of a significantly smaller amplification rate determined in the linear calculations. This alludes to the possibility that the shape of the first azimuthal mode might be the result of nonlinear interaction of the dominant modes.

The second azimuthal mode displays strongly altered mode shapes in comparison to the linear results. In contrast, the radial profiles of the third and fourth mode correspond very well with the data obtained from the linear calculations, in particular for the radial and the azimuthal components. This suggests, that at this streamwise location (within the recirculation region, upstream of recompression), the azimuthal modes that were found to linearly exhibit the largest amplification rates also dominate in the nonlinear case.

Downstream of the recompression region, however, the picture changes drastically.

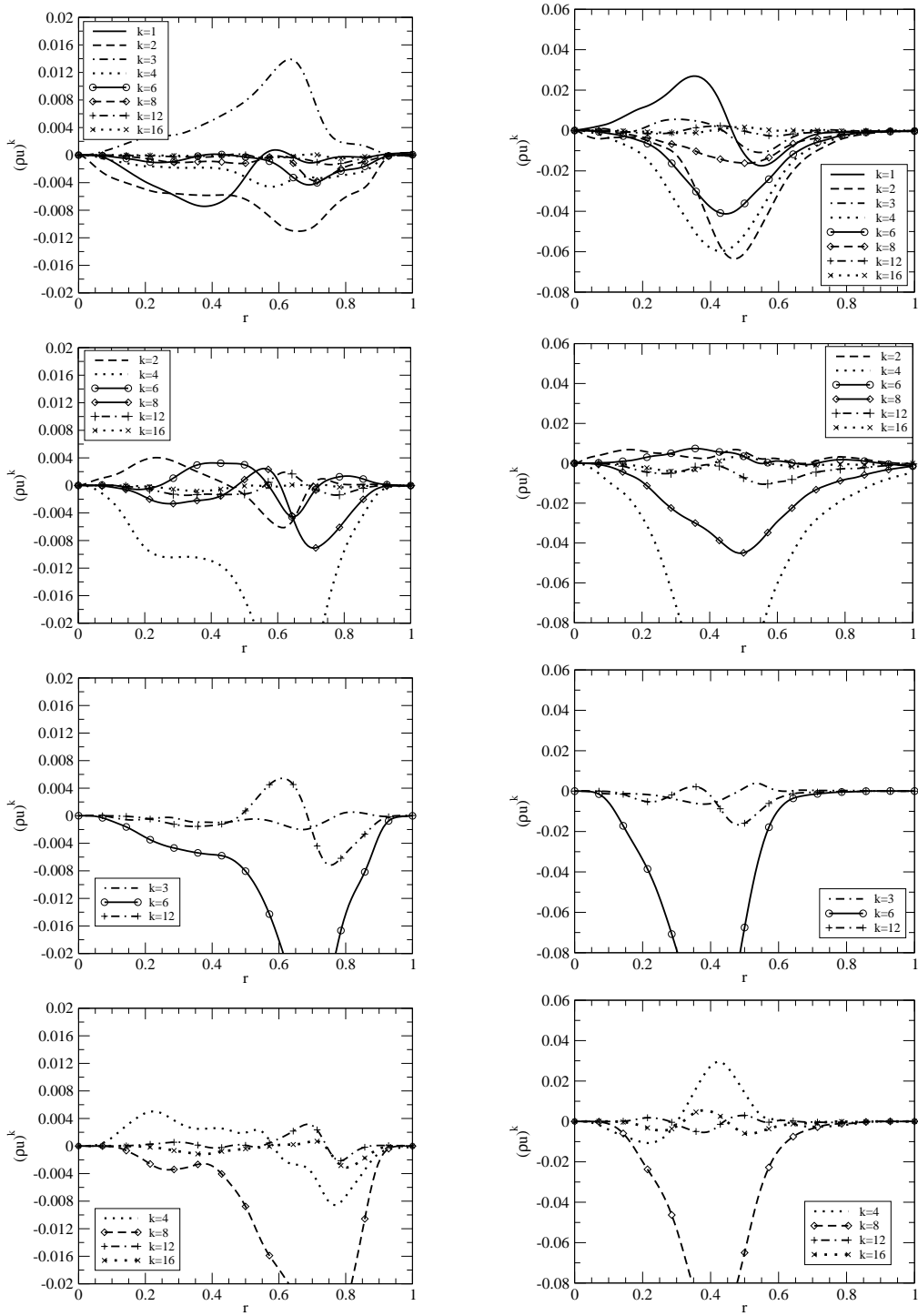


Figure 6.13 Time-averaged radial mode-shapes of $(pu)^k$ obtained from DNS for half-, quarter-, $1/6^{th}$ - and $1/8^{th}$ -cylinder (from top to bottom); $z = 2.5$ (left), $z = 9$ (right), $Re_D = 30,000$, $M = 2.46$.

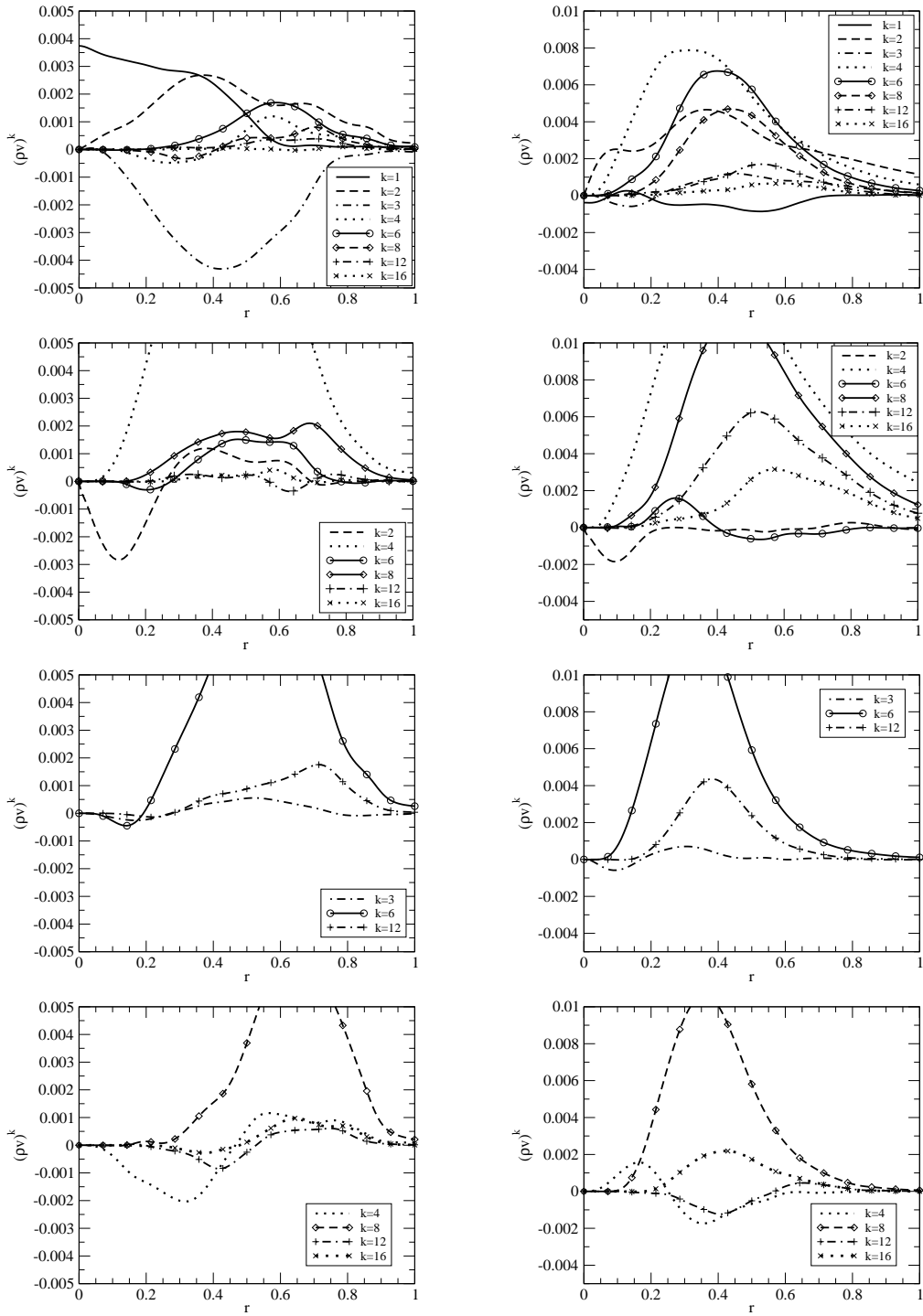


Figure 6.14 Time-averaged radial mode-shapes of $(pv)^k$ obtained from DNS for half-, quarter-, $1/6^{th}$ - and $1/8^{th}$ -cylinder (from top to bottom); $z = 2.5$ (left), $z = 9$ (right), $Re_D = 30,000$, $M = 2.46$.

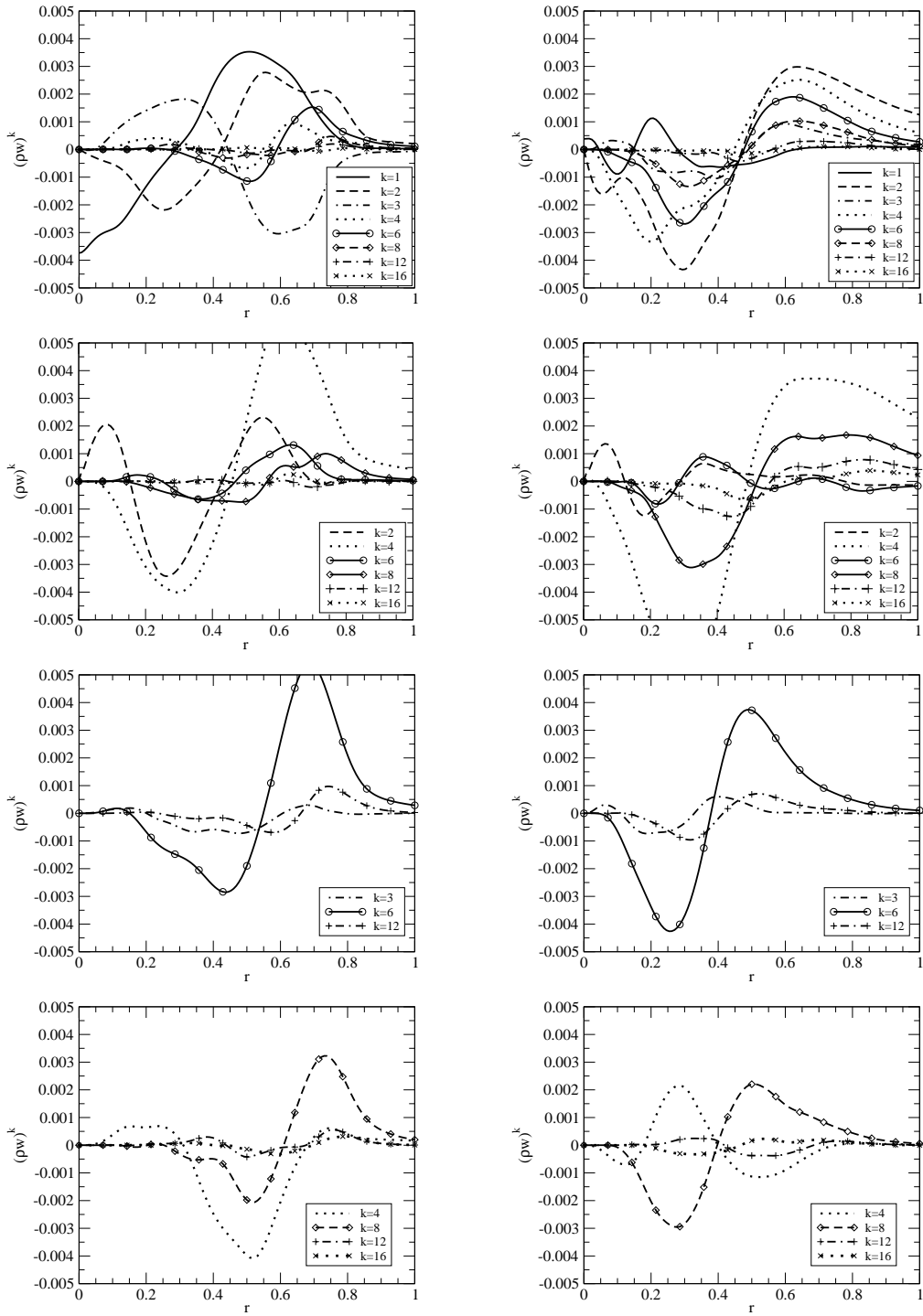


Figure 6.15 Time-averaged radial mode-shapes of $(\rho w)^k$ obtained from DNS for half-, quarter-, $1/6^{th}$ - and $1/8^{th}$ -cylinder (from top to bottom); $z = 2.5$ (left), $z = 9$ (right), $Re_D = 30,000$, $M = 2.46$.

When reviewing the top right plots of figures 6.13 – 6.15, it can be concluded that the radial distributions of all modes has changed, suggesting that a strong nonlinear interaction between all modes occurs in, or downstream of, the recompression region. This notion is supported by the observation that most modes shown in the graphs, except $k = 1$, exhibit similar mode-shapes. The maximum amplitude of the first mode of all velocity components is exceeded by the higher azimuthal modes, in particular modes $k = 2, 4, 6$. It is interesting to note that mode $k = 3$ is not among the most significant modes, in spite of the largest growth rate found in the linear case and the highest amplitudes of the radial profiles obtained from the DNS at $z = 2.5$. It is likely that modes $k = 2$ and $k = 4$, both having large amplification rates in the linear case, nonlinearly interact with each other. Thereby they become the most dominant modes and augment the importance of modes $k = 6$ and $k = 8$ (as seen for the radial component in figure 6.14, top right).

This corroborates the above assumption that when long wavelength modes reach large amplitudes, higher wavenumber modes are nonlinearly generated, leading to the formation of smaller scale structures. More evidence to support this conjecture can be found by scrutinizing the mode-shapes obtained from DNS of different circumferential domain-sizes. Examining the amplitude distributions for all domain sizes (figures 6.13 – 6.15), the following observations can be made. At $z = 2.5$, when excluding all odd modes (quarter-cylinder calculation), the mode-shape of $k = 2$ is considerably different than in the half-cylinder case, in fact it resembles the profile of mode $k = 4$, in particular for the azimuthal component. The fact that the shape of $k = 2$ is strongly altered in the absence of $k = 1$ indicates that the two modes strongly interact with each other in the half-cylinder case, as already mentioned when discussing the temporal spectra shown in figure 6.5. The change in the amplitude distribution in the second mode, for the case that the first mode is omitted, is even more pronounced at $z = 9$, especially for the streamwise component. The amplitude distributions of modes $k = 4, 6, 8, 12$ appear to remain fairly unchanged from the half-cylinder case

for both streamwise locations, with $k = 4$ exhibiting the largest maximum amplitude. Presumably, this is due to the fact that, in the absence of all odd modes, energy from $k = 0$ is transferred to the even modes through nonlinear interactions. In addition, mode $k = 4$ has the largest (linear) growth rate of the modes included in the quarter-cylinder calculations.

For the $1/6^{th}$ -cylinder calculations, the most dominant mode is $k = 6$ in contrast to the half-cylinder case, where, in the recirculation region, the amplitude of $k = 3$ was considerably larger. Scrutinizing the smallest circumferential domain-size shown in figures 6.13 – 6.15, it can be observed that the radial profiles of mode $k = 4$ are altered from the cases with larger domain sizes. This might be an indication, that $k = 4$ interacts strongly with mode $k = 1$ and $k = 2$ in the respective cases. In particular for the streamwise and radial components, mode $k = 8$ clearly is the most dominant mode. It should also be noted that for all calculations of cases with a circumferential extent with $\theta < \pi$, $(\rho u)^k \gg (\rho v)^k > (\rho w)^k$, in contrast to the half-cylinder case, where the radial and the azimuthal component were similar in magnitude.

To conclude the discussion of the amplitude distributions of the azimuthal modes, the most striking observation when comparing the results for the different domain sizes with each other is the fact that it is always the first higher harmonic of the fundamental wavelength that is the most dominant one, i.e., in the quarter-cylinder case the most dominant mode is $k = 4$, in the $1/6^{th}$ -cylinder case mode $k = 6$, etc. Furthermore, regardless of the wavenumber, the mode shape of the most dominant mode is always the same for all domain sizes. For all domain sizes with $\theta < \pi$, the magnitude of the dominant mode is significantly larger than those in the half-cylinder case. This can be attributed to the fact that the dominant mode obtains energy directly from the spatial mean and does not have to “share” this energy with the excluded modes through nonlinear interaction.

As mentioned above, a meaningful figure of merit for determining the effect of the dominant modes on the mean flow are visualizations of endviews at different downstream locations. Figure 6.1 illustrated what kind of wake patterns can be expected when particular modes are significant. Three different quantities are selected for visualization for the following reasons: First, the amplitude distributions discussed above revealed that the streamwise velocity component is dominant for virtually all cases. Therefore, total vorticity was chosen as it contains all directional derivatives of the streamwise velocity component. Second, the visualization of streamwise vorticity is intended to clarify whether longitudinal vortices are present in the mean. Third, because symmetric Fourier transforms are used in the azimuthal direction, the circumferential mean of the azimuthal velocity component is zero. Thus, even small amplitudes in the higher modes of w can easily be detected in endviews of the azimuthal velocity component, facilitating the identification of streamwise structures.

The same characteristic locations as those chosen for the discussion of the radial profiles are selected to show the time-averaged endviews. Figure 6.16 shows the endviews for all circumferential domain-sizes (from top to bottom) at the downstream location $z = 3$. This location is within the recirculation region and merely half a radius downstream of the upstream position for which the radial amplitude distributions were shown in figures 6.13 – 6.15. The figures displaying the azimuthal velocity component only show the domain computed, whereas, for the graphs of vorticity, the data from the calculations were mirrored and duplicated the respective number of times to show the results for the entire cylinder. This allows for a more convenient comparison between results for different domain sizes and provides a better impression of the resulting wake patterns.

The shear layer (at $r \approx 0.7$) is most prominent in the visualization of total vorticity, as this quantity includes the radial derivative of the streamwise velocity component. However, several distortions can be observed on the inside of the shear layer, which indicate that structures might be present in the mean flow. To assess whether

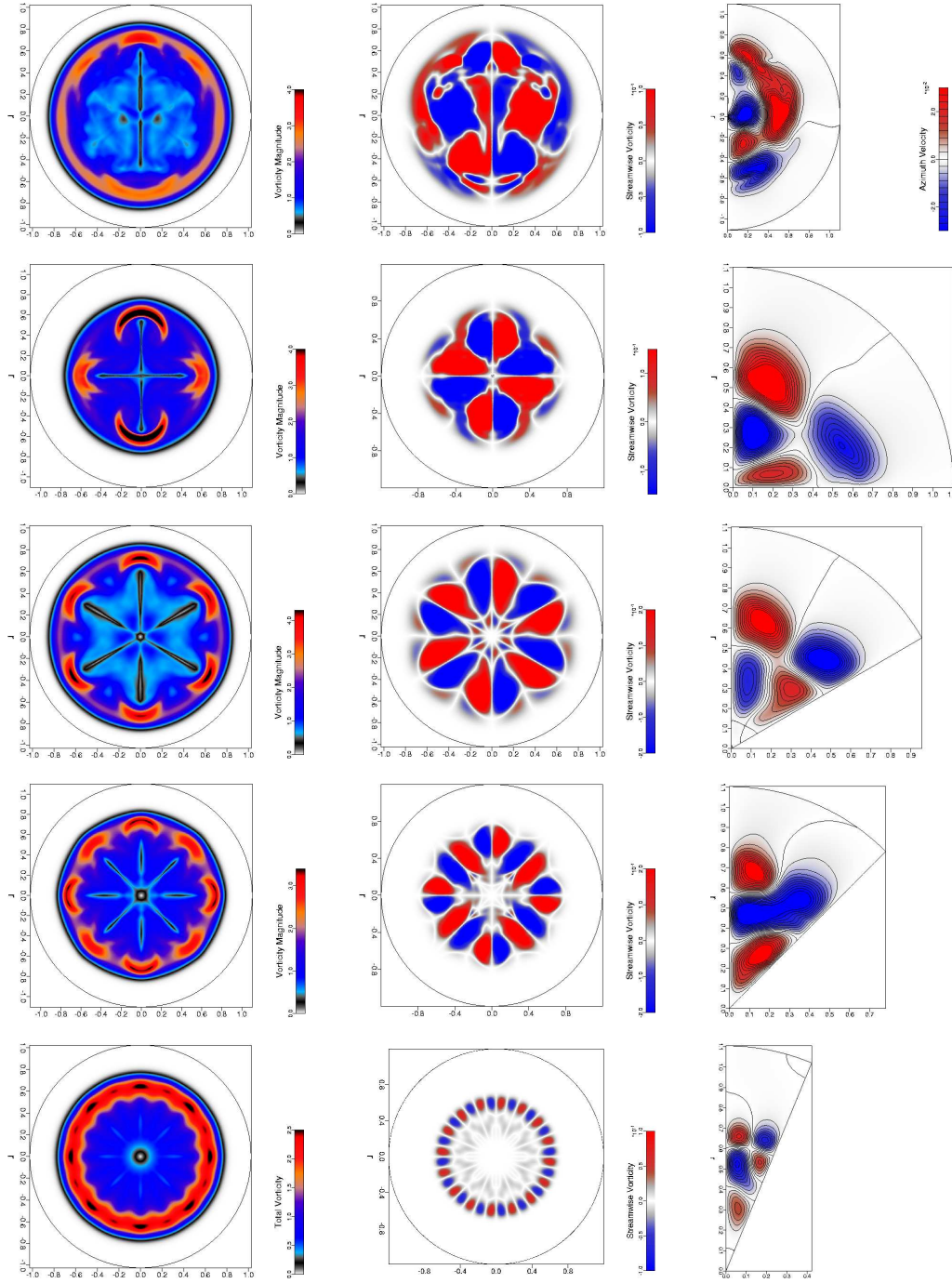


Figure 6.16 Endviews of time-averaged contours of total vorticity (left), streamwise vorticity (center), and azimuthal velocity (right) upstream of the recompression region at $z = 3$ for half-, quarter-, $1/6^{th}$, $1/8^{th}$ and $1/16^{th}$ -cylinder (from top to bottom); $Re_D = 30,000$, $M = 2.46$.

these structures are of longitudinal nature, the focus is shifted to the visualization of mean streamwise vorticity, which does not include any component of the streamwise derivatives. As opposed to the vorticity magnitude, the streamwise vorticity also contains information about the direction of rotation. The positive and negative values denote clockwise and counterclockwise rotation, respectively.

Within the shear layer, negative streamwise vorticity is found in the mean flow for $0 \leq \theta \leq \frac{2\pi}{3}$, pinched at $\theta \approx \frac{\pi}{3}$. Positive values of streamwise vorticity are seen for $\frac{2\pi}{3} \leq \theta \leq \pi$. In the interior of the recirculation region, the same behavior can be observed, except for a reversed orientation and a more pronounced separation of the structures. The visualization of the mean azimuthal velocity component displays a similar behavior, i.e., three structures within the recirculation region and two structures in the shear layer. The occurrence of only one sign change and the presence of distinctive features at $\theta \approx \frac{\pi}{3}$ and $\theta \approx \frac{2\pi}{3}$ implies that the mean flow is mainly the result of a superposition of modes $k = 2$ and $k = 3$. These modes were also found to be the dominant ones in the discussion of the radial amplitude distributions at $z = 2.5$. The resulting pattern observed in the endviews further suggests that these most significant modes are non-oscillatory in time, see discussion of figure 6.1. This is further supported, recalling that the modes $k = 2$ and $k = 3$ not only were the (linearly) most amplified modes but also showed monotonous growth in time, as opposed to higher azimuthal modes (see figures 5.8 and 6.2).

For all other circumferential domain-sizes, scrutinizing the visualizations of streamwise vorticity and the azimuthal velocity component shows two pairs of counter-rotating structures within the integration domain. One pair is embedded in the shear layer, the other is present within the recirculation region, with a reversed orientation. When looking at contours of total vorticity, it seems that for each pair of counter-rotating structures observed in contours of streamwise vorticity and azimuthal velocity, one vorticity peak appears in the shear layer. This behavior is caused by the entrainment and ejection of fluid from the recirculation region in the presence of

longitudinal structures. The quarter-cylinder case therefore exhibits a “four-lobe”-structure, the $1/6^{th}$ -cylinder calculations a “six-lobe” structure as sketched in figure 6.1. In consideration of the results found discussing the radial mode-shapes, these patterns are generated by the azimuthal modes $k = 4$, $k = 6$, $k = 8$ and $k = 16$ for the respective calculations. Similar to the half-cylinder case, these modes are most likely non-oscillatory in time.

Downstream of recompression (figure 6.17), the mean values of total vorticity are reduced, mainly because the radial gradient of the streamwise velocity component is significantly smaller in the trailing wake than in the shear layer. The maximum values of streamwise vorticity and the azimuthal velocity component remain roughly unchanged. This indicates that in the mean the longitudinal structures persist throughout the strong pressure gradient in the recompression region. This supports the assumption, that longitudinal structures are generated within the recirculation region and eventually travel downstream. In the half-cylinder case, a “four-lobe” structure emerges, with the largest extension at $\theta = 0$ and $\theta = \pi$. This can be attributed to the “flapping” motion of the wake, which, due to the imposed symmetry, is restricted to the $\theta = 0$ and $\theta = \pi$ plane. If full Fourier transforms were employed, the flapping movement could continuously select different planes and the average could therefore be more circular. This explanation is substantiated by the endview of the quarter-cylinder case, where mode $k = 1$ is excluded and the “four-lobe” structure is prominent. Recalling that the amplitude distribution of the fourth mode had the largest amplitude suggests that for the quarter-cylinder, a steady mode $k = 4$ is the most dominant mode and responsible for the “four-lobe” pattern. In the half-cylinder case, the largest amplitudes found in the mode-shapes were for modes $k = 2$ and $k = 4$. Therefore, the “four-lobe” structure observed for this case might be a superposition of an oscillatory mode $k = 2$ and a steady mode $k = 4$. In contrast to the upstream position discussed above, no contribution of mode $k = 3$ can be observed. This explains the strongly decreased magnitude of the third mode seen in

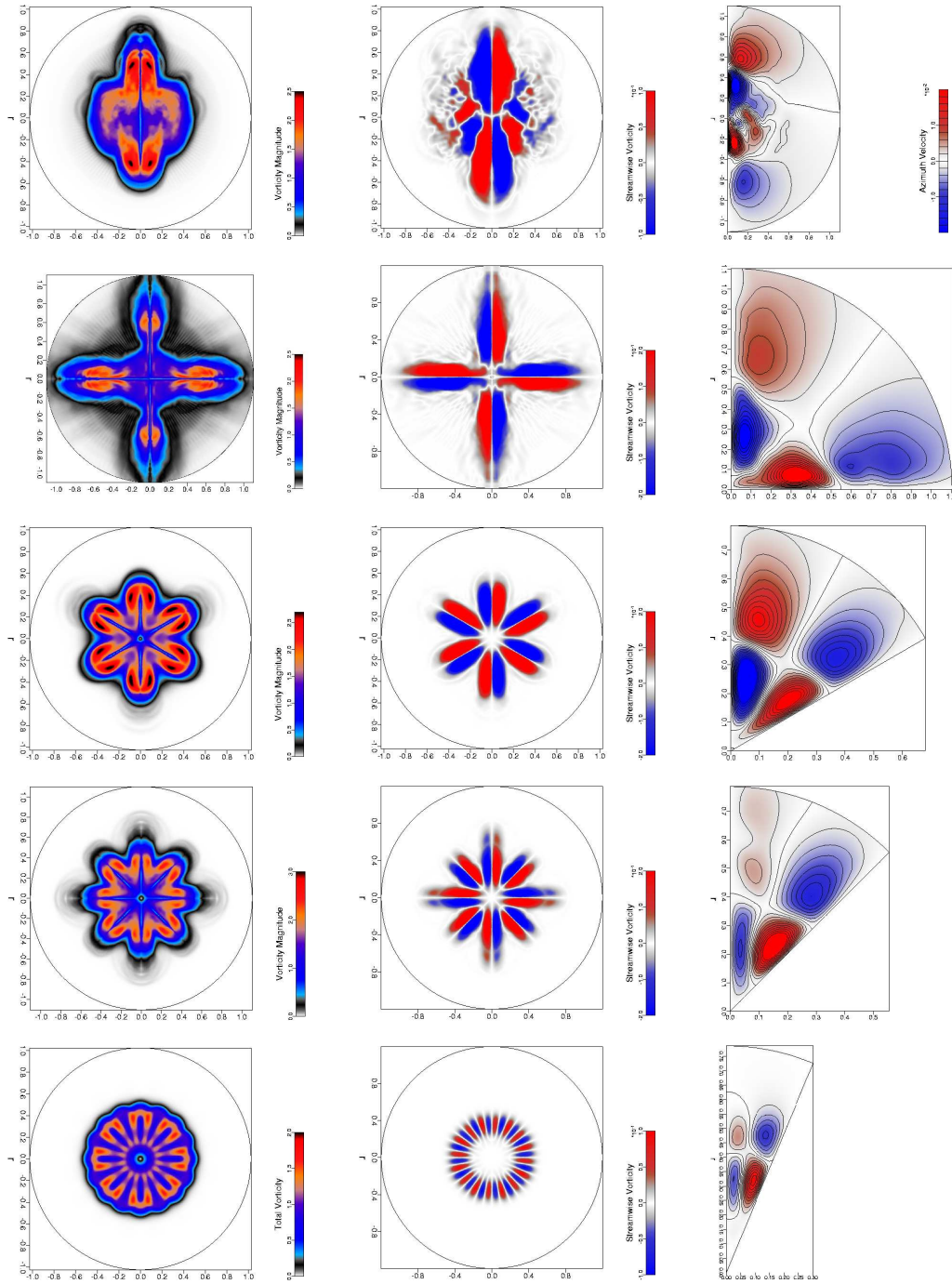


Figure 6.17 Endviews of time-averaged contours of total vorticity (left), streamwise vorticity (center), and azimuthal velocity (right) downstream of the recompression region at $z = 9$ for half-, quarter-, $1/6^{th}$, $1/8^{th}$ and $1/16^{th}$ -cylinder (from top to bottom); $Re_D = 30,000$, $M = 2.46$.

the amplitude distribution at $z = 9$.

For all other calculations, the picture remains unchanged from the location $z = 2.5$, except that the longitudinal structures are more elongated along the symmetry/periodicity axis. The endview of the vorticity magnitude of the $1/16^{th}$ -cylinder reveals that the structures present in the flow are not energetic enough to produce a significant azimuthal variation of the mean flow. In addition, the radial extent of the wake is smaller for the $1/8^{th}$ - and $1/16^{th}$ -cylinder cases than for the cases with a larger circumferential domain-size due to the fact that the recompression region is much further downstream and the far-wake has not yet spread as much.

In order to obtain a more complete image of the averaged flow field, the visualizations of averaged iso-contours of $Q = 0.05$ are presented in figure 6.18. Perspective views from downstream towards the base are shown for the four largest circumferential domain-sizes. The flow direction is from left to right. For the half-cylinder case, shown on top, only the computed data is visualized. For all other cases, however, the available data was mirrored at the symmetry plane for clarity. The graphs on the left side are views from the “outside”, i.e., from the free-stream towards the axis and the graphs on the right side show the perspective view from the “inside”, with the radial axis directed into the page. For all cases, it can be seen that the mean longitudinal structures seen in the endviews within the recirculation region at $z = 2.5$ (figure 6.16) and in the trailing wake at $z = 9$ (figure 6.17) are connected. Also, the azimuthal modulation of the shear layer can be observed in the mean. This modulation, being apparent in the mean, most likely is due to the presence of a global mode and presumably leads to the creation of the longitudinal structures. Another similarity between all cases is the occurrence of the same number streamwise vortices in the mean flow.³

³If the half-cylinder case had also been mirrored, four streamwise vortices would be displayed, however, in order to allow for a clearer view into the recirculation region, only the computed domain is shown.

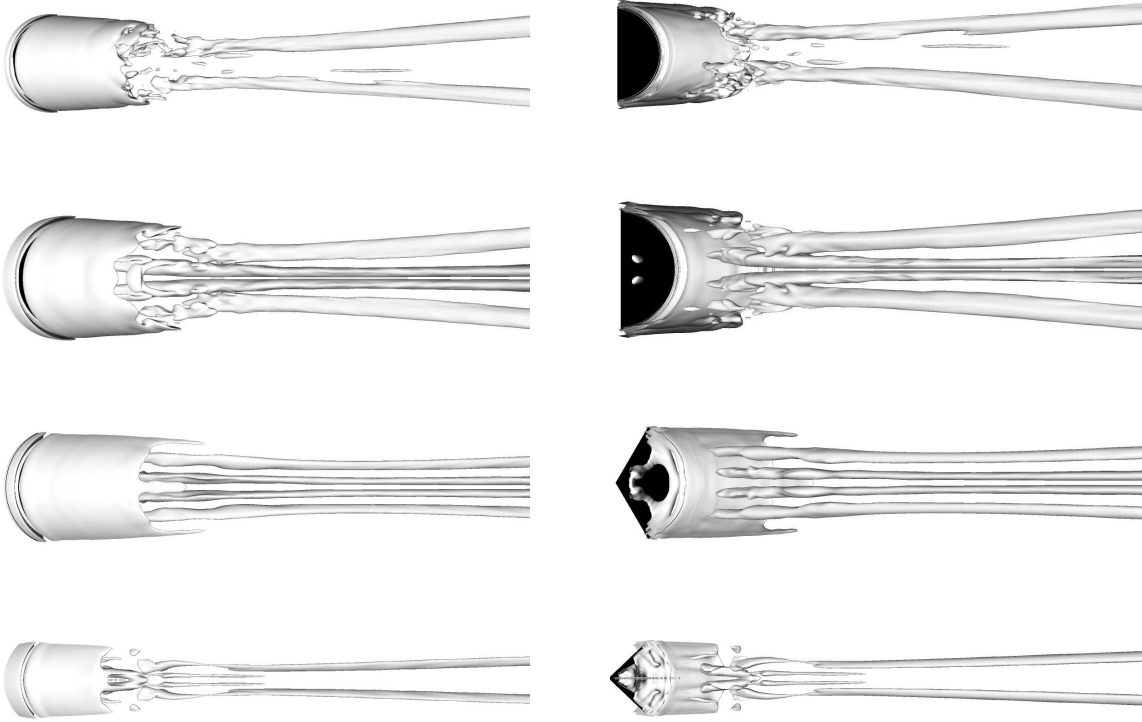


Figure 6.18 Time-averaged iso-contours of $Q = 0.05$, perspective view from downstream towards the base, flow is from left to right; from the “outside” (left) and from the “inside” (right); half-cylinder, quarter-cylinder, $1/6^{th}$ -cylinder and $1/8^{th}$ -cylinder from top to bottom; $Re_D = 30,000$, $M = 2.46$.

This was already evident in the endviews shown above and can be attributed to the fact that it is always the first higher harmonic of the fundamental wavelength that is the most dominant one, as shown when discussing the mode-shapes presented in figures 6.13 – 6.15.

In order to evaluate the effect of the different wake patterns on the base pressure and the recirculation length, the mean streamwise velocity along the axis and the pressure coefficient along the base are shown for all cases in figure 6.19. The axisymmetric solution, that was used as the basic state for the linear stability investigations and that served as initial condition for the DNS of all domain sizes is

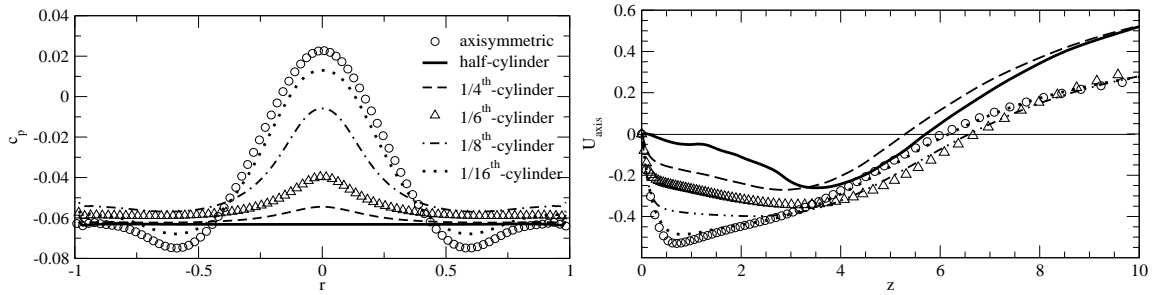


Figure 6.19 Averaged pressure coefficient (left) and streamwise axis-velocity (top) for all circumferential domain-sizes; $Re_D = 30,000$, $M = 2.46$.

included for comparison. For the half-cylinder case, the recirculation length of the separation bubble is decreased to $z = 5.3$ versus $z = 6.1$ for the axisymmetric case. However, even more significant than the decrease in recirculation length is the drastic change of the shape of the profile within the recirculation region. Not only has the location of the maximum reverse velocity considerably moved downstream, its value has also strongly decreased. These differences are a consequence of the mixing of low speed fluid contained in the recirculation region with the outer high-momentum fluid through the structures discussed above. The pressure distribution along the base, obtained from the half-cylinder calculation, is completely flat, as opposed to the axisymmetric case, where a strong radial variation, with a pronounced maximum at the axis, is visible.

For the quarter-cylinder case, the base-pressure coefficient is very similar to that found in the half-cylinder case, displaying only a slight radial variation. The data obtained from the quarter-cylinder calculation show an even shorter recirculation length. As was shown in the discussion of the radial profiles (figure 6.13), mode $k = 4$ contains a significantly larger amount of energy than in the half-cylinder case. Therefore, it is suggested, that the structures generated in this case contain more energy, thus entraining more low momentum fluid from the reverse-flow region. The location of the maximum reverse-velocity is slightly farther upstream, albeit with

roughly the same magnitude. These observations reinforce the earlier conclusion, that mode $k = 1$ only plays a minor role for the present flow conditions. The main effects that can be attributed to mode $k = 1$ are a short plateau in the streamwise axis-velocity at $z \approx 1$, that can only be seen in the half-cylinder case, and causing a perfectly flat pressure distribution.

Scrutinizing the results obtained from the calculation of the $1/6^{th}$ -cylinder verify that the azimuthal modes $k = 2$ and $k = 4$ are the most relevant modes for this Reynolds number. Both modes are excluded in this case and the recirculation length strongly increases, eclipsing even the value of the axisymmetric solution. The base-pressure distribution also exhibits a more pronounced radial variation, with the mean value being higher than the mean magnitude found for the larger domain sizes.

In the simulations of the $1/8^{th}$ - and $1/16^{th}$ -cylinder the amplitude levels of the dominant modes are not large enough to significantly modify the mean flow or to generate any significant structures. Hence, these cases fail to reproduce the results of the half-cylinder case, i.e., a flat pressure distribution along the base and a short recirculation region.

From the above results, it is not clear whether merely the unsteadiness of the flow is responsible for a flat pressure-profile on the base, or whether the three-dimensionality, i.e., the effects of higher azimuthal modes, is the origin of the fundamentally different results. In order to clarify this, an axisymmetric calculation at $Re_D = 400,000$, a Reynolds number which is significantly larger than the threshold value for an absolute instability with respect to the axisymmetric mode (see section 5), was conducted that became highly unsteady.

The mean pressure coefficient distribution along the base for the unsteady case is compared with the steady results from axisymmetric calculations at lower Reynolds numbers in figure 6.20. As for the steady lower Reynolds number cases, a strong radial distribution with a pronounced peak at the axis can be seen. The peak maximum is fairly constant for all cases, which can be attributed to the similar maximum reverse

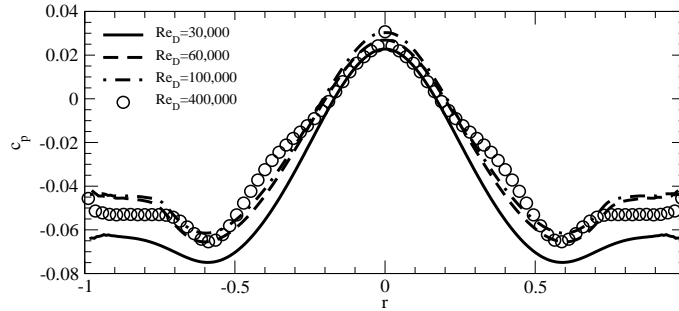


Figure 6.20 Pressure coefficient on the base obtained from axisymmetric DNS calculations for various Reynolds numbers; $M = 2.46$

velocity at all Reynolds numbers and the same slope of the streamwise axis-velocity at the base. The fact that the result from the highly unsteady axisymmetric calculation does not show any significant deviation from the steady cases demonstrates that the flat pressure distribution on the base, found for the three-dimensional DNS, is not caused by the axisymmetric mode. Therefore, the flat pressure distribution on the base must be a direct consequence of higher azimuthal modes.

The time-averaged streamwise axis-velocity versus streamwise coordinate for this Reynolds number is included in figure 5.1. It appears that the main effect of the structures, which are a consequence of the absolute instability with respect to the axisymmetric mode, is the presence of a long constant velocity region at $1.25 < z < 6$. Due to the small variation of pressure in the radial direction within the recirculation region, this leads to a fairly constant pressure for the same interval. This corresponds to the results obtained for incompressible backward-facing steps, which are dominated by two-dimensional structures (rollers), as discussed by Terzi (2004). The axisymmetric structures present at the highest Reynolds number also cause entrainment of low-speed fluid from the recirculation region, thereby reversing the trend of increasing recirculation length for increasing Reynolds numbers.

In conclusion, further evidence was presented supporting the claim that the first

azimuthal mode might be a nonlinear product of the dominant modes, i.e., a sub-harmonic of the most important higher modes. Comparing various circumferential domain-sizes with each other, it was found that the first higher harmonic of the fundamental wavelength was the most dominant mode for all cases. In addition, regardless of the wavenumber, the mode-shape of the most dominant mode always exhibits the same mode-shape. A modulation of the shear layer was also apparent from the mean flow data, building confidence in the suggestion that global modes are present which presumably lead to the creation of longitudinal structures within the recirculation region. In the half-cylinder case, the base pressure distribution is entirely flat. It was demonstrated that this is caused by azimuthal modes with low wavenumbers. Once the low wavenumber modes are eliminated, a radial variation of the pressure at the base with a peak at the axis is obtained, and the mean pressure is slightly increased.

6.1.4 Turbulent Statistics

In order to obtain averaged turbulent quantities, first the running averages of the conservative variables needed to be converged. The calculations were then continued, reading in the converged running averages and computing the mean values of the velocity components, temperature and molecular stresses at start-up. During the calculation, at every time-step, these mean quantities were subtracted from the instantaneous values, thereby obtaining the fluctuations of all quantities. The final step was to assemble all turbulent quantities, such as K , ε and the turbulent stresses and average those over time.⁴

Side- and endviews of the averaged turbulent kinetic energy, K , the turbulent dissipation rate, ε and several Reynolds-stresses, $\overline{u'_i u'_j}$, are shown in figure 6.21 for data obtained from the half-cylinder calculation. The sideviews of K , ε and the turbulent shear-stress $\overline{u'v'}$ illustrate that no significant fluctuations are present prior

⁴Typically, the running averages for the turbulent statistics were also computed for at least six flow-through-times.

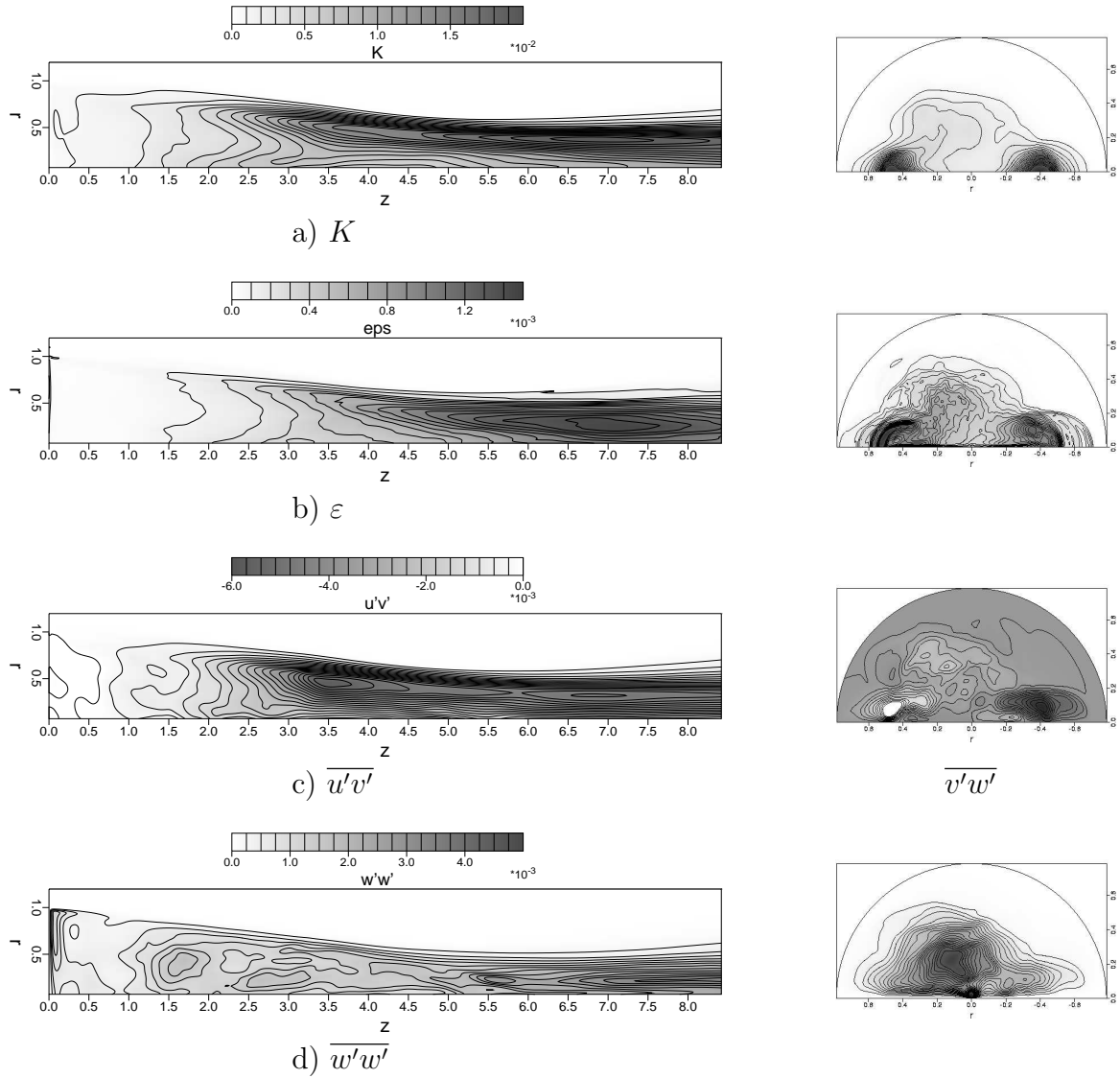


Figure 6.21 Azimuthal average of turbulent statistics; sideviews (left) and endviews at $z = 7$ (right) for half-cylinder case; $Re_D = 30,000$, $M = 2.46$.

to roughly two radii downstream of the base. Furthermore, it can be observed that the highest activity is present on the inside of the shear layer, with the magnitudes of the respective quantities increasing in the downstream direction. In order to quantify and find the streamwise location of the maximum values, the radial maxima of each variable over the streamwise coordinate are shown in figure 6.22. For reference, the mean recirculation length is denoted by the vertical dashed line. The radial maximum

of the TKE, the turbulent dissipation rate and all normal stress components, $\overline{u'_i u'_i}$, are located downstream of the mean reattachment point. In contrast, the maximum of the most significant shear-stress component, $\overline{u'v'}$, is located upstream of the mean reattachment point, at $z \approx 3.5$. Because the shear-stress component can be related to the radial gradient of the mean streamwise velocity component, $\overline{u'v'} \sim \frac{\partial \overline{u}}{\partial r}$, this behavior can most likely be attributed to the decreasing shear-layer gradient in the streamwise direction. These observations are in contrast to the findings by Herrin & Dutton (1997) who reported that the maxima of most turbulence quantities were located *upstream* of the mean reattachment point. However, in their case, the flow was fully turbulent, whereas the flow currently investigated is of transitional nature.

The endviews for both K and ε at $z = 7$, downstream of the mean reattachment point, where the highest levels of most turbulent quantities were found, reflect the “four-lobe” structure of the wake discussed above. The most dominant structures seen in the mean streamwise vorticity, shown in figure 6.17, appear to generate the largest number of small-scale structures, evidenced by the highest level of K and ε at these locations. This corroborates the assumption made earlier, that the small scales are generated by large-scale structures and, therefore, are a consequence of additional instabilities. The strong azimuthal variation of the turbulent quantities further shows the necessity of solving the transport equations for K and ε fully three-dimensional, as stated in section 3. In addition, the side- and endviews of the azimuthal normal stress component confirm that turbulent fluctuations in the azimuthal direction can not be neglected.

It can be seen in figure 6.22, that, for all circumferential domain-sizes, $\overline{u'u'}$ is the dominant turbulent-stress component. The other two normal-stress components are fairly similar to each other in magnitude and shape, such that $\overline{u'u'} \gg \overline{v'v'} \approx \overline{w'w'}$. The profiles of K and the streamwise normal stress component are very similar due

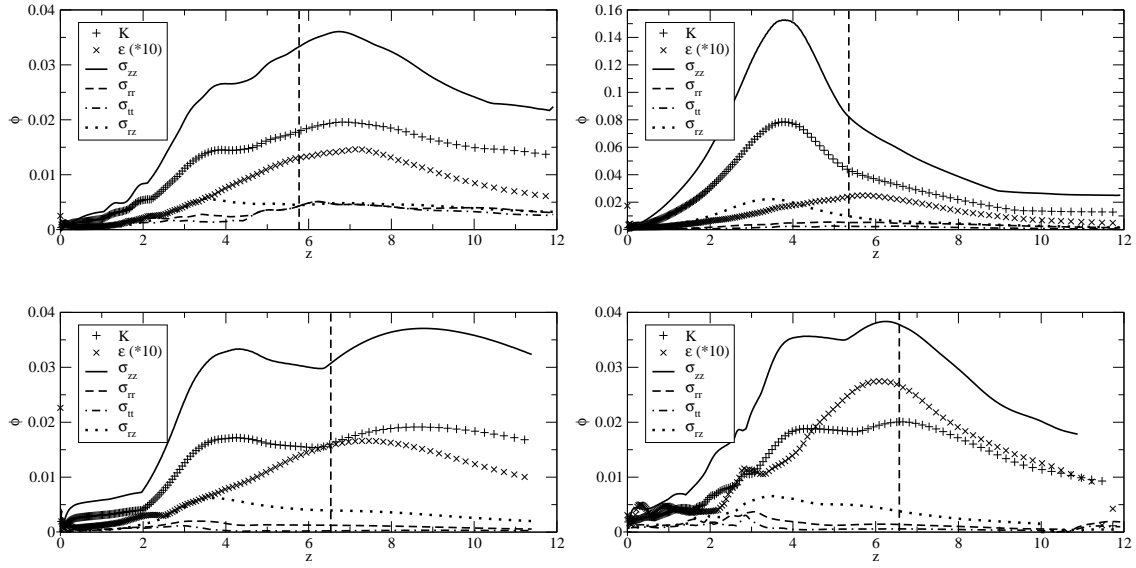


Figure 6.22 Radial maxima of various averaged turbulent statistics over streamwise coordinate obtained from DNS for half-cylinder (top left), quarter-cylinder (top right), $1/6^{th}$ -cylinder (bottom left) and $1/8^{th}$ -cylinder (bottom right); vertical dashed line denotes the respective mean reattachment length; $Re_D = 30,000$, $M = 2.46$.

to the relation

$$K = \frac{1}{2} (\overline{u'u'} + \overline{v'v'} + \overline{w'w'}) \approx \frac{1}{2} \overline{u'u'} . \quad (6.3)$$

The TKE is roughly one order of magnitude larger than the turbulent dissipation rate ε . It is also interesting to note, that the shear-stress component $\overline{u'v'}$ has its maximum within the recirculation region, with magnitudes significantly larger than those of $\overline{v'v'}$ and $\overline{w'w'}$ in that region. However, for both the half-cylinder and the quarter-cylinder calculations, the values of the two normal stresses increase in the downstream direction while the shear-stress decreases so that downstream of the mean reattachment point $\overline{v'v'} \approx \overline{w'w'} \geq \overline{u'v'}$. The TKE and $\overline{u'u'}$ distributions both reach a plateau at the streamwise location where the shear-stress reaches its maximum value in the half-cylinder and $1/8^{th}$ -cylinder calculation, before increasing further towards their global maxima. A possible explanation for this behavior is that, once the flow has transitioned, the turbulence production remains fairly constant. Only when the flow becomes subjected to the strong streamwise pressure gradient in the

reattachment region, the turbulence production increases significantly.

In the quarter-cylinder case, however, a striking difference can be observed. K and $\overline{u'u'}$ increase monotonically until attaining their global maxima noticeably upstream of the mean reattachment point. Their maxima coincide with the location of the maximum of the shear-stress component $\overline{u'v'}$. The magnitudes reached at the peaks are significantly larger than for all other cases. This suggests, that for this case the transition process is more violent than for the other cases, immediately generating more energetic structures that lead to higher values in the turbulent statistics. The values of all quantities downstream of the global maximum become similar to those seen in the other cases, thus no different turbulence generation mechanisms appear to be present in the trailing wake. This suggestion is supported by the fact that the shape of the turbulent dissipation rate resembles the distributions obtained from the other cases, with the location of the maximum value remaining downstream of the mean reattachment point.

Finally, the availability of the distribution of the turbulent dissipation rate is useful as another criterion for determining whether the calculation is well enough resolved. The Kolmogorov length-scale can be computed and compared with the grid-spacing. For the half-cylinder case, the maximum value of ε was found to be $\varepsilon \approx 0.0015$, which leads to a Kolmogorov length-scale of $L_K = \mathcal{O}(10^{-3})$. As can be seen from figure 6.21, the location of this maximum is approximately at $(z, r) = (7, 0.25)$. The numerical grid resolution at this point is $\Delta z = 0.0524 = \mathcal{O}(10 \cdot L_K)$, $\Delta r = 0.008 = \mathcal{O}(L_K)$ and $r\Delta\theta = 0.25 \cdot \frac{\pi}{128} = 0.00616 = \mathcal{O}(L_K)$. Hence, the numerical resolution in the radial and the azimuthal direction are on the order of the Kolmogorov length-scale. In the streamwise direction, the grid-spacing is roughly one order of magnitude larger than L_K , which is at the lower limit of what is considered adequate for resolving the relevant length-scales. However, as the estimate for the Kolmogorov length-scale is based on the maximum of ε and the streamwise grid becomes finer approaching the base, the streamwise resolution is also considered to be sufficient. Recall, that the

temporal resolution and the resolution in the azimuthal direction were already found to be sufficient through the discussion of the temporal development of the Fourier modes in section 6.1.1.

In summary, in the half-cylinder case, the maximum values of all turbulence quantities, except the turbulent shear-stress was found downstream of the mean reattachment point. The turbulent Reynolds shear-stress exhibited a maximum upstream of the recompression region because of the relation to the mean shear layer gradient, which is decreasing considerably farther downstream. Endviews illustrate that a strong azimuthal variation of the turbulence quantities is present, substantiating the claim that transport equation for K and ε need to be solved fully three-dimensional for the present flow. Finally, the turbulence dissipation rate was used to estimate the Kolmogorov length-scale, and it was determined that the spatial resolution of the calculations were adequate.

6.1.5 Flow Control

From the hydrodynamic stability investigations, using both spatial and temporal simulations, it was concluded that the azimuthal modes $k = 1, 2, 3, 4$ are the dominant modes for supersonic axisymmetric wakes at $Re_D = 30,000$. In particular the second mode is responsible for a mean “four-lobe” wake structure, significant entrainment of fluid from the recirculation region, and, consequently, a low base-pressure. This is supported by the fact that, for cases where mode $k = 2$ was excluded, i.e., all calculations with a circumferential domain-size smaller than a quarter-cylinder, an increase in the mean base-pressure was observed.

The knowledge gained from these calculations motivated the use of flow control methods to exploit and/or counteract the instability mechanisms present in the flow, such that a pressure increase at the base, and, consequently, a drag reduction could

be accomplished. To that end, several calculations were conducted at $M = 2.46$ and $Re_D = 30,000$ employing flow control, designed to weaken the dominance of the low-wavenumber modes. Disturbances were introduced into the approach boundary layer, just upstream of separation (center of disturbance at $r = 1.05$, $z = -0.15$) through a time-periodic volume force \hat{F}_{VF}^k , which was described in section 3.7. The volume force was added to the right-hand-side (RHS) of the radial momentum equation (2.4) in Fourier space, thus a specific azimuthal mode could be forced. The disturbances were either steady or periodic in time with a frequency ω and a disturbance amplitude A_{dist} , according to equation (3.2). Two separate mechanisms for altering the near-wake were investigated:

1. Longitudinal vortices were introduced into the initial shear-layer, imposing symmetries on the flow in the $r - \theta$ plane and constraining helical modes with low mode-numbers.
2. Axisymmetric vortices were generated, which, due to compressibility effects, do not experience significant growth in the streamwise direction, but reduce the energy transfer from the mean flow to oblique disturbances, thereby decreasing the growth of helical structures.

To emulate steady vortex generators which introduce longitudinal vorticity into the

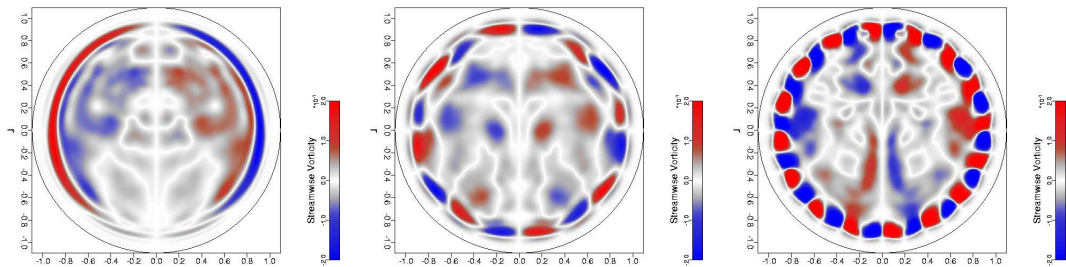


Figure 6.23 Endviews of time-averaged streamwise vorticity in the initial shear-layer at $z=1$; steady azimuthal forcing of $k = 4$, $k = 8$ and $k = 16$ from left to right; $Re_D = 30,000$, $M = 2.46$.

shear layer, the volume force \hat{F}_{VF}^k was added to a specific azimuthal mode of the RHS with $\omega = 0$. Three cases were examined: forcing either mode $k = 4$, $k = 8$ or $k = 16$, hence generating 8, 16 or 32 counter-rotating longitudinal structures in the circumferential direction. The resulting structures are illustrated in figure 6.23 by contours of streamwise vorticity in an endview at a location close to the base ($z = 1$). In order to produce axisymmetric vorticity, the axisymmetric mode $k = 0$ was disturbed periodically with $\omega = 0.4166$. This frequency was selected because it corresponded to the most unstable streamwise wavelength for the axisymmetric mode that was found using temporal calculations.

An interval of the temporal development of the azimuthal Fourier modes in a region of high activity, after the initial transient is overcome, is shown in figures 6.24 (a) – (d). In contrast to the unforced case presented in figure 6.4, high-frequency oscillations are present throughout the entire interval and no intermittency can be observed for all forced cases, except when steady forcing of mode $k = 4$ is applied. This suggests that the structures introduced into the flow, whether streamwise or axisymmetric, lead to instabilities which continuously produce small-scale structures.

In order to identify the dominant frequencies in the flow, the data of the azimuthal Fourier modes of density at a location in the developing wake were Fourier-transformed in time. Figure 6.25 shows the amplitudes of selected azimuthal modes versus the Strouhal number based on diameter for all forced cases. In all cases a significantly broader range of time-scales and larger amplitudes than for the unforced case could be observed. This is in agreement with the previous observation, that the intermittency of the unforced calculations at this Reynolds number, is destroyed for all cases investigated.

For the case employing periodic axisymmetric forcing, the forcing frequency clearly manifests itself as a peak in $k = 0$, $k = 2$ and $k = 3$ at $St_D = 0.833$, even though the time signal was acquired in the trailing wake (note that the non-dimensionalization of

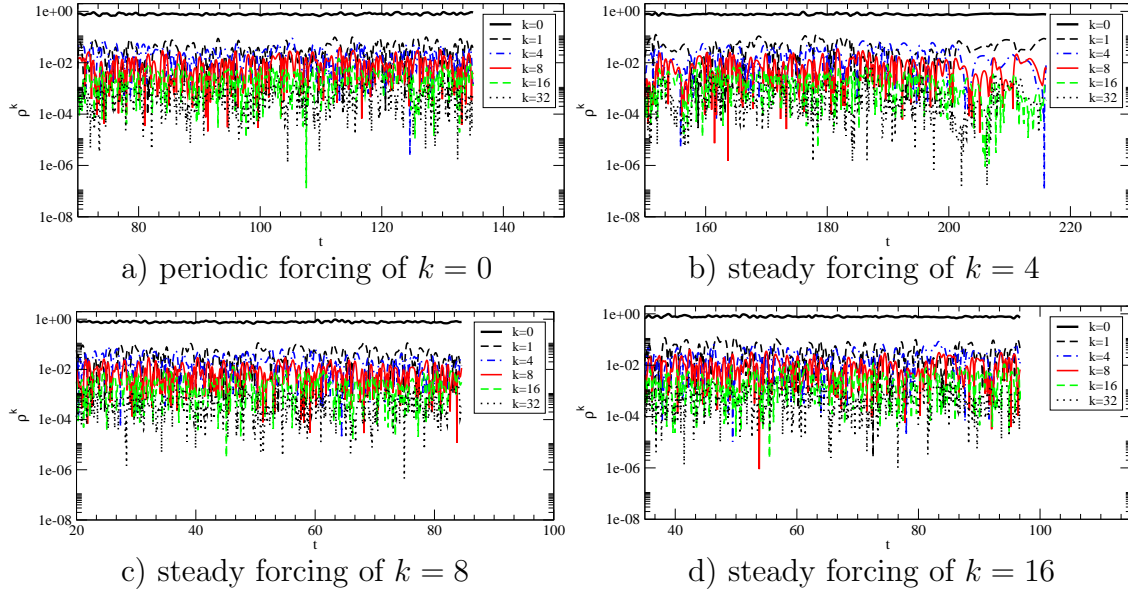


Figure 6.24 Temporal development of Fourier modes of ρ in a region of high activity for volume-forced cases; $z = 10.13$, $r = 0.45$, $Re_D = 30,000$, $M = 2.46$.

all quantities was performed with R as reference length whereas the Strouhal number is based on the diameter $D = 2R$ of the body). It can also be seen that subharmonics with half and one quarter of the forcing-frequency are generated. Compared to the unforced case, no significant reduction in the amplitudes of mode $k = 2$ can be detected for the forced cases. However, the contribution of the other modes increases, in particular the first azimuthal mode $k = 1$ shows multiple pronounced peaks in the low-frequency range for the cases where longitudinal vorticity was introduced. In order to determine how the different forcing mechanisms affect the generation and evolution of coherent structures, visualizations of instantaneous iso-contours of $Q = 0.1$ are shown in the following figures. For the case employing periodic axisymmetric forcing (6.26 a), the vortices appearing in the trailing wake are very similar to the unforced case. The axisymmetric structures generated just upstream of separation by the periodic forcing can be observed in the shear layer. However, an azimuthal modulation caused by the dominant helical modes is visible. When employing steady forcing of mode $k = 4$ (figure 6.26 b), the resulting base flow appears to be very similar

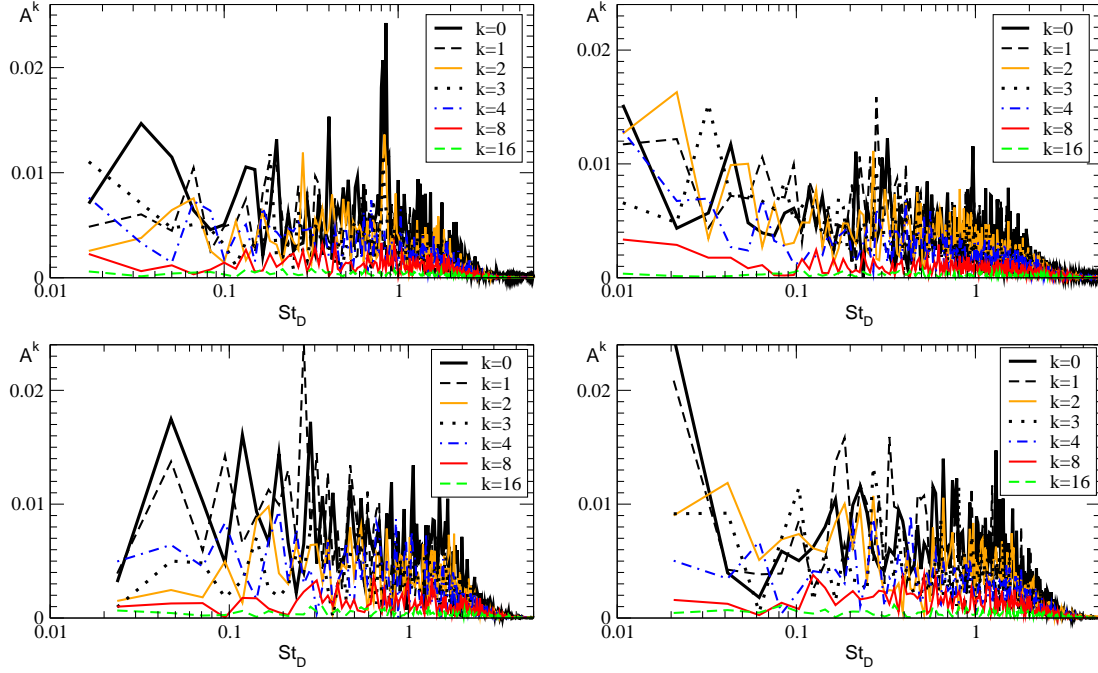


Figure 6.25 Fourier decomposition in time of Fourier modes of ρ in a region of high activity, periodic forcing of $k = 0$ top left, steady forcing of $k = 4$ top right, steady forcing of $k = 8$ bottom left, steady forcing of $k = 16$ bottom right; $z = 10.13$, $r = 0.45$, $Re_D = 30,000$, $M = 2.46$.

to the unforced case. This confirms that $k = 4$ is a significant mode in the natural case. The same kind of (upstream travelling) helical structures can be detected in the inner shear-layer and the longitudinal structures forming in the recirculation region extend into the trailing wake. Once these structures detach, they travel downstream, forming hairpin vortices. Consequently, forcing a low wavenumber such as $k = 4$ does not seem to introduce structures that visibly affect the flow field. Figure 6.27 a) shows that the opposite is true for the case where mode $k = 8$ is forced. Here, longitudinal vortices emerge from the forcing location and can be observed in the initial shear-layer. Also, a considerably larger amount of longitudinal structures can be observed than for the unforced case or the two forced cases discussed above. The diameter of these streamwise vortices appears to be smaller than for the other cases as well. Using steady forcing of mode $k = 16$ (figure 6.27 b), longitudinal structures, originating in

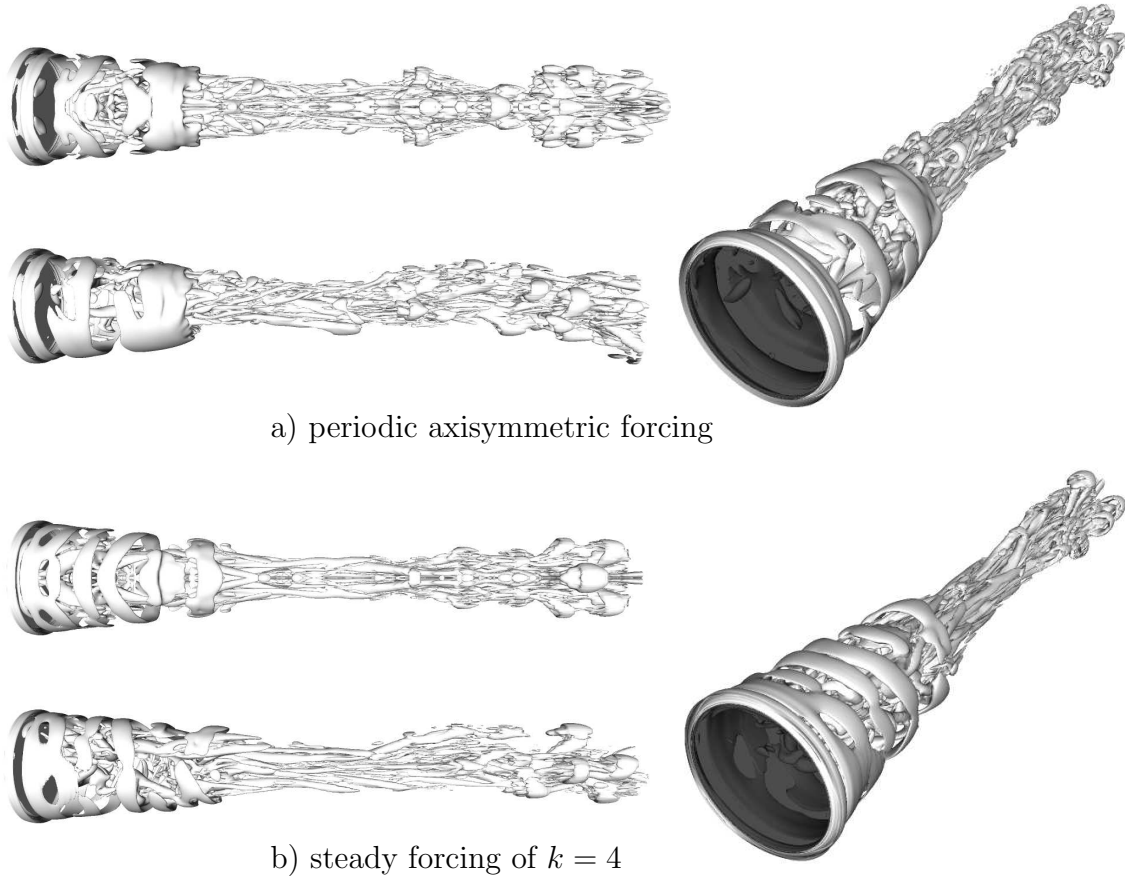


Figure 6.26 Instantaneous iso-contours of $Q = 0.1$ for forced cases, top- and side-view (top and bottom, left) and perspective view from inflow towards outflow (right); $Re_D = 30,000$, $M = 2.46$.

the approach flow, can be observed in the shear layer. As for the case where $k = 8$ is forced, a denser clustering of streamwise structures with a reduced diameter (versus the unforced case) can be detected in the recompression region and in the trailing wake. This observation supports the notion that the longitudinal structures are a consequence of additional instabilities that occur when the global modes with low wavenumber reach high amplitudes and cause a significant circumferential modulation of the near-wake. For the forced cases, the introduced longitudinal structures cause a strong azimuthal variation of the shear layer, thereby leading to the formation of a large number of streamwise vortices within the recirculation region.

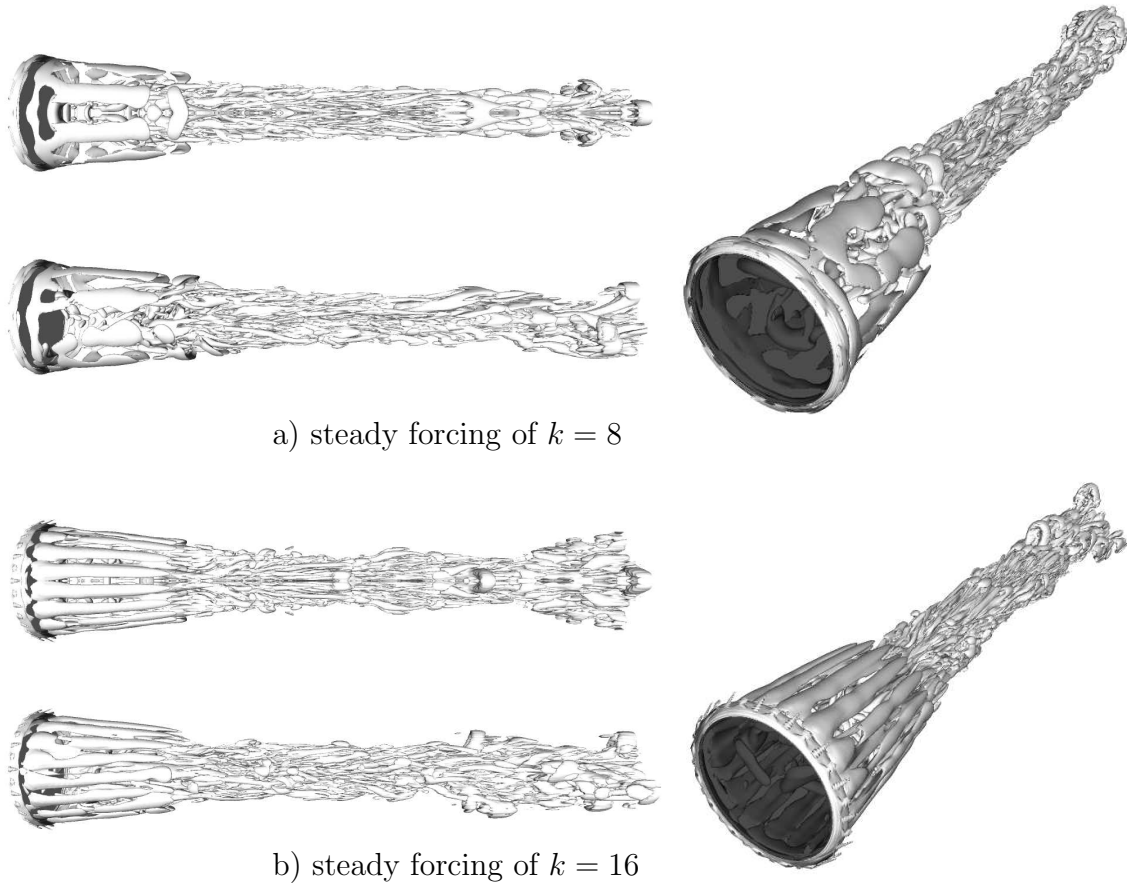


Figure 6.27 Instantaneous iso-contours of $Q = 0.1$ for forced cases, top- and side-view (top and bottom, left) and perspective view from inflow towards outflow (right); $Re_D = 30,000$, $M = 2.46$.

For all forced cases, a flapping motion of the far wake, as for the unforced case, can be observed, implying that the contribution of mode $k = 1$ is considerable in this region. This explains the significance of $k = 1$ in the frequency spectra shown in figure 6.25. However, for the cases where steady forcing is applied to modes $k = 8$ or $k = 16$, no significant lateral movement was observed for the near-wake or the initial trailing-wake, suggesting that the introduction of longitudinal vortices prevents low-wavenumber modes from becoming dominant in this region.

To evaluate the effect of the forcing on the mean flow, time-averaged quantities

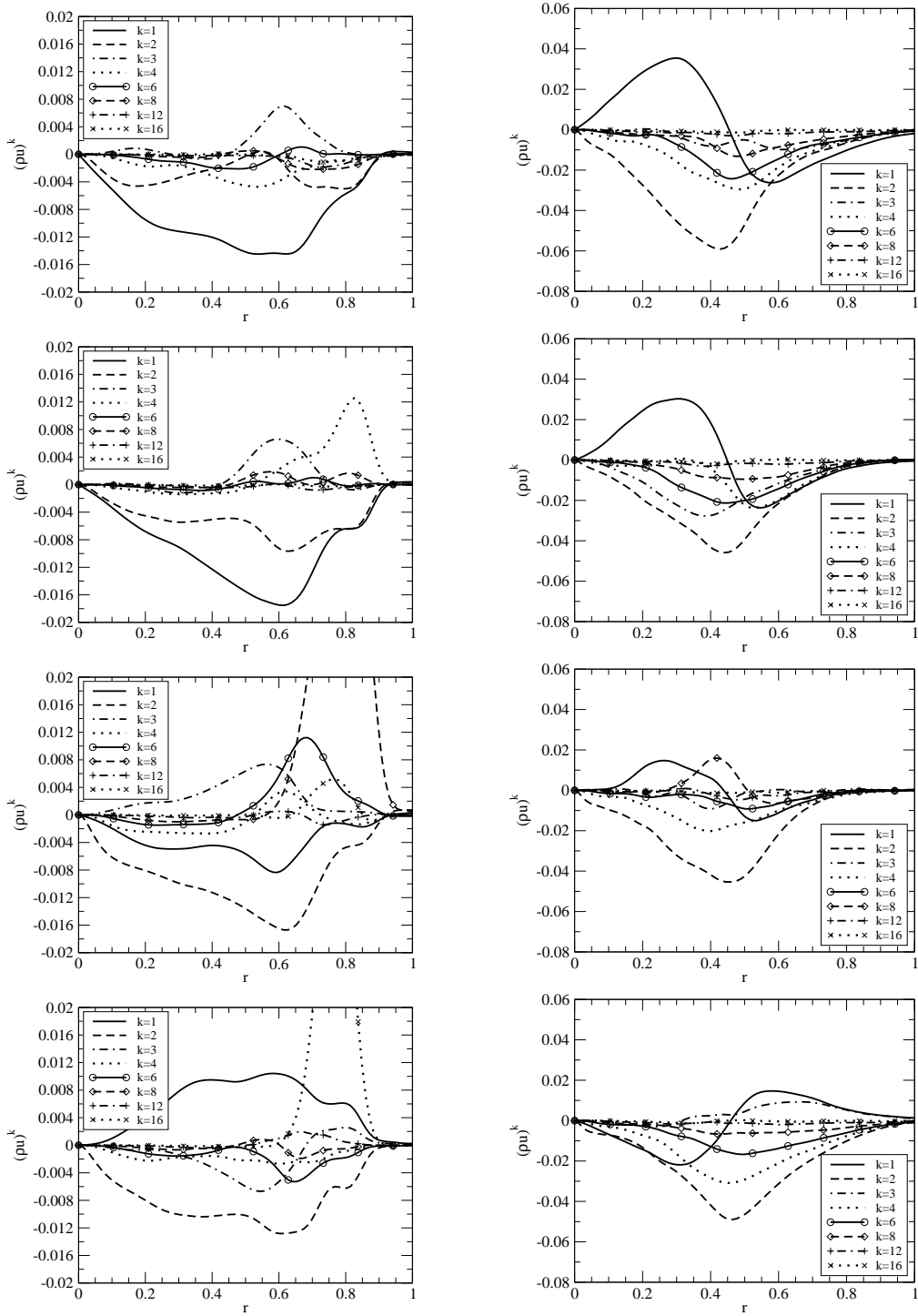


Figure 6.28 Time-averaged radial profiles of azimuthal Fourier modes of (ρu) obtained from DNS, forcing $k = 0$, $k = 4$, $k = 8$ and $k = 16$ cases (from top to bottom); $z = 2.5$ (left), $z = 9$ (right); $Re_D = 30,000$, $M = 2.46$.

are scrutinized in the following. The averaged radial profiles of several azimuthal Fourier modes of the streamwise velocity component are shown in figure 6.28 for all forced cases. Note that all graphs were scaled as in the unforced case in figure 6.13 to allow for a direct comparison of the amplitudes. Comparing the data obtained from the case where the axisymmetric mode was disturbed periodically to the unforced case shows several differences: At the upstream location $z = 2.5$, the mode-shape of the first azimuthal mode shows a changed radial distribution and possesses the largest amplitude. The amplitude distributions of azimuthal modes with $k > 1$ are quite similar to the unforced case, both in shape and magnitude. Looking at the downstream location $z = 9$, the mode-shapes resemble those found in the unforced case. Modes $k = 4$ and $k = 6$, which showed large amplitudes in the unforced case, appear to be considerably weakened by the periodic forcing. For the case where mode $k = 4$ is forced steadily, a significant peak in that mode is visible in the shear layer (at $r = 0.8$) at the upstream location, $z = 2.5$. The mode-shape of the first mode resembles that of the case employing axisymmetric forcing. For the higher modes, except $k = 4$, the amplitude distributions are similar to those found in the unforced case. The radial profiles obtained in the trailing wake again show a strong similarity to the unforced case, except that modes $k = 2$, $k = 4$ and $k = 6$ are not as dominant.

When employing steady forcing of either mode $k = 8$ or $k = 16$, a significant peak within the shear layer is visible at the upstream location in the forced mode. The fact that several azimuthal modes possess larger amplitudes at the upstream location than the first azimuthal mode confirms the observation made while discussing the instantaneous visualizations of Q : The introduced longitudinal vortices prevent the first mode from reaching large amplitudes. In the case where mode $k = 8$ is forced, the large amplitude of that mode seems to be maintained in the downstream direction. Therefore, a large contribution of $k = 8$ can be detected at the location in the trailing wake. In general, however, the amplitudes of all modes possess considerably smaller values than for all other cases. No large contribution of mode $k = 16$ can be observed

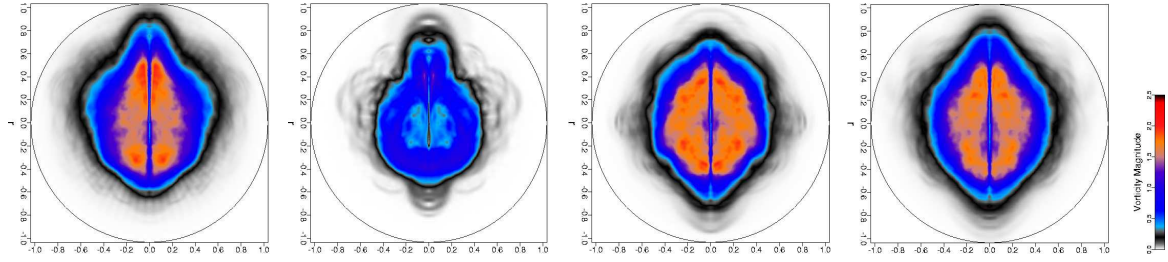


Figure 6.29 Endviews of time-averaged contours of total vorticity in the trailing wake at $z = 9$; from left to right: periodic axisymmetric forcing, steady azimuthal forcing of $k = 4$, steady azimuthal forcing of $k = 8$, steady azimuthal forcing of $k = 16$; $Re_D = 30,000$, $M = 2.46$.

at $z = 9$ for the case where that mode is forced, even though it shows a pronounced peak at $z = 2.5$. For the two latter cases, it can also be observed that modes $k = 4$ and $k = 6$ possess reduced amplitudes versus the unforced case.

Endviews of time-averaged total vorticity at $z = 9$ are shown in figure 6.29, in order to assess whether the wake structure was modified by the various forcing mechanisms. In contrast to the unforced case, which displayed a pronounced “four-lobe” structure, the wake-structure of all forced cases becomes significantly more circular. Even though no symmetries were introduced in form of longitudinal vortices to weaken low wavenumber modes for this case, the resulting wake pattern differs noticeably from the unforced case. For the case where steady forcing of $k = 4$ was employed, a strong reduction in the level of total vorticity can be detected. The wake pattern is also considerably changed from the unforced case. This is in good agreement with the reduced amplitudes seen for the higher modes in the amplitude distributions presented above. When forcing mode $k = 8$, the vorticity levels in the trailing wake are higher than when $k = 4$ is forced. Remnants of the introduced longitudinal structures can be detected, creating a weak “eight-lobe” pattern. This was expected in light of the large amplitude of $k = 8$ visible in the radial profiles at $z = 9$. When forcing $k = 16$, approximately the same vorticity level is present as for the case forcing $k = 8$. In agreement with the small amplitude of $k = 16$ at the

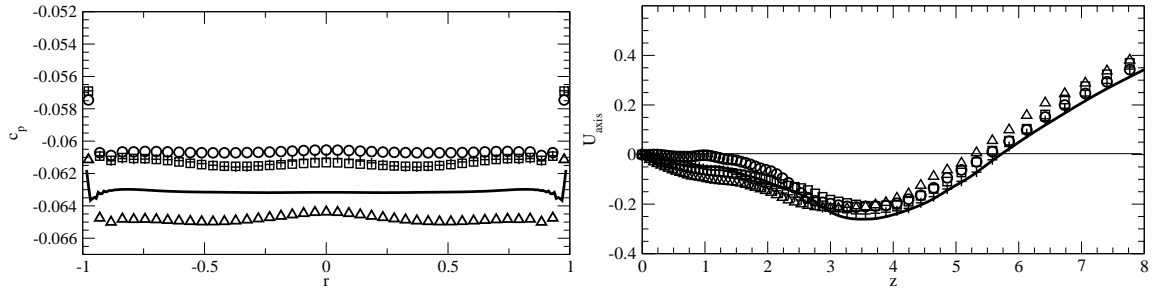


Figure 6.30 Pressure coefficient on base (left) and streamwise velocity along axis of symmetry (right); unforced case (—), periodic forcing of $k = 0$ with $\omega = 0.4166$ (+), steady forcing of $k = 4$ (\square), steady forcing of $k = 8$ (\circ), steady forcing of $k = 16$ (\triangle); $Re_D = 30,000$, $M = 2.46$.

downstream location $z = 9$, no trace of the introduced longitudinal structures can be observed in the endview. Rather, the resulting pattern slightly resembles that of the unforced case, albeit the four-lobe structure is by far not as pronounced.

The time-averaged streamwise velocity along the axis and the mean pressure coefficient along the base from the forced cases are compared to the unforced case in figure 6.30. Forcing the axisymmetric mode periodically results in a similar streamwise axis-velocity profile than that obtained from the unforced case. However, the mean pressure coefficient at the base is increased by approximately 3.5%. When forcing higher azimuthal modes, the recirculation length is slightly decreased. This is due to the increased entrainment of low-speed fluid from the recirculation region by the longitudinal structures introduced into the shear layer. The same recirculation length is predicted by the calculations where either mode $k = 8$ or $k = 16$ is forced. However, when forcing $k = 16$, a further reduction of the recirculation length can be observed. Responsible for the reduction is the increased mixing caused by the larger number of longitudinal structures in the shear layer. It is noteworthy, however, that in the near-wake region, the profiles of the streamwise axis-velocity differ significantly for the cases forcing higher modes. When forcing mode $k = 4$, the data follows closely that of the unforced case. In contrast, when mode $k = 8$ is forced, the slope at the

base becomes shallower, but the profile dips to the same value of reverse velocity obtained from all other cases further downstream. For the case, where the largest number of streamwise vortices is introduced into the shear layer, the opposite is the case and the slope at the base becomes steeper. The changing behavior of the streamwise axis-velocity distribution also translates to different mean pressure values at the base. When forcing mode $k = 4$, a very similar pressure distribution on the base is obtained as for the case where axisymmetric forcing was employed. Forcing mode $k = 8$ appears to be the most successful case in augmenting base-pressure, showing a 6% increase over the unforced case. For the case where $k = 16$ is forced, the gain in preventing the dominance of the low wavenumbers seems to be outweighed by the increased mixing in the shear layer, leading to a slightly decreased pressure coefficient on the base.

In summary, for all cases employing flow control, except forcing $k = 4$, continuous generation of small-scale structures was observed and no intermittency was present. Forcing the axisymmetric mode has the same effect as observed in experiments (e.g., Bourdon & Dutton, 2001) at a much higher Reynolds number. Due to the high compressibility in the shear layer, the two-dimensional mode is not significantly amplified, but it diminishes the energy transfer from the mean flow to the helical modes. As a consequence, the vorticity levels and mixing are decreased, resulting in less entrainment and, thus, in a higher base-pressure. Furthermore, the structures present in the flow are very similar to the unforced case, i.e., helical structures appear in the shear layer and streamwise vortices are present in the recirculation region and in the trailing wake. This is also true for the case where the fourth mode is forced, confirming that mode $k = 4$ is an important mode in the unforced case. However, when forcing higher modes, longitudinal structures emerge from the forcing location, leading to a reduced flapping of the initial shear-layer and a larger amount of streamwise structures in the trailing wake. The longitudinal vortices, introduced into the shear layer, lead to an

increased entrainment and, for the case of forcing $k = 16$, the pressure is decreased, as seen in the experiments. When forcing $k = 4$ or $k = 8$, however, the base-pressure is increased. This is in contrast to the observations made by Bourdon & Dutton (2001), where the introduced longitudinal structures always reduced the base-pressure. From the data obtained when forcing $k = 4$ and $k = 8$, it is suggested that preventing the dominance of the low wavenumber modes outweighs the increased mixing. Therefore, it appears as if flow control is a viable tool for drag reduction in supersonic base flows.

6.1.6 Summary

Hydrodynamic stability investigations of supersonic axisymmetric wakes at $Re_D = 30,000$ and $M = 2.46$ were conducted using DNS and TDNS. One of the advantages of conducting numerical experiments was exploited: The ability to deliberately exclude certain physical effects. By employing DNS for various circumferential domain-sizes, the influence of various azimuthal modes on the flow could be investigated. It was confirmed that the flow is absolutely unstable with respect to at least the first eight azimuthal modes. The unstable modes sporadically lead to the generation of large-scale structures, causing the flow to exhibit an intermittent behavior. It was shown that the structures in the initial shear-layer are of helical nature, due to the high compressibility of the flow in this region. It is proposed that unstable global modes within the recirculation region lead to the generation of longitudinal structures within the recirculation region. These streamwise structures eventually overcome the adverse pressure gradient in the recompression region and travel downstream, producing hair-pin structures in the trailing wake.

For sufficiently large circumferential domain-sizes, the range of unstable modes is sufficiently large to cause further instabilities that lead to the generation of small-scale structures. For the smallest domain sizes investigated, a viscous cut-off of the high wavenumbers prevents the azimuthal modes to grow linearly. In addition, because the

long wavenumbers are eliminated in the small domain sizes, the large wavenumbers cannot be generated nonlinearly either. Consequently, no small-scale structures are generated for these cases. Local stability calculations suggest that the helical structures present in the shear layer and the longitudinal structures within the trailing wake are a consequence of local instabilities. In addition, the baroclinic torque was identified as another important vorticity production mechanism. The largest contribution of vorticity production or destruction through baroclinic torque was found in regions subject to high compressibility, i.e., the outer boundary of shear-layer and the trailing wake.

The structures present in the flow have a substantial effect on the mean flow, causing a decrease in recirculation length and base-pressure. Moreover, the azimuthal modes with low wavenumbers are responsible for an entirely flat pressure-distribution on the base. The azimuthal modes $k = 2$ and $k = 4$ appear to be the most dominant for this Reynolds number, producing a “four-lobe” wake-pattern. Considerable evidence was found that the first azimuthal mode receives a significant amount of its energy through the nonlinear interaction of higher modes, in particular between $k = 3$ and $k = 4$. Furthermore, turbulence statistics revealed that turbulence quantities, such as K and ε , experience a strong azimuthal variation. This necessitates the implementation of a three-dimensional solver for turbulence transport equations.

It was illustrated that the base pressure was increased when the most dominant modes were excluded. Consequently, flow control was applied to the base flow, designed such that the (naturally) most dominant modes could be weakened. The continuous introduction of structures resulted in a larger amount of small-scale structures than in the unforced case and the destruction of intermittency. An increase in base-pressure of up to 6% was accomplished when introducing longitudinal structures into the initial shear-layer by employing steady forcing of mode $k = 8$. It appears that preventing the dominance of the low-wavenumber modes outweighs the increased mixing caused by additional longitudinal structures in the shear layer.

6.2 DNS for $Re_D = 60,000$

The linear stability calculations conducted in section 5.2 showed a significant increase in the growth rates of disturbances at $Re_D = 60,000$ compared to lower Reynolds numbers, in particular for the higher azimuthal modes. Therefore, the study that was conducted for supersonic axisymmetric wakes at $Re_D = 30,000$, was repeated for $Re_D = 60,000$ in order to evaluate whether a significant change in the wake-behavior would occur. DNS were conducted for a half-cylinder, a quarter-cylinder, $1/6^{th}$, $1/8^{th}$ and $1/16^{th}$ of a cylinder.

All calculations were performed on the same streamwise/radial grid, with 812×130 points in the streamwise and the radial directions, respectively, with the smallest grid-spacing at the corner being $\Delta z_c = \Delta r_c = 0.01$. In the radial direction, the grid-spacing was equidistant between $0 < r < 1$ and then strong stretching was used between $1 < r < 5$. This grid enabled the use of less total radial points than in the lower Reynolds number case, for which, in hindsight, a smaller amount of radial points would have been sufficient. In the streamwise direction, stretching was used throughout the entire domain. However, using 812 points for $0 < z < 10$ resulted in only a modest stretching with a ratio $\frac{\Delta z_{max}}{\Delta z_{min}} = 2.35$. In the azimuthal direction, the half-cylinder case was computed with 128 Fourier modes after a preliminary calculation with 64 modes did not show a sufficient decay in the amplitudes of the highest Fourier modes. The domains with smaller circumferential extent were then computed with 64, 42, 32, and 16 Fourier modes, respectively, in order to maintain the same grid resolution for all cases. For all other relevant parameters, see table D.7 in Appendix D.

6.2.1 Time-Dependent Results

The amplitudes of the azimuthal Fourier modes were monitored at both the pulse location and a location farther downstream. Exponential growth of the Fourier modes was observed for all cases, until a nonlinear saturation state was reached, implying

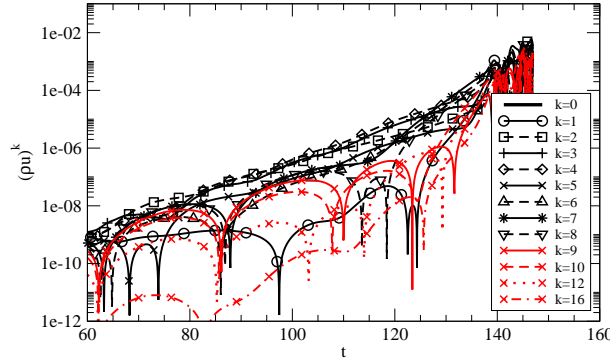


Figure 6.31 Temporal development of Fourier modes of (ρu) at disturbance location $z = 2.5$, $r = 0.5$ at start-up for half-cylinder calculation; $Re_D = 60,000$, $M = 2.46$.

that the flow is absolutely unstable with respect to azimuthal modes for all circumferential domain-sizes investigated, i.e., for the azimuthal modes $k \leq 8$. Representative for all circumferential domain-sizes, the temporal development of the Fourier modes of (ρu) for the start-up transient of the half-cylinder case is shown in figure 6.31. As seen in the results obtained from the linearized N-S calculations at $z = 2.5$, modes $k = 3$ and $k = 4$ possess the largest growth rates. The nonlinear interaction between these two modes manifests itself in an increased growth of mode $k = 1$, starting at $t \approx 110$. For $t > 115$, the nonlinear interaction between $k = 3$ and $k = 4$ can be observed in the increased growth rates of modes $k = 6$ and $k = 7$. For $t > 125$, the amplitude of $k = 4$ appears to become large enough to induce an increased growth of the subharmonic $k = 8$. From these observations, it appears that $k = 4$ is a strong contributor in the nonlinear generation process of higher modes. In contrast to the lower Reynolds number case, the first azimuthal mode $k = 1$ becomes the most amplified mode for $t > 130$.

Sideviews of instantaneous total vorticity for the plane $\theta = 0^\circ$ and $\theta = \theta_{max}$ of the respective calculations are shown in figures 6.32 (a) to (e). Unlike for the lower Reynolds number, figures (a), (b) and (d) do not look significantly different. The flow has fully transitioned to turbulence at a streamwise location of $z \approx 5$ and dis-

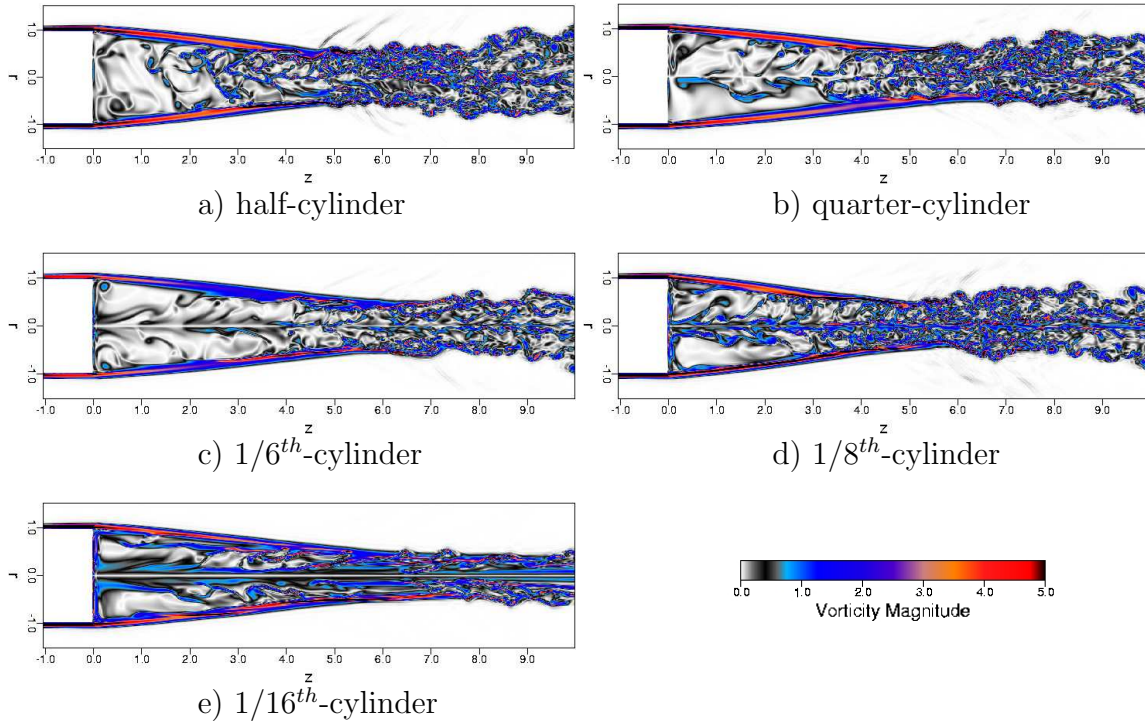


Figure 6.32 Sideviews of instantaneous contours of total vorticity; top half $\theta = 0^\circ$, bottom half a) $\theta = 180^\circ$, b) $\theta = 90^\circ$, c) $\theta = 60^\circ$, d) $\theta = 45^\circ$ and e) $\theta = 22.5^\circ$; $Re_D = 60,000$, $M = 2.46$.

plays small-scale structures that presumably are a consequence of secondary/tertiary instabilities occurring in the presence of large-scale structures. However, the $1/6^{th}$ -cylinder case (figure 6.32 c) appears to contain a smaller range of length-scales than the two larger circumferential domain-sizes and the $1/8^{th}$ -cylinder case, and transition occurs further downstream. This hints at a high significance of modes $k = 2, 4$ at this Reynolds number, as the second and fourth modes are included in (a) and (b), but not in (c). Also, in the calculation of the $1/16^{th}$ -cylinder, where $k = 4$ is eliminated, a considerably smaller range of length-scales can be observed. Nevertheless, a significantly larger amount of structures is visible than for the smallest azimuthal domain-size at $Re_D = 30,000$, and several structures can be detected in the shear layer. As in the lower Reynolds number case, structures can be seen to develop in

the inner part of the shear layer, in qualitative agreement with the higher Reynolds number experiments of Herrin & Dutton (1995).

The temporal development of the Fourier modes of density in a region of high activity, here at $z = 7.85$ and $r = 0.465$, once a fully nonlinear saturation state is reached, is shown in figures 6.33 (a) to (e). The decay in energy over the azimuthal modes amounts to approximately three orders of magnitude for cases (a) to (d), indicating that a significantly broader range of length-scales than for the lower Reynolds number flow is present. Also, no intermittency can be observed for any of the cases (a)–(d). Note, that only an interval of 10 time-units is shown in contrast to 60 time-

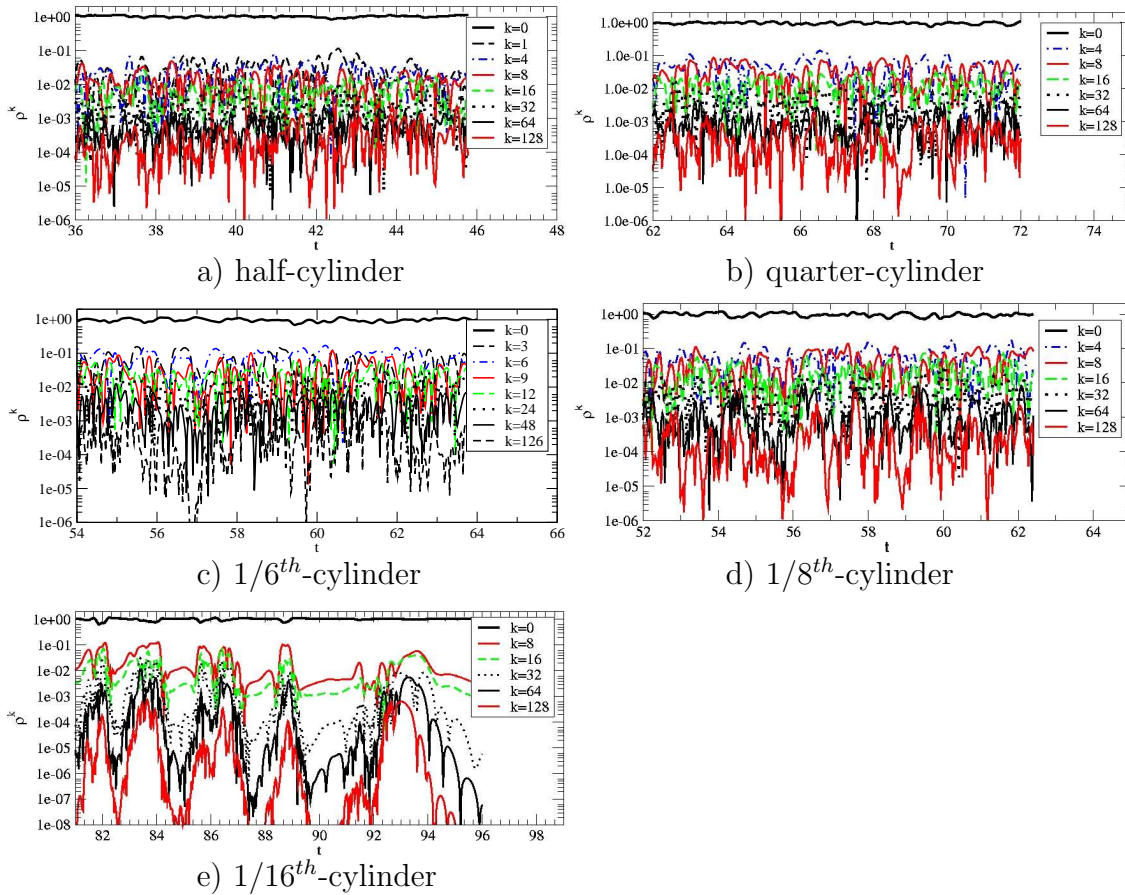


Figure 6.33 Temporal development of higher Fourier modes of ρ in a region of high activity; $z = 7.85$, $r = 0.465$, $Re_D = 60,000$, $M = 2.46$.

units for the lower Reynolds number cases, due to the smaller time-scales present. Only the smallest domain size, depicted in figure 6.33 (e), shows a high degree of intermittency, and the amplitudes of the higher modes are several orders of magnitude smaller than for the larger domain sizes.

The Fourier-decomposition of the time signal for all cases is shown in figure 6.34. In contrast to the $Re_D = 30,000$ case, it is evident that a significant amount of energy is contained in frequencies with $St_D \geq 1$. The temporal resolution appears to be sufficient for these cases, as exponential decay is observed towards higher St_D . For the half-cylinder case, mode $k = 1$ shows a prominent peak at $St_D = 0.175$. This value is noticeably higher than for the $Re_D = 30,000$ case ($St_D = 0.08$). Structures with this frequency seem to have a great effect on the azimuthal mean flow, evidenced

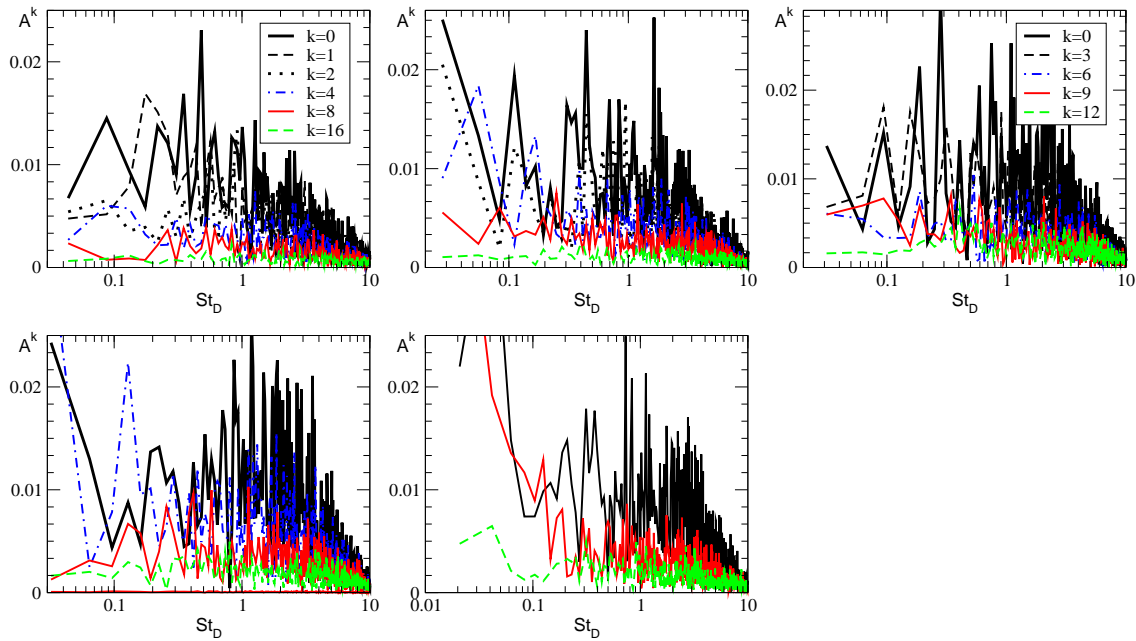


Figure 6.34 Fourier decomposition in time of higher Fourier modes of ρ in a region of high activity, half-cylinder top left, quarter-cylinder top center, $1/6^{th}$ -cylinder top right, $1/8^{th}$ -cylinder bottom left, $1/16^{th}$ -cylinder bottom center; $z = 7.85$, $r = 0.465$, $Re_D = 60,000$, $M = 2.46$.

by the peak of $k = 0$ at twice the frequency $St_D = 0.35$. Mode $k = 2$ and $k = 4$ appear to have the largest impact on the azimuthal mean in the lower frequency range for the quarter-cylinder case, displaying several peaks at $St_D < 1$. For larger Strouhal numbers, mode $k = 2$ appears to be the dominant higher mode. However, for this region no further assumptions can be made of which modes have the most pronounced effect on mode $k = 0$. It can only be observed that the mean flow possesses a dominant frequency with $St_D = 1.63$.

In contrast to the lower Reynolds number case, for the $1/6^{th}$ -cylinder case the largest amount of energy is contained in $k = 3$. A significant maximum of $k = 3$ at $St_D = 0.09$ coincides with $k = 9$ and nonlinearly generates a peak in the azimuthal mean at the same frequency. It is likely that this maximum of $k = 3$ is responsible for a higher harmonic of $k = 0$, $k = 6$ and $k = 9$ at $St_D = 0.18$. The global maximum of $k = 0$ found at $St_D = 0.28$ appears to be generated by the third mode as well, which shows a pronounced peak at $St_D = 0.14$.

The $1/8^{th}$ -cylinder case is dominated by modes $k = 4$ and $k = 8$ which exhibit strong peaks at frequencies as high as $St_D = 5$ with significant nonlinear effects on the azimuthal mean. Mode $k = 4$ has its most prominent maximum at $St_D = 0.12$ which is double the frequency of that found in the lower Reynolds number case. In contrast to the lower Reynolds number case, the $1/16^{th}$ -cylinder result displays a broad range of frequencies for modes $k = 0$, $k = 8$ and $k = 16$.

In summary, all cases with a circumferential domain-size larger than $0 \leq \theta \leq \pi/4$ appear to fully transition to turbulence downstream of the recompression region and no intermittency can be detected. In contrast to the lower Reynolds number case, a considerable amount of energy can be found in frequencies with $St_D \geq 1$ while maxima for lower azimuthal modes at low frequencies confirm the presence of large-scale structures in the flow. Preliminary evidence was found that modes $k = 2$ and $k = 4$ might be the most significant azimuthal modes for the current flow conditions.

6.2.2 Coherent Structures

The Q -criterion was chosen in order to visualize coherent structures in the flow. Figure 6.35 shows two perspective views and a time-sequence of sideviews of instantaneous iso-contours of $Q = 0.1$ for the half-cylinder case. The difference between the time-levels is $\Delta t = 3.08$, allowing free-stream fluid to travel approximately 3 radii downstream. Qualitatively, a similar picture can be observed as in the lower Reynolds number case, i.e., helical structures are present within the shear layer and streamwise structures reside in the recirculation region, extending into the trailing wake. However, the amount of longitudinal structures has drastically increased, in particular in the inner part of the shear layer. Also, a much larger amount of hairpin structures, such as the structure denoted by “C”, can be detected downstream of the recompression region. Most certainly this is due to the increased number of unstable modes at the higher Reynolds number. In addition, larger growth rates enable disturbances to reach large amplitudes on a shorter time-scale. This enables the formation of structures before the disturbances are convected out of the unstable region. Thus, potentially a larger amount of large-scale structures can occur. These, in turn, lead to additional instabilities, responsible for the generation of small-scale structures, as shown by means of total vorticity in figure 6.32 (a).

Recall that, at the lower Reynolds number (see section 6.1.2), the helical structures were found to travel upstream. This was attributed to the considerably smaller compressibility in the negative velocity region of the shear layer, permitting disturbances to reach sufficiently large amplitudes such that structures can be detected. When scrutinizing the time-sequence of the present case, it can be observed that the visible helical structures, marked “A” and “B”, do not show any significant transitional movement over roughly one flow-through-time. This implies that the amplification rate is increased such that disturbances reach a nonlinear saturation level in a higher compressibility region, i.e., where the mean shear-layer velocity is close to zero.

Visualizations of iso-contours of Q for the quarter-cylinder case (not shown for brevity) did not reveal significant differences from the half-cylinder case. A large amount of streamwise structures was observed within the recirculation region. Nevertheless, the helical structures in the shear layer were by far not as pronounced as for the larger domain size. Contrary to the $Re_D = 30,000$ case, the trailing wake also appears to contain a large amount of hairpin vortices. This implies that the exclusion of odd azimuthal modes at this Reynolds number does not change the wake-behavior significantly.

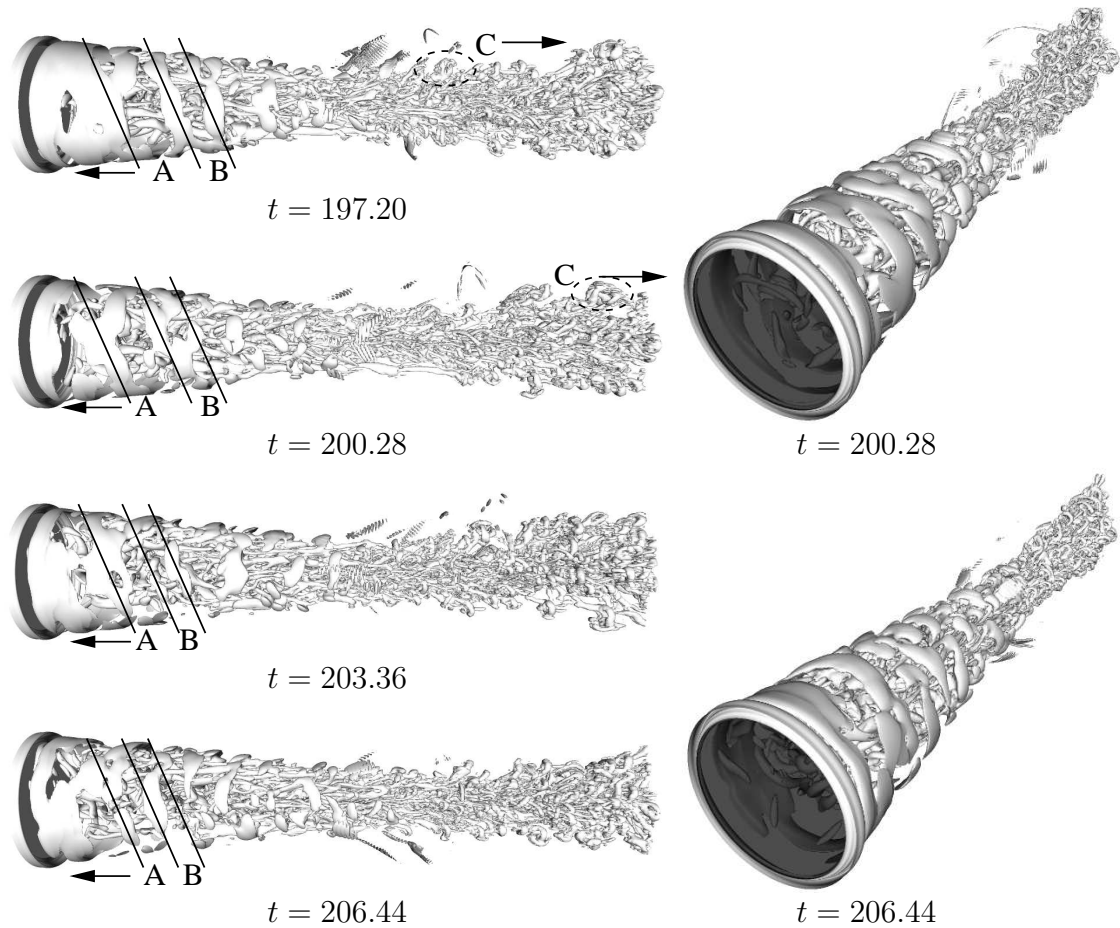


Figure 6.35 Instantaneous iso-contours of $Q = 0.1$ for half-cylinder case, sideviews (left) and perspective views from inflow towards outflow (right); $Re_D = 60,000$, $M = 2.46$.

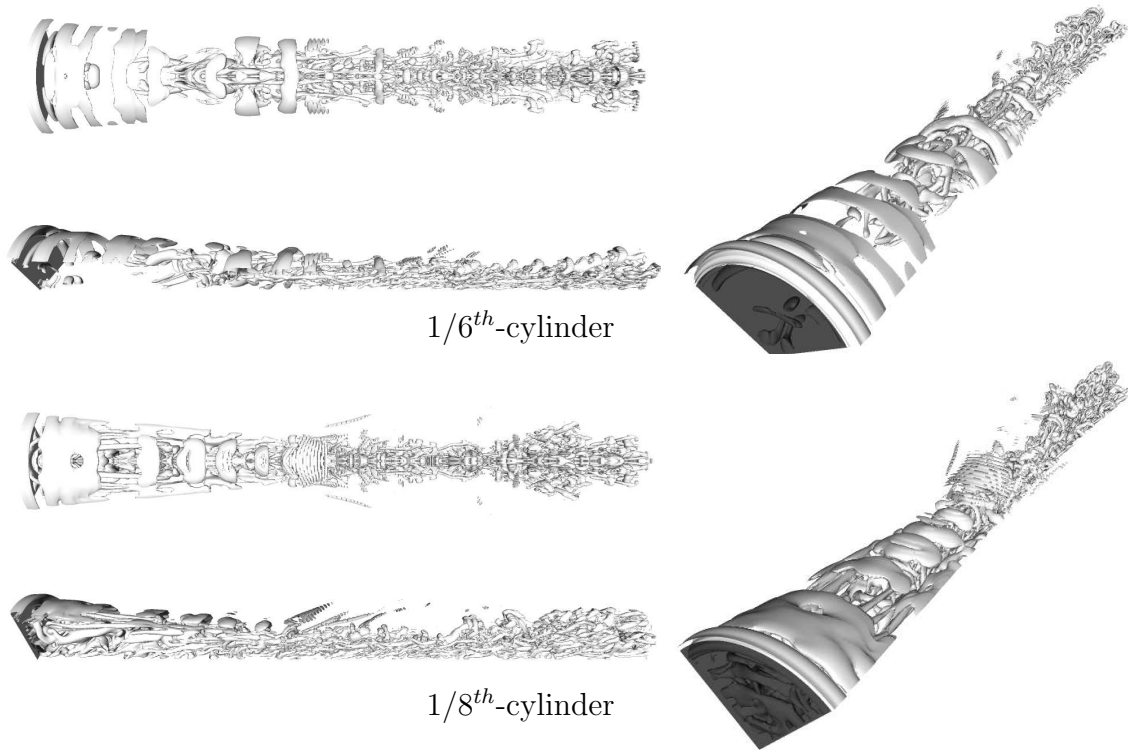


Figure 6.36 Instantaneous iso-contours of $Q = 0.1$; top- and sideviews (left) and perspective view from inflow towards outflow (right); $Re_D = 60,000$, $M = 2.46$.

Several visualizations of iso-contours of $Q = 0.1$ are shown for the $1/6^{th}$ - and the $1/8^{th}$ -cylinder cases in figure 6.36. It can be observed that for both cases, in spite of the considerably reduced azimuthal domain-size, a large amount of structures is present. Even though mode $k = 3$ is contained in the $1/6^{th}$ -cylinder calculation, which was shown to exhibit the (linearly) largest growth rates of all azimuthal modes, the amount of streamwise structures in the recirculation region and hairpin vortices in the trailing wake is decreased. However, in the $1/8^{th}$ -cylinder case, a large amount of longitudinal structures can be detected within the recirculation region, in particular in the inner part of the shear layer. As already suggested when discussing the sideviews of total vorticity (figure 6.32), this implies that mode $k = 4$ is important for the flow currently discussed. Further evidence for the importance of mode $k = 4$ can be found when scrutinizing the visualizations of instantaneous iso-contours of

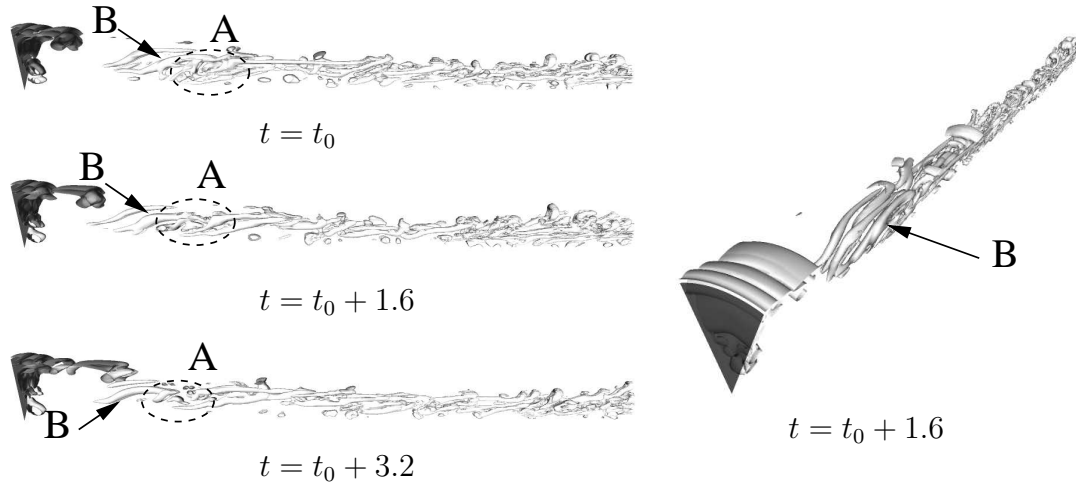


Figure 6.37 Instantaneous iso-contours of $Q = 0.1$ for $1/16^{th}$ -cylinder case; time-sequence of sideviews (left) and perspective view from inflow towards outflow (right); $Re_D = 60,000$, $M = 2.46$.

$Q = 0.1$ for the $1/16^{th}$ -cylinder case in figure 6.37. Here, the exclusion of $k = 4$ leads to a considerably smaller amount of structures. It is, however, interesting to observe the formation of “braids”, denoted with “B”, associated with an axisymmetric, upstream travelling, clockwise rotating roller, marked with “A”. Similar structures were observed in LES of a mixing layer by Lesieur & Metais (1996). This scenario also strongly resembles figure 6.6 in Terzi (2004), where a narrow spanwise domain was chosen for the simulation of a backward facing step at low Mach number. In the present case, the azimuthal extent of the integration domain is comparable in size and the axisymmetric structure occurs in a subsonic region. Therefore, a comparison of the two cases appears to be feasible. Terzi (2004) concluded that the braids possibly form as a consequence of an centrifugal instability of the instantaneous streamlines of the axisymmetric rollers. It could be that this mechanism might also be partly responsible for the generation of the streamwise structures observed in the current case.

In conclusion, helical structures can be detected in the shear layer as for the lower Reynolds number case. However, due to the increased number of unstable modes at

the higher Reynolds number, a considerably larger amount of streamwise structures within the recirculation region can be detected. These structures, in addition to increased growth-rates of instabilities, lead to a greater number of hairpin vortices in the trailing wake. As opposed to the lower Reynolds number case, the $1/8^{th}$ -cylinder calculation displays a large amount of hairpin vortices. As for the lower Reynolds number, it is suggested that a large number of streamwise structures is generated within the recirculation region through the azimuthal modulation of the near-wake due to the presence of global modes. In addition, it is also proposed that axisymmetric rollers within the recirculation region might contribute to the generation of streamwise structures. Further evidence was found that modes $k = 2$ and $k = 4$ are significant for the current flow conditions.

6.2.3 Mean Flow and Turbulent Statistics

Running averages, taken over at least ten flow-through times, were obtained from all calculations in order to evaluate the impact of the most dominant azimuthal Fourier modes on the mean flow. The time-averaged radial profiles of several azimuthal Fourier modes for all three conservative velocity components are shown in figures 6.38 – 6.40. The same characteristic streamwise locations were chosen as in the lower Reynolds number case and the amplitude range was matched to allow for a direct comparison of the amplitudes. In general, it can be observed that the streamwise component is considerably larger than the remaining velocity components. Therefore, the discussion of the radial profiles will focus on the streamwise component. At the location $z = 2.5$ the radial and the azimuthal components possess similar magnitudes. Within the trailing wake, however, the magnitude of the radial component is considerably larger than the azimuthal component.

For the half-cylinder case at $z = 2.5$, the overall values of the first mode are of the same order as those of the dominant modes, in spite of a significantly smaller

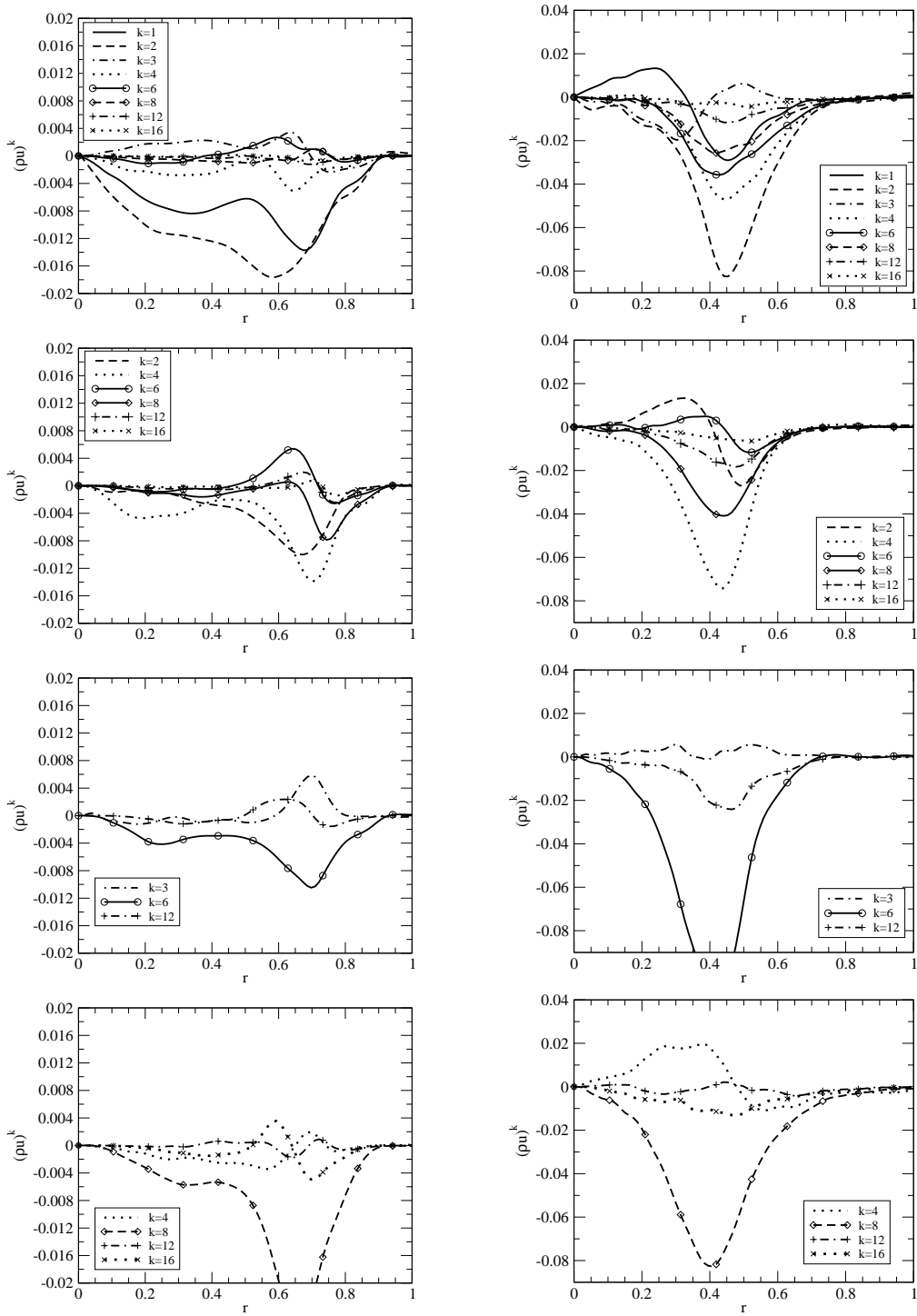


Figure 6.38 Time-averaged radial profiles of azimuthal Fourier modes of (ρu) obtained from DNS for half-, quarter-, 1/6th- and 1/8th-cylinder (from top to bottom); $z = 2.5$ (left), $z = 7$ (right), $Re_D = 60,000$, $M = 2.46$.

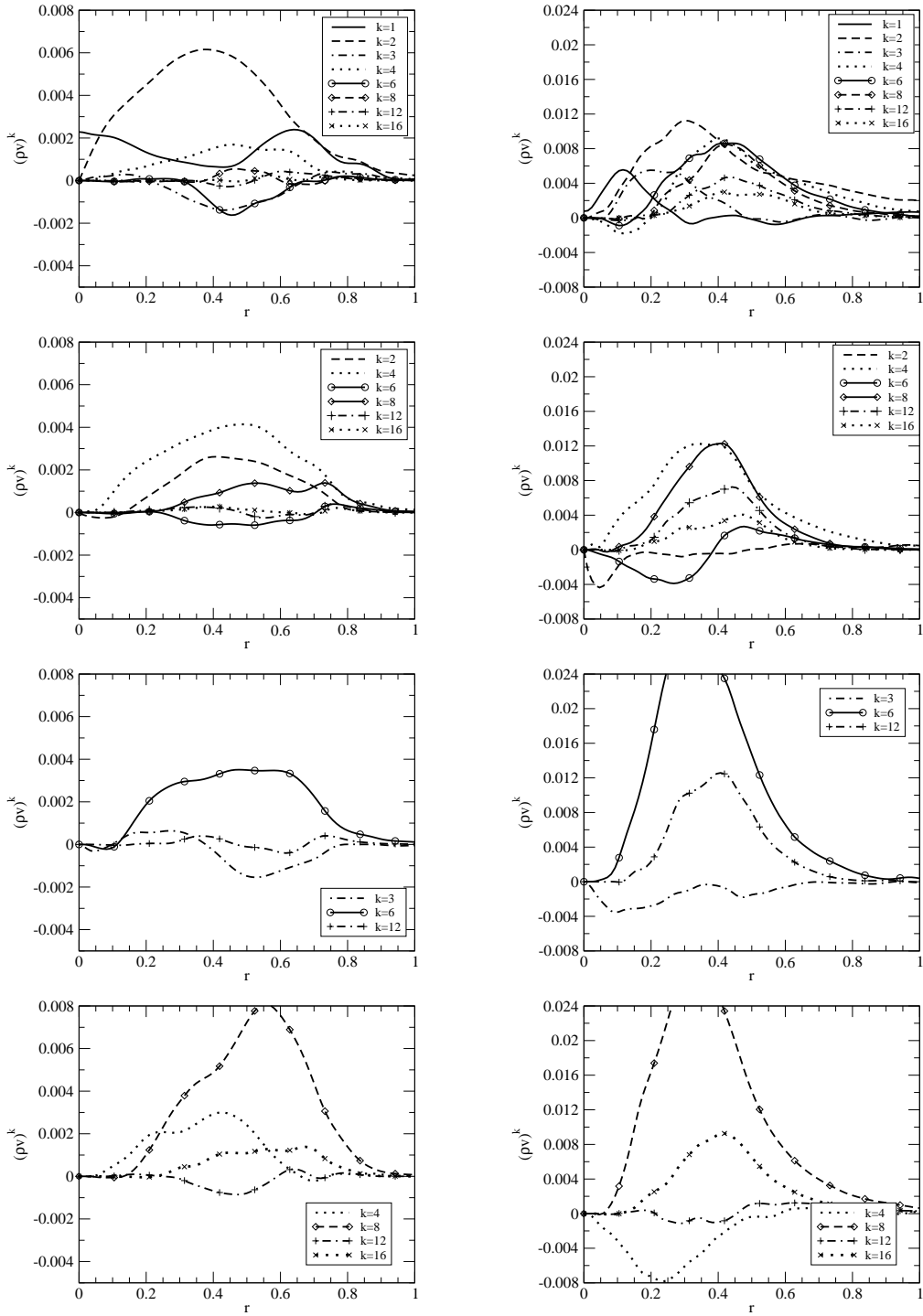


Figure 6.39 Time-averaged radial profiles of azimuthal Fourier modes of (ρv) obtained from DNS for half-, quarter-, 1/6th- and 1/8th-cylinder (from top to bottom); $z = 2.5$ (left), $z = 7$ (right), $Re_D = 60,000$, $M = 2.46$.

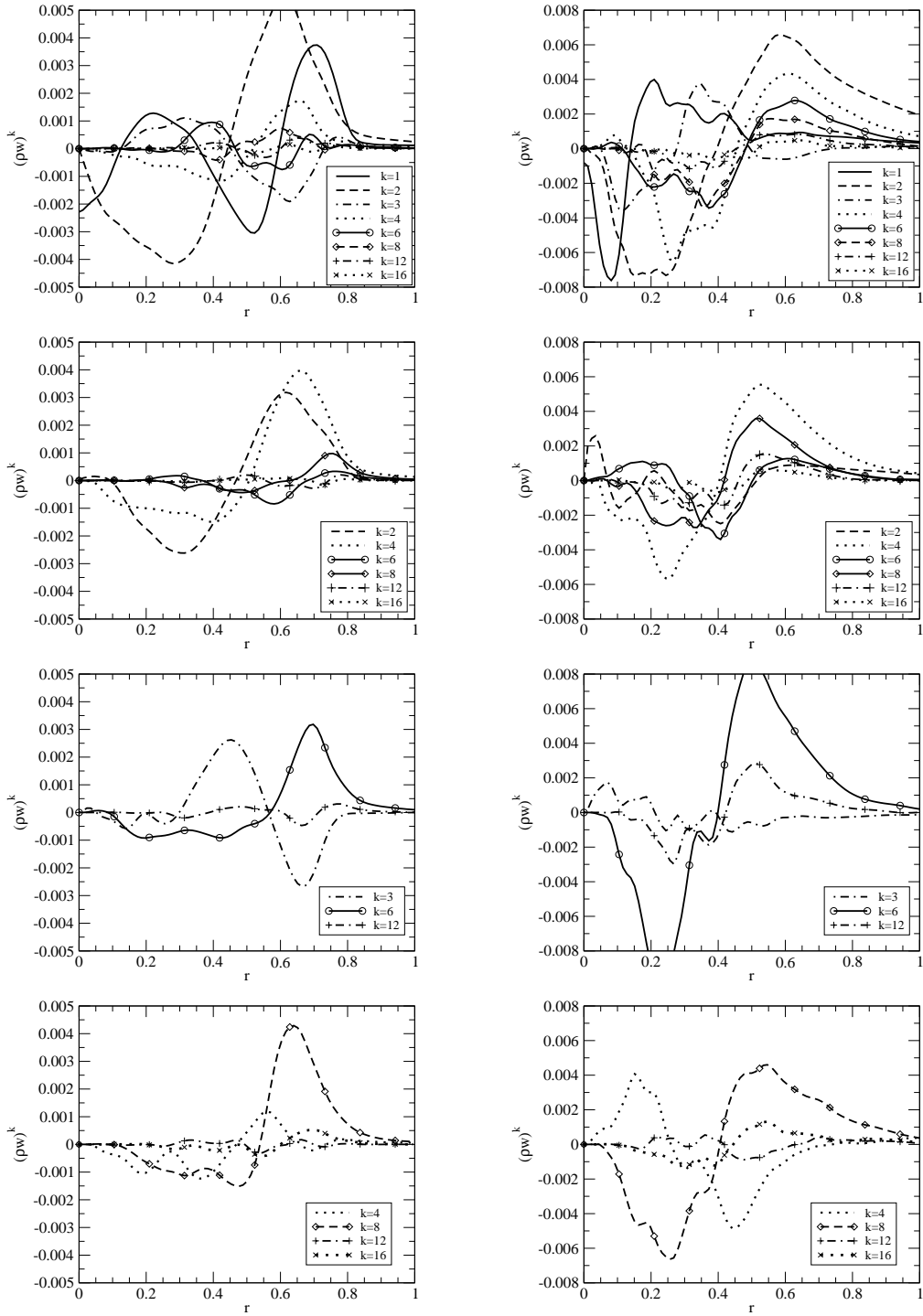


Figure 6.40 Time-averaged radial profiles of azimuthal Fourier modes of (ρw) obtained from DNS for half-, quarter-, $1/6^{th}$ - and $1/8^{th}$ -cylinder (from top to bottom); $z = 2.5$ (left), $z = 7$ (right), $Re_D = 60,000$, $M = 2.46$.

amplification rate observed in the linear calculations. This constitutes additional evidence that the first azimuthal mode might be a subharmonic of the most important higher modes. This is supported by the observation that the mode-shape of $k = 1$ has little in common with the results obtained from linear calculations, i.e., it is likely to mainly be the result of nonlinear interaction with other modes. In fact, the amplitude distribution shows similarities with some of the higher modes. Furthermore, mode $k = 2$ possesses the largest magnitude, even though, in the linear calculations, the largest linear growth was found for $k = 3$ and $k = 4$. The significance of mode $k = 3$ at this streamwise position is strongly decreased, compared to the lower Reynolds number. In contrast to the lower Reynolds number case, none of the azimuthal modes shows strong resemblance with the mode-shapes obtained in the linear calculations. This implies that, even at this upstream location, significant nonlinear interactions with other modes occur. For the downstream location $z = 7$, the nonlinear interaction between the modes is even more pronounced as evidenced by the similarity between the mode-shapes of all modes (top right graphs of figures 6.38 – 6.40). The amplitude distributions resemble those obtained for the lower Reynolds number, with the second mode showing the largest amplitude. Furthermore, large amplitudes are found for modes $k = 2, 4, 6$ and even $k = 5$ and $k = 8$.

When scrutinizing the amplitude distributions for all domain sizes computed, the following observations can be made: The profiles are fairly similar to those found in the lower Reynolds number case, except for the high-amplitude regions which are confined to a smaller radial extent. For all domain sizes, the first higher harmonic of the fundamental wavelength is the most dominant mode, i.e., in the quarter-cylinder case the most dominant mode is $k = 4$, in the $1/6^{th}$ -cylinder case mode $k = 6$, etc. Furthermore, regardless of the wavenumber, the mode-shape of the most dominant mode is always the same and possesses roughly the same amplitude for all domain sizes. The amplitude distributions of modes $k = 4, 6, 8, 12$ remain fairly unchanged for both streamwise locations.

To conclude the discussion of the amplitude distributions, it is found that the first higher harmonic of the fundamental wavelength is the most dominant one, possessing the same mode-shape for all cases. For all domain sizes with $\theta < \pi$, the maxima of the dominant modes are considerably larger than the corresponding maximum amplitudes found for the half-cylinder case. It is supposed that this is due to the fact that the energy that would be distributed among the most important modes in the half-cylinder case now is mostly contained in the dominant mode.

The same two characteristic locations as for the low Reynolds number case are selected to show time-averaged endviews of total vorticity, the streamwise vorticity component and the azimuthal velocity component for all cases. Figure 6.41 shows the endviews for all circumferential domain-sizes at the downstream location $z = 3$ (close to the position for which the radial amplitude distributions were shown in figures 6.38 – 6.40). The endviews of the half-cylinder case confirm the results found in the radial amplitude distributions: In contrast to the lower Reynolds number, mode $k = 3$ is insignificant and the second azimuthal mode dominates the flow at this streamwise location. On the inside of the shear layer, negative streamwise vorticity and positive azimuthal velocity are found in the mean for $0 \leq \theta < \frac{\pi}{2}$. Positive values of streamwise vorticity and negative azimuthal velocity are seen for $\theta > \frac{2\pi}{3}$. The occurrence of the sign-change at $\theta > \frac{\pi}{2}$ supports that $k = 2$ is dominant. The superposition of higher modes with $k = 2$ most likely is the reason for the sign-change not occurring exactly at $\theta = \frac{\pi}{2}$. In the interior of the recirculation region, a noticeable azimuthal variation of regions of positive and negative vorticity is visible, in particular when looking at the streamwise vorticity component. This indicates a significant contribution of higher azimuthal modes.

For all smaller circumferential domain-sizes, two counter-rotating structures appear to be confined within the azimuthal domain boundaries. However, unlike the $Re_D = 30,000$ case, the separation between the structures on the inside of the shear-

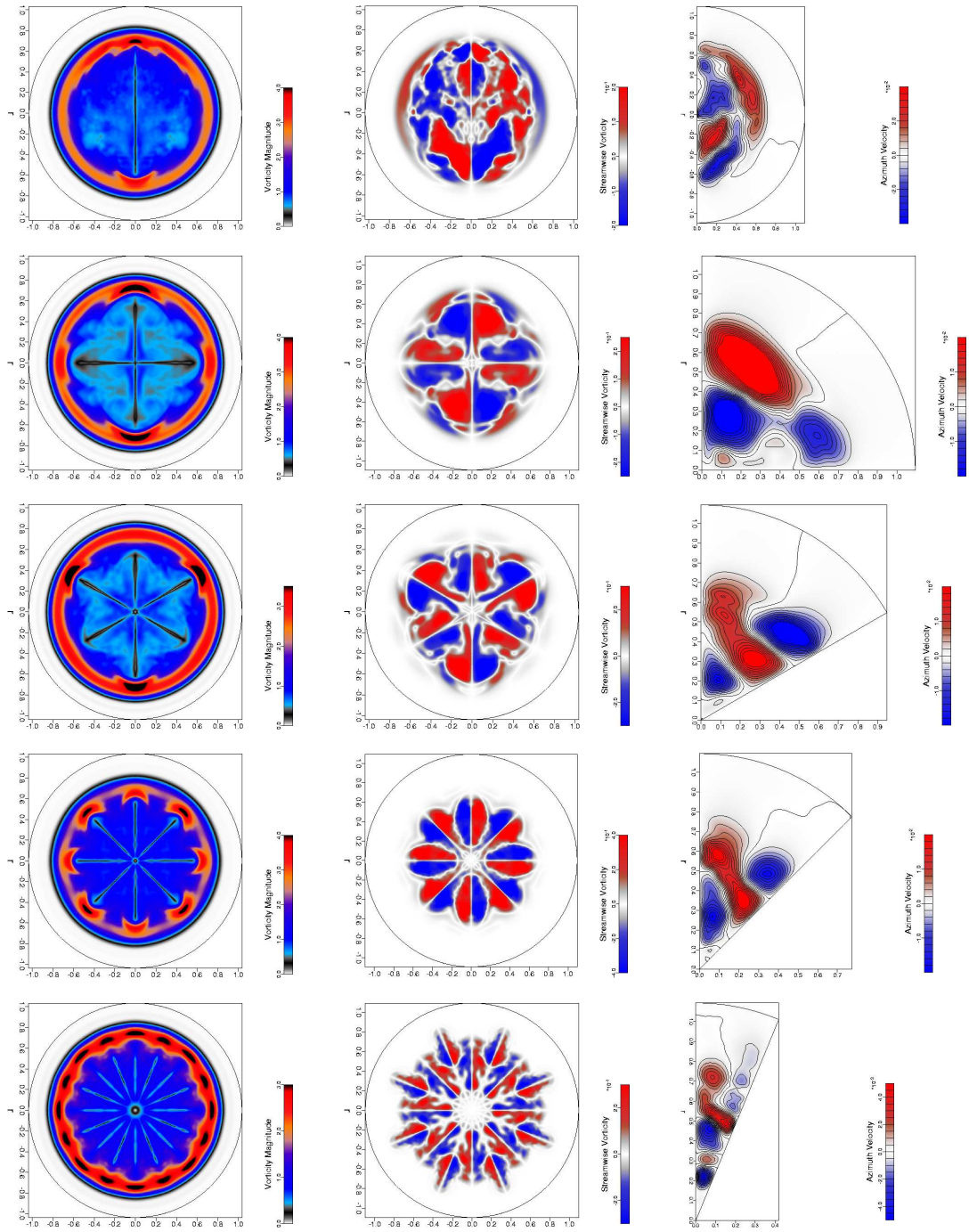


Figure 6.41 Endviews of time-averaged total vorticity (left), streamwise vorticity (center), and azimuthal velocity (right) upstream of the recompression region at $z = 3$ for half-, quarter-, $1/6^{th}$ -, $1/8^{th}$ - and $1/16^{th}$ -cylinder (from top to bottom); $Re_D = 60,000$, $M = 2.46$.

layer and the pair within the recirculation region is not as pronounced. For the $1/6^{th}$ -, $1/8^{th}$ - and $1/16^{th}$ -cylinder cases, the inner and outer regions of positive azimuthal velocity are connected to each other. Furthermore, the amplitude distributions showed that the fundamental azimuthal mode for each domain size plays a significantly larger role than in the lower Reynolds number case. These modes appear to be non-oscillatory, evidenced by the fact that the “ k -lobe” wake patterns possess n dominant “lobes”, where k is the first higher harmonic and n is the fundamental azimuthal wavelength of the respective calculation.

To adjust for the difference in mean recirculation length, the locations selected downstream of the recompression region are $z = 7$ for the four largest domain sizes and $z = 9$ for the smallest case, depicted in figure 6.42. For all cases, the streamwise vorticity component does not change versus the location at $z = 3$, suggesting that the longitudinal structures present in the mean persist throughout the recompression region. In the half-cylinder case, it is evident that the wake pattern is the result of a superposition of several dominant modes. Looking at the visualization of total vorticity and recalling the data presented in the radial amplitude distributions of the azimuthal modes, the wake-structure is most likely composed of non-oscillatory (in time) modes $k = 2, 4, 5, 6$ and $k = 8$. The largest extent of the wake is in the $\theta = 0$ and $\theta = \pi$ directions, for the same reasons as stated for the lower Reynolds number case. For the quarter-cylinder case, also considering the amplitude distribution presented in figures 6.38–6.40, the wake pattern most likely is composed of steady contributions of modes $k = 4$ and $k = 8$, leading to an “eight-lobe” structure. Because the mode $k = 4$ is dominant for this case, every second “lobe” is more significant, which can be seen particularly well in the visualization of the streamwise vorticity component.

In order to assess the effect of the most dominant structures on the mean flow, the time-averaged streamwise velocity along the axis and the pressure coefficient along the base are compared for all cases in figure 6.43. In the half-cylinder case, the energetic large structures reduce the recirculation length by 24.4% compared to the

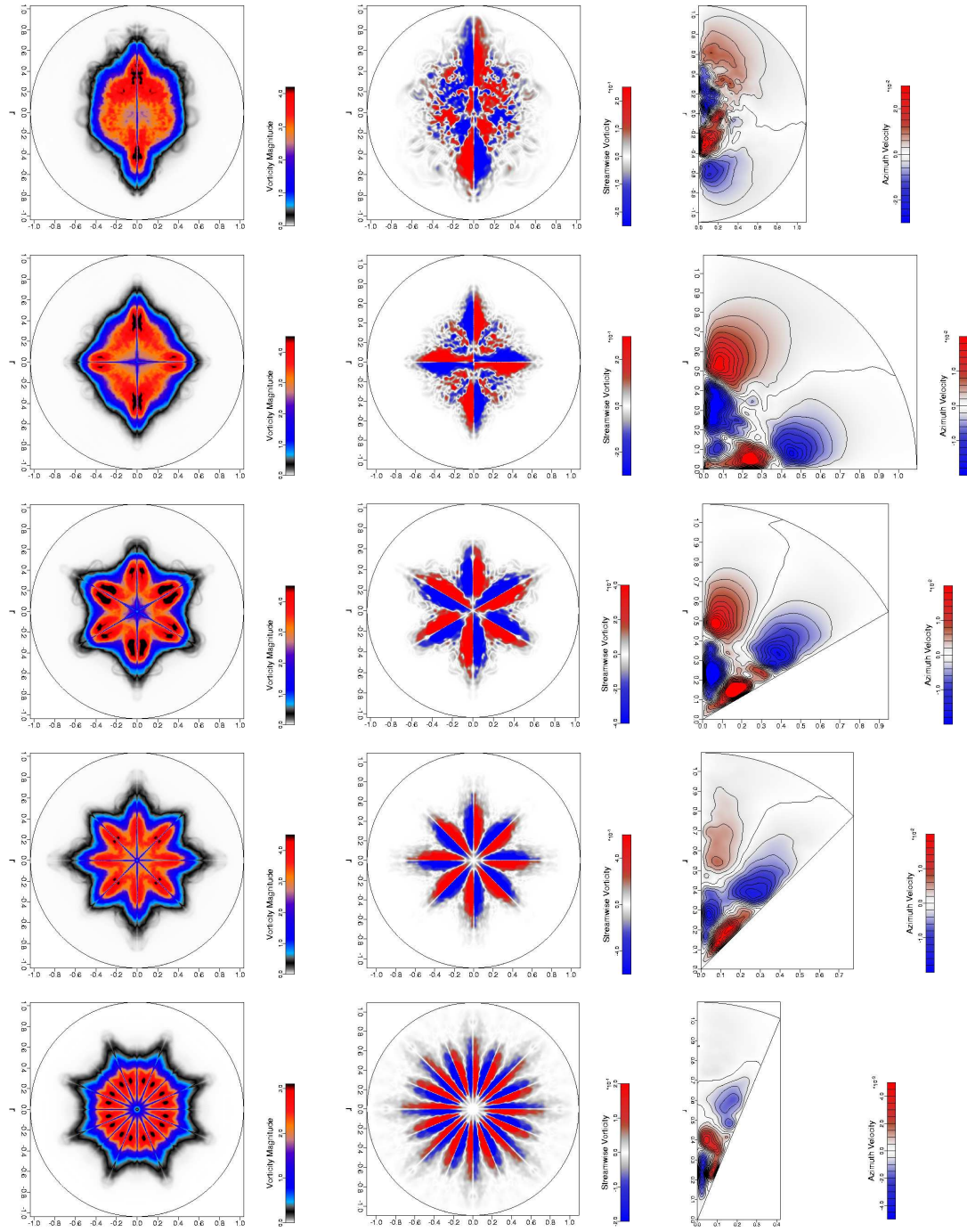


Figure 6.42 Endviews of time-averaged total vorticity (left), streamwise vorticity (center), and azimuthal velocity (right) downstream of the recompression region at $z = 7$ for half-, quarter-, $1/6^{th}$ -, and $z = 9$ for $1/8^{th}$ - and $1/16^{th}$ -cylinder (from top to bottom); $Re_D = 60,000$, $M = 2.46$.

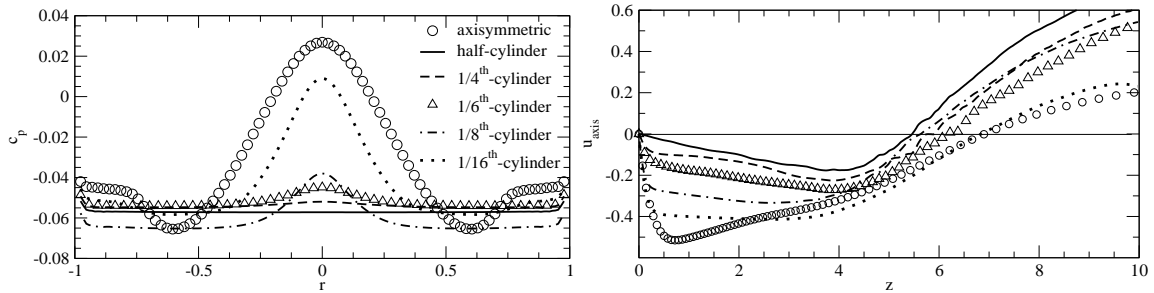


Figure 6.43 Time-averaged pressure coefficient (left) and streamwise axis-velocity (right) for all circumferential domain-sizes; $Re_D = 60,000$, $M = 2.46$.

axisymmetric calculation, i.e., the mean reattachment point moves from $z = 6.9$ to $z = 5.2$. Note that the reduction of the recirculation length amounted to only 13.2% in the lower Reynolds number case. The pressure distribution along the base is entirely flat, albeit the mean value is slightly decreased compared to the lower Reynolds number case. As the contribution of the higher azimuthal modes has increased for the present case, it can be concluded that helical modes are indeed responsible for decreasing the base-pressure, and thus, increasing the base-drag. The data from the quarter-cylinder case is very close to that of the half-cylinder case. Only a minimal radial variation of base-pressure can be observed. This implies that the effect of mode $k = 1$ on the mean flow becomes less significant as the Reynolds number is increased. The base-pressure profile obtained from the 1/6th-cylinder calculation only shows a marginal peak at the axis. However, the recirculation length is longer than for both the quarter-cylinder and the 1/8th-cylinder calculations, reconfirming that the structures generated by $k = 2$ and $k = 4$ are most energetic, entraining a large amount of fluid from the recirculations region and thereby shortening the separation bubble. The streamwise velocity along the axis obtained from the 1/8th-cylinder case nearly coincides with that of the quarter-cylinder case for $z > 5$. However, in the recirculation region, the magnitude of the reverse flow is significantly higher. Compared to the lower Reynolds number case, the base-pressure profile of the 1/8th-cylinder case is

fairly flat. Only the result from the smallest domain size exhibits a very pronounced peak, approaching the solution of the axisymmetric calculation. The behavior observed here is in line with the findings for the lower Reynolds number case, namely that modes with large wavelengths are mainly responsible for producing an entirely flat pressure distribution on the base.

Sideviews of the averaged turbulent kinetic energy, K , the turbulent dissipation rate, ε , and two Reynolds-stress components, $\overline{u'_i u'_j}$, are shown in figure 6.44 for data obtained from the half-cylinder calculation. The results are similar to the lower Reynolds number case, i.e., the main contribution of the turbulent quantities occurs in the inner shear-layer and the recompression region. However, significant fluctuations already appear roughly 1.5 radii downstream of the base due to the accelerated transition at the higher Reynolds number. In addition, the overall magnitudes of the turbulent quantities are considerably increased compared to the $Re_D = 30,000$ case. From figure 6.44, it can also be extracted that all turbulent quantities reach their maximum values downstream of the mean reattachment point. Only the Reynolds shear-stress appears to exhibit its global maximum upstream of the recompression region, due to the decreasing mean shear-layer gradient. Endviews were also scrutinized (not shown here) and displayed a strong azimuthal variation of all turbulent

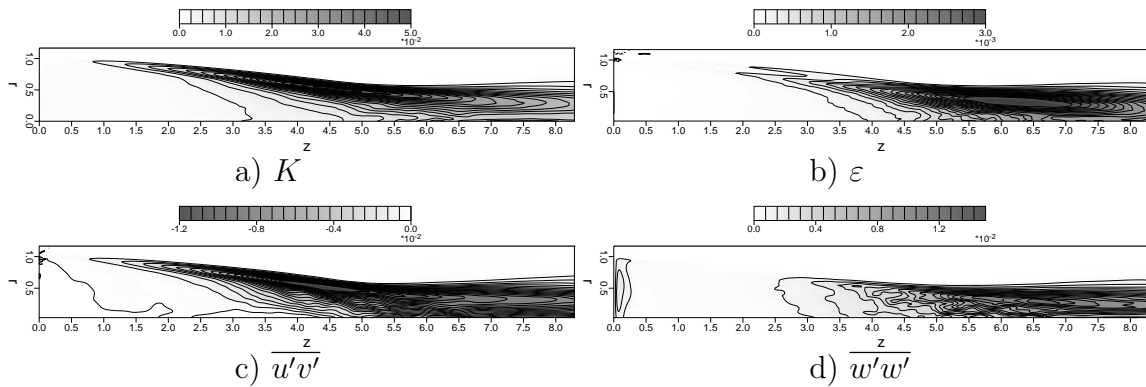


Figure 6.44 Azimuthal average of turbulent statistics; sideviews for half-cylinder case; $Re_D = 60,000$, $M = 2.46$.

quantities. This confirms that a three-dimensional solver for turbulent transport equations is required for calculations employing turbulence models in the present research. The distribution of the turbulent dissipation rate, ε , was used to estimate the Kolmogorov length-scale, in order to verify that the resolution of the DNS was adequate. The largest value of ε was found to be $\sim 3 \cdot 10^3$, resulting in $L_K \sim 2 \cdot 10^3$. At this maximum location, the numerical grid-resolution in the radial direction was $\Delta r = 0.01 = \mathcal{O}(L_K)$, $\Delta z = 0.022 = \mathcal{O}(10 \cdot L_K)$ and $r\Delta\theta = 0.4 \cdot \frac{\pi}{256} = 0.0049 = \mathcal{O}(L_K)$. Thus, the numerical resolution in the radial and the azimuthal direction are on the order of the Kolmogorov length-scale. As for the lower Reynolds number case, the grid-resolution in the streamwise direction is at the lower limit of what is considered adequate for resolving the relevant length-scales. Nevertheless, the grid-spacing becomes finer when approaching the base. Therefore, the spatial resolution is considered to be sufficient. The temporal resolution of the simulations was already determined to be adequate in section 6.2.1.

To summarize, further evidence was gathered suggesting that modes $k = 2$ and $k = 4$ are the dominant modes at $Re_D = 60,000$. However, the mean wake pattern observed in the half-cylinder case cannot be attributed to a single dominant mode, but rather is a result of the superposition of several higher azimuthal modes. By reducing the circumferential extent of the integration domain and, thereby, excluding azimuthal modes, the importance of modes $k = 2, 4$ could be verified. For all smaller domain sizes, it was found that the first higher harmonic of the fundamental wavelength is the most dominant mode, possessing a similar amplitude and mode-shape. Sideviews of several turbulent quantities reveal that the turbulence level is considerably increased over the lower Reynolds number case. The Kolmogorov length-scale was estimated and it was verified that the grid resolution of the DNS was sufficient to resolve all relevant scales.

6.2.4 Summary

DNS of supersonic axisymmetric wakes at $Re_D = 60,000$ and $M = 2.46$ were conducted for various circumferential domain-sizes. All cases with a circumferential domain-size larger than $0 \leq \theta < \pi/8$ fully transition to turbulence downstream of the recompression region and do not exhibit intermittency. As opposed to the lower Reynolds number case, a considerable amount of energy can be found in frequencies with $St_D \geq 1$ while maxima for lower azimuthal modes at low frequencies attest the presence of large-scale structures in the flow. As for the lower Reynolds number case, helical structures can be detected in the shear layer. However, both the increased amount of unstable modes and larger growth-rates result in a greater number of streamwise structures within the recirculation region and hairpin vortices in the trailing wake. In addition to the mechanisms identified for the lower Reynolds number, it is also suggested that axisymmetric rollers within the recirculation region might contribute to the generation of streamwise structures.

Overall, it was found that $k = 2$ and $k = 4$ are the most important modes for the half-cylinder case. This was verified by conducting simulations of domains with smaller circumferential extents, thus excluding various azimuthal modes. The mean wake pattern observed in the half-cylinder case appears to be composed of a superposition of multiple azimuthal modes. Similar to the $Re_D = 30,000$ case, for all smaller domain sizes, the first higher harmonic of the fundamental wavelength is the most dominant mode. Finally, the magnitudes of the turbulent quantities were found to be considerably increased over the lower Reynolds number case.

6.3 DNS for $Re_D = 100,000$

Calculations for several azimuthal domain sizes were performed for an additional Reynolds number: $Re_D = 100,000$. This was the highest Reynolds number feasible using DNS with the resources that were available for the present work. DNS of a half-cylinder, a quarter-cylinder, $1/8^{th}$ and $1/16^{th}$ of a cylinder were conducted. For the lower Reynolds numbers, the $1/16^{th}$ -cylinder case did not exhibit any significant deviation from the axisymmetric solution in the mean. However, at $Re_D = 100,000$, the flow fully transitioned to turbulence for the $1/16^{th}$ -cylinder case and the mean flow was altered significantly versus the axisymmetric solution. For that reason, a calculation with a domain size further reduced to a $1/32^{nd}$ -cylinder was conducted. All calculations were performed on the same streamwise/radial grid with 1272×160 points in the streamwise and the radial direction, respectively. The smallest grid-spacing at the corner was $\Delta z_c = \Delta r_c = 0.008$. In the azimuthal direction, the simulation of the half-cylinder was conducted with 128 symmetric spectral modes, for the cases with smaller circumferential extents, 64, 32, 24 and 16 Fourier modes were used. All further parameters are compiled in table D.7 in Appendix D.

6.3.1 Time-Dependent Results

Sideviews of instantaneous total vorticity are shown for several cases in figures 6.45 (a) to (d). In contrast to the lower Reynolds numbers, all cases, including the $1/16^{th}$ -cylinder case, exhibit a broad range of length-scales. In the half-cylinder case, the flow appears to transition to turbulence considerably farther upstream than at lower Reynolds numbers. This is attested by the occurrence of small-scale structures in the inner part of the shear layer at $z \approx 2$. The sideviews of computations with a smaller domain size reveal that the transition to turbulence is delayed, with small-scale structures appearing at $z \approx 3.5$. This implies that the first mode $k = 1$, which is eliminated in all calculations with $0 \leq \theta < \pi$, plays a significant role within the

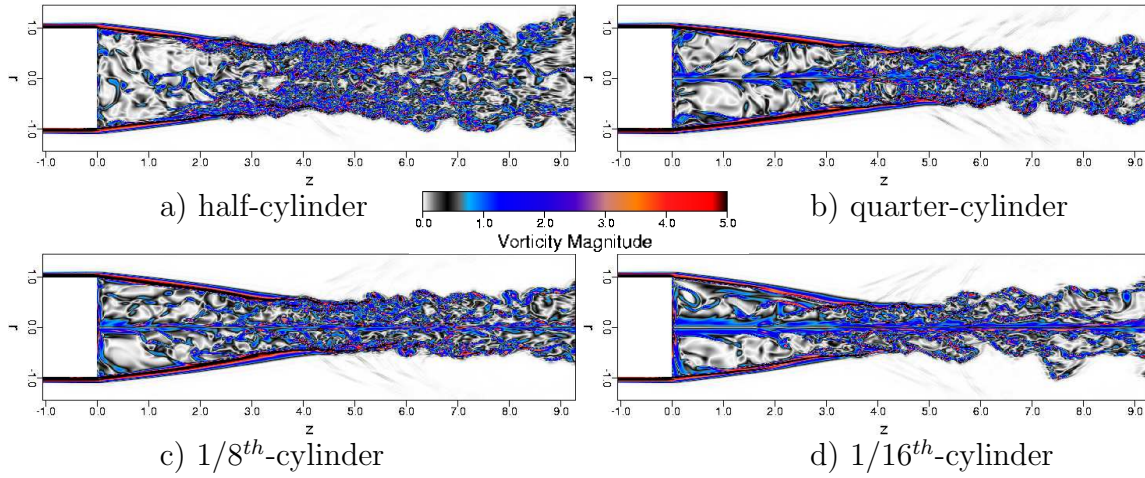


Figure 6.45 Sideviews of contours of instantaneous total vorticity; top half $\theta = 0^\circ$, bottom half a) $\theta = 180^\circ$, b) $\theta = 90^\circ$, c) $\theta = 45^\circ$ and d) $\theta = 22.5^\circ$; $Re_D = 100,000$, $M = 2.46$.

recirculation region. The fact that the $1/16^{th}$ -cylinder case exhibits a broad range of length-scales indicates that mode $k = 8$ reaches sufficiently large amplitudes which permit additional instabilities to arise.

For all circumferential domain-sizes, exponential growth of the azimuthal Fourier modes was observed until a nonlinear saturation state was reached. This implies that the flow is absolutely unstable with respect to azimuthal modes for all circumferential domain-sizes investigated, i.e., for the azimuthal modes $k \leq 8$.

The temporal development of the Fourier modes of density in a region of high activity, at $z = 8.27$ and $r = 0.3362$, is shown in figures 6.46 (a) to (d). At this Reynolds number, the decay in energy over the azimuthal modes amounts to approximately three orders of magnitude, indicating that a broad range of length-scales is present.

For all cases shown, no intermittency can be observed. Note, that only an interval of 8 time-units is shown, in contrast to 60 and 10 time-units for the $Re_D = 30,000$ and $Re_D = 60,000$ cases, respectively. The high-frequency fluctuations within this short time-interval attests that the range of time-scales has increased as well. As

mentioned before, the $1/16^{th}$ -cylinder case looks very similar to the larger azimuthal domain sizes, as opposed to lower Reynolds numbers, where the smallest domain sizes showed strong intermittency and hardly any high-frequency oscillations. Here, significant temporal variations of the azimuthal mean $k = 0$ at the probe point can be observed, indicating that the amplitudes of the azimuthal modes are sufficiently large to cause considerable nonlinear interaction with the zeroth mode. Because 24 Fourier modes were used for the $1/16^{th}$ -cylinder, the highest mode corresponds to $k = 192$ and is included in figure 6.46 (d).

The $1/32^{nd}$ -cylinder was simulated using 16 Fourier modes. This corresponds to 256 azimuthal modes in the half-cylinder case. The data obtained from this calculation indicates that the azimuthal modes do not reach large enough amplitudes to alter the mean flow. Thus, for the smallest domain size, the flow remains axisymmetric, implying that the circumferential extent of the domain is close to the short-wave cutoff for the helical instabilities. Recalling that this behavior was observed for the $1/16^{th}$ -cylinder case at $Re_D = 30,000$ confirms that a viscous cutoff is responsible for

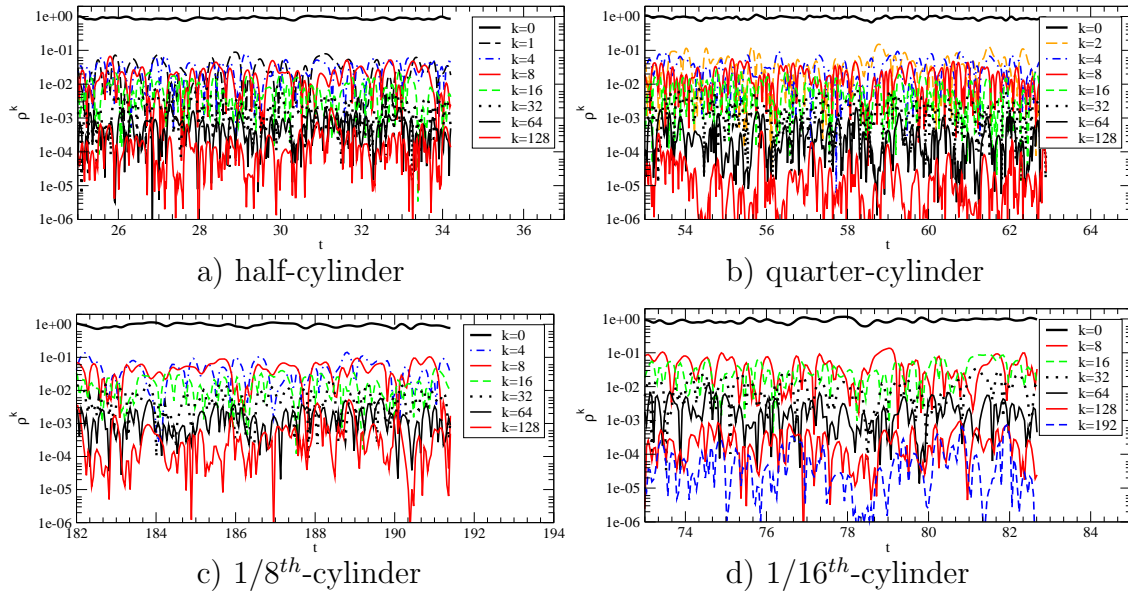


Figure 6.46 Temporal development of Fourier modes of ρ in a region of high activity; $z = 8.27$, $r = 0.336$, $Re_D = 100,000$, $M = 2.46$.

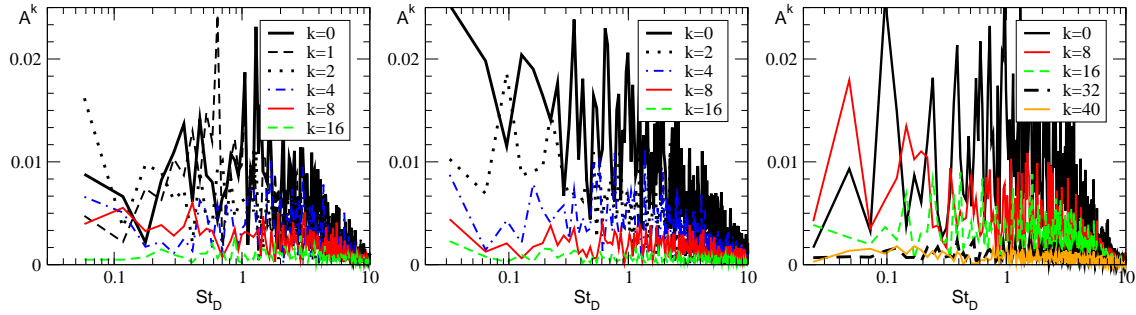


Figure 6.47 Fourier decomposition in time of Fourier modes of ρ in a region of high activity, half-cylinder, quarter-cylinder and $1/16^{th}$ -cylinder from left to right; $z = 7.85$, $r = 0.465$, $Re_D = 100,000$, $M = 2.46$.

the flow becoming stable with respect to three-dimensional instabilities for sufficiently small azimuthal domain-sizes.

The Fourier-decompositions of the time signal for three cases are shown in figure 6.47. As for the $Re_D = 60,000$ case, it is evident that a significant amount of energy is contained in frequencies with $St_D \geq 1$, even for the $1/16^{th}$ -cylinder case. The temporal resolution appears to be sufficient for these cases, as exponential decay is observed towards higher St_D . For the half-cylinder case, mode $k = 1$ shows a local maximum, at a slightly higher Strouhal number ($St_D = 0.19$) than for the $Re_D = 60,000$ case. A prominent peak in the first mode, however, can be found at a noticeably higher Strouhal number of 0.62. Structures with this frequency seem to have a great effect on the azimuthal mean flow, evidenced by the peak of $k = 0$ at twice the frequency, $St_D = 1.24$. In addition, mode $k = 4$ displays multiple peaks in both the high- and low-frequency range. For the quarter-cylinder case, mode $k = 2$ exhibits the largest amplitudes in the lower frequency range, showing peaks at $St_D = 0.1$ and $St_D = 0.21$. Nevertheless, mode $k = 4$ appears to have the largest impact on the azimuthal mean, as the peak at $St_D = 0.16$ nonlinearly creates spikes in mode $k = 0$ at $St_D = 0.32$ and $St_D = 0.64$. For larger Strouhal numbers, it is

not clear whether $k = 2$ or $k = 4$ is the dominant higher mode. The $1/8^{th}$ -cylinder case (not shown here) is dominated by modes $k = 4$ and $k = 8$ which exhibit strong peaks at frequencies as high as $St_D = 2$ with significant nonlinear effects on the azimuthal mean. In contrast to the lower Reynolds number cases, the $1/16^{th}$ -cylinder data displays a broader range of frequencies for modes $k = 0$, $k = 8$ and $k = 16$. The most pronounced peak for $k = 8$ is found at $St_D = 0.05$, creating the largest amplitudes in $k = 0$ at twice the frequency ($St_D = 0.1$).

In summary, at $Re_D = 100,000$, the flow fully transitions to turbulence for all circumferential domain-sizes, except the $1/32^{nd}$ -cylinder, and does not display intermittency. A large amount of energy is contained in the high-frequency range, with the temporal spectra indicating that modes $k = 2$ and $k = 4$ are dominant.

6.3.2 Coherent Structures

Instantaneous streamwise density gradients are shown in figure 6.48. To illustrate the topology of the flow field, figure 6.48 shows streamwise density gradients. Displaying density gradients is similar to using a Schlieren technique with the light source

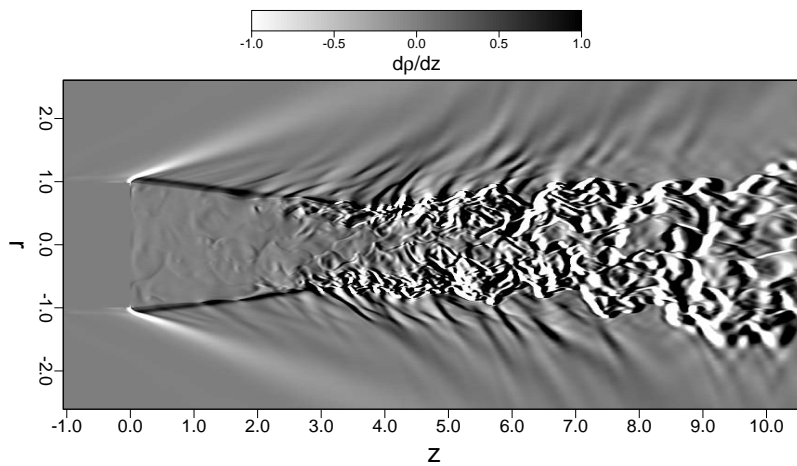


Figure 6.48 Instantaneous streamwise density gradient; $Re_D = 100,000$, $M = 2.46$.

upstream of the body. The most prominent features of the flow are visible: The expansion fan emanating from the base corner, the recompression shock system realigning the shear layer with the axis and, most importantly, the occurrence of large, coherent structures. First large-scale structures are visible at approximately 1 radius downstream of the base, evidenced by shocklets. A broad range of large- and small-scale structures can be observed, causing a significantly decreased recirculation length, as will be shown when discussing mean flow results in section 6.3.3.

With the flow transitioning rapidly after separation and displaying a broad range of length- and time-scales, a comparison to the (higher Reynolds number) UIUC case is attempted. In the experiments, the identification of coherent structures was achieved through a Mie-scattering technique. Bourdon & Dutton (1998) exploited the fact that ethanol vapor, that is carried in the supply air, condenses at flow speeds close to sonic conditions. The condensing vapor was illuminated with planar laser-sheets and high-speed snapshots were taken to obtain instantaneous visualizations of large-scale structures. In order to compare data obtained from DNS with the experimental data, contours of instantaneous local Mach number were chosen for visualization and the color map was adjusted such that the resulting picture resembles the figures presented by Bourdon & Dutton (1998). Endviews of DNS data are shown in figure 6.49 for streamwise positions that correspond to locations “C”, “D” and “E” in Bourdon & Dutton (1998), and are compared to the figures obtained from the experiments.

At the location upstream of mean reattachment, $z = 3.5$, mushroom-like structures can be detected within the inside of the shear layer. These structures strongly resemble those visualized in the experiments at a comparable location (“C”) and indicate the existence of streamwise vortices within the shear layer. Over a longer time-interval, approximately 12–14 mushroom-like structures could be observed instantaneously, in good agreement with the typical number of 10–14 observed in the

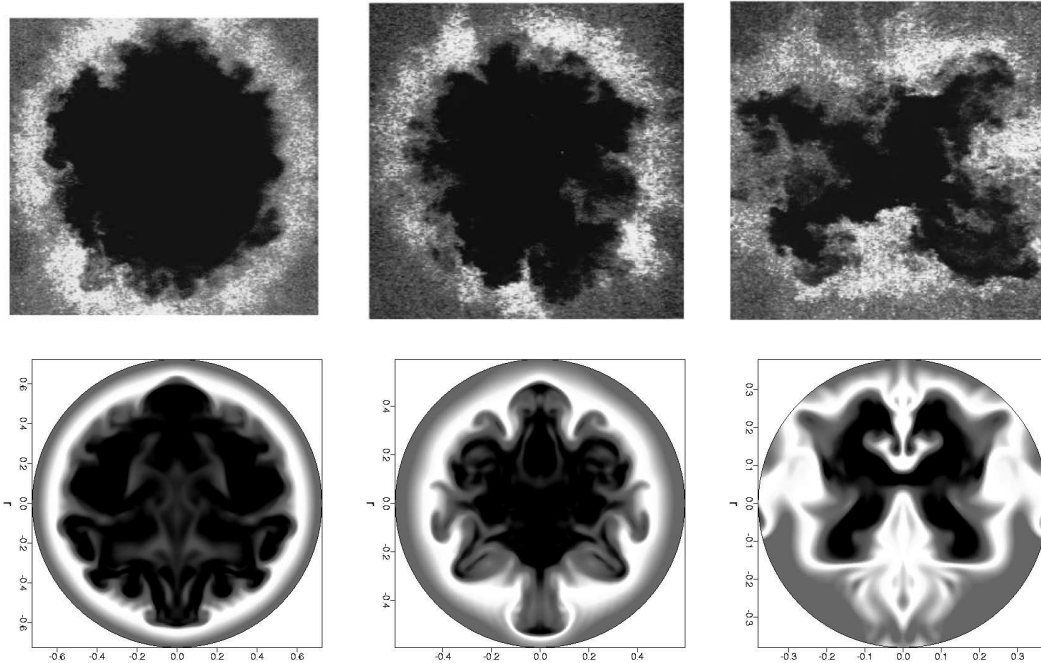


Figure 6.49 Endviews of contours of instantaneous local Mach number; $Re_D = 100,000$, $M = 2.46$ (bottom), compared with visualizations from experiment by Bourdon & Dutton (1998); $Re_D = 3,300,000$, $M = 2.46$ (top); locations “C”, “D” and “E” are shown from left to right.

experiment. The streamwise location $z = 4.0$ is within the recompression region and corresponds to position “D” in the experiments. Here, the number of instantaneous mushroom-shaped structures has reduced to roughly 8–10 structures, comparable with the number of vortices observed at UIUC. This indicates that the streamwise structures undergo an amalgamation in the streamwise direction which intuitively seems inevitable in light of the lateral convergence of the shear layer. In the developing wake, at $z = 6.5$ (corresponding to location “E” in the experiments), only four structures are visible for some instances, as was also the case in the experiments. The four-lobe structure observed in the developing wake is a further indication that modes $k = 2$ and $k = 4$ might be the dominant modes. The off-center location of the wake is a further indication of the flapping motion, most likely caused by mode $k = 1$. Due to the strong similarities between the DNS results and the experimental data,

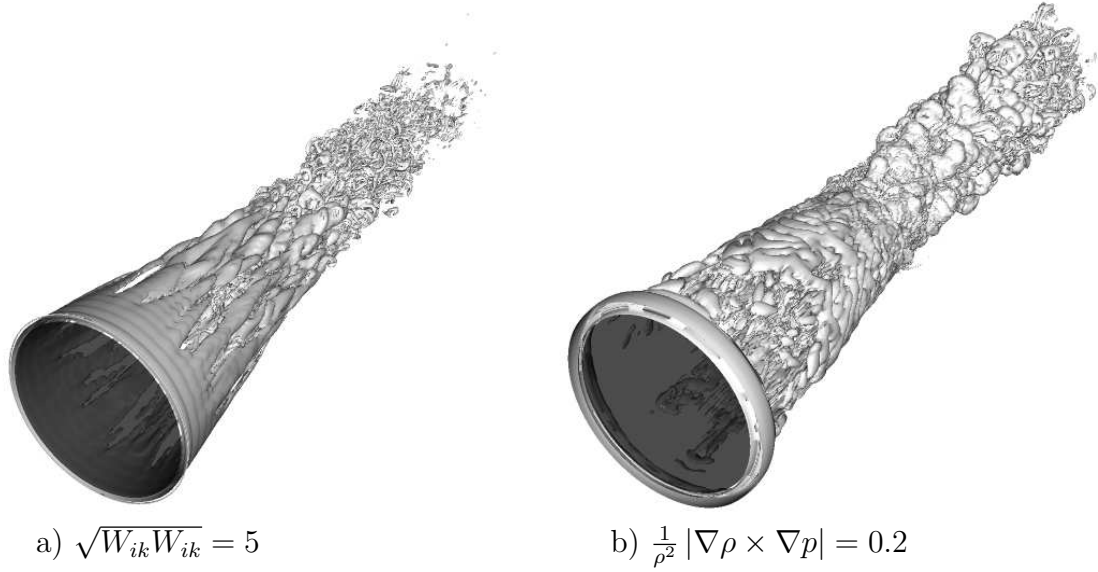


Figure 6.50 Instantaneous perspective views for half-cylinder case; $Re_D = 100,000$, $M = 2.46$.

it is conjectured that the same instability mechanisms are present. It is therefore proposed that modes $k = 2$ and $k = 4$ might also be dominant in the high Reynolds number case investigated at UIUC.

For the purpose of obtaining a more detailed picture of the flow-field, visualizations of iso-surfaces of the total vorticity $\sqrt{W_{ik}W_{ik}}$ and the magnitude of baroclinic torque ($\frac{1}{\rho^2} |\nabla \rho \times \nabla p|$) are shown in figure 6.50. The visualization of $\sqrt{W_{ik}W_{ik}} = 5$ confirms the presence of streamwise vortices within the shear layer, which are responsible for the mushroom-shaped structures observed in the endviews. Note, that these vortices were *not* introduced with forcing as in the cases presented in section 6.1.5, but occur naturally. This is an indication that in this region, modes with high wavenumbers reach large amplitudes. It appears that the streamwise structures do not persist throughout the recompression region. Instead, they seem to break up, forming a considerable number of hairpin vortices downstream of the recompression region. Nevertheless, this does not exclude the occurrence of a four-lobe wake struc-

ture, as seen in the endviews above. The small-scale structures merely cause an additional modulation of the lobes. When scrutinizing the visualization of the magnitude of baroclinic torque, it can be observed that a significant amount of vorticity generation occurs in the shear layer. Just downstream of separation, it appears as if “patches” with a regular azimuthal spacing are present. These might be responsible for the generation of the longitudinal vortices visible in contours of total vorticity. Upstream of the recompression region, it seems as if mainly the axisymmetric vorticity component is produced by the baroclinic torque mechanism, albeit experiencing a strong circumferential variation. In the trailing wake, a large amount of hairpin vortices can be observed. The above results lead to the conclusion that the visualization of the magnitude of baroclinic torque is another viable diagnostic tool for identifying coherent structures (c.f. Terzi, Sandberg & Fasel, 2006).

The visualization of contours of $Q = 0.1$, shown in figure 6.51, reveals several additional features of the flow. First, helical structures are present in the shear layer. These structures possess a considerably smaller streamwise extent and exhibit an azimuthal modulation with a considerably higher wavenumber than in the lower

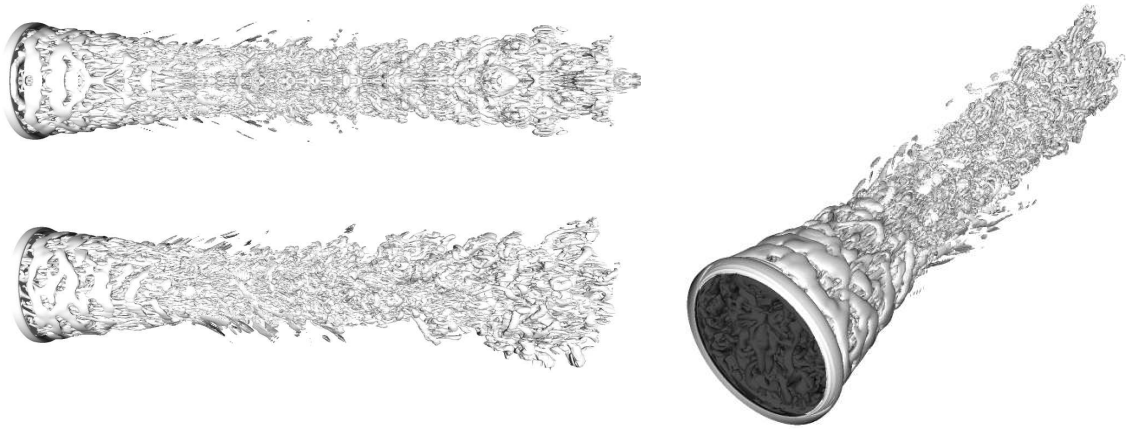


Figure 6.51 Instantaneous iso-contours of $Q = 0.1$ for half-cylinder case, topview and sideview (left) and perspective view from inflow towards outflow (right); $Re_D = 100,000$, $M = 2.46$.

Reynolds number cases. This is consistent with the observation of the streamwise vortices, which constitute evidence for the presence of high-amplitude short wavelength modes. Furthermore, the helical structures can only be observed in the initial part of the shear layer. Farther downstream, the increased growth rate of further instabilities causes the structures to break down to smaller scales. In a time-series (not shown here), it was observed that the helical structures slowly travel downstream. Second, the sideview reveals that a noticeable flapping of the wake occurs, implying that mode $k = 1$ is a significant contributor to the overall solution. Third, a great amount of streamwise structures within the recirculation region can be observed, featuring a considerably decreased diameter when compared to the lower Reynolds number cases. The visualizations for the quarter- and $1/8^{th}$ -cylinder cases are not presented at this point, as they did not reveal any additional information.

However, a time-sequence for the $1/16^{th}$ -cylinder case is shown in figure 6.52 to support the hypothesis proposed in section 6.2.2: Longitudinal structures within the recirculation region, or braids, might possibly be a consequence of centrifugal instabilities that arise in the presence of strong instantaneous streamline curvature. In general, it can be observed that, in spite of the narrow domain, a large number of hairpin structures can be observed in the trailing wake. For better visibility, an enlargement of the recirculation region is shown for the time-series. A pair of axisymmetric rollers, that are composed of several smaller-scale structures, are present in the recirculation region at $t = t_0$ and are denoted by “A” and “B”. A streamwise structure (“C”) is most likely formed as a consequence of a centrifugal instability, caused by strong instantaneous streamline curvature. Furthermore, an axisymmetric structure, denoted by “D” is positioned close to the axis, roughly one radius downstream of the base. At the next time-step, the two clockwise rotating rollers are located farther upstream, with C following their motion. In the following time-instant, it can be observed that D is deflected off the base in the radial direction towards the shear layer. The lack of azimuthal variation of D indicates that an axisymmetric stagnation

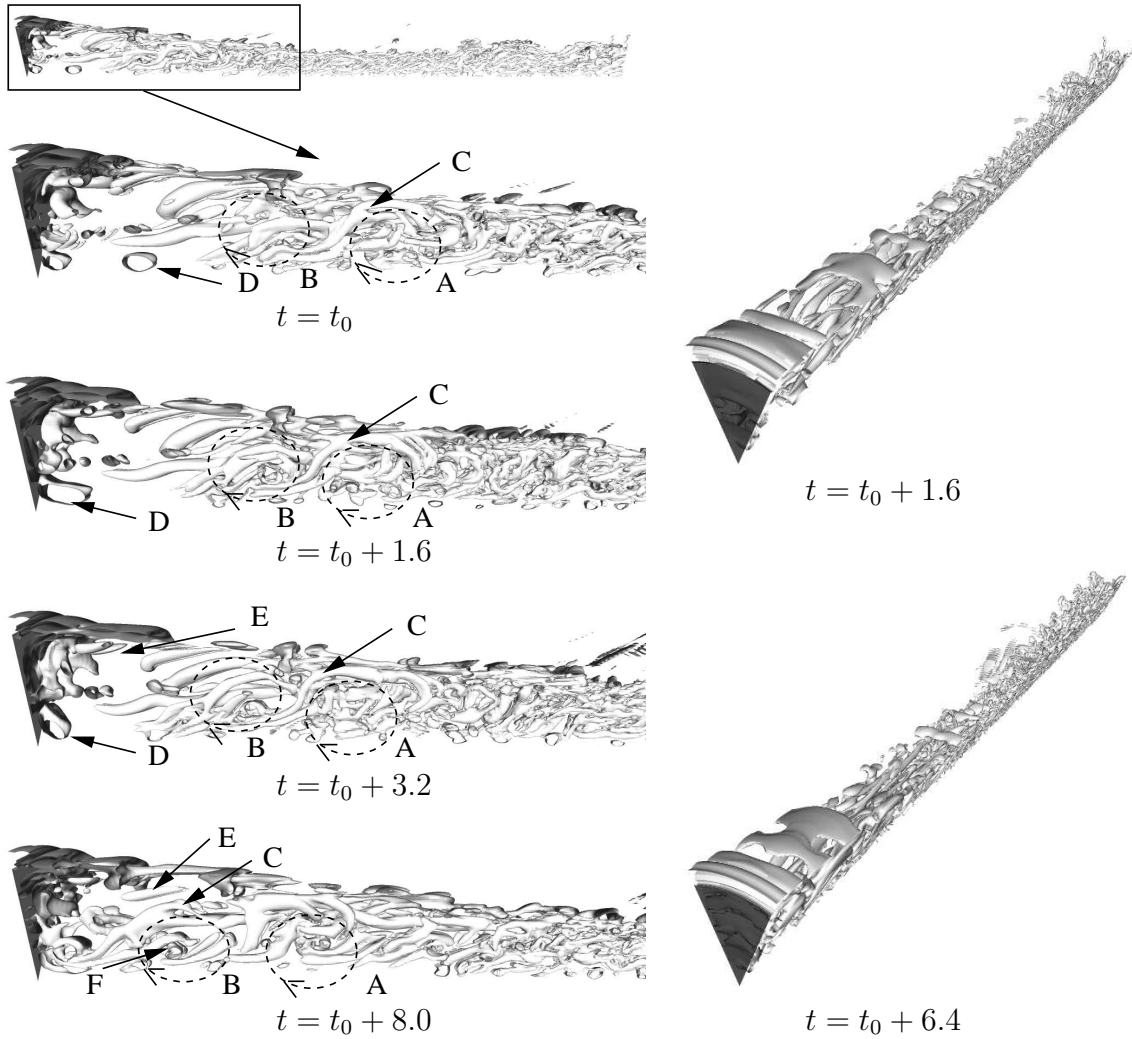


Figure 6.52 Instantaneous iso-contours of $Q = 0.1$ for 16th-cylinder case; time-sequence of sideviews (left) and perspective view from inflow towards outflow (right); $Re_D = 100,000$, $M = 2.46$.

point flow impinges on the base. This leads to a pressure peak at the axis, as will be shown later when discussing mean flow results. At $t = t_0 + 3.2$, streamwise structures (“E”) can be observed which closely resemble those found in figure 6.9 for the 1/8th-cylinder case at $Re_D = 30,000$. In the last time-instance shown, even smaller axisymmetric rollers can be observed (“F”), which in turn appear to generate additional streamwise structures within the recirculation region. In conclusion, it appears as if at least two separate mechanisms for the generation of longitudinal structures

are present within the recirculation zone: Firstly, as discussed for the $Re_D = 30,000$ case in section 6.1.2, the global modes lead to the generation of longitudinal structures within the recirculation region. Secondly, braids appear to be generated in the presence of axisymmetric rollers and are, therefore, most likely a consequence of a centrifugal instability.

In summary, transition to turbulence occurs rapidly and shocklets are visible roughly one radius downstream of the base, indicating the presence of large-scale structures. Endviews were compared with the UIUC data and a remarkable resemblance was found. At an upstream location, the same kind and number of mushroom-like structures was detected as in the experiments. Contours of total vorticity revealed that streamwise vortices in the initial shear-layer form the mushroom-shaped structures. In the developing wake, the DNS data instantaneously displayed a four-lobe structure, in good agreement with the visualizations obtained at UIUC. This four-lobe structure is a further indication that modes $k = 2$ and $k = 4$ are the dominant modes, both in the DNS at $Re_D = 100,000$ and the experiments at $Re_D = 3,300,000$. Visualizations of Q confirmed the presence of helical structures within the shear layer, which are subject to a strong high-wavenumber azimuthal variation, most likely caused by the streamwise structures in the shear layer. In light of the observations made for the lower Reynolds number cases, it is suggested that the longitudinal structures are partly generated as a consequence of global modes within the recirculation region. Additional evidence was gathered for the hypothesis that longitudinal structures within the recirculation region are generated as a consequence of centrifugal instabilities, occurring in the presence of axisymmetric rollers. In general, the strong similarities between the DNS and the UIUC case suggest that the same instability mechanisms are present, implying that results obtained from the DNS might be transferrable to the UIUC case.

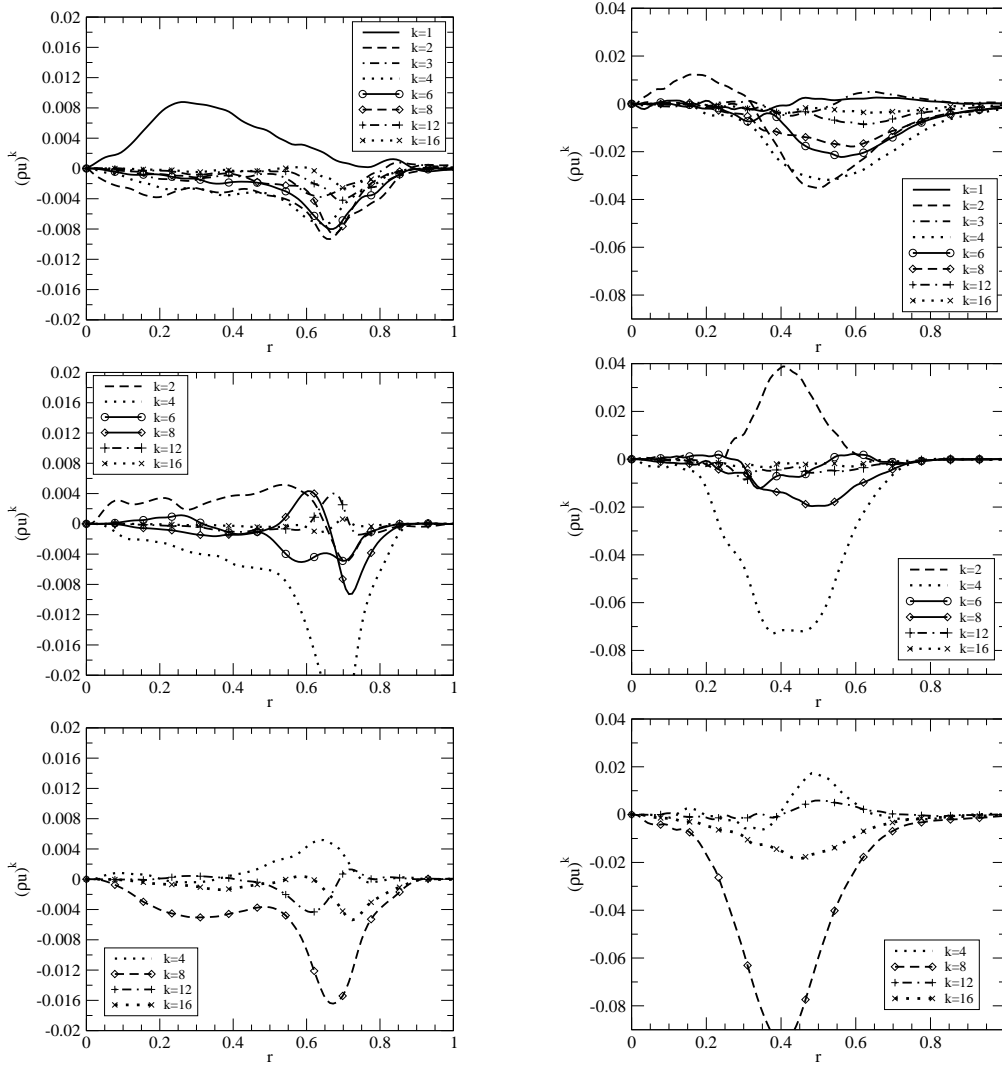


Figure 6.53 Time-averaged radial profiles of azimuthal Fourier modes of (ρu) obtained from DNS for half-, quarter- and $1/8^{th}$ -cylinder (from top to bottom); $z = 2.5$ (left), $z = 7$ (right), $Re_D = 100,000$, $M = 2.46$.

6.3.3 Mean Flow and Turbulent Statistics

Running averages were taken over at least ten flow-through-times for all domain sizes in order to evaluate the impact of the most dominant azimuthal Fourier modes on the mean flow. The averaged radial profiles of several azimuthal Fourier modes for all three conservative velocity components are shown in figures 6.53 – 6.55. For the half-

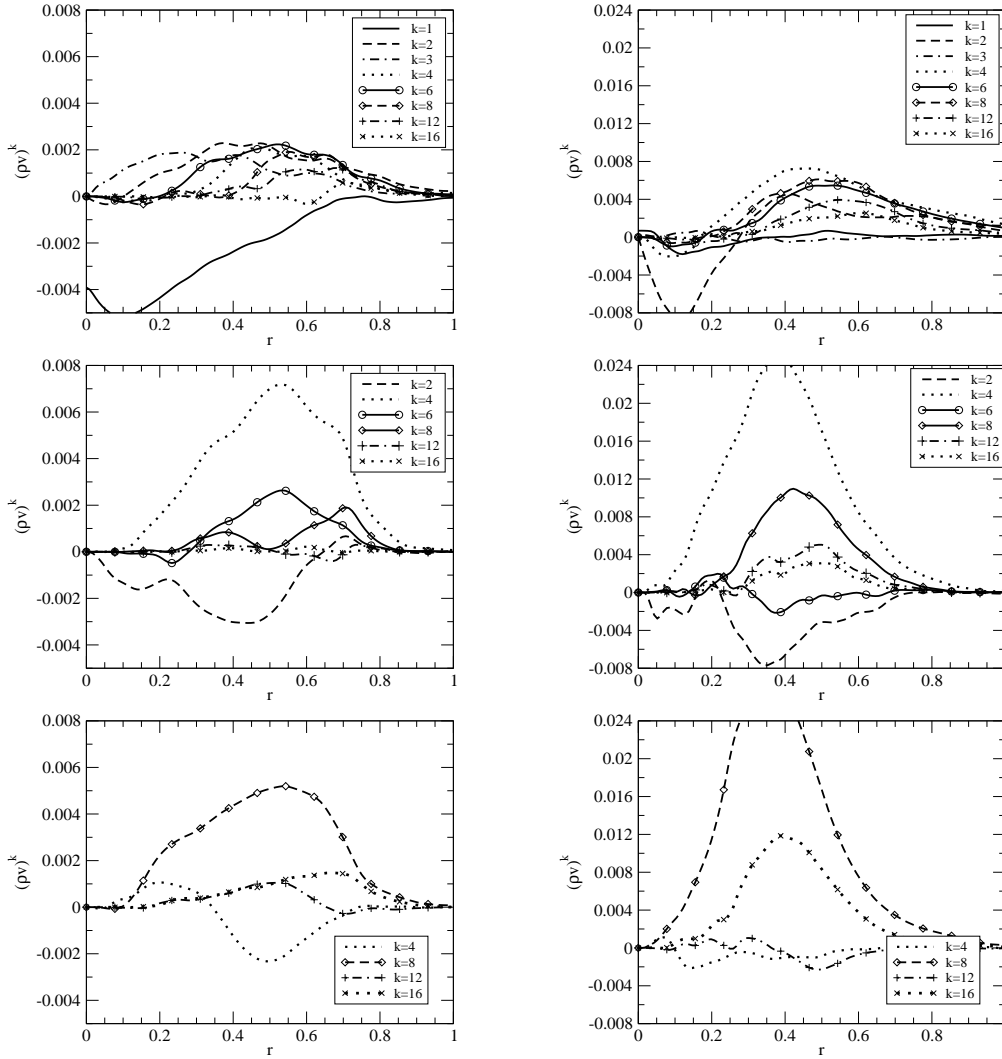


Figure 6.54 Time-averaged radial profiles of azimuthal Fourier modes of (ρv) obtained from DNS for half-, quarter- and $1/8^{th}$ -cylinder (from top to bottom); $z = 2.5$ (left), $z = 7$ (right), $Re_D = 100,000$, $M = 2.46$.

cylinder case at $z = 2.5$, the streamwise component appears to be the dominant one and, therefore, will be the main focus in the discussion of the modes-shapes. However, compared to the linear calculations and the lower Reynolds number DNS, the radial and the azimuthal components have considerably increased their significance. For the lower Reynolds number cases, it was suggested that the first mode is a subharmonic of some of the higher modes, evidenced by a shape fundamentally different from the one

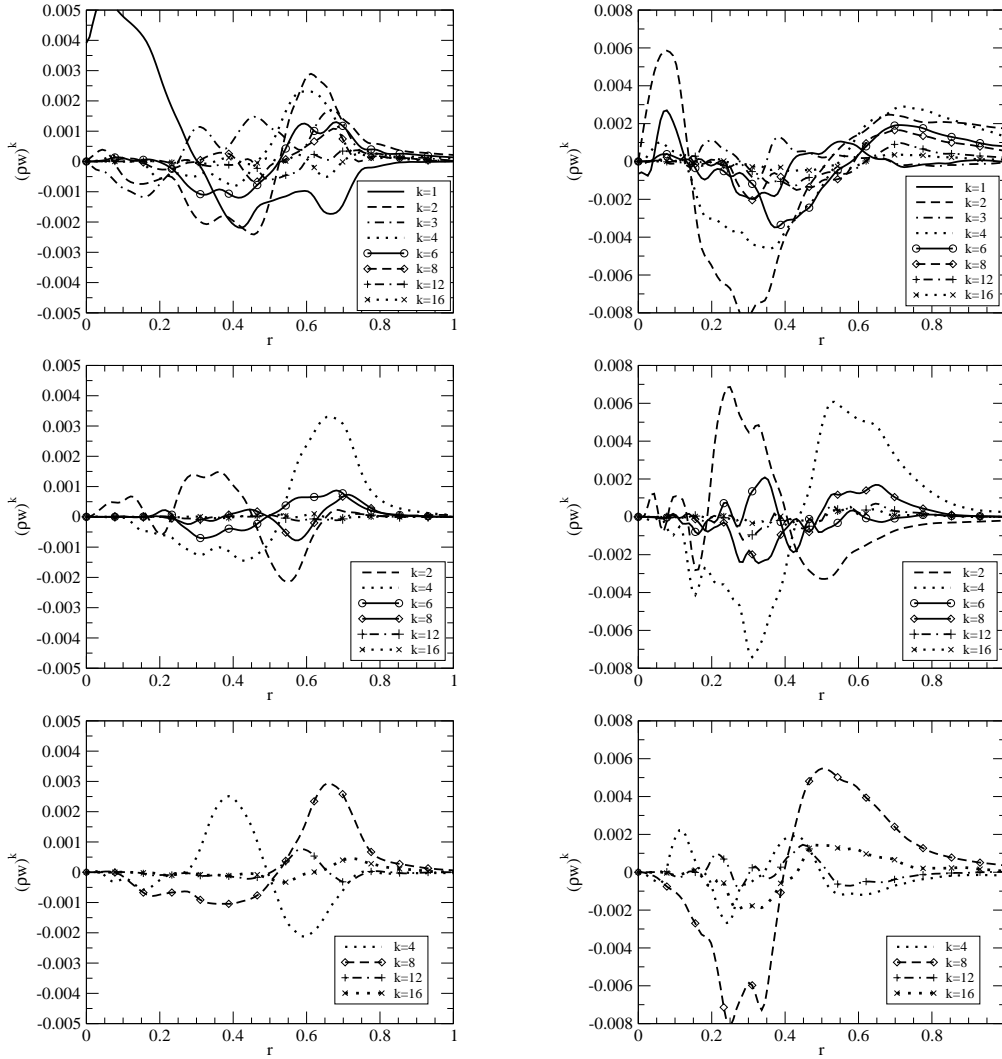


Figure 6.55 Time-averaged radial profiles of azimuthal Fourier modes of (pw) obtained from DNS for half-, quarter- and $1/8^{th}$ -cylinder (from top to bottom); $z = 2.5$ (left), $z = 7$ (right), $Re_D = 100,000$, $M = 2.46$.

obtained in the linear calculations. For the present case the amplitude distribution of the first azimuthal mode is similar to that found in the linear calculations (see figures 5.4 – 5.6). This suggests that $k = 1$ might not be a subharmonic of other azimuthal modes, but is generated autonomously. As opposed to the lower Reynolds number cases, all higher modes exhibit their maxima at $z \approx 0.65$. This confirms the findings of the linear stability calculations: The shear-layer mode becomes increasingly dominant

for larger Reynolds numbers. Several mode-shapes resemble each other and possess similar amplitudes, with the most significant modes being $k = 2, 4, 6, 8$. The large amplitudes of higher modes within the shear layer constitute further evidence for the presence of longitudinal structures in the shear layer.

For the downstream location (top right graphs in figures 6.53 – 6.55), several qualitative differences compared to the lower Reynolds numbers can be observed: Firstly, all modes exhibit smaller amplitudes, in particular the low-wavenumber modes. It is suggested that an increased energy transfer to higher modes, caused by the considerably increased level of turbulence, is the reason for this observation. Secondly, the maximum amplitude of the first azimuthal mode is close to an order of magnitude smaller than the dominant modes, even though it was the most dominant mode at the upstream position. In addition, it can be observed that modes $k = 2$ and $k = 4$ display the largest amplitudes in the mean. This confirms that they are dominant modes, as was supposed when observing a four-lobe wake-pattern in the trailing wake in figure 6.49.

The amplitude distributions obtained for all other domain sizes are fairly similar to those found at $Re_D = 60,000$. For all domain sizes, the first higher harmonic of the fundamental wavelength is the most dominant mode, i.e., in the quarter-cylinder case the most dominant mode is $k = 4$, in the $1/8^{th}$ -cylinder case mode $k = 8$, etc. In addition, the shape of the most dominant mode is similar for all cases.

To conclude the discussion of the amplitude distributions at $Re_D = 100,000$, it is found that within the trailing wake, modes $k = 2$ and $k = 4$ possess the largest amplitudes. In addition, the first azimuthal mode does not appear to be a subharmonic of higher modes. As for the lower Reynolds numbers, for smaller domain sizes, the first higher harmonic of the fundamental wavelength is the most dominant one, possessing a similar mode-shape. In contrast to the lowest Reynolds number investigated, higher modes display a maximum at $r \sim 0.65$, confirming TDNS results that the shear-layer mode becomes dominant at this Reynolds number.

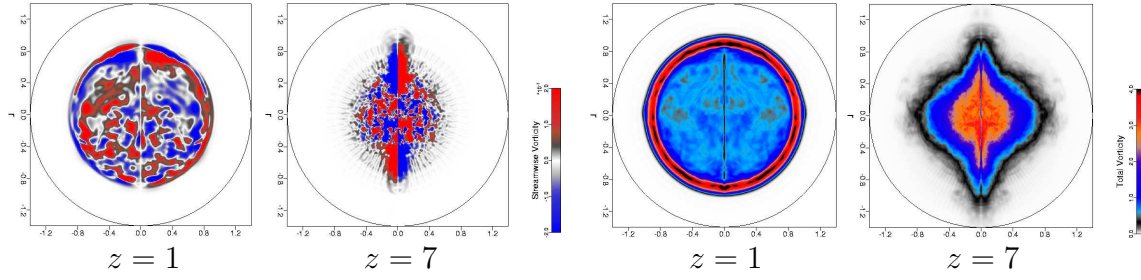


Figure 6.56 Endviews of time-averaged streamwise vorticity (left two) and total vorticity (right two); $Re_D = 100,000$, $M = 2.46$.

Endviews of time-averaged streamwise and total vorticity are shown for $z = 1$ and $z = 7$ in figure 6.56. In contrast to the lower Reynolds number cases, the visualization of streamwise vorticity reveals several structures on the inside of the shear layer at $z = 1$. For the contours of total vorticity, a strong azimuthal variation within the shear layer can be observed. This further confirms the presence of streamwise structures within the shear layer, as observed in the figures of instantaneous flow quantities above. At the streamwise location $z = 7$, a pronounced four-lobe structure is visible in both streamwise and total vorticity. This supports the results found in the discussion of instantaneous endviews and time-averaged radial profiles, leading to the conclusion that $k = 2$ and $k = 4$ are the most important modes. For the smaller domain sizes, the results correspond to the data deduced from the radial mode-shapes. Thus, as the dominant modes of the respective case are the first subharmonic of the fundamental wavelength, a k -lobe structure is visible, with k being the number of the dominant mode. The results resemble those presented for the $Re_D = 60,000$ case and are, therefore, not shown here.

The effect of the dominant structures on the recirculation length and the base-pressure is compared for all cases in figure 6.57. As for the lower Reynolds number cases, in the half-cylinder calculation the pressure-distribution along the base is entirely flat. However, the mean pressure value has decreased considerably and is more

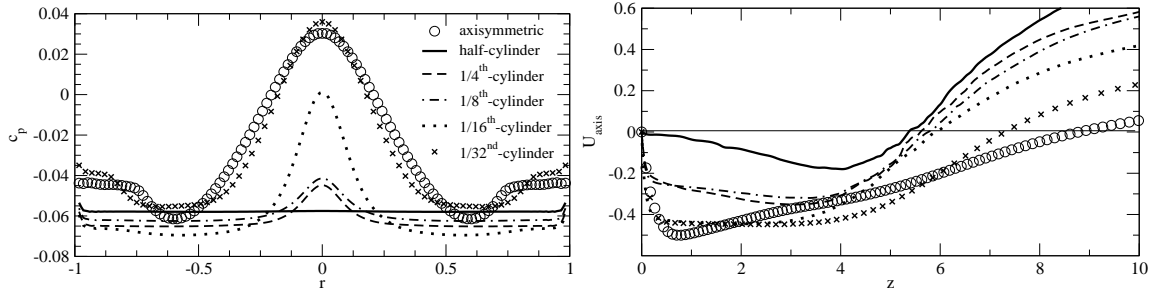


Figure 6.57 Time-averaged pressure coefficient (left) and streamwise axis-velocity (right) for all circumferential domain-sizes; $Re_D = 100,000$, $M = 2.46$.

than 10% smaller than for the $Re_D = 60,000$ case. A fast transition process, leading to energetic structures is responsible for a dramatic decrease in recirculation length (the mean reattachment shifts from $z = 8.5$ to $z = 5.3$) and a strongly reduced reverse flow velocity within the recirculation region. With the mean reattachment point considerably closer to the base, the turning angle at the base-corner is increased, leading to a larger pressure drop over the expansion fan. Invoking the thin-layer approximation of pressure only changing marginally across the shear layer can be used to explain the decreased base-pressure.

Unlike the lower Reynolds number cases, the results obtained from both the quarter-cylinder and the $1/8^{th}$ -cylinder calculations are very similar to each other. The mean pressure coefficient is higher than in the half-cylinder case and a slight radial variation with a peak at the axis can be observed. Furthermore, the mean reattachment location is considerably farther downstream, and the reverse flow maximum is much higher than in the half-cylinder case. The drastic differences that result in the elimination of mode $k = 1$ for these cases support the above observations, that mode $k = 1$ is significant within the recirculation region for this Reynolds number. The similarity in the data from the quarter-cylinder and the $1/8^{th}$ -cylinder calculations suggest that the flow-pattern and the structures generated by the dominant modes of the respective calculation ($k = 4$ and $k = 8$) are similar.

As already indicated by the above results, the $1/16^{th}$ -cylinder case produces sufficiently energetic structures to considerably reduce the recirculation length. In fact, the mean reattachment point is located only marginally downstream of that of the two larger cases, in spite of a significantly larger maximum reverse flow velocity within the recirculation region. The pressure peak at the axis is more pronounced. However, in contrast to the lower Reynolds numbers, the deviation from the larger circumferential domain-sizes is confined to a considerably smaller radial extent. Thus, it can be concluded that the long-wavelength modes, i.e., $k = 1$, $k = 2$ are essential in obtaining an entirely flat profile. Because the higher modes do not reach amplitudes large enough to affect the mean flow, the results from the $1/32^{nd}$ -cylinder calculation deviate significantly from the other cases and are fairly similar to those obtained in the axisymmetric calculations.

The radial maxima of turbulence quantities over the streamwise coordinate are shown in figure 6.58. In contrast to the lower Reynolds number cases, the radial

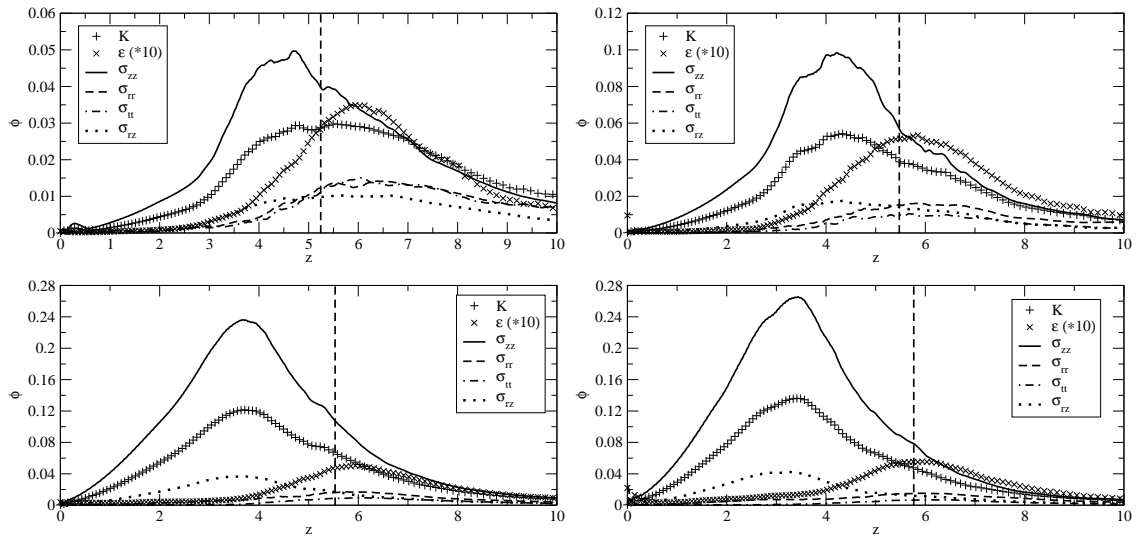


Figure 6.58 Radial maxima of various averaged turbulent statistics over streamwise coordinate obtained from DNS for half-cylinder (top left), quarter-cylinder (top right), $1/8^{th}$ -cylinder (bottom left) and $1/16^{th}$ -cylinder (bottom right); vertical dashed line denotes the respective mean reattachment length; $Re_D = 100,000$, $M = 2.46$.

maxima of TKE and $\overline{u'u'}$ are located upstream of the mean reattachment point for all cases. This is in agreement with the observations by Herrin & Dutton (1997) and constitutes further proof that the base flow at $Re_D = 100,000$ is similar to the experiment at $Re_D = 3,300,000$. The maximum dissipation rate can be found just downstream of the mean reattachment point, however, this quantity was not measured in the experiments and, therefore, no comparison can be made. In general, the values of all quantities are higher than at the lower Reynolds numbers, in particular the $1/8^{th}$ - and $1/16^{th}$ -cylinder cases exhibit strongly increased amplitudes even exceeding those found for the larger domain sizes. As suggested earlier, this can most likely be explained by the fact that a large amount of energy is transferred directly to the most important modes. Due to the omission of modes by conducting calculations with smaller domain sizes, this energy cannot be redistributed to the modes excluded through nonlinear interaction and results in highly energetic structures.

In conclusion, the mode-shapes suggest that the first azimuthal mode is generated autonomously at the upstream location $z = 2.5$. For the higher modes, the shear-layer mode appears to become dominant, confirming results obtained with linear stability simulations. Large amplitudes of the higher modes in the shear layer are an indication of streamwise vortices, which were observed in endviews of time-averaged streamwise and total vorticity. In the trailing wake, $k = 2$ and $k = 4$ display the largest amplitudes, leading to a very pronounced four-lobe structure of the wake in the mean. For all smaller domain sizes, the first higher harmonic of the fundamental wavelength is the most dominant mode, possessing a similar amplitude and mode-shape. The mean base-pressure of the current case is further decreased over the lower Reynolds number cases. Only the mean base-pressure value for the $1/16^{th}$ -cylinder case is noticeably higher than in the half-cylinder case. In light of the forced cases presented in section 6.1.5, this implies that the dominance of modes $k = 1$ to $k = 4$ needs to be diminished in order to possibly achieve a drag-reduction. Finally,

turbulence statistics support the notion that the case at $Re_D = 100,000$ is similar to the UIUC experiments.

6.3.4 Summary

DNS of supersonic axisymmetric wakes at $Re_D = 100,000$ and $M = 2.46$ were conducted for several azimuthal domain-sizes. The increased amplification rates of instabilities resulted in transition to turbulence for domain sizes up to $0 \leq \theta \leq \pi/8$. No intermittency could be observed for these cases. Considerable evidence was found showing that modes $k = 2$ and $k = 4$ are the dominant modes. Contours of instantaneous total vorticity revealed that streamwise structures are present in the shear layer. These longitudinal structures appear to reside in the shear layer over long time-periods, as they were also detected in time-averaged endviews of streamwise and total vorticity. Helical structures that were observed in visualizations of Q experience a strong azimuthal variation, presumably caused by the streamwise structures in the shear layer. A time-sequence of $Q = 0.1$ for the $1/16^{th}$ -cylinder case showed further evidence for the hypothesis that longitudinal structures within the recirculation region are possibly generated as a consequence of centrifugal instabilities, occurring in the presence of axisymmetric rollers.

Endviews of instantaneous Mach number revealed the presence of mushroom-shaped structures in the shear layer, caused by the streamwise vortices in the shear layer. These mushroom-like structures are similar in shape and number to those observed in the (higher Reynolds number) experiments. At a location farther downstream, a four-lobe wake pattern can be observed, in good agreement with the experimental results. These strong similarities between the DNS data and the experiments suggest that the same instability mechanisms are present for both cases. Therefore it is speculated that modes $k = 2$ and $k = 4$ might also be dominant modes in the UIUC experiments, generating the four-lobe structure in the developing wake.

7. RESULTS - FLOW SIMULATION METHODOLOGY

As has already been mentioned in the introduction, high Reynolds number flows feature a very broad spectrum of time- and length-scales. Direct Numerical Simulations (DNS) of wakes at high Reynolds numbers, as investigated in the experiments at UIUC, with sufficient resolution in all three dimensions and in time are out of reach with present supercomputers, as will be shown in this chapter. Even fully resolved DNS of the transitional wakes, like those presented in the previous chapter are computationally very expensive, with typical run times of several thousand CPU hours per flow-through time. Therefore, other approaches will now be considered for the calculation of supersonic base flows. Axisymmetric RANS and three-dimensional FSM calculations will be presented first for the transitional cases and then for the high Reynolds number UIUC-case.

The FSM was first employed for transitional wakes for several reasons: Primarily, in order to evaluate whether the approach is able to represent a transitional flow in general. Capturing the laminar-turbulent transition is a tough task for any flow simulation strategy, as the additional dissipation from turbulence models frequently inhibits or significantly delays the mechanisms leading to transition. Furthermore, a vast amount of data were available from the previously discussed DNS, such that a detailed comparison between FSM results and DNS data could be made. Finally, as the FSM is still in the development process, a large number of calculations was anticipated. Choosing a lower Reynolds number resulted in more moderate grid-requirements and, therefore, reasonable computational times. In particular, the fact that the approach boundary layer is laminar for the transitional cases significantly decreased the necessary grid-spacing in the radial direction at the wall and, thus, also allowed for considerably larger time steps, substantially reducing the turn-around time for each calculation.

For the transitional cases, first axisymmetric RANS calculations were conducted, employing a variety of turbulence models. These calculations were essential in order to generate an initial condition for the three-dimensional FSM calculations, and to determine which closure was best suited as the underlying turbulence model for FSM. The same code was used for both RANS and FSM calculations. In order to conduct RANS calculations, the contribution function presented in section 2.3 was set to unity, therefore using the sub-grid quantities computed with the specified turbulence closure in an unmodified way. When conducting FSM calculations, the contribution function was computed as specified in equation (2.38). As for the DNS, for all transitional cases, it was assumed that the approach flow is laminar. Therefore, the contribution function was manually set to zero in the approach flow, such that no model was employed and the boundary layer remained laminar.

7.1 Transitional Wake at $Re_D = 30,000$

Initially, an axisymmetric computation using no turbulence model was carried out on a grid significantly coarser than that used for the DNS calculations presented in section 6.1. 152 and 85 points were used in the streamwise and the radial directions, respectively, with the smallest grid spacing $\Delta r_c = \Delta z_c = 0.01R$ at the corner. The converged solution served as initial condition for the axisymmetric RANS calculations and will be denoted by “no model” in the following. For a complete listing of all relevant parameters, see table D.8 in Appendix D.

7.1.1 Axisymmetric RANS Calculations

Axisymmetric RANS calculations were conducted, employing the “standard” $K - \varepsilon$ model (STKE), the original explicit algebraic stress model (EASM) by Speziale (1997) and the generalized version of the explicit algebraic stress model $EASM_\alpha$ by Rumsey *et al.* (2000), all presented in section 2.2.1. For the calculations employing

the EASM, the constants α_i (equation 2.14) were computed assuming that $\frac{P}{\epsilon} = \frac{c_{\epsilon 2}-1}{c_{\epsilon 1}-1}$. It turned out, that for the lowest Reynolds number investigated, the wall-distance independent function $f_{\epsilon 2}$ (equation 2.34) reached values significantly larger than unity. The destruction term in the transport equation for ϵ was thereby scaled to unphysically large values, creating an imbalance between the turbulence quantities. This either lead to an unsteady solution of the flow field, or a decay of TKE to zero. Therefore, for the lowest Reynolds number discussed here, the standard, wall-distance dependent wall-damping function $f_{\epsilon 2}(N)$ (see equation 2.33) was employed.

As mentioned above, for all cases where the approach boundary layer was assumed to be laminar, the contribution function was set to zero, such that no model contributions were added to the filtered Navier-Stokes equations. The transport equations for K and ϵ , however, were still solved for in the approach flow region, constituting an inflow condition for K and ϵ at the inflow of the wake-region. Thereby the values of K and ϵ in the approach flow region have a considerable effect on the global solution of the calculations. For the transitional cases, K was initially set to zero in the approach flow to be consistent with the laminar flow assumption. Regardless of which turbulence model was used, at this Reynolds number, K did not evolve to non-zero values in the approach region. If, however, a non-zero initial condition was specified for K , the calculation would “see” the laminar inflow profile as a thick, high Reynolds number boundary layer and produce large values of K in the approach flow. This led to an overprediction of the eddy-viscosity in the shear layer, and, consequently, resulted in a shortened recirculation region.

Figure 7.1 shows the pressure coefficient c_p over the base and the streamwise velocity component along the axis, obtained from axisymmetric “no model”, STKE model, EASM and EASM $_{\alpha}$ calculations. For reference, the data from the DNS, discussed in section 6.1 is added to the graphs. In contrast to the axisymmetric “no model” computation, all axisymmetric RANS calculations underpredict the recirculation length significantly and, consequently, also predict too low a pressure on the

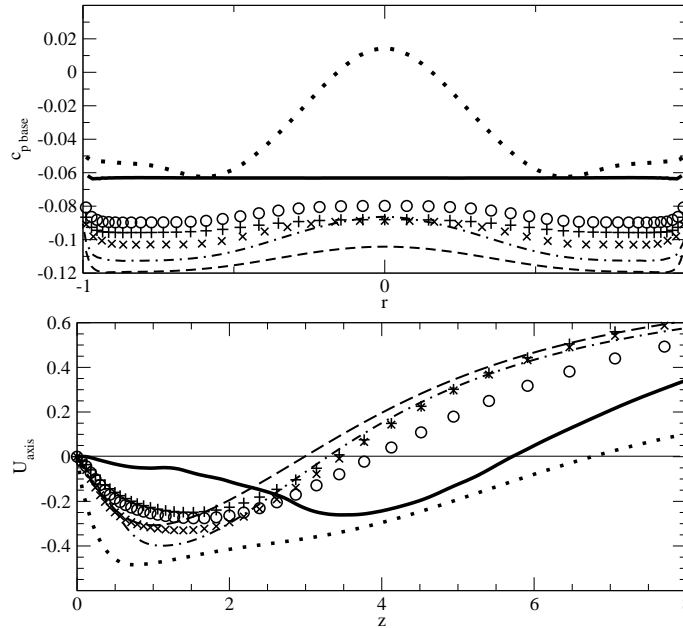


Figure 7.1 Pressure coefficient (top) and streamwise axis-velocity (bottom) from RANS calculations; data from DNS with 64 modes (—), axisymmetric “no model” calculation ($\cdot \cdot \cdot$), STKE model (— —), EASM (— \cdot —), EASM $_{\alpha}$ (\circ), EASM $_{\alpha}$ without c.e. (+), EASM $_{\alpha}$ with K non-zero in approach flow (\times); $Re_D = 30,000$, $M = 2.46$.

base. The pressure distribution on the base also shows a considerable radial variation, albeit with different strength for different models. The calculation employing the STKE model yields the shortest recirculation length and the lowest pressure value with the strongest radial variation. This is most likely due to the overprediction of the eddy viscosity in the shear layer and within the recirculation region. When using the original EASM, the recirculation length is slightly increased over the results from the STKE calculation, as is the base-pressure. This behavior is due to the prediction of lower levels of turbulent viscosity, as shown below in figure 7.2. The EASM calculations, however, required smaller time-steps, presumably due to an increased stiffness of the equations, caused by the function $f(\eta, \xi)$ (see equation 2.15) reaching values larger than unity in the expansion wave and at the base/axis intersection. The results obtained from the calculation employing the EASM $_{\alpha}$ showed a significant im-

provement in terms of the numerical stability, most likely because of the decreased stiffness of the equations by computing the production over dissipation ratio locally. This resulted in the largest permissible time-step being close to twice as large as for the other two models. The pressure distribution from the EASM_α calculation showed the highest value and the least radial variation of all models used. Also, the largest recirculation length was obtained with the most recent model and the maximum reverse velocity was not overpredicted as strongly as when using the other closures.

An additional axisymmetric RANS calculation, employing the EASM_α was conducted, neglecting the compressible extensions (c.e.) in order to evaluate their impact on the solution. It can be observed that both the base-pressure and the recirculation length are slightly decreased if no c.e. are used. This was expected as figures showing the distribution of the turbulent Mach number (not included here) revealed that M_T reaches values of up to 0.5 in the recompression region. The turbulent Mach number is a measure for the compressibility of the flow and the basis of the models by Sarkar *et al.* (1991) for both the pressure dilatation and the compressible dissipation (see equation 2.26). In addition, the calculation employing the EASM_α was repeated, allowing for a non-zero distribution of K in the approach flow. The recirculation

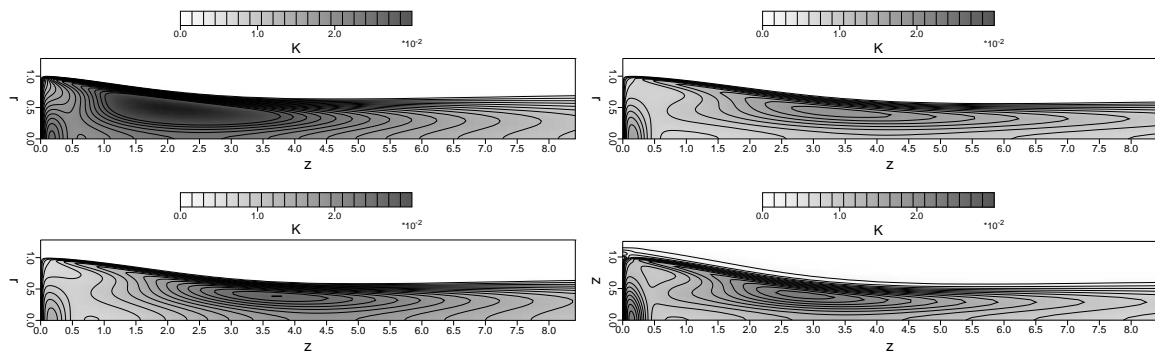


Figure 7.2 Distribution of TKE obtained from axisymmetric RANS calculations; STKE model (top left), EASM_α (top right), EASM_α without c.e. (bottom left), EASM_α with K non-zero in approach flow (bottom right); $Re_D = 30,000$, $M = 2.46$.

length was also shortened and the base-pressure was slightly decreased for this case. Figure 7.2 shows the distribution of the TKE obtained from the axisymmetric RANS calculations. When compared to the results obtained with DNS, shown in figure 6.21, all RANS models overpredict K throughout the recirculation region, with the STKE model showing the highest values, leading to the shortest recirculation length, as shown in figure 7.1. In addition, the maxima of K are located much further upstream than for the DNS. Also, a peak can be observed at the axis/base intersection, caused by the stagnation point. Comparing the data from the EASM_α calculations with each other confirms that either neglecting the compressible extensions, or allowing for a non-zero K -distribution in the approach flow lead to increased levels of TKE in the shear layer and the recirculation region, resulting in larger values of turbulent viscosity and, consequently, to a decreased recirculation length.

In conclusion, the EASM_α appears to be the best suited model for the flow under consideration, showing a recirculation length and a base-pressure closest to the DNS results, due to appropriately reduced levels of turbulent production. It also appears as if the compressible extensions used in the current work slightly improve the solution. Nevertheless, even the most successful RANS calculation is far from reproducing the physically correct flat base-pressure distribution and streamwise velocity distribution along the axis of the DNS. It is therefore suggested, that in order to correctly predict supersonic base flows, the unsteady structures need to be included in the simulations. This hypothesis will be tested in the next section.

7.1.2 3-D FSM Calculations

The FSM calculations were conducted, using the STKE model, the EASM and the EASM_α as underlying closures. The results from the respective axisymmetric RANS computations discussed above were used as initial conditions. The same coarse

streamwise/radial grid was employed for the calculations and only four azimuthal Fourier modes were used. For further parameters, see table D.8 in Appendix D. Once the flow field was fully three-dimensional, calculations with different closures and varying the constant β in the contribution function were conducted over at least 15 flow-through-times in order to obtain converged averages of various flow quantities.

In figure 7.3 contour plots of the time-averaged contribution function for different values of β are presented. Note that the model contribution decreases for decreasing β . For all cases, the contribution is clearly largest in the shear layer and in the recompression region. These are locations where the computational grid is not fine enough to resolve the large local gradients. The contribution function maintains elevated values downstream of the recompression region, mainly because the streamwise resolution becomes very coarse due to the highly stretched grid. Within the recirculation region, the values of $f(\Delta/L_K)$ are merely a few percent and, therefore, unsteady structures that are present in the flow are only barely damped by the turbulent viscosity of the utilized closure. The unsteadiness leads to the modification of the mean

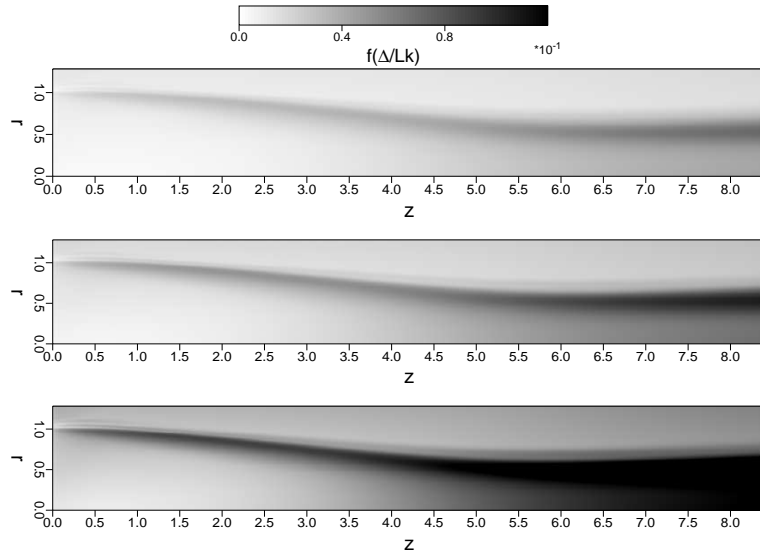


Figure 7.3 Mean contribution function $f(\Delta/L_K)$ for FSM using EASM_α for, top to bottom, $\beta = 6 \cdot 10^{-4}$, $\beta = 1 \cdot 10^{-3}$, $\beta = 2 \cdot 10^{-3}$; $Re_D = 30,000$, $M = 2.46$.

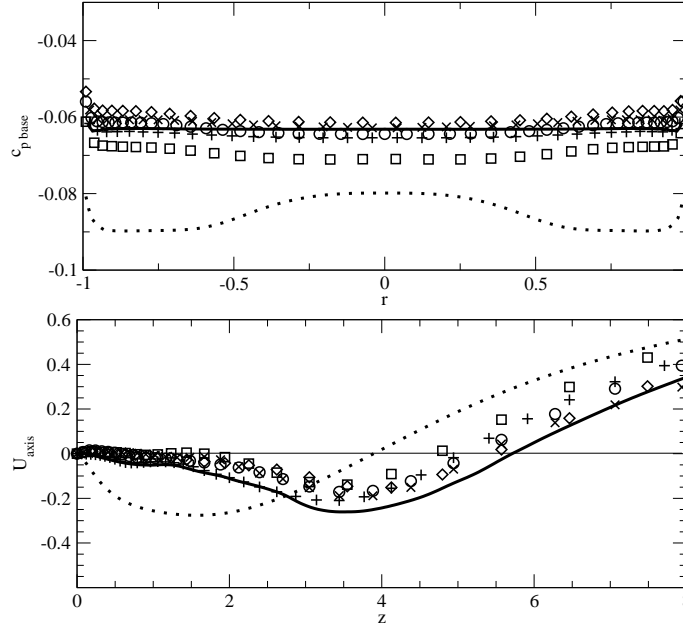


Figure 7.4 Time-averaged pressure coefficient (top) and streamwise axis-velocity (bottom) from FSM calculations; data from DNS with 64 modes (—), axisymmetric EASM_α calculation (···), FSM using STKE model with $\beta = 1 \cdot 10^{-3}$ (+), FSM using EASM with $\beta = 1 \cdot 10^{-3}$ (×), FSM using EASM_α with $\beta = 6 \cdot 10^{-4}$ (□), FSM using EASM_α with $\beta = 1 \cdot 10^{-3}$ (○), FSM using EASM_α with $\beta = 2 \cdot 10^{-3}$ (◇); $Re_D = 30,000$, $M = 2.46$.

flow as can be seen in the pressure distribution on the base or from the streamwise axis-velocity in figure 7.4.

In order to determine what the best choice for β is, the time-averaged base-pressure coefficient c_p and the streamwise velocity component along the axis, obtained from all FSM calculations are shown in figure 7.4. For comparison, the data from the DNS and the results from the axisymmetric RANS, using the EASM_α, are added to the graphs. For all FSM calculations, the base-pressure distribution is reasonably flat and the mean value corresponds quite well with the DNS result. The fact that the FSM calculations, using only 4 azimuthal Fourier modes, can reproduce the flat pressure profile on the base confirms the conclusion made in section 6.1.3: The flat pressure distribution on the base is caused by unsteady structures which are a consequence of

azimuthal modes with large wavelengths, i.e., modes $k = 1$ through $k = 4$.

The FSM calculations also show much better agreement with the DNS data for the streamwise axis-velocity. Not only is the recirculation length predicted more accurately, also the maximum reverse velocity is located at approximately $z = 3.5$. Even the small plateau, present at $z \approx 1.3$ and most likely an artefact of the unsteady structures, is reproduced. When scrutinizing the time-averaged quantities shown in figure 7.4, it appears as if the solution depends more strongly on the choice of β than on the underlying turbulence model employed in the calculation. For the smallest value of β investigated here, the mean pressure value at the base is underpredicted and the recirculation length is the shortest obtained from any FSM calculation conducted for this case. The best agreement with the DNS data is found for $\beta = 1 \cdot 10^{-3}$ or $\beta = 2 \cdot 10^{-3}$, regardless of the closure employed for the calculation.

To demonstrate that good agreement of the significantly coarser FSM calculations with the DNS data is not only achieved for individual, one-dimensional profiles, the mean radial velocity and pressure fields of an FSM calculation are compared to the DNS results in figure 7.5. Good agreement is found for the entire flow-field.

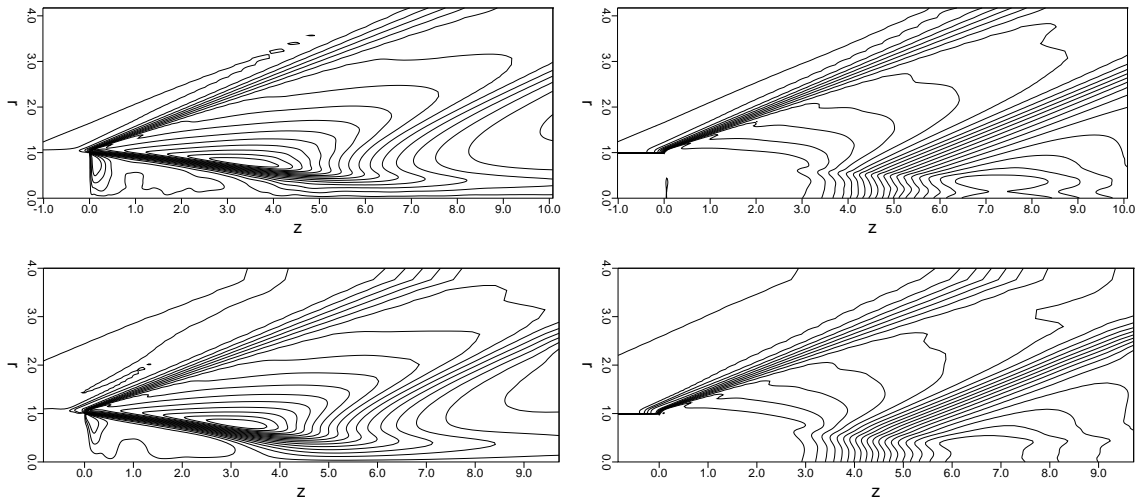


Figure 7.5 Time-averaged radial velocity field (right) and mean pressure field (left) from DNS (top) and FSM (STKE) with $\beta = 2 \cdot 10^{-3}$ (bottom); $Re_D = 30,000$, $M = 2.46$.

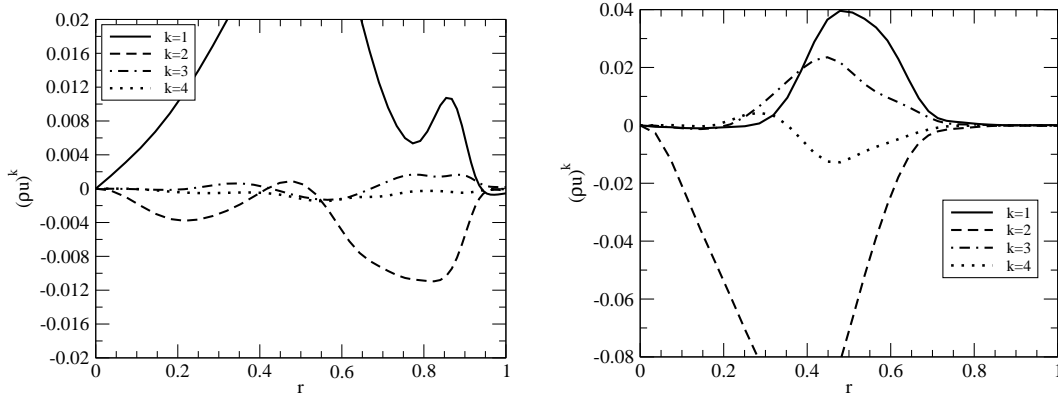


Figure 7.6 Time-averaged mode-shapes of $(\rho u)^k$ obtained from FSM calculations using the EASM_α with $\beta = 1 \cdot 10^{-3}$; $z = 2.5$ (left) and $z = 9$ (right), $Re_D = 30,000$, $M = 2.46$.

Finally, the time-averaged mode-shapes of the streamwise velocity component for the first four azimuthal modes, obtained from the FSM calculation employing the EASM_α with $\beta = 1 \cdot 10^{-3}$, are shown in figure 7.6. The range of the y-coordinate was chosen to be the same as in figure 6.13, thus allowing for a direct comparison of the magnitudes of the individual modes to the DNS results. Good agreement is found for the mode-shape of the second azimuthal mode. For modes $k = 3$ and $k = 4$, the mode-shapes are similar to the DNS data, except that the amplitudes are significantly reduced, due to the damping effect of the turbulence model, which affects larger wavenumbers to a larger degree. The first azimuthal mode exhibits a different behavior than that obtained from DNS, however, the mode-shapes resemble closely those found in the linear calculations, shown in figure 5.4. This confirms the assumption made previously, that the mode-shape of the first mode might be the result of nonlinear interaction between higher modes, in particular $k = 3$ and $k = 4$. By neglecting modes with $k > 4$ and/or reducing the amplitudes of modes $k = 3$ and $k = 4$, the nonlinear interaction is reduced and the mode-shape of the first mode remains fairly unchanged from that predicted by linear theory.

The calculations discussed so far were conducted using very coarse computational

grids and, therefore, approach the URANS limit of the FSM, i.e., the contribution function possesses values larger than 10%. For that reason, only the largest structures are resolved (and not dissipated by the turbulence model). The identification of coherent structures is therefore deferred to FSM calculations of higher Reynolds numbers, where finer grids were utilized.

In summary, FSM calculations of supersonic axisymmetric wakes at $Re_D = 30,000$ and $M = 2.46$ are capable of reproducing DNS results with reasonable accuracy. In particular the pressure distribution on the base is predicted accurately. FSM appears to succeed in sufficiently scaling down the model contribution in the relevant regions so as not to inhibit the physical instability mechanisms which give rise to the generation of large structures. These structures need to be captured by the calculations to obtain a physically accurate flow field. The decreased spatial and temporal resolution requirements, compared to a DNS, by far outweigh the increased computational effort required for solving additional transport equations and assembling all closure terms. This leads to a significant reduction in computational cost, as shown in table 7.1. The above results also illustrate that the FSM approach is not linked to a specific turbulence model but is a general strategy for solving unsteady, three-dimensional flows. However, for the case currently discussed, the $EASM_\alpha$ showed several advan-

	DNS	FSM (STKE)	FSM ($EASM_\alpha$)
points in z	516	152	152
points in r	200	85	85
modes in θ	64	4	4
dt	$1.19 \cdot 10^{-3}$	$1.5 \cdot 10^{-3}$	$2.6 \cdot 10^{-3}$
CPU hours	1780*	2.65	1.64

Table 7.1 Comparison of computational cost on *HP Alpha* per flow-through-time ($t - t_0 \approx 12$) for FSM and DNS calculations; * denotes CPU time on *SGI Origin 3900*, for a comparison of the performance of both computer architectures, see Appendix C.6.2; $Re_D = 30,000$, $M = 2.46$.

tages over the other closures employed, amongst others increased numerical stability reducing the computational time, and more accurate levels of eddy-viscosity in the shear layer and the recirculation region. Finally, the results obtained by FSM calculations confirm that for the $Re_D = 30,000$ case, the first azimuthal mode is highly influenced by the nonlinear interaction of higher modes and that the flat pressure distribution at the base is caused by structures generated by modes $k = 1$ to $k = 4$.

7.2 Transitional Wake at $Re_D = 60,000$

As for the lower Reynolds number case, an axisymmetric computation using no turbulence model (“no model”) was carried out to obtain an initial condition for the axisymmetric RANS calculations. Two separate computational grids were utilized. The coarse grid had 162 points in the streamwise direction and 90 points in the radial direction with the smallest grid spacing $\Delta r_c = \Delta z_c = 0.02R$ at the corner. For the fine computational grid, 302x130 points were employed in the streamwise and the radial directions, respectively, and the finest spacing at the corner of the body was $\Delta r_c = \Delta z_c = 0.01R$. For additional parameters, see table D.8 in Appendix D.

7.2.1 Axisymmetric RANS Calculations

In contrast to the $Re_D = 30,000$ case, the Reynolds number appears to be sufficiently large to allow for the use of the wall-distance independent version of the $EASM_\alpha$, using the wall-damping function $f_{\varepsilon 2}$ given in equation (2.34). Several calculations were conducted on both computational grids, varying the constant c_T , and using the wall-distance dependent version $f_{\varepsilon 2}(N)$ given in equation (2.33) for comparison, to determine the influence of the choice of wall-treatment on the global solution. Based on the results from the above case, the $EASM_\alpha$ was employed for this study. For all cases conducted at $Re_D = 60,000$, the contribution function was again set to zero in the approach flow to account for laminar flow. As discussed above, K was initially set

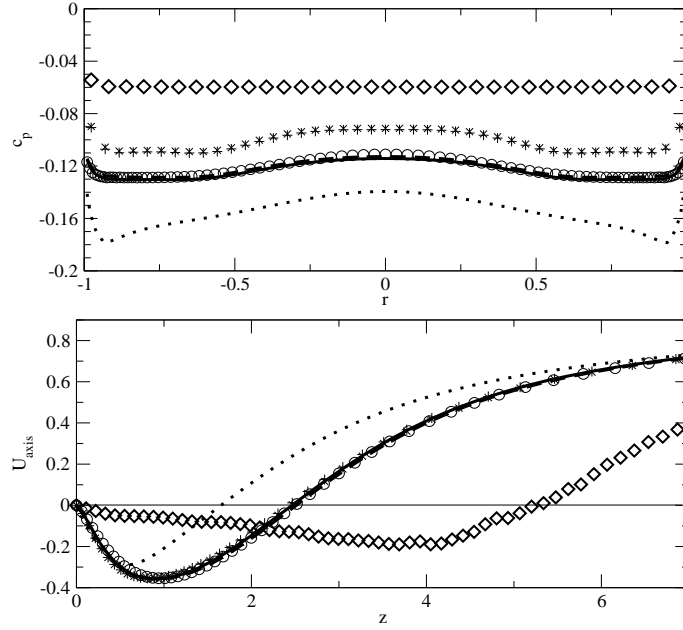


Figure 7.7 Pressure coefficient on base (top) and streamwise velocity along axis of symmetry (bottom); data from DNS, 128 modes (\diamond), coarse grid $f_{\varepsilon 2}(N)$ (—), coarse grid $c_T = 4.56$ (---), coarse grid $c_T = 4.65$ (\circ), coarse grid $f_{\varepsilon 2}(N)$, STKE model (\cdots), fine grid $f_{\varepsilon 2}(N)$ (+), fine grid $c_T = 4.56$ (\times); $Re_D = 60,000$, $M = 2.46$.

to zero in the boundary layer region to be consistent with the laminar approach-flow assumption.

Figure 7.7 shows the centerline velocities and the radial distributions of the pressure coefficient c_p on the base. For reference, the DNS results discussed in section 6.2.3 are included. The calculation employing the STKE model, which was conducted for comparison, displays the shortest recirculation region, resulting in a far too low base-pressure with a strong radial variation. The difference to the solutions obtained from the calculations using the $EASM_\alpha$ is more pronounced than for the lower Reynolds number. When looking at the streamwise axis-velocity, the data obtained from calculations employing the $EASM_\alpha$ with $f_{\varepsilon 2}(N)$, $c_T = 4.56$ or $c_T = 4.65$ practically collapse into one curve, independent of the computational grid that was utilized. However, the recirculation length is still significantly underpredicted. This

is likely caused by the large values of K close to the base and in the initial shear-layer, as the model mistakes this laminar region for a turbulent region.

Only when scrutinizing the base-pressure, a difference between the coarse and the fine computational grid becomes visible. For the fine grid, c_p is slightly larger than for the coarse grid. Nevertheless, the data of calculations using $f_{\varepsilon 2}(N)$ or $c_T = 4.56$ coincide for both grids. Overall, the values found for c_T with calibration calculations of turbulent boundary layers (section 4.5) appear to be transferrable to the base flow case. It is noteworthy that, for the wake, the global solution is less sensitive to the value of c_T than for the turbulent boundary layer. In addition to producing superior axisymmetric RANS results, the EASM_α was, as for the lower Reynolds number case, numerically more stable than both the STKE model and the original EASM.

7.2.2 3-D FSM Calculations

For the FSM calculations, only the EASM_α was employed as it produced the best axisymmetric results and allowed for the largest time-steps. As initial condition for the FSM calculations, the axisymmetric RANS data was used and the desired number of azimuthal Fourier modes was added. The flow was then initially pulsed in the higher Fourier modes of density to achieve faster development of three-dimensionality. From the experience with the lower Reynolds number wake and following the suggestion by Speziale (1998b), the value of the constant β in the contribution function, equation (2.38), was initially set to $\beta = 2 \cdot 10^{-3}$ and then varied.

Figure 7.8 (a) – (d) shows sideviews of instantaneous total vorticity for FSM calculations on both computational grids with different values of β compared to the DNS. The DNS calculation displays a broad range of scales. For both the FSM calculation on the fine grid and the FSM using the coarse grid with $\beta = 2 \cdot 10^{-4}$, the small-scale structures vanish and only some large-scale structures (on the order of the shear-layer thickness) are resolved on the respective computational grid. The

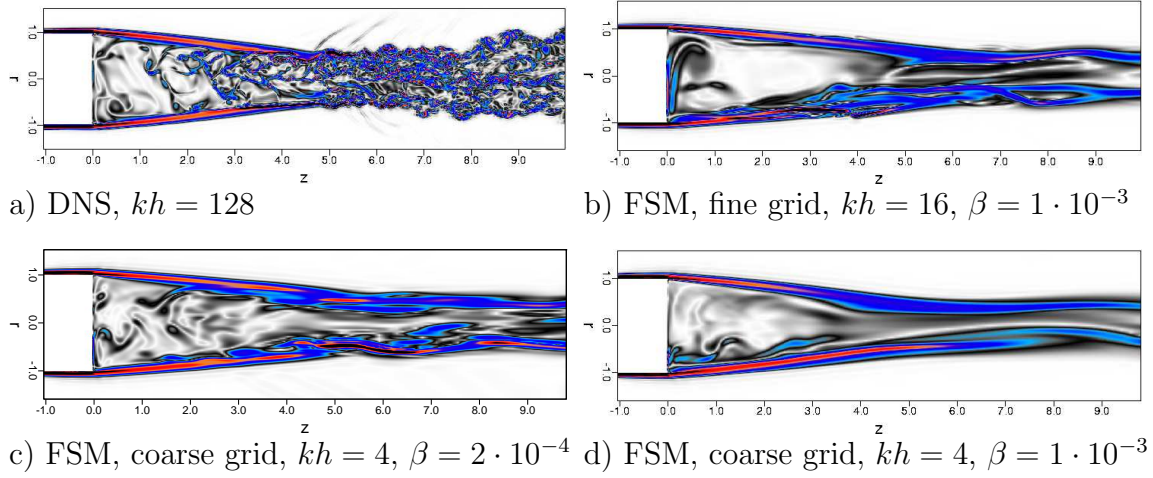


Figure 7.8 Sideviews of contours of instantaneous total vorticity; $Re_D = 60,000$, $M = 2.46$.

values of the time-averaged contribution functions are shown in figure 7.9 for the plane $\theta = 0^\circ$. Clearly, the largest contribution of the turbulence model is provided in the shear layer, reaching values of up to 5% downstream of recompression. The very low value of $f(\Delta/L_K)$ within the recirculation region and the initial shear layer allows for the formation of structures. Increasing β to $1 \cdot 10^{-3}$ on the coarse grid leads to much higher values of the contribution function, as can be seen in figure 7.9. The distribution of $f(\Delta/L_K)$ is very similar to other cases, however, the absolute values are significantly larger, with a maximum of $f(\Delta/L_K) > 10\%$ downstream of recompression. This results in the complete removal of structures, as can be seen in figure 7.8 d), and only a flapping motion of the flow remains, implying that the calculation approaches the URANS-limit of the FSM strategy.

The above results show that similar shapes and values of the contribution function can be obtained with either very coarse grids, using a small value of β , or using finer grids with larger values of β . For a quantitative evaluation of the performance of the FSM on different computational grids and varying β , the time-averaged streamwise velocity along the axis of symmetry and the time-averaged pressure coefficient on the base are examined.

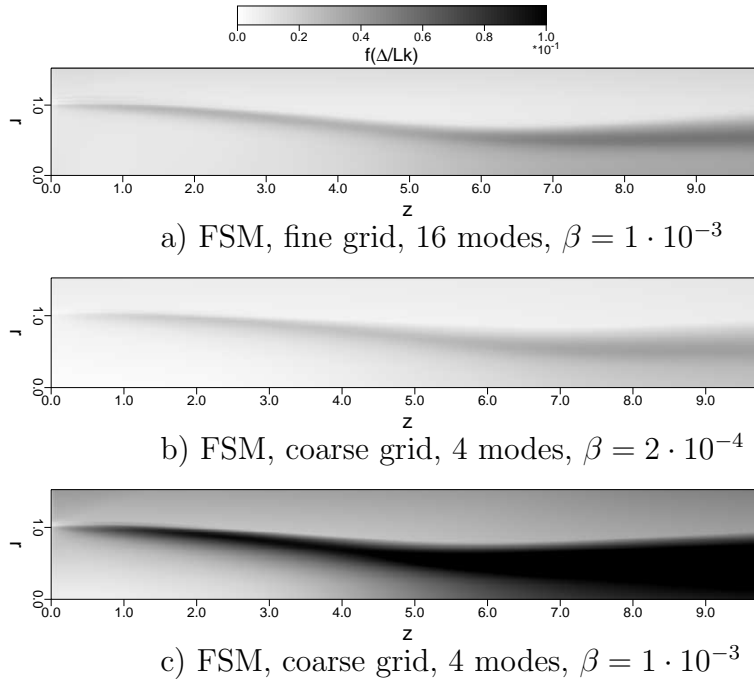


Figure 7.9 Time-averaged contribution function $f(\Delta/L_K)$ for FSM; $Re_D = 60,000$, $M = 2.46$.

First, the results obtained on a fixed computational grid with varying β are shown in figure 7.10. The data from the DNS and the axisymmetric RANS calculation used as initial condition are included for reference. In contrast to the axisymmetric RANS calculations, the pressure distribution obtained by all FSM computations is practically flat, with the magnitude close to the value predicted with DNS. This further confirms that the flat base-pressure is a consequence of the unsteadiness caused by azimuthal modes with low wavenumbers. The best agreement between an FSM calculation and the DNS is achieved by setting $\beta = 1 \cdot 10^{-3}$ or $\beta = 2 \cdot 10^{-3}$. The best match between an FSM calculation and the DNS data in terms of streamwise axis-velocity is also achieved for $\beta = 2 \cdot 10^{-3}$. For smaller values of β , the recirculation region becomes too long. Keeping β constant at $4 \cdot 10^{-3}$ and increasing the number of Fourier modes from 4 to 8 on the coarse computational grid only marginally affects the solution. However, when employing 16 Fourier modes with the same computational grid and $\beta = 4 \cdot 10^{-3}$, the recirculation length is overpredicted and, as a consequence, so is the

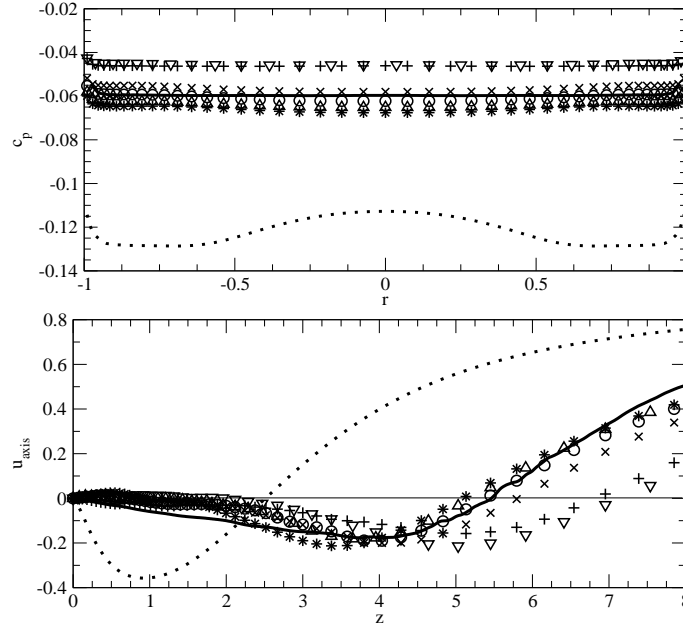


Figure 7.10 Time-averaged pressure coefficient (top) and streamwise axis-velocity (bottom) for FSM on coarse grid with 4 Fourier modes unless noted otherwise; DNS, 128 modes (—), axisymmetric RANS ($\cdot \cdot \cdot$), $\beta = 2 \cdot 10^{-4}$ (+), $\beta = 1 \cdot 10^{-3}$ (\times), $\beta = 2 \cdot 10^{-3}$ (\circ), $\beta = 4 \cdot 10^{-3}$ (\star), $\beta = 4 \cdot 10^{-3}$ and 8 modes (\triangle), $\beta = 4 \cdot 10^{-3}$ and 16 modes (∇); $Re_D = 60,000$, $M = 2.46$.

base pressure. In fact, the results resemble the data obtained with 4 Fourier modes utilizing $\beta = 2 \cdot 10^{-4}$, shown in figure 7.10. Increasing the resolution, here the number of Fourier modes, has the same effect as decreasing β : It leads to smaller values of the contribution function. Consequently, a larger amount of structures has to be resolved by the grid in order to reproduce a physically correct flow field. The streamwise/radial grid, however, apparently is too coarse to capture all relevant structures that are not accounted for by the proper amount of turbulence model. In other words, the contribution from the turbulence model is too small to remove the scales that cannot be resolved on the computational grid. This can be confirmed by looking at the radial amplitude distributions of the FSM calculation on the coarse grid, using too small a value of β , shown in figure 7.11. At the upstream location, as a result of the small values of the contribution function in this region, the magnitudes of all modes

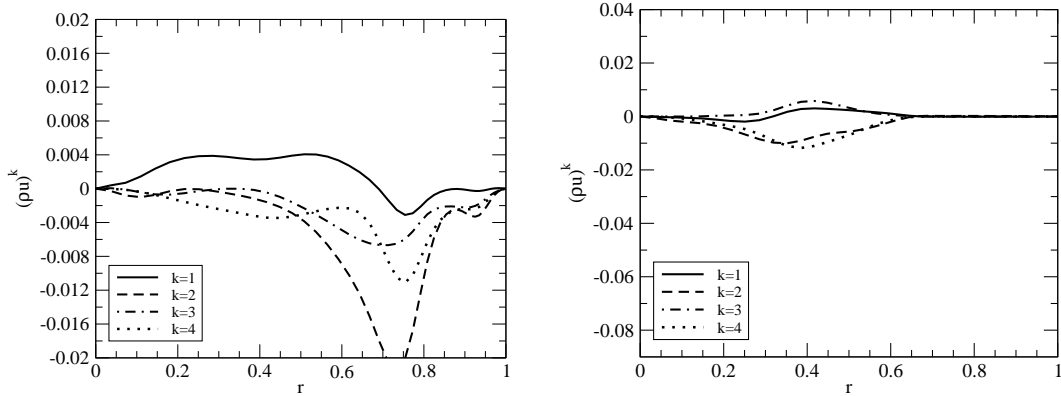


Figure 7.11 Time-averaged mode-shapes of $(\rho u)^k$; FSM calculation on coarse grid with 4 Fourier modes and $\beta = 2 \cdot 10^{-4}$; $z = 2.5$ (left) and $z = 7$ (right); $Re_D = 60,000$, $M = 2.46$.

correspond roughly to those found in DNS. However, mode $k = 4$ is significantly larger in the FSM case. At the downstream location $z = 7$, the fourth mode even possesses the largest magnitude of all modes, an indication that an accumulation of energy in the highest azimuthal mode of the calculation occurs. The energy accumulations reveals the lack of resolution or, alternatively, too little model contribution. In general, at the downstream location, the amplitudes of all modes are strongly reduced versus the DNS case, due to the larger value of the contribution function in this region with larger grid-spacing. Nevertheless, even though the computation was underresolved and the turbulence model contribution was insufficient, the mode shapes show reasonable agreement with the DNS results.

To avoid the above deficiency of the FSM approach, the grid was refined in order for the calculation to resolve the important scales on the computational grid when they are not removed by the model. Because the resolution in the streamwise direction was significantly coarser than in the DNS and since high-order compact stencils are employed in the radial direction with just 40 points less than in the DNS, it was decided to only increase the streamwise resolution to 392 points with $\Delta z_c = 0.01R$ at the corner. Further details of calculations conducted on the fine grid, can be found in table D.8 in Appendix D. The streamwise/radial grid-resolution in combination

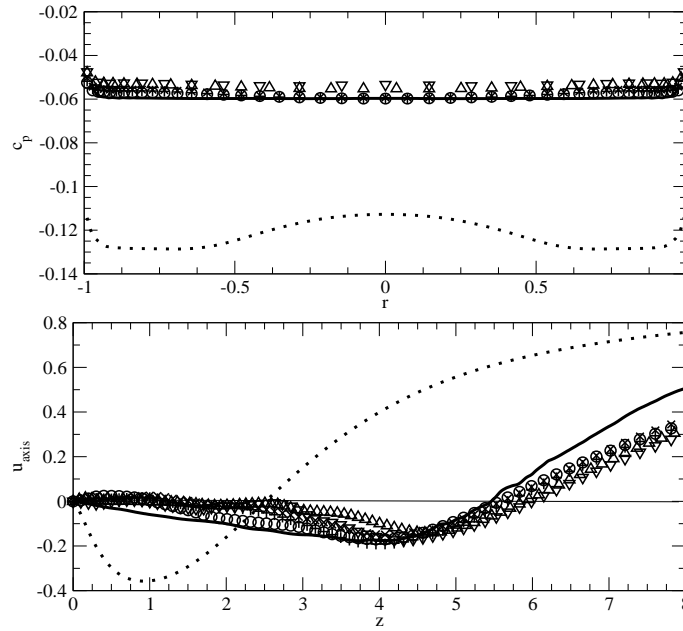


Figure 7.12 Time-averaged pressure coefficient on base (top) and streamwise velocity along axis (bottom) for FSM calculations on fine grid; DNS, 128 modes (—), axisymmetric RANS ($\cdot \cdot \cdot$), $\beta = 1 \cdot 10^{-3}$ and 16 modes (\triangle), $\beta = 1 \cdot 10^{-3}$ and 32 modes (∇), $\beta = 4 \cdot 10^{-3}$ and 8 modes (\circ), $\beta = 4 \cdot 10^{-3}$ and 16 modes ($+$), $\beta = 4 \cdot 10^{-3}$ and 32 modes (\times); $Re_D = 60,000$, $M = 2.46$.

with a larger number of Fourier modes approaches the requirements of “traditional” LES, such as Smagorinsky-type LES.

Figure 7.12 shows the averaged streamwise velocity along the axis of symmetry and the averaged pressure coefficient on the base, obtained from FSM calculations on the fine grid for changing β and different numbers of azimuthal Fourier modes. Choosing $\beta = 1 \cdot 10^{-3}$, the recirculation length and the base-pressure are slightly overpredicted. However, unlike for the coarse-grid case, increasing the number of azimuthal modes from 16 to 32, the same mean base-pressure profile is obtained and the streamwise axis-velocity distribution changes only marginally. It also appears as if the dependence of the solution on the constant β is not as strong as for the FSM calculation on the coarser grid. When increasing the value of β to $4 \cdot 10^{-3}$, the results are only slightly changed from the cases using $\beta = 1 \cdot 10^{-3}$ and the best agreement

with the DNS results is achieved. Again, when increasing the number of azimuthal Fourier modes from 8 to either 16, or even to 32, the solutions continue to agree well with the DNS results. This implies that the model contribution provided by $f(\Delta/L_K)$ corresponds to what is required for a particular resolution, i.e., the FSM is successful in removing the appropriate amount of energy that cannot be resolved on the respective grid. However, it seems as if this behavior can only be observed if the resolution of the calculations approaches that of “traditional” LES in *all* directions. It should also be noted, that the value of β which leads to the best agreement with the DNS data is similar to the value that resulted in the best match for the lower Reynolds number case.

For a more detailed comparison of an FSM calculation on the fine grid with DNS data, the time-averaged mode-shapes of the streamwise velocity component are shown in figure 7.13. The computation on the fine grid using 32 Fourier modes with $\beta = 1 \cdot 10^{-3}$ was selected, as the contribution function showed values $f(\Delta/L_K) < 5\%$ for the entire computational domain, justifying a classification as (non-traditional) LES. In contrast to the data from the underresolved calculation shown in figure 7.11, the ratio between the energy of higher azimuthal modes to the first mode is similar to

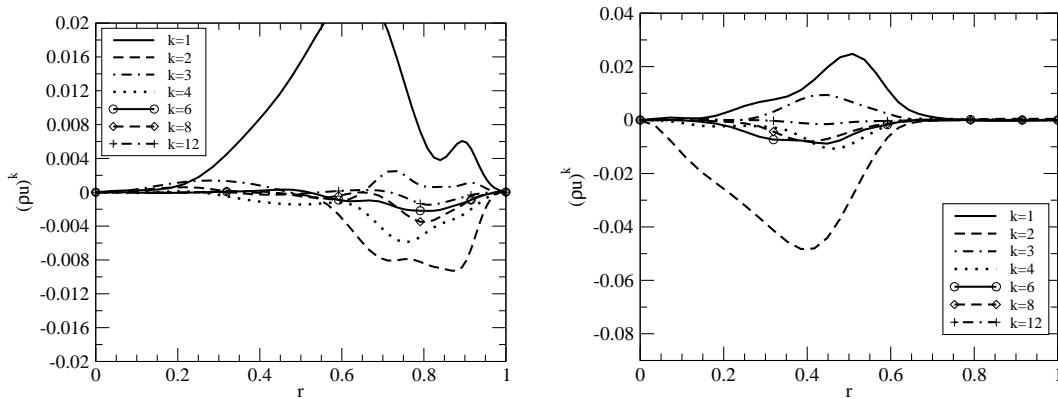


Figure 7.13 Time-averaged mode-shapes of $(\rho u)^k$; FSM calculation on fine grid with 32 modes and $\beta = 1 \cdot 10^{-3}$; $z = 2.5$ (left) and $z = 7$ (right), $Re_D = 60,000$, $M = 2.46$.

that found for the DNS presented in figure 6.38. In fact, the amplitudes of the higher modes possess smaller values relative to the first mode than in the DNS calculation. As the mode-shapes are only shown for the resolved quantities, this implies that the remaining energy of the higher azimuthal modes is provided by the turbulence model, scaled appropriately with the contribution function. Similar to the lower Reynolds number case, the amplitude distributions of most modes agree reasonably well with the mode-shapes found with DNS. Merely the first mode, $k = 1$, does not compare well with the DNS data, and, unlike for the $Re_D = 30,000$ case, shows similarity with the mode-shape found in linear calculations (see figure 5.4) only for the inner part ($r < 0.4$).

In order to assess whether the FSM succeeds in producing the same kind of coherent structures as those found in the DNS, instantaneous iso-contours of $Q = 0.1$ for the calculation using the fine grid with 32 Fourier modes and $\beta = 1 \cdot 10^{-3}$ are shown in figure 7.14. Qualitatively, similar flow features can be observed as in the DNS cases, i.e., helical structures within the shear layer, encircling longitudinal structures within the recirculation region. Also, the same type of streamwise structures are present in the trailing wake. However, due to the larger values of the contribution function in

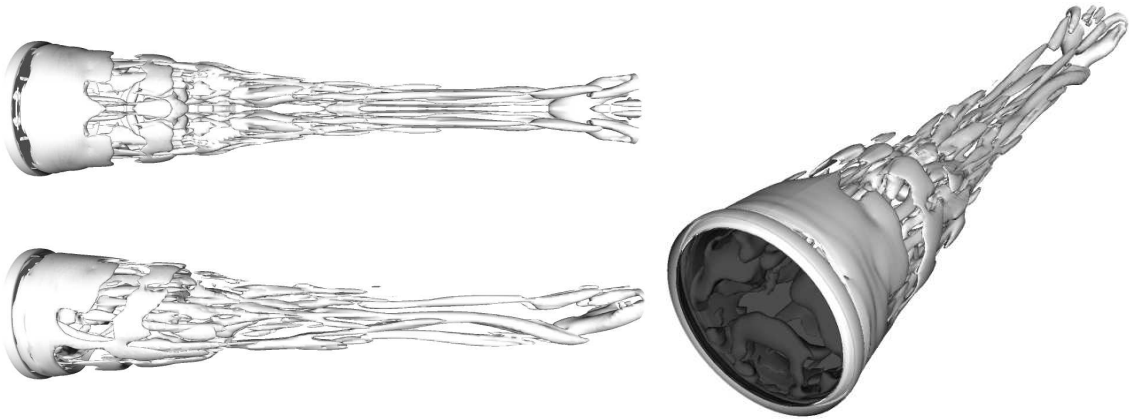


Figure 7.14 Instantaneous iso-contours of $Q = 0.1$ for FSM calculation on fine grid, 32 modes and $\beta = 1 \cdot 10^{-3}$, top- and sideview (top and bottom, left) and perspective view from inflow towards outflow (right); $Re_D = 60,000$, $M = 2.46$.

this region, and, consequently, an increased amount of turbulence viscosity, a considerably smaller amount of small-scale structures appears in the FSM calculation. Nevertheless, considering the good agreement of the mean flow results with the DNS, these small scales seem to be represented reasonably well by the turbulence model.

In summary, the results obtained with the FSM in the URANS-limit show reasonable agreement with the data from the DNS calculation. This is particularly remarkable, considering the drastic savings in computational cost due to the dramatically decreased temporal and spatial resolution requirements as shown in table 7.2. The FSM calculations conducted with a grid-resolution approaching “traditional” LES, albeit still using considerably less azimuthal Fourier modes than would be required for a Smagorinsky-type LES calculation, show even better agreement with DNS. For a constant value of β , the grid-resolution in the azimuthal direction can be significantly increased, maintaining the same correct solution. This implies that the FSM strategy successfully removes the appropriate amount of energy from the calculations that cannot be resolved on the respective grid. The FSM calculations conducted on the fine grid also appear to be successful in predicting the same kind of coherent structures as observed in the DNS. Only the amount of small scales is reduced, as they are removed by the turbulence model. Even when employing the FSM approach

	DNS	FSMc	FSMc	FSMc	FSMf	FSMf	FSMf
points in z	812	194	194	194	392	392	392
points in r	130	90	90	90	90	90	90
modes in θ	128	4	8	16	8	16	32
Δt	$1 \cdot 10^{-3}$		$2.6 \cdot 10^{-3}$		$2.6 \cdot 10^{-3}$		$1.54 \cdot 10^{-3}$
CPU hours	3798*	1.93	3.98	8.76	10.27	21.67	76.1

Table 7.2 Comparison of computational cost per flow-through-time ($t - t_0 \approx 12$) on *HP Alpha* of FSM using the coarse computational grid (FSMc), FSM conducted on the fine grid (FSMf) and DNS calculations; * denotes CPU time on *SGI Origin 3900*; for a comparison of the performance of both computer architectures, see Appendix C.6.2; $Re_D = 60,000$, $M = 2.46$.

using the fine grid, the computational costs are still considerably lower than for DNS (c.f. table 7.2).

7.3 Transitional Wake at $Re_D = 100,000$

In order to show that the contribution function $f(\Delta/L_K)$ not only provides the adequate amount of turbulence modelling for varying grid-resolutions, as shown above, but also when the Reynolds number is changed, several FSM calculations were conducted for $Re_D = 100,000$. This was the highest Reynolds number for which DNS data was available. The set-up of the FSM calculations follows the FSM calculations of the $Re_D = 60,000$ cases on the coarse grid, with all parameters listed in table D.8 in Appendix D. The time-averaged pressure coefficient and streamwise axis-velocity obtained from two FSM calculations employing 16 Fourier modes. Recall that it was

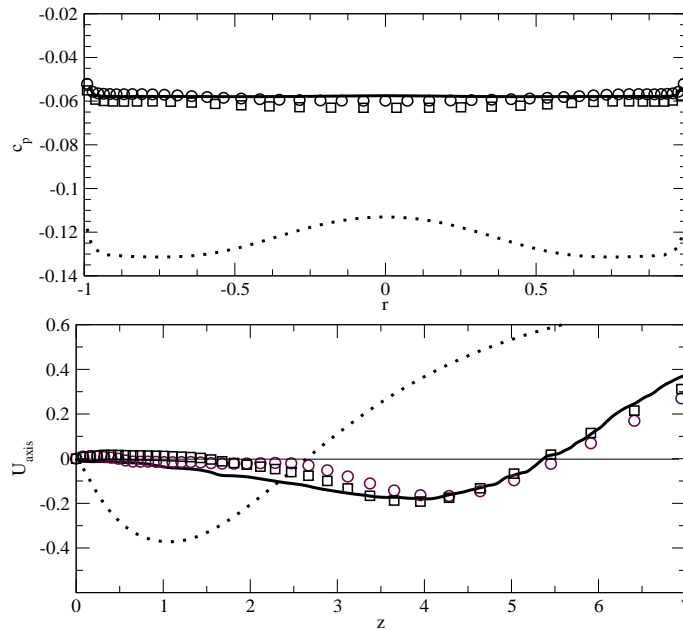


Figure 7.15 Time-averaged pressure coefficient on base (top) and streamwise velocity along axis (bottom) for FSM calculations on coarse grid with 16 modes; DNS, 128 modes (—), axisymmetric RANS (\cdots), $\beta = 2 \cdot 10^{-3}$ (\circ), $\beta = 4 \cdot 10^{-3}$ (\square); $Re_D = 100,000$, $M = 2.46$.

shown in section 6.2.4 that at this Reynolds number, azimuthal modes up to $k = 16$ contain a considerable amount of energy. are shown in figure 7.15. As for the FSM calculations at lower Reynolds numbers, best agreement with the DNS data is achieved when choosing $\beta = 2 \cdot 10^{-3}$ or $\beta = 4 \cdot 10^{-3}$. An entirely flat pressure-distribution on the base is predicted with the correct mean value and the recirculation length agrees very well with that obtained using DNS. The reduction in computational time for this case is even more dramatic than for the lower Reynolds number cases, as the DNS calculation required an increased number of grid-points and, consequently, smaller time-steps. Because the FSM calculations were conducted on the same computational grids as that used for the $Re_D = 60,000$ case, the computational cost did not increase and is listed in the sixth column of table 7.2. The above results illustrate, that on a given computational grid, the contribution function, using the same values of β , successfully provides the appropriate amount of turbulence modelling for varying Reynolds numbers.

7.3.1 Flow Control

Flow control mechanisms that were tested successfully at $M = 2.46$ and $Re_D = 30,000$ using DNS are applied to supersonic base flows at $M = 2.46$ and $Re_D = 100,000$ using FSM. The same active and passive control techniques are employed as discussed previously for $Re_D = 30,000$.

For reference and comparison, in Figure 7.16, dominant flow structures are shown for the “unforced” wake. Shown are perspective top- and sideviews of iso-contours of $Q = 0.05$ obtained from an FSM calculation of the unforced case at $Re_D = 100,000$. Helical structures can be observed in the shear layer close to the base. In addition, a large number of longitudinal structures can be seen within the recirculation region and hairpin vortices are present downstream of the recompression region.

For $Re_D = 100,000$, FSM calculations were performed with steady forcing of

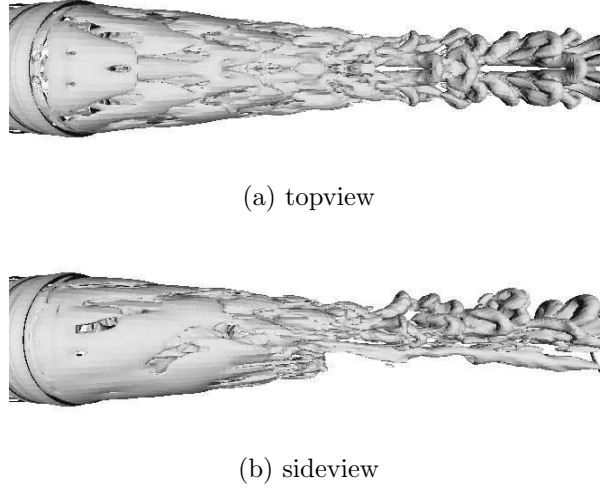


Figure 7.16 Instantaneous iso-contours of $Q = 0.05$ for the unforced case, Perspective topview and sideview with flow from left to right; FSM for $Re_D = 100,000$

modes $k = 2, 4, 8, 16$ and periodic forcing of the zeroth mode, $k = 0$. Contours of time-averaged streamwise vorticity of endviews at $z = 1$ are shown in figure 7.17 to illustrate the different development of the structures in the shear layer when employing steady forcing. Visualizations of instantaneous iso-contours of $Q = 0.05$ are shown in figure 7.18. When steady forcing with an amplitude $A_{dist} = 1.0$ is applied to the azimuthal/helical modes $k = 2$ and $k = 4$ (see Figures 7.18a and 7.18b), the flowfield resembles the unforced case and no significant longitudinal vortices emerging from the forcing location can be observed. However, once the higher modes $k = 8$

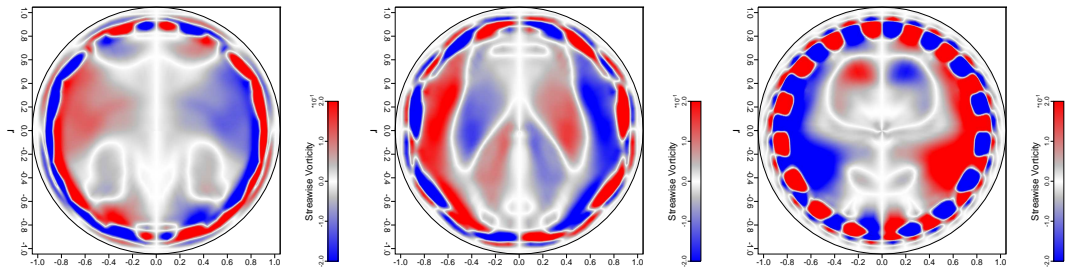


Figure 7.17 Endviews of time-averaged streamwise vorticity in the initial shear-layer at $z=1$; steady azimuthal forcing of $k = 4$, $k = 8$ and $k = 16$ from left to right; FSM for $Re_D = 100,000$.

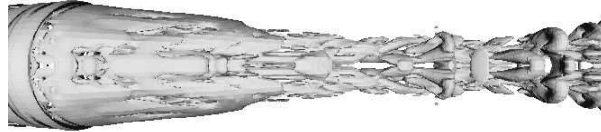
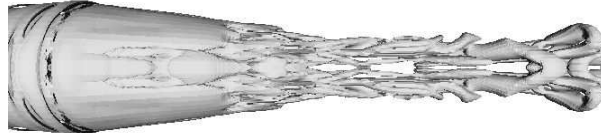
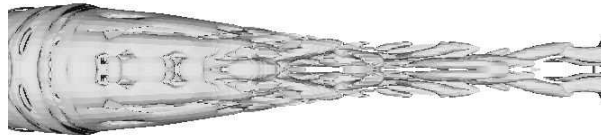
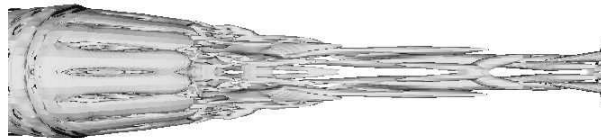
(a) steady forcing of $k = 2$ (b) steady forcing of $k = 4$ (c) steady forcing of $k = 8$ (d) steady forcing of $k = 16$

Figure 7.18 Instantaneous iso-contours of $Q = 0.05$ for steady forcing cases with $A_{dist} = 1.0$, perspective topview with flow from left to right; FSM for $Re_D = 100,000$.

and 16 are forced (see Figures 7.18c and 7.18d), the flowfield differs considerably from the unforced case. As in the lower Reynolds number case investigated using DNS, longitudinal structures can be seen emanating from the forcing location with the azimuthal spacing of these structures decreasing for the higher mode numbers. Overall, when steady forcing of the higher modes is employed, energetic longitudinal structures are produced which increase the mixing within the recirculation region.

When applying periodic axisymmetric forcing, several different frequencies were

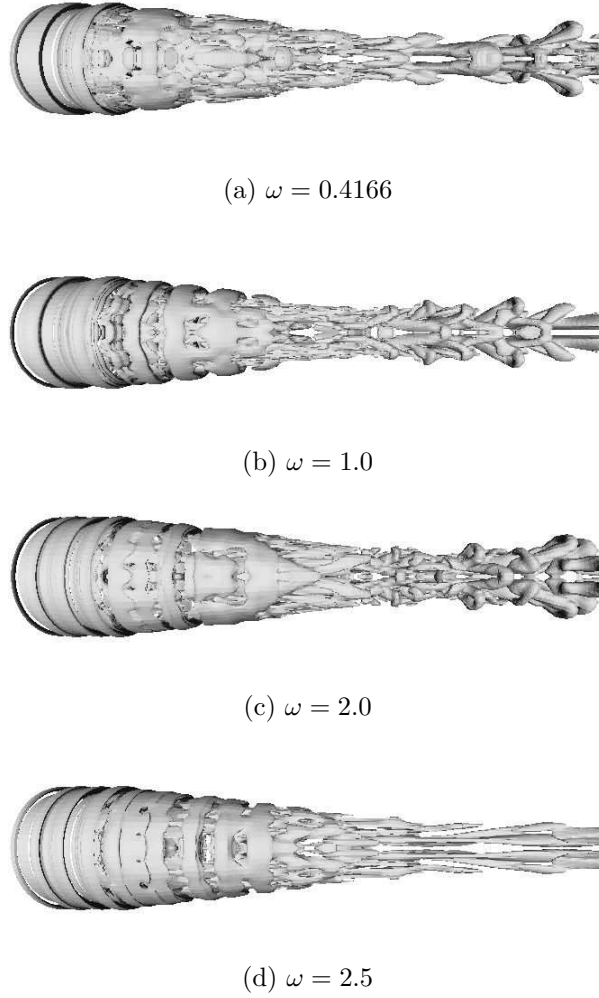


Figure 7.19 Instantaneous iso-contours of $Q = 0.05$ for periodic forcing cases with $A_{dist} = 1.0$, perspective topview with flow from left to right; FSM for $Re_D = 100,000$.

investigated. First, calculations were carried out with a frequency $\omega = 0.4166$ which corresponds to the most unstable frequency of the axisymmetric mode at $Re_D = 30,000$. However, for the unforced case at $Re_D = 100,000$, DNS conducted by Sandberg & Fasel (2004, 2006*b,a*) has revealed that a significant amount of energy is contained in frequencies with a Strouhal number greater than one. This suggests that a strong response might occur when forcing at higher frequencies. Therefore, a range of higher frequencies, $\omega = 1.0, 2.0, 2.5$, and 3.0 , was investigated. Results from

these investigations are shown in figure 7.19. Axisymmetric structures generated just upstream of the corner separation can be observed in the shear layer. However, the azimuthal modulation due to the dominant helical modes is less pronounced than was observed at $Re_D = 30,000$. When the axisymmetric mode was forced with amplitude $A_{dist} = 1.0$ and frequency $\omega = 0.4166$, the flow structures far downstream from the base the flow resemble those of the unforced flow. Higher frequencies, $\omega = 1.0$ and 2.0 , produce an increasing number of axisymmetric structures but far downstream the flow is still similar to the unforced flowfield. Finally when a high frequency $\omega = 2.5$ is used, the hair pin vortices that are present in the trailing wake for the unforced flow and low frequency cases disappear. It is suggested that at this high frequency, the energy otherwise transferred to the helical structures is now transferred to the axisymmetric mode which does not exhibit significant spatial growth. As the helical modes are far less energetic in this case, the formation of hairpin vortices is suppressed.

The time-averaged pressure coefficient along the base and the streamwise velocity

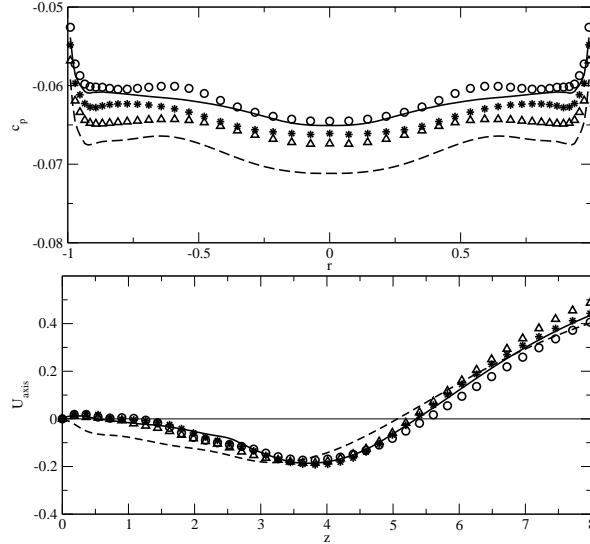


Figure 7.20 Pressure coefficient on base (left) and streamwise velocity along axis of symmetry (right) using steady forcing of higher azimuthal modes with $A_{dist} = 1.0$; unforced case (—), forcing $k = 2$, (\circ), forcing $k = 4$, (\triangle), forcing $k = 8$, ($*$), forcing $k = 16$, (— —); FSM for $Re_D = 100,000$.

along the axis are shown in figure 7.20 for steady forcing of the higher azimuthal modes and for the unforced reference case. When forcing mode $k = 2$, the recirculation length is slightly increased, resulting in a slight pressure increase. When forcing azimuthal modes with $k > 2$, the recirculation length decreases due to the entrainment of low-speed fluid from the recirculation region, as seen already in the earlier investigation of base flows at $Re_D = 30,000$. However, in contrast to the lower Reynolds number cases, the base pressure also decreases for all calculations where steady forcing was applied to $k > 2$. This is in agreement with experiments by Bourdon & Dutton (2001) at an even higher Reynolds number who did not find an increase in base pressure when generating longitudinal vortices by means of tabs on the axisymmetric body.

For periodic forcing of the axisymmetric mode, the time-averaged base-pressure coefficient and the streamwise axis-velocity are shown in figure 7.21. When forcing with a frequency $\omega = 0.4166$ the recirculation length is decreased, and, in contrast to the lower Reynolds number case, the base pressure is considerably decreased. But as

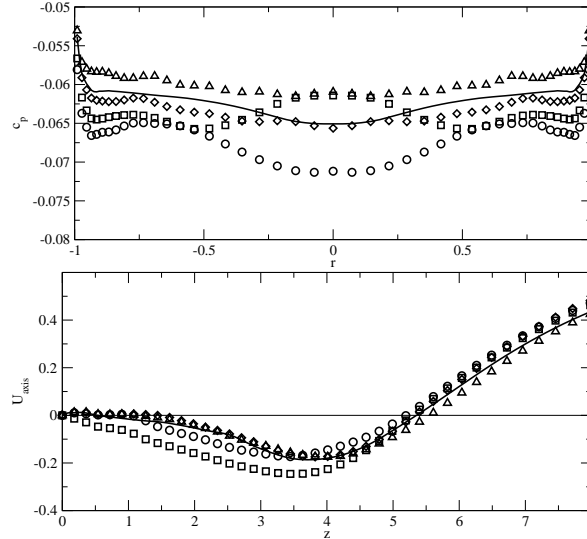


Figure 7.21 Pressure coefficient on base (left) and streamwise velocity along axis of symmetry (right) for cases with periodic forcing of axisymmetric mode, $k = 0$, $A_{dist} = 1.0$; unforced case (—), $\omega = 0.4166$ (\circ), $\omega = 1.0$ (\square), $\omega = 2.0$ (\diamond), $\omega = 2.5$ (\triangle); FSM for $Re_D = 100,000$.

the frequency increases, both the recirculation length and the base pressure increase. In fact, for $\omega = 2.5$ the base pressure is increased by 5% over the unforced case. This result is consistent with the findings of Bourdon & Dutton (2001) who found an increase in base pressure only when forcing the axisymmetric mode. Note, however, that in the experiment mode $k = 0$ was forced using an axisymmetric trip, i.e., with a steady perturbation, in contrast to the periodic forcing in our simulations.

7.4 High Reynolds Number UIUC Case

It was shown in the above sections that the FSM is capable of reproducing DNS results of transitional axisymmetric wakes with reasonable accuracy at significantly lower computational cost. However, most applications that involve base flows, such as projectiles or coasting missiles, are subject to considerably higher Reynolds numbers. As mentioned in the introduction, an extensive investigation of high Reynolds number base flows has been conducted by Dutton and co-workers at the University of Illinois at Urbana Champaign (UIUC). The results published in Herrin & Dutton (1994) will be used for reference and are denoted as “UIUC case” in the following. The flow investigated in the experiments is fully turbulent, i.e., a turbulent approach flow separates at the base corner and the shear layer that forms immediately downstream of the base also is turbulent. It will be demonstrated that fully resolved DNS of the UIUC case are out of reach for present supercomputers. Therefore, calculations of the UIUC case were conducted, employing turbulence simulation strategies.

The turbulent approach boundary layer of the high Reynolds number case constitutes an additional difficulty for the calculations. For both axisymmetric RANS and FSM calculations, a very fine grid close to the wall would be necessary in order to obtain the required resolution of $y^+ \approx 1$ for a good representation of the approach boundary layer. With the present explicit code, the small grid-spacing close to the wall would lead to time-steps so small that calculations of the entire base flow

geometry would become unpractical. To circumvent this problem, the following set-up was realized for all calculations: The RANS solution of the approach boundary layer, computed in section 4.5.2, showed very good agreement with the experimental data. Therefore, it was interpolated onto the (coarser) radial grid of the respective calculation and fixed, i.e., the approach flow remained unchanged throughout the simulations.

This approach is considerably different from what other researchers have attempted, such as full LES of the inflow (see Fureby, 1999). However, the concept is not unlike the procedure inherent in the DES approach, where the wall bounded flow region is represented by a steady RANS solution (see Forsythe & Hoffmann, 2000; Forsythe *et al.*, 2002, for example). Several aspects appear to justify this procedure for the present case: The approach boundary layer is thin relative to the radius of the base ($\delta_c = 0.1$), thereby most likely not introducing significant (low frequency) unsteadiness into the initial shear-layer. Furthermore, with the flow being supersonic and an expansion wave forming at separation, no significant feedback from the recirculation region with the approach flow is expected. This is supported by pressure measurements in the approach boundary layer by Herrin & Dutton (1994), who reported that no upstream influence from the base corner separation was evident in the data.

7.4.1 Axisymmetric RANS Calculations

Axisymmetric RANS calculations of the UIUC case were performed, in order to evaluate their performance for a fully turbulent base flow and serving as initial conditions for FSM computations. Several computational grids were used for the RANS calculations to determine the grid-dependence of the turbulence closure. The coarsest grid employed possessed 210 points in the radial direction and 256 points in the streamwise direction, with the smallest grid-spacing at the base corner being $\Delta r_c = \Delta z_c = 5 \cdot 10^{-3}$.

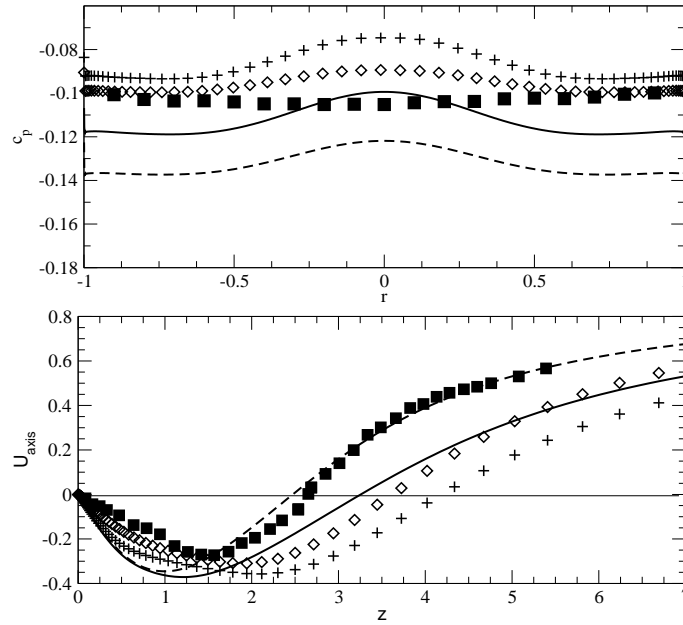


Figure 7.22 Pressure coefficient on base (top) and streamwise velocity along axis of symmetry (bottom) obtained from axisymmetric RANS calculations; UIUC case (■), STKE using c.e. (—), STKE omitting c.e. (---), EASM $_{\alpha}$ using c.e. (+), EASM $_{\alpha}$ omitting c.e. (◇); $Re_D = 3,300,000$, $M = 2.46$.

The finest grid used contained 350 and 512 points in the radial and the streamwise directions, respectively, with $\Delta r_c = \Delta z_c = 4 \cdot 10^{-4}$. For a complete listing of all relevant parameters, see table D.9 in Appendix D.

For all calculations employing the EASM $_{\alpha}$, the wall-distance independent version with $c_T = 4.45$ was used. For reference, axisymmetric RANS calculations employing the STKE model were conducted. Figure 7.22 shows the streamwise axis-velocity and the radial distributions of the pressure coefficient c_p on the base obtained from several axisymmetric RANS calculations. The data from the experiments conducted at UIUC are included for comparison. Only the results from the calculations using the coarse grid are presented, as they showed no difference from the calculations performed on the fine grid, implying that the grid-resolution was adequate. Consistent with all previous axisymmetric results, the base-pressure distribution displays a significant radial variation, which is not present in the experimental data. It can be observed, that the

calculations employing the $EASM_\alpha$ overpredict the recirculation length significantly, resulting in too high a pressure at the base. When the STKE closure is used, the recirculation length becomes slightly shorter, however, the base-pressure is underpredicted. The calculations were repeated omitting the c.e., which reduce the turbulence production, and it can be seen in figure 7.22 (bottom) that the recirculation length is reduced. In fact, the STKE model solution shows quite good agreement with the experiment in terms of recirculation length. However, the reverse flow maximum is too large and the base-pressure is underpredicted even more strongly than when the c.e. were included. The solution obtained with the $EASM_\alpha$ also shows a reduction in the recirculation length and a decrease in mean base-pressure when omitting the c.e., albeit the effect is not as pronounced as when the STKE model is used.

In order to get a more complete picture of the solution predicted with the axisymmetric RANS calculations, radial profiles of the streamwise and radial velocity components, the TKE and the dominant Reynolds shear-stress component $\overline{u'v'}$ are shown in figure 7.23 for two streamwise locations at which experimental data was available. At the streamwise location closest to the base, $z = 0.078$, the velocity profiles obtained numerically show reasonable agreement with the experimental data. However, the maximum TKE value in the shear layer is underpredicted by all turbulence closures, most severely when using the $EASM_\alpha$. In addition, the $EASM_\alpha$ also predicts too low values of K within the recirculation region. The distribution of the Reynolds shear stress $\overline{u'v'}$ is predicted reasonably well, however, the measured peak value in the shear layer is not reached by any of the RANS calculations. At the mean reattachment point $z = 2.67$, reverse flow is predicted at the axis with all turbulent closures due to the overprediction of the recirculation length, shown in figure 7.23, except when using the STKE omitting the c.e. The $EASM_\alpha$ significantly underpredicts the TKE, regardless of whether the c.e. are used or not. In contrast, the level of K has increased to values comparable to the experimental data when employing the STKE model including the c.e. The TKE is even considerably overpredicted when neglect-

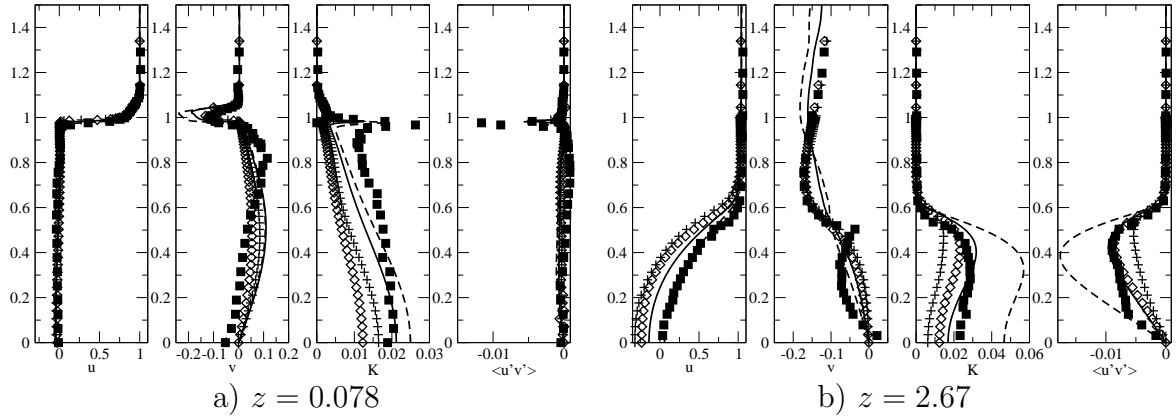


Figure 7.23 Radial profiles of u , v , K and $u'v'$ from axisymmetric RANS calculations; experiments at UIUC (■), STKE using c.e. (—), STKE omitting c.e. (---), $EASM_\alpha$ using c.e. (+), $EASM_\alpha$ omitting c.e. (◇); $Re_D = 3,300,000$, $M = 2.46$.

ing the compressibility modifications. Reasonable agreement with the experiments in terms of the Reynolds shear stress is also found when using the turbulence closures without c.e. The above observations lead to the conclusion that the TKE level at the inflow might not be sufficiently large. For that reason, the inflow conditions for K and ε were rescaled by a factor of 6, in order to correspond with the data by Dutton and co-workers at the streamwise position $z = 0.078$. Axisymmetric RANS calculations, employing both the $EASM_\alpha$ and the STKE model, were repeated using the changed inflow.

In addition to the modified approach flow conditions, the effect of altering several coefficients in the turbulence closures were investigated. Launder & Sharma (1974) specifically calibrated the coefficients contained in the transport equations for K and ε for high Reynolds number jet flows and suggested the following values: $c_{\epsilon 1} = 1.43$ and $c_{\epsilon 2} = 1.92$. Furthermore, Papp *et al.* (2002) recognized that the $EASM_\alpha$ was calibrated for homogeneous turbulent wall-bounded flows, leading to an under-prediction of mixing rates in shear layers. They therefore made an attempt to recalibrate the $EASM_\alpha$ for high Reynolds number jet flows and determined that an increase of a_1 from 0.4866 to 0.5416, in addition to using the coefficients by Launder & Sharma

(1974), had the desired effect of increasing the turbulence levels in the shear layer without adversely affecting the pressure-strain rate correlation. The similarities between the base flow and jets, such as a mean streamwise velocity profile featuring two inflection points might suggest that the coefficients calibrated for jets might also be applicable to base flows.

Results obtained from the axisymmetric RANS calculations, investigating the influence of various coefficients in the turbulence closures using rescaled inflow values for K and ε are presented in figure 7.24. The calculation employing the EASM_α with the original coefficients and using c.e. is the only case that was also conducted for the original inflow conditions, presented in figure 7.22. The effect of the significantly increased levels of K and ε in the approach flow is a drastic decrease in recircula-

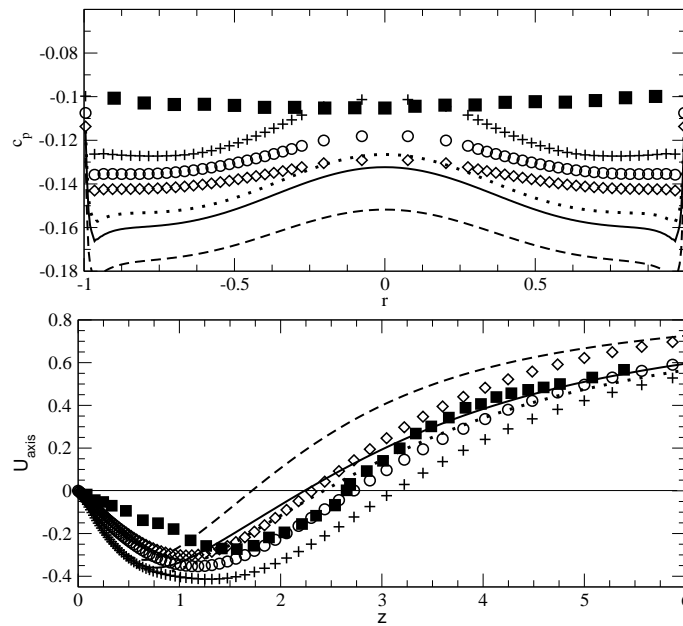


Figure 7.24 Pressure coefficient on base (top) and streamwise velocity along axis of symmetry (bottom) obtained from axisymmetric RANS calculations with modified inflow; UIUC case (■), STKE using c.e. and $c_{\epsilon 1} = 1.43$, $c_{\epsilon 2} = 1.88$ (\cdots), STKE using c.e. and $c_{\epsilon 1} = 1.44$, $c_{\epsilon 2} = 1.92$ (—), STKE omitting c.e. and $c_{\epsilon 1} = 1.44$, $c_{\epsilon 2} = 1.92$ (---), EASM_α using c.e. and original coefficients (+), EASM_α using c.e. and coefficients according to Papp *et al.* (2002) (\circ), EASM_α omitting c.e. and coefficients according to Papp *et al.* (2002) (\diamond); $Re_D = 3,300,000$, $M = 2.46$.

tion length and, consequently, base pressure. When the coefficients in the EASM_α closure are changed to the values suggested by Papp *et al.* (2002), the recirculation length is further decreased and the mean reattachment point corresponds well with the experimental data when the c.e. are included. The base pressure, however, is also further decreased and therefore underpredicts the reference data even more strongly, in particular when the compressibility extensions are not included. All calculations that were conducted with the STKE model underpredicted both the recirculation length and the base pressure significantly, especially when choosing the values of the coefficients for the turbulence closure according to Launder & Sharma (1974).

Radial profiles of the streamwise and radial velocity components, the TKE and the dominant Reynolds shear-stress component $\overline{u'v'}$ are shown for the cases with the modified inflow in figure 7.25. Four streamwise locations are selected, one immediately downstream of separation, one within the recirculation region, one at the mean reattachment point in the experiments and finally a location within the trailing wake. At the streamwise location closest to the base, $z = 0.078$, the velocity profiles obtained numerically show quite good agreement with the experimental data. In contrast to the results discussed earlier, the distribution of K corresponds well with the experimental data when using the EASM_α . The STKE closure overpredicts the TKE at this location. The Reynolds shear-stress obtained from all RANS calculations shows good agreement with the experimental data. When looking at the profiles obtained within the recirculation region, at $z = 1.26$, it can be observed that the STKE model severely overpredicts the TKE and the Reynolds shear-stress. Quite good agreement with the experimental data is found for the turbulence quantities when employing the EASM_α with the modification according to Papp *et al.* (2002). Using the original coefficients for the EASM_α , both K and $\overline{u'v'}$ are underpredicted. The converse, however, is the case for locations farther downstream. At the locations $z = 2.67$ and $z = 4$, best agreement with the experimental data for the turbulence quantities is found when using the EASM_α with the original coefficients. The recalibrated EASM_α overpredicts

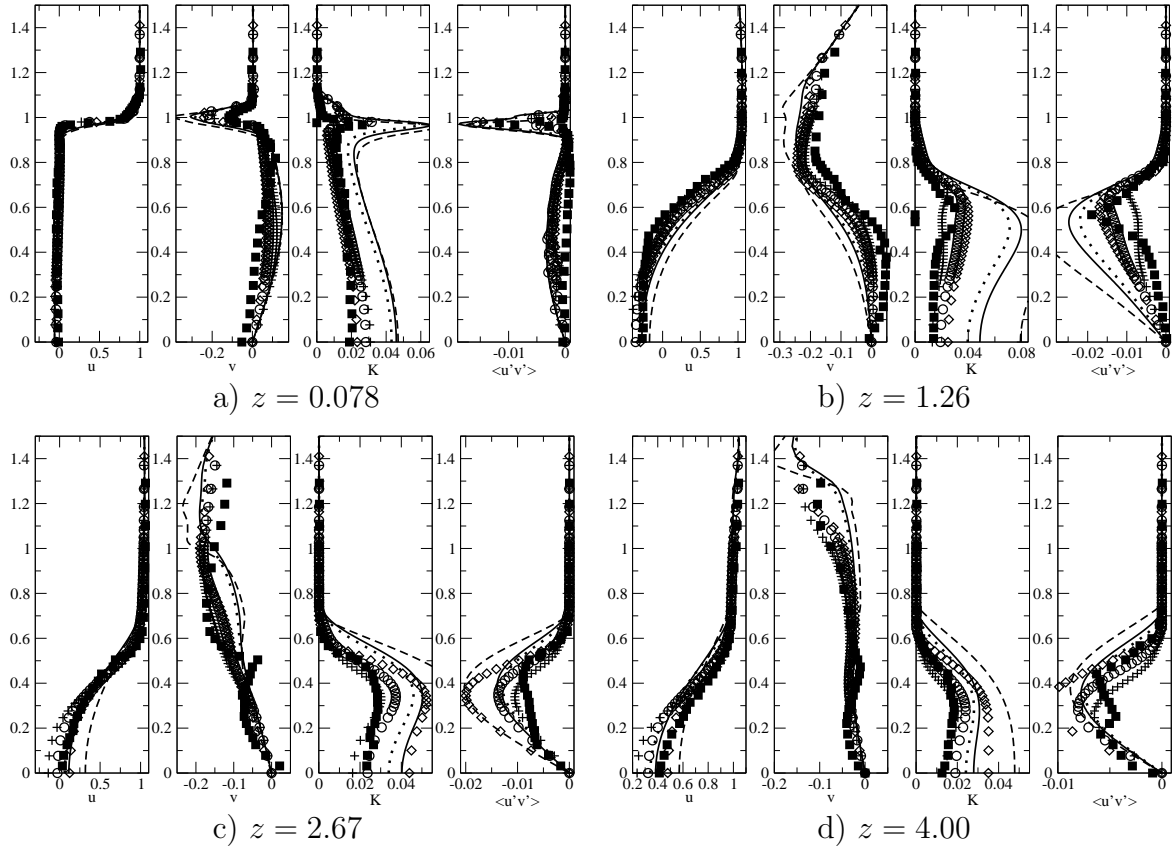


Figure 7.25 Radial profiles of u , v , K and $u'v'$ from RANS calculations using modified inflow conditions; experiments at UIUC (■), STKE using c.e. and $c_{\epsilon 1} = 1.43$, $c_{\epsilon 2} = 1.88$ (\cdots), STKE using c.e. and $c_{\epsilon 1} = 1.44$, $c_{\epsilon 2} = 1.92$ (—), STKE omitting c.e. and $c_{\epsilon 1} = 1.44$, $c_{\epsilon 2} = 1.92$ (---), EASMA $_{\alpha}$ using c.e. and original coefficients (+), EASMA $_{\alpha}$ using c.e. and coefficients according to Papp *et al.* (2002) (\circ), EASMA $_{\alpha}$ omitting c.e. and coefficients according to Papp *et al.* (2002) (\diamond); $Re_D = 3,300,000$, $M = 2.46$.

both K and $\overline{u'v'}$ at the mean reattachment points and in the trailing wake. At the two latter locations, the STKE model considerably overpredicts the maxima of both K and $\overline{u'v'}$.

From the axisymmetric RANS calculations conducted for the UIUC case, it was determined which turbulence closure, including the choice of coefficients, was the most promising underlying model for the FSM calculations. Furthermore, the RANS results will be used as initial condition for the three-dimensional unsteady simula-

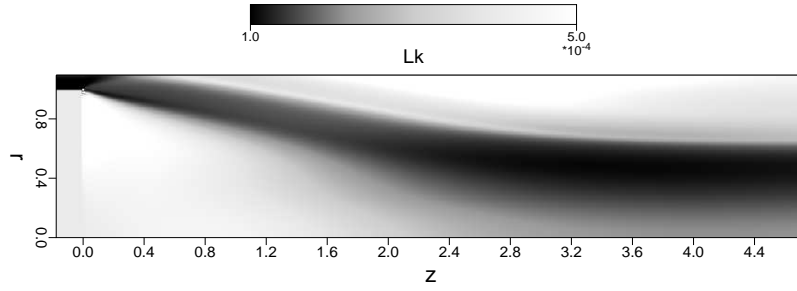


Figure 7.26 Estimate of the Kolmogorov length-scale, based on ε obtained from axisymmetric RANS calculation; $Re_D = 3,300,000$ and $M = 2.46$.

tions. Also, the data obtained from the axisymmetric RANS calculations could be used to estimate the resolution requirements of a fully resolved DNS. To that end, the Kolmogorov length-scale was computed according to $L_K = \left(\frac{\mu}{\rho Re}\right)^{3/4} / \epsilon^{1/4}$, using the ε distribution obtained from the calculation employing the EASM $_{\alpha}$ with c.e. The resulting distribution of L_K is shown in figure 7.26. It can be observed that the lowest values of the turbulent length-scale are reached in the approach boundary layer, the initial shear-layer and the recompression region. In those regions, $L_K \sim 1 \cdot 10^{-4}$, while the Kolmogorov length-scale estimate exhibits values of up to $5 \cdot 10^{-4}$ in the remaining region of interest, i.e., the recirculation region and the developing trailing wake. Assuming that a numerical code was available that either employs adaptive mesh refinement or the numerical grid was *a priori* generated such that discrete points are clustered in region where L_K takes the smallest values, the following estimate can be made for the grid-point requirement: Provided that the generation of turbulent inflow data is successfully accomplished, in the streamwise direction, roughly 8,000 points would be required for the interval $0 \leq z \leq 5$, in order to reach a resolution on the order of the Kolmogorov length-scale. From the validation calculations for the turbulent approach boundary layer (section 4.5.2), it was found that a wall-normal grid-resolution of $\Delta r_{wall} = 5 \cdot 10^{-5}$ was required to obtain $y^+ \approx 1$. Taking this into account and assuming that strong stretching can be used, the number of points required in the radial direction can be estimated to be approximately 3,000.

In the azimuthal direction, at least 1,000 Fourier modes would have to be used in order to provide sufficient grid-resolution, in particular where $r = \mathcal{O}(1)$. In total, the computational grid for a DNS of the UIUC case would therefore require $\mathcal{O}(10^{10})$ points. In addition, even if employing a fully implicit numerical code, to conduct a time-accurate simulation, one would have to adhere to the CFL limit, resulting in time-steps on the order of $dt \approx 5 \cdot 10^{-5}$. Recall, that the largest grid used for the simulations of the transitional case at $Re_D = 100,000$ contained $5.6 \cdot 10^7$ grid-points, employing a time-step $dt = 1.2 \cdot 10^{-3}$. The simulation required computation times of several months on current supercomputers. Clearly, a DNS of the UIUC case is out of reach for current high-performance computers, hence the current effort in finding other simulation strategies for unsteady high Reynolds number flows.

In summary, axisymmetric RANS calculations, using the STKE model and the $EASM_\alpha$ were conducted of the UIUC case. The effect of compressible extensions and varying model coefficients was investigated. It was shown that choosing $c_{e1} = 1.43$ and $c_{e2} = 1.92$ and using the modifications to the $EASM_\alpha$ suggested by Papp *et al.* (2002) leads to an increase in the TKE and the Reynolds shear stress, causing a decrease in recirculation length and base pressure. Conversely, incorporating c.e. as presented in section 2.2.4 resulted in decreased values of K and $\overline{u'v'}$ and, consequently, an increase in recirculation length and base pressure. The inflow values for the turbulent quantities K and ε were shown to play a significant role in the global solution. Larger values of K and ε at the inflow produce a smaller base pressure and a reduced recirculation length. In general, the $EASM_\alpha$ appears to produce more accurate distributions of turbulence quantities and a flatter base pressure distribution while allowing for faster convergence due to increased numerical stability. However, none of the RANS calculations is able to reproduce the UIUC results accurately, implying that it is essential to capture the unsteady dynamics of the large-scale structures, as was demonstrated for the transitional base flows. Finally, the RANS data was used

to illustrate the tremendous requirements of computational resources if a DNS of the UIUC case was to be attempted.

7.4.2 3-D FSM Calculations

Considering the results obtained from the axisymmetric RANS calculations, all FSM calculations of the UIUC case were conducted employing the EASM _{α} using compressible extensions and coefficients according to Papp *et al.* (2002). Initially, the same constant β for equation (2.38) was employed as for all transitional cases. However, even with the finest grid-resolution used in the $r-z$ -plane and up to 32 Fourier modes, the contribution function was on the order of 40%. Such a large amount of model contribution did not permit the formation of structures. Thus, to reduce the values of the contribution function sufficiently to allow for the generation and evolution of structures in the flow, a significantly finer grid would have been required. Instead, to enable computations not exceeding approximately one week of computing time, the constant β was decreased to values of the order of $\mathcal{O}(10^{-4})$. This resulted in $f(\Delta/L_K) < 10\%$ in the initial shear-layer and within the recirculations region, and increasing values in the trailing wake due to the strong streamwise stretching of the grid.

FSM calculations were conducted on the coarse grid presented for the axisymmetric RANS calculations and on a grid composed of the same radial grid as the coarse grid, but with a refined grid in the streamwise direction. In the experiments conducted at UIUC, longitudinal structures were observed within the shear layer. In order to capture streamwise structures within the initial shear-layer, it was determined that at least 16 Fourier modes were required. Therefore, the FSM calculations were exclusively conducted with $kh \geq 16$. For all further parameters, see table D.9 in Appendix D.

A time sequence of instantaneous iso-contours of $Q = 0.5$, obtained from the FSM

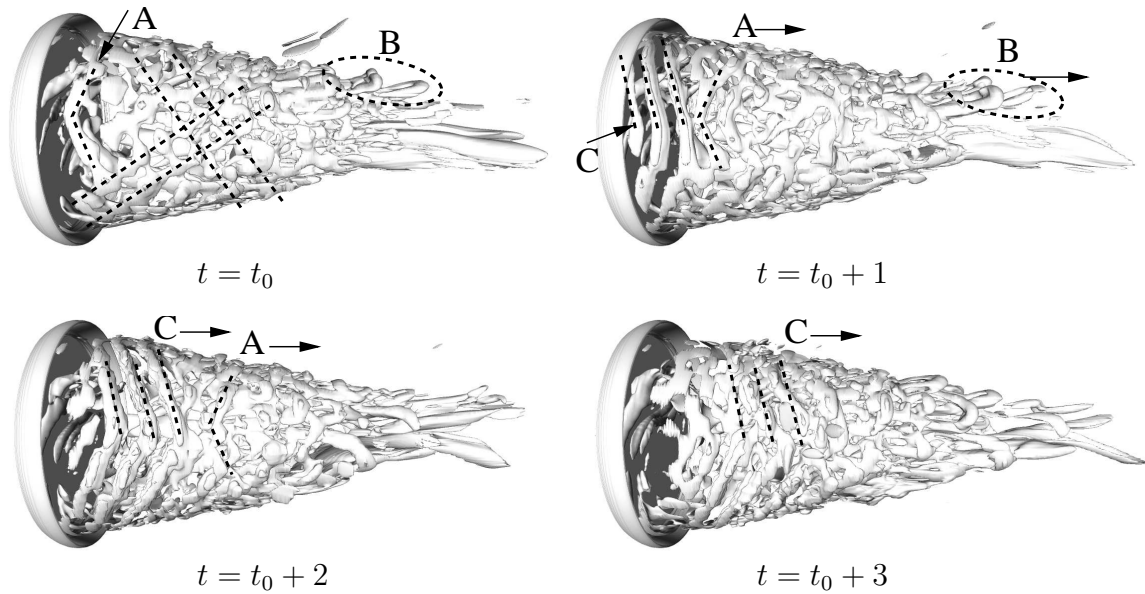


Figure 7.27 Instantaneous iso-contours of $Q = 0.5$ for FSM calculation using 16 modes and $\beta = 1 \cdot 10^{-4}$, perspective sideviews with flow from left to right; base of body shaded dark grey; $Re_D = 3,300,000$, $M = 2.46$.

calculation using the refined grid and 16 azimuthal modes are presented in figure 7.27. The time difference between each consecutive time-level is $\Delta t = 1$, which corresponds to free-stream fluid travelling one base-radius downstream. Helical structures in the shear layer can clearly be identified. In contradistinction to the low Reynolds number cases, the helical structures within the shear layer travel downstream (see, e.g., structures marked with “A” or “C”). Following the arguments used when discussing the transitional DNS results (c.f. section 6.1.2), this implies that the growth rates of the applicable instabilities are large enough to overcome the high compressibility in this region, such that visible structures form in the supersonic region of the shear layer. The high-wavenumber variation of the helical structures most likely is caused by streamwise structures in the shear layer, as observed in endviews of the experimental data and DNS data of the $Re_D = 100,000$ case. In addition, this result is also in accordance with the trend established with TDNS and LNS calculations, showing that higher azimuthal modes appear to play a significant role for increasing

Reynolds numbers. As in the transitional cases, streamwise structures are present within the recirculation region and extend into the developing wake. The structures vanish downstream of the mean reattachment point due to the large contribution of the turbulence model.

Another distinction from the transitional cases is the formation of hairpin vortices, as marked with “B”, upstream of the recompression region. These might be generated by secondary instabilities affecting the initial helical structures in the shear layer. Alternatively, they could be produced by fluid forming streamwise structures when passing the chevron-like structure of the inner shear-layer, as discussed in section 6.1.2.

In order to evaluate whether the FSM calculations are capable of reproducing the mean flow data available from the experiments, the base-pressure distribution and

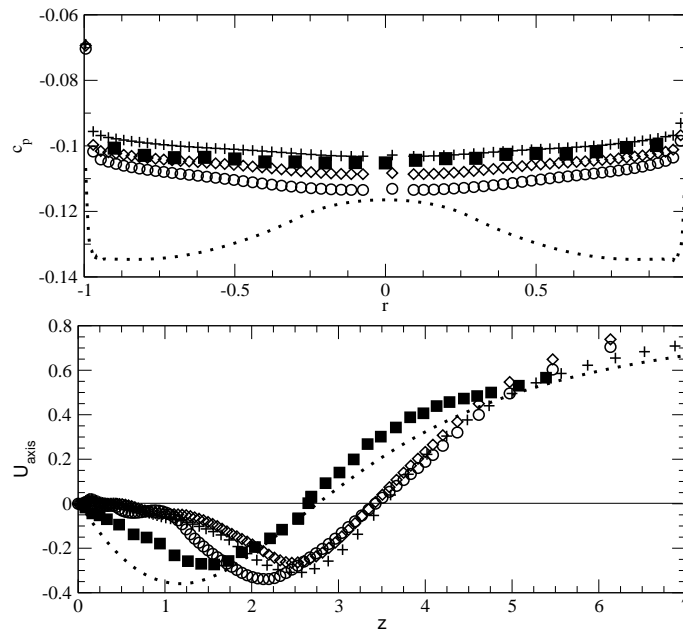


Figure 7.28 Time-averaged pressure coefficient on base (top) and streamwise velocity along axis of symmetry (bottom) obtained from FSM calculations; UIUC case (■), axisymmetric RANS calculation (\cdots), FSM with 256 streamwise points, $\beta = 1 \cdot 10^{-4}$ and 16 modes (+), FSM with 512 streamwise points, $\beta = 1 \cdot 10^{-4}$ and 16 modes (\diamond), FSM with 512 streamwise points, $\beta = 1 \cdot 10^{-4}$ and 32 modes (\circ); $Re_D = 3,300,000$, $M = 2.46$.

the streamwise axis-velocity are presented in figure 7.28. As opposed to the RANS solution, shown for comparison, the data obtained from the FSM calculations show good agreement with the experimental curve, in particular considering the radial distribution. The mean-pressure values depend on the grid-resolution of the respective calculation. Both calculations employing 16 Fourier modes show the smallest deviation from the experimental data. For the calculation on the fine grid, using 32 azimuthal modes, the pressure value is slightly underpredicted. In spite of the good results obtained for the pressure distribution, all FSM calculation overpredict the recirculation length by approximately 0.7 radii. Several reasons for this behavior are suggested: First, the values of K and ε in the (fixed) approach flow might not correspond to those present in the experiments. It was shown above, that the magnitudes of the turbulent quantities at the inflow have a pronounced effect on the global solution, in particular on the recirculation length. Second, a very small value of β was chosen for a grid that most likely was too coarse to resolve the relevant length-scales (see discussion in section 7.2.2). Third, a steady approach boundary layer is prescribed and, therefore, the generation of unsteadiness is delayed, i.e., the flow must “transition” from a steady to an unsteady state downstream of the base. The shallow slopes of the streamwise axis-velocity profiles might indeed be an indication that this is the case. The slopes resemble those found for all transitional cases from both DNS and FSM calculations. In the fully turbulent UIUC case, the slope at the base-wall is considerably steeper. All axisymmetric RANS calculations produce an even larger slope, presumably because turbulence production is overpredicted in this region.

Finally, the time-averaged mode-shapes of all resolved velocity components are presented in figure 7.29 for two streamwise locations, one within the recirculation region ($z = 2$) and one downstream of the mean reattachment point ($z = 4$). At $z = 2$, the first azimuthal mode is by far the most dominant mode. Modes $k = 2$ and $k = 3$ possess roughly the same amplitude but exhibit different mode-shapes. Higher modes exhibit fairly small amplitudes, due to the damping effect of the turbulence model.

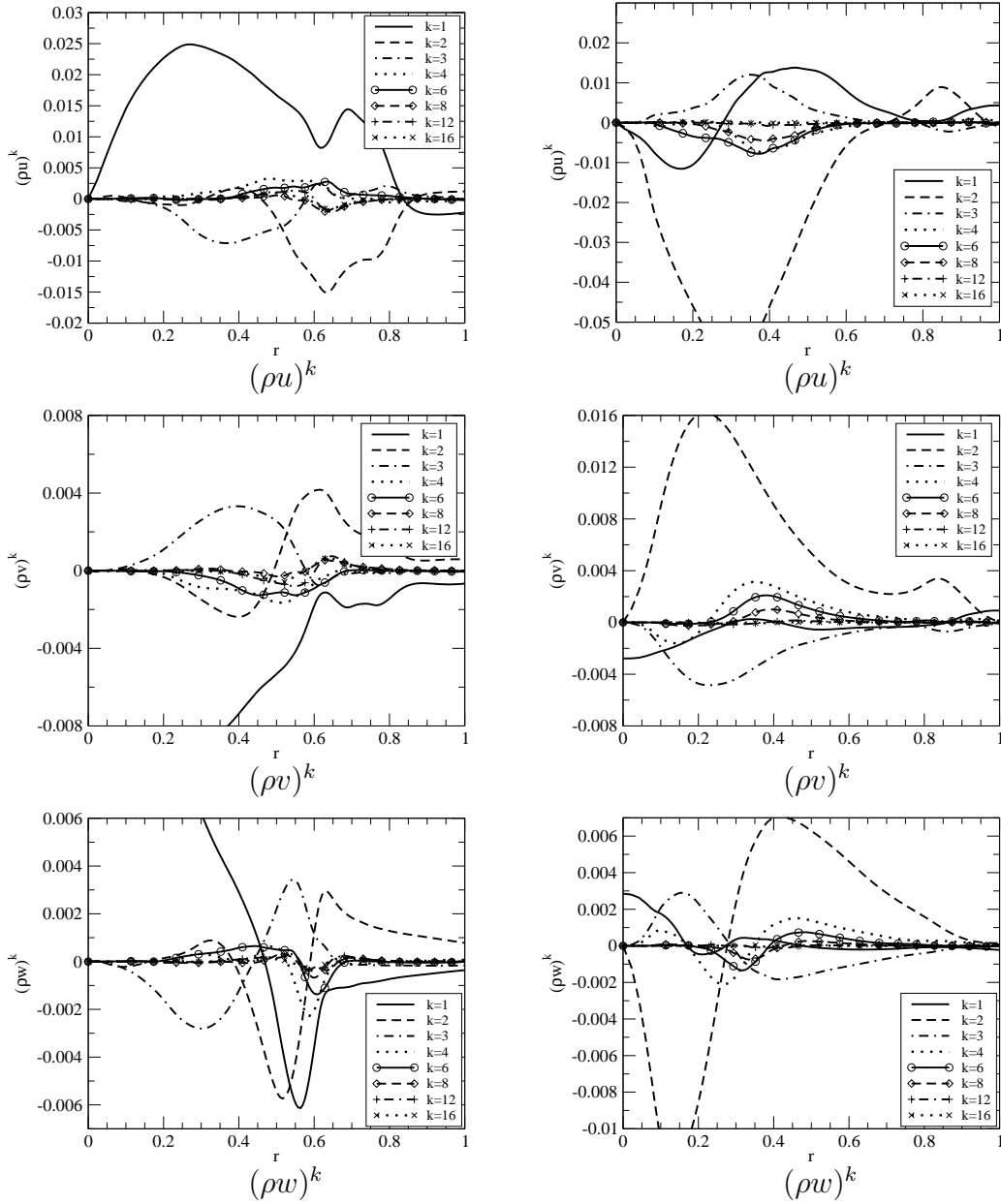


Figure 7.29 Time-averaged mode-shapes obtained from FSM calculation; fine grid (16 modes), $\beta = 1 \cdot 10^{-4}$; $z = 2$ (left) and $z = 4$ (right), $Re_D = 3,300,000$, $M = 2.46$.

At the second location, $z = 4$, a clear dominance of mode $k = 2$ can be observed. Recall, that in the $Re_D = 100,000$ case, mode $k = 2$ was also the most dominant mode, along with $k = 4$. These two modes were responsible for producing a four lobe-pattern of the wake, that compared very well with the UIUC data (see figure

6.49). However, in the figures presently discussed, the amplitudes of mode $k = 4$ are at most 20% of the most dominant mode $k = 2$. As only the time-average of the resolved scales are shown, a significant amount of the energy of $k = 4$ might be contained in the modelled portion of the spectrum.

In summary, the FSM calculations conducted of the UIUC case succeeded in reproducing the pressure distribution of the experiments with reasonable accuracy. The streamwise velocity at the axis did not agree well with the experimental data, which might be attributed to prescribing a steady approach-flow boundary layer and to overly small values of turbulent quantities at the inflow. Helical structures were identified in the shear layer, with a modulation at high wavenumbers, implying that higher azimuthal modes are relevant in this case.

7.5 Summary

Axisymmetric RANS and three-dimensional FSM calculations were conducted of transitional supersonic base flows and the UIUC case. In all cases, axisymmetric RANS calculations failed to accurately reproduce the DNS or experimental data, indicating that relevant physical mechanisms could not be captured. A strong radial variation of the base pressure was predicted by all closures and, for most cases, the recirculation length was underpredicted. Overall, the EASM _{α} appears to be the best closure of the ones considered for the calculation of supersonic base flows. It was demonstrated that the values of the turbulent quantities K and ε at the inflow have a strong impact on the global RANS solution, with larger levels of K leading to a smaller base-pressure and a decreased recirculation length. Compressible extensions were shown to decrease the turbulence levels in the shear layer, whereas the choice of model-coefficients suggested by Papp *et al.* (2002) increased turbulence levels. The results obtained from axisymmetric RANS calculations were used in order to estimate the computational

requirements for a DNS of base flow at practical Reynolds numbers, as investigated at UIUC.

For all transitional cases, FSM is capable of reproducing the DNS data with reasonable accuracy at a fraction of the computational cost. The optimal value of the parameter in the contribution function appears to be $1 \cdot 10^{-3} \leq \beta \leq 4 \cdot 10^{-3}$ for all transitional Reynolds numbers. It was shown that the FSM approach is not derived for a specific turbulence model but is a general strategy for solving unsteady, three-dimensional flows. FSM appears to sufficiently scale down the model contribution in the relevant regions so as not to inhibit the physical instability mechanisms responsible for the generation of large structures. The same kind of structures in the flow field are predicted by FSM calculations as by DNS, i.e., mainly helical structures in the shear layer and streamwise structures within the recirculations region and in the trailing wake. The FSM calculations of transitional base flows confirmed that azimuthal modes $k = 1$ to $k = 4$ are responsible for a flat base-pressure distribution. Furthermore, FSM results supported that the first mode is most likely nonlinearly generated. FSM calculations of the UIUC case revealed the presence of helical structures in the shear layer with a strong azimuthal modulation caused by higher azimuthal modes. A significant amount of streamwise structures was observed within the recirculation region and the formation of hairpin vortices upstream of the recompression region was detected.

For transitional base flows at $Re_D = 100,000$, FSM calculations have been employed to investigate the performance of flow control. For $Re_D = 100,000$, consistent with high Reynolds number experiments by Bourdon & Dutton (2001), applying steady forcing of higher azimuthal modes and thereby generating longitudinal vortices in the shear layer does not succeed in reducing the base drag. However, when forcing the axisymmetric mode, an increase of base pressure can be achieved. In the present study, it was shown that the degree of drag reduction varies with the frequency of the forcing, showing better results for increasing frequencies. Overall, from the present

preliminary investigations, it appears that periodic forcing of the axisymmetric mode has the greatest potential with regard to drag reduction.

8. SUMMARY OF THE MOST IMPORTANT RESULTS

Transitional and fully turbulent axisymmetric wakes were investigated numerically using DNS, TDNS, LNS and state-of-the-art RANS and FSM calculations. Particular emphasis was placed on identifying hydrodynamic instability mechanisms, and relating these to coherent structures that were identified with various visualization techniques. The premise for this approach is the assumption that flow instabilities lead to the formation of coherent structures and determine their evolution. The effect of unsteady structures on the mean flow and on turbulent statistics was investigated, with a particular interest on the resulting mean base-pressure which determines the base drag. This was achieved by exploiting the ability of numerical experiments to deliberately exclude certain physical effects. Employing DNS for various circumferential domain-sizes, certain azimuthal modes could be intentionally eliminated. Thus, their impact on the global wake-behavior could be scrutinized. Flow control methods designed to exploit and/or counteract instability mechanisms present in the flow were studied to determine if a drag reduction could be accomplished. Furthermore, the performance of several RANS models and a novel simulation strategy (FSM) for transitional and turbulent supersonic axisymmetric wakes was evaluated. The most important results of each chapter are summarized in the following.

Simulations of sub- and supersonic TS waves and oblique disturbances in supersonic boundary layers were presented in chapter 4. The ability of the DNS, TDNS and LNS codes, developed for this research, to accurately capture the growth of disturbance waves generated by a viscous instability was demonstrated. Low Mach number simulations of the flow field behind an axisymmetric afterbody were carried out which captured the development and evolution of coherent structures. The results quantitatively reproduced data from incompressible reference DNS. In addition, evidence was

presented that, at $Re_D = 2,000$, the flow becomes absolutely unstable with respect to both the first *and* the second helical mode. Wall-distance independent versions of the EASM and EASM $_{\alpha}$, including compressibility extensions, were applied successfully to incompressible, flat-plate turbulent boundary layers and the axisymmetric approach flow of the UIUC experiments.

In chapter 5, results of linear stability simulations were discussed. Axisymmetric wakes at $M = 2.46$ with an approach boundary layer thickness $\delta_c = 0.1$ were shown to be convectively unstable with respect to higher azimuthal modes at $Re_D = 5,000$. For larger Reynolds numbers, a pulse disturbance led to temporal amplification of higher azimuthal modes. It was concluded that the flow is absolutely unstable with respect to modes $k > 0$ for $Re_D > 5,000$, with $k = 3$ possessing the highest growth rate for Reynolds numbers up to $Re_D = 100,000$. In addition, for $Re_D > 100,000$, the flow becomes absolutely unstable with respect to the axisymmetric mode, $k = 0$. By comparing spatial with temporal results, circumstantial evidence was found suggesting the coexistence of absolutely unstable *global modes* within the recirculation region and convectively unstable *shear-layer modes*. Mode shapes obtained from spatial simulations illustrated that the global mode is dominant for low Reynolds numbers. For increasing Reynolds numbers, the shear-layer mode appears to overcome the damping effect of compressibility and gains in importance. Local stability calculations revealed that the shear-layer modes have non-zero streamwise wavenumbers, implying that they are of helical nature.

In chapter 6, DNS results were presented for three Reynolds numbers and $M = 2.46$. Special emphasis was placed on identifying the most important modes for each case and their effect on the mean flow, in particular on the base-pressure. This was accomplished by conducting simulations of various circumferential domain-sizes, deliberately eliminating azimuthal/helical modes. Thus, the effect of large-scale struc-

tures associated with particular azimuthal/helical modes on the global flow behavior could be evaluated.

By conducting DNS of various circumferential domain-sizes, it was confirmed that the flow is absolutely unstable with respect to at least the first eight azimuthal modes. At $Re_D = 30,000$, the unstable modes intermittently lead to the generation of large-scale structures. For the $1/16^{th}$ -cylinder case, a viscous cut-off of the high wavenumbers prevents linear growth of the higher azimuthal modes. In addition, because the small wavenumbers are eliminated, the large wavenumbers cannot be generated nonlinearly either. Consequently, no small-scale structures are generated for this case. For increasing Reynolds numbers, the viscous cut-off is shifted towards higher wavenumbers. This is evidenced by the $1/16^{th}$ -cylinder case at $Re_D = 100,000$ fully transitioning to turbulence and displaying a broad range of length- and time-scales. Only the $1/32^{nd}$ -cylinder does not exhibit high-frequency fluctuations. At both $Re_D = 60,000$ and $Re_D = 100,000$, all cases with a circumferential domain-size larger than $0 \leq \theta < \pi/8$ fully transition to turbulence downstream of the recompression region and do not exhibit intermittency. A considerable amount of energy can be found in frequencies with $St_D \geq 1$ while maxima for lower azimuthal modes at low frequencies attest the presence of large-scale structures in the flow.

The Q -criterion was employed to identify vortical structures within the flow. For all Reynolds numbers investigated, helical structures within the initial shear-layer were detected. All cases revealed a considerable amount of longitudinal structures within the recirculation region. It is proposed that at least two instability mechanisms are responsible for the generation of these structures: Firstly, it is suggested that global modes cause a noticeable azimuthal modulation of the flow within the recirculation region. Therefore, a chevron-like pattern is imposed onto the recirculating fluid, leading to the formation of streamwise structures. Secondly, simulations of small circumferential domain-sizes enabled the observation of axisymmetric rollers. These rollers result in instantaneous streamlines with strong curvature, most likely leading

to a centrifugal instability which is responsible for the formation of braid-like longitudinal structures. Partly, these structures travel towards the base and are deflected towards the corner of the body. Just shy of the body-corner, the flow separates off the base and the structures impinge on the shear layer, introducing disturbances. Because the shear layer is convectively unstable, the perturbations experience amplification in the streamwise direction which most likely results in the generation of additional structures. Furthermore, structures within the recirculation region are entrained by the shear layer. The vortices are strongly stretched and develop into hairpin vortices. These hairpin vortices lead to additional instabilities responsible for the generation of small-scale structures. Local stability calculations using TDNS suggest that the helical structures present in the shear layer and the longitudinal structures in the trailing wake are a consequence of local instabilities. The baroclinic torque was identified as another important vorticity production mechanism. The largest contribution of vorticity production or destruction through baroclinic torque was found in regions subject to high compressibility, i.e., the initial shear-layer and the trailing wake.

A qualitative difference that could be observed for increasing Reynolds numbers was that at $Re_D = 100,000$ streamwise structures evolved *within* the initial shear-layer. The longitudinal structures reside in the shear layer over long time-periods, evidenced by their presence in time-averaged quantities. These vortices lead to the presence of mushroom-shaped structures in the shear layer, observed in endviews of instantaneous local Mach number. The mushroom-like structures are similar in shape and number to those detected by Bourdon & Dutton (1998). At a location farther downstream, a “four-lobe” wake pattern could be observed, in good agreement with the experimental results. These strong similarities between the DNS data and the experiments imply that the same instability mechanisms are present in both the DNS at $Re_D = 100,000$ and the experiments at $Re_D = 3,300,000$.

Time-averaged data illustrated that the structures present in the flow have a substantial effect on the mean flow, causing a decrease in recirculation length and

base-pressure. Furthermore, it was demonstrated that azimuthal modes with low wavenumbers are responsible for an entirely flat pressure distribution on the base. For all Reynolds numbers investigated, the azimuthal modes $k = 2$ and $k = 4$ were found to be the most important modes in the trailing wake, producing a four-lobe wake pattern. In addition, considerable evidence was found that the first azimuthal mode receives a significant amount of its energy through the nonlinear interaction of higher modes, in particular between $k = 3$ and $k = 4$.

For $Re_D \leq 60,000$, turbulence statistics revealed that the maximum values of all turbulence quantities, except the turbulent shear-stress, were located downstream of the mean reattachment point. At $Re_D = 100,000$ the radial maxima of TKE and $\overline{u'u'}$ were located upstream of the mean reattachment point. The Reynolds shear-stress always exhibited a maximum upstream of the recompression due to the decreasing radial gradient of the shear layer in streamwise direction. A strong azimuthal variation in the turbulence quantities was also observed, suggesting that turbulence quantities need to be computed using fully three-dimensional transport-equations when helical structures are present.

Simulations of domain sizes with decreased circumferential extent illustrated that the base-pressure was increased when the most dominant modes were excluded. Consequently, flow control was applied to axisymmetric wakes at $Re_D = 30,000$, designed such that the (naturally) most dominant modes could be weakened. The continuous introduction of structures resulted in a larger amount of small-scale structures than in the unforced case and the destruction of intermittency. An increase in base-pressure of up to 6% was accomplished when introducing longitudinal structures into the initial shear-layer by employing steady forcing of mode $k = 8$. It appeared that preventing the dominance of the low wavenumber modes outweighed the increased mixing caused by additional longitudinal structures in the shear layer.

In chapter 7, axisymmetric RANS calculations, employing different turbulent clo-

tures, and three-dimensional FSM calculations were conducted of transitional supersonic axisymmetric wakes and the UIUC case. Axisymmetric RANS calculations predicted a strong radial variation of the base-pressure and, in most cases, underpredicted the recirculation length, indicating that certain relevant physical mechanisms could not be captured. It was demonstrated that the global solution is sensitive to the values of the turbulent quantities K and ε at the inflow, with larger levels of K leading to a smaller base-pressure and a decreased recirculation length. Compressibility extensions were shown to decrease the turbulence levels in the shear layer, whereas the choice of model coefficients suggested by Papp *et al.* (2002) increased turbulence levels. Of the closures considered, the EASM $_{\alpha}$ appeared to be the best suited for the calculation of supersonic axisymmetric wakes.

FSM was capable of reproducing the DNS results of transitional axisymmetric wakes with reasonable accuracy at a fraction of the computational cost. This was mainly due to the ability of FSM to sufficiently scale down the model contribution in relevant regions. Consequently, the physical instability mechanisms resulting in the generation of the structures observed in DNS were not inhibited. FSM calculations of transitional axisymmetric wakes confirmed that low wavenumber azimuthal modes are responsible for a flat base-pressure distribution. The optimal value of the parameter in the contribution function appears to be $1 \cdot 10^{-3} \leq \beta \leq 4 \cdot 10^{-3}$. In addition, it was demonstrated that the FSM approach is not derived for a specific turbulence model but is a general strategy for solving unsteady, three-dimensional flows.

FSM calculations have been employed to investigate the performance of flow control for transitional base flows at $Re_D = 100,000$. For $Re_D = 100,000$, consistent with high Reynolds number experiments by Bourdon & Dutton (2001), applying steady forcing of higher azimuthal modes and thereby generating longitudinal vortices in the shear layer does not succeed in reducing the base drag. However, when forcing the axisymmetric mode, an increase of base pressure can be achieved. From the present preliminary investigations, it appears that periodic forcing of the axisymmetric mode

has the greatest potential with regard to drag reduction.

FSM calculations of the UIUC case revealed the presence of helical structures in the shear layer with a strong azimuthal modulation caused by higher azimuthal modes. A significant amount of streamwise structures was observed within the recirculation region and the formation of hairpin vortices upstream of the recompression region was detected. Time-averaged mode-shapes showed that modes $k = 1$ and $k = 4$ contain the largest amount of energy within the recirculation region and downstream of recompression, respectively.

Appendix A: EQUATIONS IN CYLINDRICAL COORDINATES

A.1 Resolved Navier-Stokes Equations

$$\frac{\partial U}{\partial t} + \frac{\partial A}{\partial z} + \frac{\partial B}{\partial r} + \frac{1}{r} \frac{\partial C}{\partial \theta} + \frac{1}{r} D = S \quad (\text{A.1})$$

$$U = \begin{pmatrix} \bar{\rho} \\ \bar{\rho}\tilde{u} \\ \bar{\rho}\tilde{v} \\ \bar{\rho}\tilde{w} \\ \bar{\rho}E_R \\ \bar{\rho}K \\ \bar{\rho}\varepsilon \end{pmatrix} \quad (\text{A.2})$$

$$A = \begin{pmatrix} \bar{\rho}\tilde{u} \\ \rho\tilde{u}^2 + \bar{p} - (\bar{\tau}_{zz} - \bar{\rho}\sigma_{zz}) \\ \rho\tilde{u}\tilde{v} - (\bar{\tau}_{rz} - \bar{\rho}\sigma_{rz}) \\ \rho\tilde{u}\tilde{w} - (\bar{\tau}_{\theta z} - \bar{\rho}\sigma_{\theta z}) \\ \rho\tilde{u}H_R + \bar{q}_z + Q_z - \tilde{u}(\bar{\tau}_{zz} - \bar{\rho}\sigma_{zz}) - \tilde{v}(\bar{\tau}_{rz} - \bar{\rho}\sigma_{rz}) - \tilde{w}(\bar{\tau}_{\theta z} - \bar{\rho}\sigma_{\theta z}) \\ \bar{\rho}\tilde{u}K - \left(\frac{\bar{\mu}}{Re} + \frac{\mu_T}{\sigma_K}\right) \frac{\partial K}{\partial z} \\ \bar{\rho}\tilde{u}\varepsilon - \left(\frac{\bar{\mu}}{Re} + \frac{\mu_T}{\sigma_\varepsilon}\right) \frac{\partial \varepsilon}{\partial z} \end{pmatrix}$$

$$B = \begin{pmatrix} \bar{\rho}\tilde{v} \\ \rho\tilde{v}\tilde{u} - (\bar{\tau}_{rz} - \bar{\rho}\sigma_{rz}) \\ \bar{\rho}\tilde{v}^2 + \bar{p} - (\bar{\tau}_{rr} - \bar{\rho}\sigma_{rr}) \\ \rho\tilde{v}\tilde{w} - (\bar{\tau}_{r\theta} - \bar{\rho}\sigma_{r\theta}) \\ \bar{\rho}\tilde{v}H_R + \bar{q}_r + Q_r - \tilde{u}(\bar{\tau}_{rz} - \bar{\rho}\sigma_{rz}) - \tilde{v}(\bar{\tau}_{rr} - \bar{\rho}\sigma_{rr}) - \tilde{w}(\bar{\tau}_{r\theta} - \bar{\rho}\sigma_{r\theta}) \\ \bar{\rho}\tilde{v}K - \left(\frac{\bar{\mu}}{Re} + \frac{\mu_T}{\sigma_K}\right) \frac{\partial K}{\partial r} \\ \bar{\rho}\tilde{v}\varepsilon - \left(\frac{\bar{\mu}}{Re} + \frac{\mu_T}{\sigma_\varepsilon}\right) \frac{\partial \varepsilon}{\partial r} \end{pmatrix}$$

$$C = \begin{pmatrix} \bar{\rho}\tilde{w} \\ \rho\tilde{u}\tilde{w} - (\bar{\tau}_{\theta z} - \bar{\rho}\sigma_{\theta z}) \\ \rho\tilde{v}\tilde{w} - (\bar{\tau}_{r\theta} - \bar{\rho}\sigma_{r\theta}) \\ \bar{\rho}\tilde{w}^2 + \bar{p} - (\bar{\tau}_{\theta\theta} - \bar{\rho}\sigma_{\theta\theta}) \\ \bar{\rho}\tilde{w}H_R + \bar{q}_\theta + Q_\theta - \tilde{u}(\bar{\tau}_{\theta z} - \bar{\rho}\sigma_{\theta z}) - \tilde{v}(\bar{\tau}_{r\theta} - \bar{\rho}\sigma_{r\theta}) - \tilde{w}(\bar{\tau}_{\theta\theta} - \bar{\rho}\sigma_{\theta\theta}) \\ \bar{\rho}\tilde{w}K - \left(\frac{\bar{\mu}}{Re} + \frac{\mu_T}{\sigma_K}\right) \frac{1}{r} \frac{\partial K}{\partial \theta} \\ \bar{\rho}\tilde{w}\varepsilon - \left(\frac{\bar{\mu}}{Re} + \frac{\mu_T}{\sigma_\varepsilon}\right) \frac{1}{r} \frac{\partial \varepsilon}{\partial \theta} \end{pmatrix}$$

$$D = \begin{pmatrix} \bar{\rho}\tilde{v} \\ \bar{\rho}\tilde{u}\tilde{v} - (\bar{\tau}_{rz} - \bar{\rho}\sigma_{rz}) \\ \bar{\rho}\tilde{v}^2 - \bar{\rho}\tilde{w}^2 - (\bar{\tau}_{rr} - \bar{\rho}\sigma_{rr}) + (\bar{\tau}_{\theta\theta} - \bar{\rho}\sigma_{\theta\theta}) \\ 2\bar{\rho}\tilde{v}\tilde{w} - 2(\bar{\tau}_{r\theta} - \bar{\rho}\sigma_{r\theta}) \\ \bar{\rho}\tilde{v}H_R + \bar{q}_r + Q_r - \tilde{u}(\bar{\tau}_{rz} - \bar{\rho}\sigma_{rz}) - \tilde{v}(\bar{\tau}_{rr} - \bar{\rho}\sigma_{rr}) - \tilde{w}(\bar{\tau}_{r\theta} - \bar{\rho}\sigma_{r\theta}) \\ \bar{\rho}\tilde{v}K - \left(\frac{\bar{\mu}}{Re} + \frac{\mu_T}{\sigma_K}\right) \frac{\partial K}{\partial r} \\ \bar{\rho}\tilde{v}\varepsilon - \left(\frac{\bar{\mu}}{Re} + \frac{\mu_T}{\sigma_\varepsilon}\right) \frac{\partial \varepsilon}{\partial r} \end{pmatrix}$$

$$S = \begin{pmatrix} 0 \\ 0 \\ 0 \\ 0 \\ (1 - a_2M_T)\bar{\rho}\sigma_{ik}\tilde{S}_{ik} + (1 - a_3M_T^2)\bar{\rho}\varepsilon - (\bar{\tau}_{ik} - \bar{p}\delta_{ik})\frac{\partial}{\partial x_k}\left[\frac{\mu_T}{\sigma_\rho}\frac{\partial}{\partial x_i}\left(\frac{1}{\bar{\rho}}\right)\right] \\ - (1 - a_2M_T)\bar{\rho}\sigma_{ik}\tilde{S}_{ik} - (1 - a_3M_T^2)\bar{\rho}\varepsilon + \left(\frac{\partial \bar{p}}{\partial x_i} - \frac{\partial \bar{\tau}_{ik}}{\partial x_k}\right)\frac{\mu_T}{\sigma_\rho}\frac{\partial}{\partial x_i}\left(\frac{1}{\bar{\rho}}\right) \\ - C_{\varepsilon 1}\bar{\rho}^{\frac{1}{\tau}}\sigma_{ik}\left(\tilde{S}_{ik} - \frac{1}{3}\tilde{S}_{jj}\delta_{ik}\right) - C_{\varepsilon 2}f_{\varepsilon 2}\bar{\rho}^{\frac{\varepsilon}{\tau}} + C_{\varepsilon 3}\bar{\rho}\sqrt{Re_T}\frac{\varepsilon}{\tau} - \frac{4}{3}\bar{\rho}\varepsilon\tilde{S}_{jj} \end{pmatrix}$$

The full expansion of the turbulent production terms in cylindrical coordinates results in

$$\begin{aligned} \sigma_{ik}\tilde{S}_{ik} &= \sigma_{zz}\tilde{S}_{zz} + \sigma_{rr}\tilde{S}_{rr} + \sigma_{\theta\theta}\tilde{S}_{\theta\theta} \\ &+ 2\left(\sigma_{rz}\tilde{S}_{rz} + \sigma_{\theta z}\tilde{S}_{\theta z} + \sigma_{\theta r}\tilde{S}_{\theta r}\right), \end{aligned} \quad (\text{A.3})$$

$$\begin{aligned} \sigma_{ik}\left(\tilde{S}_{ik} - \frac{1}{3}\tilde{S}_{jj}\delta_{ik}\right) &= \sigma_{zz}\left[\tilde{S}_{zz} - \frac{1}{3}\left(\tilde{S}_{zz} + \tilde{S}_{rr} + \tilde{S}_{\theta\theta}\right)\right] \\ &+ \sigma_{rr}\left[\tilde{S}_{rr} - \frac{1}{3}\left(\tilde{S}_{zz} + \tilde{S}_{rr} + \tilde{S}_{\theta\theta}\right)\right] \\ &+ \sigma_{\theta\theta}\left[\tilde{S}_{\theta\theta} - \frac{1}{3}\left(\tilde{S}_{zz} + \tilde{S}_{rr} + \tilde{S}_{\theta\theta}\right)\right] \\ &+ 2\left(\sigma_{rz}\tilde{S}_{rz} + \sigma_{\theta z}\tilde{S}_{\theta z} + \sigma_{\theta r}\tilde{S}_{\theta r}\right). \end{aligned} \quad (\text{A.4})$$

The compressible extensions involving the turbulent mass-flux can be written out as

$$\begin{aligned}
(\bar{\tau}_{ik} - \bar{p}\delta_{ik}) \frac{\partial}{\partial x_k} \left[\frac{\mu_T}{\sigma_\rho} \frac{\partial}{\partial x_i} \left(\frac{1}{\bar{\rho}} \right) \right] &= (\bar{\tau}_{zz} - \bar{p}) \frac{\partial}{\partial z} \left[\frac{\mu_T}{\sigma_\rho} \frac{\partial}{\partial z} \left(\frac{1}{\bar{\rho}} \right) \right] \\
&+ (\bar{\tau}_{rr} - \bar{p}) \frac{\partial}{\partial r} \left[\frac{\mu_T}{\sigma_\rho} \frac{\partial}{\partial r} \left(\frac{1}{\bar{\rho}} \right) \right] \\
&+ (\bar{\tau}_{\theta\theta} - \bar{p}) \frac{1}{r} \frac{\partial}{\partial \theta} \left[\frac{\mu_T}{\sigma_\rho} \frac{1}{r} \frac{\partial}{\partial \theta} \left(\frac{1}{\bar{\rho}} \right) \right] \\
&+ \bar{\tau}_{rz} \left\{ \frac{\partial}{\partial z} \left[\frac{\mu_T}{\sigma_\rho} \frac{\partial}{\partial r} \left(\frac{1}{\bar{\rho}} \right) \right] + \frac{\partial}{\partial r} \left[\frac{\mu_T}{\sigma_\rho} \frac{\partial}{\partial z} \left(\frac{1}{\bar{\rho}} \right) \right] \right\} \\
&+ \bar{\tau}_{\theta z} \left\{ \frac{\partial}{\partial z} \left[\frac{\mu_T}{\sigma_\rho} \frac{1}{r} \frac{\partial}{\partial \theta} \left(\frac{1}{\bar{\rho}} \right) \right] + \frac{1}{r} \frac{\partial}{\partial \theta} \left[\frac{\mu_T}{\sigma_\rho} \frac{\partial}{\partial z} \left(\frac{1}{\bar{\rho}} \right) \right] \right\} \\
&+ \bar{\tau}_{\theta r} \left\{ \frac{\partial}{\partial r} \left[\frac{\mu_T}{\sigma_\rho} \frac{1}{r} \frac{\partial}{\partial \theta} \left(\frac{1}{\bar{\rho}} \right) \right] + \frac{1}{r} \frac{\partial}{\partial \theta} \left[\frac{\mu_T}{\sigma_\rho} \frac{\partial}{\partial r} \left(\frac{1}{\bar{\rho}} \right) \right] \right\} ,
\end{aligned} \tag{A.5}$$

$$\begin{aligned}
\left(\frac{\partial \bar{p}}{\partial x_i} - \frac{\partial \bar{\tau}_{ik}}{\partial x_k} \right) \frac{\mu_T}{\sigma_\rho} \frac{\partial}{\partial x_i} \left(\frac{1}{\bar{\rho}} \right) &= \frac{\mu_T}{\sigma_\rho} \left\{ \left(\frac{\partial \bar{p}}{\partial z} - \frac{\partial \bar{\tau}_{zz}}{\partial z} \right) \frac{\partial}{\partial z} \left(\frac{1}{\bar{\rho}} \right) \right. \\
&+ \left(\frac{\partial \bar{p}}{\partial r} - \frac{\partial \bar{\tau}_{rr}}{\partial r} \right) \frac{\partial}{\partial r} \left(\frac{1}{\bar{\rho}} \right) \\
&+ \left(\frac{1}{r} \frac{\partial \bar{p}}{\partial \theta} - \frac{1}{r} \frac{\partial \bar{\tau}_{\theta\theta}}{\partial \theta} \right) \frac{1}{r} \frac{\partial}{\partial \theta} \left(\frac{1}{\bar{\rho}} \right) \\
&+ \left(\frac{\partial \bar{p}}{\partial r} - \frac{\partial \bar{\tau}_{rz}}{\partial z} \right) \frac{\partial}{\partial r} \left(\frac{1}{\bar{\rho}} \right) \\
&+ \left(\frac{\partial \bar{p}}{\partial z} - \frac{\partial \bar{\tau}_{rz}}{\partial r} \right) \frac{\partial}{\partial z} \left(\frac{1}{\bar{\rho}} \right) \\
&+ \left(\frac{1}{r} \frac{\partial \bar{p}}{\partial \theta} - \frac{\partial \bar{\tau}_{\theta z}}{\partial z} \right) \frac{1}{r} \frac{\partial}{\partial \theta} \left(\frac{1}{\bar{\rho}} \right) \\
&+ \left(\frac{\partial \bar{p}}{\partial z} - \frac{1}{r} \frac{\partial \bar{\tau}_{\theta z}}{\partial \theta} \right) \frac{\partial}{\partial z} \left(\frac{1}{\bar{\rho}} \right) \\
&+ \left(\frac{1}{r} \frac{\partial \bar{p}}{\partial \theta} - \frac{\partial \bar{\tau}_{\theta r}}{\partial r} \right) \frac{1}{r} \frac{\partial}{\partial \theta} \left(\frac{1}{\bar{\rho}} \right) \\
&+ \left. \left(\frac{\partial \bar{p}}{\partial r} - \frac{1}{r} \frac{\partial \bar{\tau}_{\theta r}}{\partial \theta} \right) \frac{\partial}{\partial r} \left(\frac{1}{\bar{\rho}} \right) \right\} .
\end{aligned}$$

(A.6)

The individual components of the viscous stress-tensor and the strain-rate tensor are, respectively,

$$\bar{\tau}_{zz} = \frac{2\bar{\mu}}{Re} \left[\tilde{S}_{zz} - \frac{1}{3} \left(\tilde{S}_{zz} + \tilde{S}_{rr} + \tilde{S}_{\theta\theta} \right) \right] \quad (\text{A.7})$$

$$\bar{\tau}_{rr} = \frac{2\bar{\mu}}{Re} \left[\tilde{S}_{rr} - \frac{1}{3} \left(\tilde{S}_{zz} + \tilde{S}_{rr} + \tilde{S}_{\theta\theta} \right) \right] \quad (\text{A.8})$$

$$\bar{\tau}_{\theta\theta} = \frac{2\bar{\mu}}{Re} \left[\tilde{S}_{\theta\theta} - \frac{1}{3} \left(\tilde{S}_{zz} + \tilde{S}_{rr} + \tilde{S}_{\theta\theta} \right) \right] \quad (\text{A.9})$$

$$\bar{\tau}_{rz} = \frac{2\bar{\mu}}{Re} \tilde{S}_{rz} \quad (\text{A.10})$$

$$\bar{\tau}_{\theta z} = \frac{2\bar{\mu}}{Re} \tilde{S}_{\theta z} \quad (\text{A.11})$$

$$\bar{\tau}_{\theta r} = \frac{2\bar{\mu}}{Re} \tilde{S}_{\theta r} \quad (\text{A.12})$$

$$\tilde{S}_{zz} = \frac{\partial \tilde{u}}{\partial z} \quad (\text{A.13})$$

$$\tilde{S}_{rr} = \frac{\partial \tilde{v}}{\partial r} \quad (\text{A.14})$$

$$\tilde{S}_{\theta\theta} = \frac{1}{r} \frac{\partial \tilde{w}}{\partial \theta} + \frac{\tilde{v}}{r} \quad (\text{A.15})$$

$$\tilde{S}_{rz} = \frac{1}{2} \left(\frac{\partial \tilde{u}}{\partial r} + \frac{\partial \tilde{v}}{\partial z} \right) \quad (\text{A.16})$$

$$\tilde{S}_{\theta z} = \frac{1}{2} \left(\frac{\partial \tilde{w}}{\partial z} + \frac{1}{r} \frac{\partial \tilde{u}}{\partial \theta} \right) \quad (\text{A.17})$$

$$\tilde{S}_{\theta r} = \frac{1}{2} \left(\frac{1}{r} \frac{\partial \tilde{v}}{\partial \theta} + r \frac{\partial}{\partial r} \frac{\tilde{w}}{r} \right) . \quad (\text{A.18})$$

A.2 Derivation of Turbulent Kinetic Energy Equation

To derive the turbulent kinetic energy equation, the primitive-variable form of the instantaneous momentum equation is multiplied by the fluctuating velocity vector (u_i'') and averaged in time. For simplicity the asterisks are dropped while deriving the equations, however, the variables are all dimensional:

$$\overline{\rho u_i'' u_{i,t}} + \overline{\rho u_i'' u_k u_{i,k}} = \overline{-u_i'' p_{,i}} + \overline{u_i'' \tau_{ik,k}} \quad (\text{A.19})$$

The unsteady term can be simplified as follows:

$$\begin{aligned}
 \overline{\rho u_i'' u_{i,t}} &= \overline{\rho u_i'' (\tilde{u}_i + u_i'')_{,t}} \\
 &= \overline{\rho u_i'' \tilde{u}_{i,t} + \rho u_i'' u_{i,t}''} \\
 &= \overline{\rho \left(\frac{1}{2} u_i'' u_i'' \right)_{,t}} \\
 &= (\bar{\rho} K)_{,t} - \frac{1}{2} \overline{u_i'' u_i'' \rho_{,t}}
 \end{aligned} \tag{A.20}$$

using

$$\bar{\rho} K = \frac{1}{2} \overline{\rho u_i'' u_i''} \tag{A.21}$$

For the convective term the following steps are performed:

$$\begin{aligned}
 \overline{\rho u_i'' u_{k,(u_i),k}} &= \overline{\rho u_i'' [\tilde{u}_k + u_k''] \tilde{u}_{i,k} + u_k u_{i,k}''} \\
 &= \overline{\rho u_i'' \tilde{u}_k \tilde{u}_{i,k} + \rho u_i'' u_k'' \tilde{u}_{i,k} + \rho u_k u_i'' u_{i,k}''} \\
 &= \overline{\bar{\rho} \sigma_{ik} \tilde{u}_{i,k} + \rho u_k \left(\frac{1}{2} u_i'' u_i'' \right)_{,k}} \\
 &= \bar{\rho} \sigma_{ik} \tilde{u}_{i,k} + \overline{\left(\rho u_k \frac{1}{2} u_i'' u_i'' \right)_{,k}} - \frac{1}{2} \overline{u_i'' u_i'' (\rho u_k)_{,k}} \\
 &= \bar{\rho} \sigma_{ik} \tilde{u}_{i,k} + \overline{\left(\rho u_k \frac{1}{2} u_i'' u_i'' + \rho u_k'' \frac{1}{2} u_i'' u_i'' \right)_{,k}} - \frac{1}{2} \overline{u_i'' u_i'' (\rho u_k)_{,k}} \\
 &= \bar{\rho} \sigma_{ik} \tilde{u}_{i,k} + \overline{\left(\bar{\rho} \tilde{u}_k K + \rho u_k'' \frac{1}{2} u_i'' u_i'' \right)_{,k}} - \frac{1}{2} \overline{u_i'' u_i'' (\rho u_k)_{,k}}
 \end{aligned} \tag{A.22}$$

The pressure term can be simplified as follows:

$$\overline{u_i'' p_{,i}} = \overline{u_i'' \bar{p}_{,i}} + \overline{u_i'' p'_{,i}} = \overline{u_i'' \bar{p}_{,i}} + \overline{(u_i'' p')_{,i}} - \overline{p' u_{i,i}''} \tag{A.23}$$

And finally the diffusion term is just rewritten:

$$\overline{u_i'' \tau_{ik,k}} = \overline{(\tau_{ik} u_i'')_{,k}} - \overline{\tau_{ik} u_{i,k}''} \tag{A.24}$$

This gives

$$\begin{aligned}
 \frac{\partial}{\partial t} (\bar{\rho} K) &+ \frac{\partial}{\partial x_k} \left[\bar{\rho} \tilde{u}_k K - \overline{\tau_{ik} u_i''} - \overline{\rho u_k'' \frac{1}{2} u_i'' u_i''} - \overline{u_i'' p'} \right] \\
 &= -\bar{\rho} \sigma_{ik} \tilde{u}_{i,k} - \overline{\bar{\rho} \sigma_{ik} u_{i,k}''} - \overline{u_i'' \bar{p}_{,i}} + \overline{p' u_{i,i}''}
 \end{aligned} \tag{A.25}$$

The first term on the right-hand-side is the turbulent kinetic energy production, the second is by definition the dissipation rate

$$\overline{\tau_{ik} u''_{i,k}} = \bar{\rho} \varepsilon \quad , \quad (\text{A.26})$$

the second last is the pressure work and the last term is called the pressure dilatation (those two also appear in the term Π_p of the averaged energy equation). On the left hand side, the spatial derivative is taken of molecular diffusion and turbulent transport of turbulent kinetic energy (2^{nd} , 3^{rd} and 4^{th} terms) which is modelled as follows (c.f. Wilcox, 1998):

$$\overline{\tau_{ik} u''_i} + \overline{\rho u''_k \frac{1}{2} u''_i u''_i} + \overline{u''_i p'} = \left(\mu + \frac{\mu_T}{\sigma_K} \right) \frac{\partial K}{\partial x_k} \quad (\text{A.27})$$

The final form of the K -equation is:

$$\boxed{\frac{\partial}{\partial t} (\bar{\rho} K) + \frac{\partial}{\partial x_k} \left[\bar{\rho} \tilde{u}_k K - \left(\mu + \frac{\mu_T}{\sigma_K} \right) \frac{\partial K}{\partial x_k} \right] = -\bar{\rho} \sigma_{ik} \frac{\partial \tilde{u}_i}{\partial x_k} - \bar{\rho} \varepsilon - \overline{u''_i \frac{\partial \bar{p}}{\partial x_i}} + \overline{p' \frac{\partial u''_i}{\partial x_i}}} \quad (\text{A.28})$$

So far, the transport equation for turbulent kinetic energy has only been presented in index notation. The extension to the cylindrical coordinate system is straight-forward for all vector operators. For the expansion of the tensor products, i.e., the production terms, see equations A.2–A.4

A.3 Derivation of Linearized Navier-Stokes Equations

The derivation of the linearized Navier-Stokes equations is demonstrated in detail for the continuity equation. For brevity, only the final result is given for the remaining equations. The continuity equation is

$$\frac{\partial}{\partial t} (\rho) + \frac{\partial}{\partial z} (\rho u) + \frac{\partial}{\partial r} (\rho v) + \frac{1}{r} \frac{\partial}{\partial \theta} (\rho w) + \frac{1}{r} (\rho v) = 0 \quad . \quad (\text{A.29})$$

Decomposing all variables into a basic state $(\check{\phi})$ and a disturbance variable $(\acute{\phi})$, as described in section 2.5, yields

$$\begin{aligned} \frac{\partial}{\partial t} (\check{\rho} + \acute{\rho}) &+ \frac{\partial}{\partial z} [(\check{\rho} + \acute{\rho}) (\check{u} + \acute{u})] + \frac{\partial}{\partial r} [(\check{\rho} + \acute{\rho}) (\check{v} + \acute{v})] \\ &+ \frac{1}{r} \frac{\partial}{\partial \theta} [(\check{\rho} + \acute{\rho}) (\check{w} + \acute{w})] + \frac{1}{r} [(\check{\rho} + \acute{\rho}) (\check{v} + \acute{v})] = 0 \end{aligned} \quad (\text{A.30})$$

Subtracting products of basic-state variables, as they satisfy the continuity equation for the basic state, setting $\check{w} = 0$ and dropping all products containing more than one disturbance variable results in

$$\boxed{\frac{\partial}{\partial t} (\acute{\rho}) + \frac{\partial}{\partial z} (\acute{\rho}\check{u} + \acute{\rho}\acute{u}) + \frac{\partial}{\partial r} (\acute{\rho}\check{v} + \acute{\rho}\acute{v}) + \frac{1}{r} \frac{\partial}{\partial \theta} (\acute{\rho}\acute{w}) + \frac{1}{r} (\acute{\rho}\check{v} + \acute{\rho}\acute{v}) = 0 .} \quad (\text{A.31})$$

The final form of the linearized axial momentum equation is

$$\boxed{\begin{aligned} \frac{\partial}{\partial t} (\acute{\rho}\check{u} + \acute{\rho}\acute{u}) &+ \frac{\partial}{\partial z} (\acute{\rho}\check{u}\acute{u} + \acute{\rho}\acute{u}\check{u} + \acute{\rho}\check{u}\check{u} + \acute{p} - \acute{\tau}_{zz}) + \frac{\partial}{\partial r} (\acute{\rho}\check{u}\acute{v} + \acute{\rho}\acute{u}\check{v} + \acute{\rho}\check{u}\check{v} - \acute{\tau}_{rz}) \\ &+ \frac{1}{r} \frac{\partial}{\partial \theta} (\acute{\rho}\check{u}\acute{w} - \acute{\tau}_{\theta z}) + \frac{1}{r} (\acute{\rho}\check{u}\acute{v} + \acute{\rho}\acute{u}\check{v} + \acute{\rho}\check{u}\check{v} - \acute{\tau}_{rz}) = 0 , \end{aligned}} \quad (\text{A.32})$$

where the viscous stresses can be linearized as follows:

$$\tau_{ik} = \frac{2(\check{\mu} + \acute{\mu})}{Re} \left[\left(\check{S}_{ik} + \acute{S}_{ik} \right) - \frac{1}{3} \left(\check{S}_{jj} + \acute{S}_{jj} \right) \delta_{ik} \right] , \quad (\text{A.33})$$

$$\acute{\tau}_{ik} = \frac{2\check{\mu}}{Re} \left[\acute{S}_{ik} - \frac{1}{3} \acute{S}_{jj} \delta_{ik} \right] + \frac{2\acute{\mu}}{Re} \left[\check{S}_{ik} - \frac{1}{3} \check{S}_{jj} \delta_{ik} \right] . \quad (\text{A.34})$$

By using Sutherland's law, the molecular viscosity is a nonlinear function of temperature. A Taylor series approximation is computed for Sutherland's law:

$$\check{\mu} + \acute{\mu} = (\check{T} + \acute{T})^{\frac{3}{2}} \frac{1 + \mathcal{R}_{Su}}{(\check{T} + \acute{T}) + \mathcal{R}_{Su}} , \quad (\text{A.35})$$

$$\check{\mu} + \acute{\mu} = \check{T}^{\frac{3}{2}} \frac{1 + \mathcal{R}_{Su}}{\check{T} + \mathcal{R}_{Su}} \left[1 + \frac{3\acute{T}}{2\check{T}} - \frac{\acute{T}}{\check{T} + \mathcal{R}_{Su}} \right] . \quad (\text{A.36})$$

Using only the leading order term of the Taylor series approximation, the linearized disturbance viscosity becomes

$$\dot{\mu} = \check{\mu} \dot{T} \left[\frac{3}{2\check{T}} - \frac{1}{\check{T} + \mathcal{R}_{Su}} \right] \quad \text{with} \quad \check{\mu} = \check{T}^{\frac{3}{2}} \frac{1 + \mathcal{R}_{Su}}{\check{T} + \mathcal{R}_{Su}} . \quad (\text{A.37})$$

Following the procedure discussed above, the final form of the linearized radial momentum equation is

$$\begin{aligned} \frac{\partial}{\partial t} (\rho\check{v} + \check{\rho}v) &+ \frac{\partial}{\partial z} (\check{\rho}\check{u}v + \check{\rho}u\check{v} + \rho\check{u}\check{v} - \dot{\tau}_{rz}) + \frac{\partial}{\partial r} (\check{\rho}\check{v}v + \check{\rho}v\check{v} + \rho\check{v}\check{v} + \dot{p} - \dot{\tau}_{rr}) \\ &+ \frac{1}{r} \frac{\partial}{\partial \theta} (\check{\rho}\check{v}w - \dot{\tau}_{r\theta}) + \frac{1}{r} (\check{\rho}\check{v}v + \check{\rho}v\check{v} + \rho\check{v}\check{v} - \dot{\tau}_{rr} + \dot{\tau}_{\theta\theta}) = 0 . \end{aligned} \quad (\text{A.38})$$

The linearized azimuthal momentum equation becomes

$$\begin{aligned} \frac{\partial}{\partial t} (\rho\check{w}) &+ \frac{\partial}{\partial z} (\check{\rho}\check{u}w - \dot{\tau}_{\theta z}) + \frac{\partial}{\partial r} (\check{\rho}\check{v}w - \dot{\tau}_{r\theta}) \\ &+ \frac{1}{r} \frac{\partial}{\partial \theta} (\dot{p} - \dot{\tau}_{\theta\theta}) + \frac{1}{r} (2\check{\rho}\check{v}w - 2\dot{\tau}_{r\theta}) = 0 . \end{aligned} \quad (\text{A.39})$$

The linearized energy equation can be written as

$$\begin{aligned} \frac{\partial}{\partial t} (\rho\check{E} + \check{\rho}E) &+ \frac{\partial}{\partial z} (\check{\rho}\check{u}\check{H} + \check{\rho}u\check{H} + \rho\check{u}\check{H} + \dot{q}_z - (u\dot{\tau}_{zz}) - (v\dot{\tau}_{rz}) - (w\dot{\tau}_{\theta z})) \\ &+ \frac{\partial}{\partial r} (\check{\rho}\check{v}\check{H} + \check{\rho}v\check{H} + \rho\check{v}\check{H} + \dot{q}_r - (u\dot{\tau}_{rz}) - (v\dot{\tau}_{rr}) - (w\dot{\tau}_{r\theta})) \\ &+ \frac{1}{r} \frac{\partial}{\partial \theta} (\check{\rho}\check{w}\check{H} + \dot{q}_\theta - (u\dot{\tau}_{\theta z}) - (v\dot{\tau}_{r\theta}) - (w\dot{\tau}_{\theta\theta})) \\ &+ \frac{1}{r} (\check{\rho}\check{v}\check{H} + \check{\rho}v\check{H} + \rho\check{v}\check{H} + \dot{q}_r - (u\dot{\tau}_{rz}) - (v\dot{\tau}_{rr}) - (w\dot{\tau}_{r\theta})) = 0 . \end{aligned} \quad (\text{A.40})$$

The total energy of the basic state, the linearized total energy and the linearized heat-flux vector are

$$\begin{aligned} \check{E} &= \frac{1}{\gamma Ec} \check{T} + \frac{1}{2} (\check{u}\check{u} + \check{v}\check{v}) \quad , \quad \dot{E} = \frac{1}{\gamma Ec} \dot{T} + (\check{u}\dot{u} + \check{v}\dot{v}) \quad , \\ \dot{q}_i &= -\frac{1}{PrEcRe} \left(\check{\kappa} \frac{\partial \dot{T}}{\partial x_i} + \dot{\kappa} \frac{\partial \check{T}}{\partial x_i} \right) , \end{aligned} \quad (\text{A.41})$$

respectively. The ratio of pressure and density that is contained in the total enthalpy is again linearized using a Taylor series approximation

$$\frac{1}{\check{\rho} + \acute{\rho}} \approx \frac{1}{\check{\rho}} - \frac{\acute{\rho}}{\check{\rho}^2} + \frac{\acute{\rho}^2}{\check{\rho}^3} \dots \quad (\text{A.42})$$

$$\begin{aligned} \frac{\check{p} + \acute{p}}{\check{\rho} + \acute{\rho}} &\approx (\check{p} + \acute{p}) \left(\frac{1}{\check{\rho}} - \frac{\acute{\rho}}{\check{\rho}^2} \right) \\ \check{H} = \check{E} + \frac{\check{p}}{\check{\rho}} \quad , \quad \acute{H} = \acute{E} + \frac{\acute{p}}{\check{\rho}} - \frac{\check{p}\acute{\rho}}{\check{\rho}^2} . \end{aligned} \quad (\text{A.43})$$

Furthermore, the linearized dissipation terms are

$$(u_i \acute{\tau}_{ik}) = \check{u}_i \acute{\tau}_{ik} + \acute{u}_i \check{\tau}_{ik} \quad \text{with} \quad \check{\tau}_{ik} = \frac{2\check{\mu}}{Re} \left[\check{S}_{ik} - \frac{1}{3} \check{S}_{jj} \delta_{ik} \right] . \quad (\text{A.44})$$

In the linearized code, the variables

$$U = \begin{pmatrix} U_1 \\ U_2 \\ U_3 \\ U_4 \\ U_5 \end{pmatrix} = \begin{pmatrix} \acute{\rho} \\ \acute{\rho}\check{u} + \check{\rho}\acute{u} \\ \acute{\rho}\check{v} + \check{\rho}\acute{v} \\ \acute{\rho}\acute{w} \\ \acute{\rho}\acute{E} + \check{\rho}\check{E} \end{pmatrix} \quad (\text{A.45})$$

are solved for. In contrast to the full N-S code, where the conservative variables are Fourier transformed into physical space so that the RHS, containing nonlinear terms, can be assembled, the primitive disturbance quantities need to be deduced from the conservative variables as follows

$$\acute{u} = \frac{U_2 - \acute{\rho}\check{u}}{\check{\rho}} , \quad (\text{A.46})$$

$$\acute{v} = \frac{U_3 - \acute{\rho}\check{v}}{\check{\rho}} , \quad (\text{A.47})$$

$$\acute{w} = \frac{U_4}{\check{\rho}} , \quad (\text{A.48})$$

$$\acute{T} = \gamma Ec \left[\frac{U_5 - \acute{\rho}\check{E}}{\check{\rho}} - (\acute{u}\check{u} + \acute{v}\check{v}) \right] . \quad (\text{A.49})$$

In order to close the system of equations, the disturbance pressure is then computed through the linearized equation of state for a perfect gas

$$\acute{p} = \frac{1}{\gamma M^2} \left(\check{\rho}\acute{T} + \acute{\rho}\check{T} \right) . \quad (\text{A.50})$$

A.3.1 High Reynolds Number Extension

Pursuing the approach described in section 2.5, only the knowledge of the basic state of the eddy viscosity is required. It can be computed from the basic states of ρK and $\rho \varepsilon$ (which are known, e.g., from axisymmetric RANS calculations) as

$$\check{\mu}_T = c_\mu \frac{(\rho \check{K})^2}{(\rho \check{\varepsilon})} = c_\mu \frac{\check{\rho} \check{K}^2}{\check{\varepsilon}} , \quad (\text{A.51})$$

with $c_\mu = 0.09$. For the closure of the turbulent Reynolds stress-tensor, only the linear term is used from the EASM $_\alpha$, and the nonlinear terms are dropped

$$\rho \sigma_{ik} = \frac{2}{3} \rho K \delta_{ik} - 2\mu_T \left(S_{ik} - \frac{1}{3} S_{jj} \delta_{ik} \right) . \quad (\text{A.52})$$

With $\dot{\mu}_T = 0$, the disturbance Reynolds stress-tensor becomes

$$(\rho \acute{\sigma}_{ik}) = \frac{2}{3} \acute{\rho} \check{K} \delta_{ik} - 2\check{\mu}_T \left(\acute{S}_{ik} - \frac{1}{3} \acute{S}_{jj} \delta_{ik} \right) , \quad (\text{A.53})$$

and can be subtracted from $\acute{\tau}_{ik}$ before the outer derivatives are taken. The turbulent heat flux vector is

$$\acute{Q}_i = -\frac{1}{\gamma Ec} \frac{\check{\mu}_T}{Pr_T} \frac{\partial \acute{T}}{\partial x_i} . \quad (\text{A.54})$$

Furthermore, the following source term needs to be added to the energy equation

$$(\rho \acute{\sigma}_{ik}) \check{S}_{ik} + (\rho \check{\sigma}_{ik}) \acute{S}_{ik} + \acute{\rho} \check{\varepsilon} , \quad (\text{A.55})$$

where

$$(\rho \check{\sigma}_{ik}) = \frac{2}{3} (\rho \check{K}) \delta_{ik} - 2\check{\mu}_T \left(\check{S}_{ik} - \frac{1}{3} \check{S}_{jj} \delta_{ik} \right) . \quad (\text{A.56})$$

Finally, when computing the linearized dissipation terms for the energy equation (see equation A.44), $\check{\tau}_{ik}$ needs to be replaced by $\check{\tau}_{ik} - (\rho \check{\sigma}_{ik})$.

A.4 Equations in Fourier Space

A.4.1 Azimuthal Fourier Transforms

For the present investigation, exclusively symmetric Fourier transforms were used in the azimuthal direction. Therefore, the symmetry with respect to the azimuthal

direction of every flow variable needs to be established in order to replace the physical function values with the appropriate sine or cosine transform. Table A.1 shows the symmetry with respect to the azimuthal direction for all flow variables. Rewriting the governing equations (equations 3.1) as Fourier series gives

$$\begin{aligned}
& \frac{\partial}{\partial t} \sum_{k=0}^{kh} \begin{pmatrix} \hat{U}_1^k \cos \alpha_\theta^k \theta \\ \hat{U}_2^k \cos \alpha_\theta^k \theta \\ \hat{U}_3^k \cos \alpha_\theta^k \theta \\ \hat{U}_4^k \sin \alpha_\theta^k \theta \\ \hat{U}_5^k \cos \alpha_\theta^k \theta \\ \hat{U}_6^k \cos \alpha_\theta^k \theta \\ \hat{U}_7^k \cos \alpha_\theta^k \theta \end{pmatrix} + \frac{\partial}{\partial z} \sum_{k=0}^{kh} \begin{pmatrix} \hat{A}_1^k \cos \alpha_\theta^k \theta \\ \hat{A}_2^k \cos \alpha_\theta^k \theta \\ \hat{A}_3^k \cos \alpha_\theta^k \theta \\ \hat{A}_4^k \sin \alpha_\theta^k \theta \\ \hat{A}_5^k \cos \alpha_\theta^k \theta \\ \hat{A}_6^k \cos \alpha_\theta^k \theta \\ \hat{A}_7^k \cos \alpha_\theta^k \theta \end{pmatrix} + \frac{\partial}{\partial r} \sum_{k=0}^{kh} \begin{pmatrix} \hat{B}_1^k \cos \alpha_\theta^k \theta \\ \hat{B}_2^k \cos \alpha_\theta^k \theta \\ \hat{B}_3^k \cos \alpha_\theta^k \theta \\ \hat{B}_4^k \sin \alpha_\theta^k \theta \\ \hat{B}_5^k \cos \alpha_\theta^k \theta \\ \hat{B}_6^k \cos \alpha_\theta^k \theta \\ \hat{B}_7^k \cos \alpha_\theta^k \theta \end{pmatrix} \\
& + \frac{1}{r} \frac{\partial}{\partial \theta} \sum_{k=0}^{kh} \begin{pmatrix} \hat{C}_1^k \sin \alpha_\theta^k \theta \\ \hat{C}_2^k \sin \alpha_\theta^k \theta \\ \hat{C}_3^k \sin \alpha_\theta^k \theta \\ \hat{C}_4^k \cos \alpha_\theta^k \theta \\ \hat{C}_5^k \sin \alpha_\theta^k \theta \\ \hat{C}_6^k \sin \alpha_\theta^k \theta \\ \hat{C}_7^k \sin \alpha_\theta^k \theta \end{pmatrix} + \frac{1}{r} \sum_{k=0}^{kh} \begin{pmatrix} \hat{D}_1^k \cos \alpha_\theta^k \theta \\ \hat{D}_2^k \cos \alpha_\theta^k \theta \\ \hat{D}_3^k \cos \alpha_\theta^k \theta \\ \hat{D}_4^k \sin \alpha_\theta^k \theta \\ \hat{D}_5^k \cos \alpha_\theta^k \theta \\ \hat{D}_6^k \cos \alpha_\theta^k \theta \\ \hat{D}_7^k \cos \alpha_\theta^k \theta \end{pmatrix} = 0, \tag{A.57}
\end{aligned}$$

where all Fourier coefficients are a function of the radial and streamwise direction $\hat{\phi} = \hat{\phi}(r, z)$, k is the azimuthal mode-number and α_θ^k is the azimuthal wavenumber. The Fourier transform routines are implemented such that if $\alpha_\theta^k = k$, the azimuthal domain-length spans the interval $[0, \pi]$. However, when computing domains with a circumferential extent less than π , in addition to changing the boundary conditions and the symmetry conditions at the axis (section 3.2 and Appendix B), the wavenumber needs to be scaled according to the computed domain-size. The scaling factor is determined as the fraction of π that shall be computed. For example, if $1/8^{th}$ of a cylinder is to be computed ($0 \leq \theta \leq \frac{\pi}{4}$), then $\alpha_\theta^k = 4 \cdot k$.

For the validation cases described in section 4.3, the wavenumber (for $\lambda_\theta \ll r_{wall}$) can be calculated as

$$\alpha_\theta^k = \frac{k \cdot r_{wall}}{\lambda_\theta}. \tag{A.58}$$

The azimuthal derivatives are taken in Fourier space and thus the derivatives for

each azimuthal Fourier mode k are

$$\left(\frac{\partial \hat{\phi}}{\partial \theta} \right)_k = \pm \alpha_{\theta}^k \hat{\phi}_k, \quad (\text{A.59})$$

where $+$ holds for symmetric variables and $-$ for anti-symmetric variables, respectively (see table A.1).

By commuting the derivatives and the summation, and by exploiting linear independence of the sine and cosine bases, an equation for each mode k can be obtained:

$$\frac{\partial}{\partial t} \begin{pmatrix} \hat{U}_1^k \\ \hat{U}_2^k \\ \hat{U}_3^k \\ \hat{U}_4^k \\ \hat{U}_5^k \\ \hat{U}_6^k \\ \hat{U}_7^k \end{pmatrix} + \frac{\partial}{\partial z} \begin{pmatrix} \hat{A}_1^k \\ \hat{A}_2^k \\ \hat{A}_3^k \\ \hat{A}_4^k \\ \hat{A}_5^k \\ \hat{A}_6^k \\ \hat{A}_7^k \end{pmatrix} + \frac{\partial}{\partial r} \begin{pmatrix} \hat{B}_1^k \\ \hat{B}_2^k \\ \hat{B}_3^k \\ \hat{B}_4^k \\ \hat{B}_5^k \\ \hat{B}_6^k \\ \hat{B}_7^k \end{pmatrix} + \frac{1}{r} \begin{pmatrix} \alpha_{\theta}^k \hat{C}_1^k + \hat{D}_1^k \\ \alpha_{\theta}^k \hat{C}_2^k + \hat{D}_2^k \\ \alpha_{\theta}^k \hat{C}_3^k + \hat{D}_3^k \\ -\alpha_{\theta}^k \hat{C}_4^k + \hat{D}_4^k \\ \alpha_{\theta}^k \hat{C}_5^k + \hat{D}_5^k \\ \alpha_{\theta}^k \hat{C}_6^k + \hat{D}_6^k \\ \alpha_{\theta}^k \hat{C}_7^k + \hat{D}_7^k \end{pmatrix} = 0, \quad (\text{A.60})$$

$$k = 0, \dots, kh.$$

Finally, this set of equations is discretized employing finite differences in the radial and the streamwise directions as described in section 3.3.

variable / equation	θ	z
ρ, E	even	even
u	even	odd
v, w	odd	even
K, ε	even	even
continuity, r -momentum and energy-equation	even	even
z -momentum	even	odd
θ -momentum	odd	even
K -equation, ϵ -equation	even	even

Table A.1 Symmetries for FFTs in the streamwise (z) and the azimuthal (θ) directions for all variables and equations.

A.4.2 Streamwise Fourier Transforms for Temporal Simulations

For temporal simulations, full Fourier transforms are utilized in the streamwise direction. However, it was decided to write the code flexible enough to have the capability of using symmetric Fourier transforms in the streamwise direction for flow scenarios justifying that assumption. To that end, a “symmetry” was defined for full Fourier transforms in the streamwise direction that rather denotes the arrangement of the Fourier coefficients than describes a physical property of a variable. The full Fourier series has the real form

$$\phi(r, z) = \hat{\phi}^0(r) + 2 \sum_{l=1}^{lh} \left[\hat{\phi}_C^l(r) \cos \alpha_z^l z - \hat{\phi}_S^l(r) \sin \alpha_z^l z \right], \quad (\text{A.61})$$

where the subscripts C and S denote the coefficients for the cosine and sine parts of the series, respectively, and lh is the number of utilized “full” modes containing both a sine and a cosine part. In the streamwise direction, the domain-length is a parameter of the calculation, in contrast to the azimuthal direction which is fixed to π or fractions of π . Therefore, the streamwise wavenumber α_z^l is defined as

$$\alpha_z^l = \begin{cases} \frac{2\pi l}{\lambda_z} & : 1 \leq l \leq lh, \\ -\frac{2\pi(l-L)}{\lambda_z} & : lh + 1 \leq l \leq ls + la \end{cases} \quad (\text{A.62})$$

where λ_z is the fundamental wavelength and, at the same time, the streamwise length of the domain. The number of cosine and sine modes are denoted by ls and la . The full transforms are separated into “symmetric” and “antisymmetric” transforms which arrange the sine and cosine parts in different ways. For a “symmetric” variable, the coefficients for the cosine-series are always stored before the coefficients of the sine-series and vice versa. This has the advantage, that when the modes $ls+1 \leq l \leq ls+la$ are dropped, symmetric Fourier transforms are recovered in the streamwise direction with the correct symmetry properties of all variables. Even more important is that this approach also works in the other direction, i.e., a symmetric calculation can easily be extended to a simulation with full Fourier transforms by appending the missing

sine or cosine parts (coefficients set to zero). Table A.1 shows the “symmetries” of the flow variables in the streamwise direction. Substituting the appropriate streamwise Fourier series representation of all flow variables¹ into equation A.60 results in

$$\begin{aligned}
& \frac{\partial}{\partial t} \left[\sum_{l=0}^{ls} \begin{pmatrix} \hat{U}_{1C}^{l,k}(r) \cos \alpha_z^l z \\ \hat{U}_{2S}^{l,k}(r) \sin \alpha_z^l z \\ \hat{U}_{3C}^{l,k}(r) \cos \alpha_z^l z \\ \hat{U}_{4C}^{l,k}(r) \cos \alpha_z^l z \\ \hat{U}_{5C}^{l,k}(r) \cos \alpha_z^l z \end{pmatrix} + \sum_{l=ls+1}^{ls+la} \begin{pmatrix} \hat{U}_{1S}^{l,k}(r) \sin \alpha_z^l z \\ \hat{U}_{2C}^{l,k}(r) \cos \alpha_z^l z \\ \hat{U}_{3S}^{l,k}(r) \sin \alpha_z^l z \\ \hat{U}_{4S}^{l,k}(r) \sin \alpha_z^l z \\ \hat{U}_{5S}^{l,k}(r) \sin \alpha_z^l z \end{pmatrix} \right] \\
& + \frac{\partial}{\partial z} \left[\sum_{l=0}^{ls} \begin{pmatrix} \hat{A}_{1C}^{l,k}(r) \sin \alpha_z^l z \\ \hat{A}_{2S}^{l,k}(r) \cos \alpha_z^l z \\ \hat{A}_{3C}^{l,k}(r) \sin \alpha_z^l z \\ \hat{A}_{4C}^{l,k}(r) \sin \alpha_z^l z \\ \hat{A}_{5C}^{l,k}(r) \sin \alpha_z^l z \end{pmatrix} + \sum_{l=ls+1}^{ls+la} \begin{pmatrix} \hat{A}_{1S}^{l,k}(r) \cos \alpha_z^l z \\ \hat{A}_{2C}^{l,k}(r) \sin \alpha_z^l z \\ \hat{A}_{3S}^{l,k}(r) \cos \alpha_z^l z \\ \hat{A}_{4S}^{l,k}(r) \cos \alpha_z^l z \\ \hat{A}_{5S}^{l,k}(r) \cos \alpha_z^l z \end{pmatrix} \right] \\
& + \frac{\partial}{\partial r} \left[\sum_{l=0}^{ls} \begin{pmatrix} \hat{B}_{1C}^{l,k}(r) \cos \alpha_z^l z \\ \hat{B}_{2S}^{l,k}(r) \sin \alpha_z^l z \\ \hat{B}_{3C}^{l,k}(r) \cos \alpha_z^l z \\ \hat{B}_{4C}^{l,k}(r) \cos \alpha_z^l z \\ \hat{B}_{5C}^{l,k}(r) \cos \alpha_z^l z \end{pmatrix} + \sum_{l=ls+1}^{ls+la} \begin{pmatrix} \hat{B}_{1S}^{l,k}(r) \sin \alpha_z^l z \\ \hat{B}_{2C}^{l,k}(r) \cos \alpha_z^l z \\ \hat{B}_{3S}^{l,k}(r) \sin \alpha_z^l z \\ \hat{B}_{4S}^{l,k}(r) \sin \alpha_z^l z \\ \hat{B}_{5S}^{l,k}(r) \sin \alpha_z^l z \end{pmatrix} \right] \\
& + \frac{1}{r} \frac{\partial}{\partial \theta} \left[\sum_{l=0}^{lh} \begin{pmatrix} \hat{C}_{1C}^{l,k}(r) \cos \alpha_z^l z \\ \hat{C}_{2S}^{l,k}(r) \sin \alpha_z^l z \\ \hat{C}_{3C}^{l,k}(r) \cos \alpha_z^l z \\ \hat{C}_{4C}^{l,k}(r) \cos \alpha_z^l z \\ \hat{C}_{5C}^{l,k}(r) \cos \alpha_z^l z \end{pmatrix} + \sum_{l=ls+1}^{ls+la} \begin{pmatrix} \hat{C}_{1S}^{l,k}(r) \sin \alpha_z^l z \\ \hat{C}_{2C}^{l,k}(r) \cos \alpha_z^l z \\ \hat{C}_{3S}^{l,k}(r) \sin \alpha_z^l z \\ \hat{C}_{4S}^{l,k}(r) \sin \alpha_z^l z \\ \hat{C}_{5S}^{l,k}(r) \sin \alpha_z^l z \end{pmatrix} \right] \\
& + \frac{1}{r} \left[\sum_{l=0}^{ls} \begin{pmatrix} \hat{D}_{1C}^{l,k}(r) \cos \alpha_z^l z \\ \hat{D}_{2S}^{l,k}(r) \sin \alpha_z^l z \\ \hat{D}_{3C}^{l,k}(r) \cos \alpha_z^l z \\ \hat{D}_{4C}^{l,k}(r) \cos \alpha_z^l z \\ \hat{D}_{5C}^{l,k}(r) \cos \alpha_z^l z \end{pmatrix} + \sum_{l=ls+1}^{ls+la} \begin{pmatrix} \hat{D}_{1S}^{l,k}(r) \sin \alpha_z^l z \\ \hat{D}_{2C}^{l,k}(r) \cos \alpha_z^l z \\ \hat{D}_{3S}^{l,k}(r) \sin \alpha_z^l z \\ \hat{D}_{4S}^{l,k}(r) \sin \alpha_z^l z \\ \hat{D}_{5S}^{l,k}(r) \sin \alpha_z^l z \end{pmatrix} \right] = 0 \quad .(A.63)
\end{aligned}$$

Again the derivatives and the summation are commuted, and linear independence of the sine and cosine bases is exploited. With the understanding that the Fourier coefficients $\hat{\phi}_i^{l,k}(r)$ contain both the cosine and the sine coefficients, ordered in the

¹For brevity, only the DNS transport equations are presented here. For calculations employing certain turbulence models, the additional transport equations for K and ε can be treated like the energy equation.

following way for “symmetric” and “antisymmetric” variables or equations

$$\begin{array}{c} \text{“symmetric”} \end{array} \begin{pmatrix} \hat{\phi}^0(r) \\ \hat{\phi}_C^1(r) \\ \vdots \\ \hat{\phi}_C^{ls}(r) \\ \hat{\phi}_S^{ls+1}(r) \\ \vdots \\ \hat{\phi}_S^{ls+la}(r) \end{pmatrix}, \quad \begin{pmatrix} \hat{\phi}^0(r) \\ \hat{\phi}_S^1(r) \\ \vdots \\ \hat{\phi}_S^{ls}(r) \\ \hat{\phi}_C^{ls+1}(r) \\ \vdots \\ \hat{\phi}_C^{ls+la}(r) \end{pmatrix} \begin{array}{c} \text{“anti-symmetric”} \end{array}, \quad (\text{A.64})$$

the final set of the transport equations in double spectral space takes the form:

$$\begin{aligned}
 \frac{\partial}{\partial t} \begin{pmatrix} \hat{U}_1^{l,k}(r) \\ \hat{U}_2^{l,k}(r) \\ \hat{U}_3^{l,k}(r) \\ \hat{U}_4^{l,k}(r) \\ \hat{U}_5^{l,k}(r) \end{pmatrix} + \alpha_z^l \begin{pmatrix} \hat{A}_1^{l,k}(r) \\ \hat{A}_2^{l,k}(r) \\ \hat{A}_3^{l,k}(r) \\ \hat{A}_4^{l,k}(r) \\ \hat{A}_5^{l,k}(r) \end{pmatrix} + \frac{\partial}{\partial r} \begin{pmatrix} \hat{B}_1^{l,k}(r) \\ \hat{B}_2^{l,k}(r) \\ \hat{B}_3^{l,k}(r) \\ \hat{B}_4^{l,k}(r) \\ \hat{B}_5^{l,k}(r) \end{pmatrix} \\
 + \frac{1}{r} \begin{pmatrix} \alpha_\theta^k \hat{C}_1^{l,k}(r) + \hat{D}_1^{l,k}(r) \\ \alpha_\theta^k \hat{C}_2^{l,k}(r) + \hat{D}_2^{l,k}(r) \\ \alpha_\theta^k \hat{C}_3^{l,k}(r) + \hat{D}_3^{l,k}(r) \\ -\alpha_\theta^k \hat{C}_4^{l,k}(r) + \hat{D}_4^{l,k}(r) \\ \alpha_\theta^k \hat{C}_5^{l,k}(r) + \hat{D}_5^{l,k}(r) \end{pmatrix} = 0 \\
 k = 0, \dots, kh \quad , \quad l = 0, \dots, ls + la.
 \end{aligned} \quad (\text{A.65})$$

The equations have now reduced to a system of PDEs that only depends on time and the radial direction. As already mentioned in section 3.9, due to the short streamwise extent of the computational domain, no domain-decomposition can be utilized. In order to reduce computational time, a parallelization over the Fourier modes is therefore implemented. To that end, the azimuthal and streamwise Fourier modes are collected to combined modes. The benefit of this arrangement is that the number of combined modes typically becomes sufficiently large ($kl = (kh + 1)(lh + 1) - 1$) to ensure an efficient parallelization over the modes. Additionally, looping over a single index also improves the parallel efficiency by decreasing the number of loops and simplifies the algorithm. For the radial derivatives, finite differences are used which are described in section 3.3.

Appendix B: SYMMETRY CONDITIONS

variable/equation	1/2	1/4	1/6	1/8	1/16
$\rho, \rho u, \rho E$	even/odd	even/even	even/odd	even/even	even/even
$\rho v, \rho w$	odd/even	odd/odd	odd/even	odd/odd	odd/odd
$\rho K, \rho \varepsilon$	even/odd	even/even	even/odd	even/even	even/even
continuity	even/odd	even/even	even/odd	even/even	even/even
z -momentum	odd/even	odd/odd	odd/even	odd/odd	odd/odd
r -momentum	odd/even	odd/odd	odd/even	odd/odd	odd/odd
θ -momentum	even/odd	even/even	even/odd	even/even	even/even
energy	even/odd	even/even	even/odd	even/even	even/even
K -transport	even/odd	even/even	even/odd	even/even	even/even
ε -transport	even/odd	even/even	even/odd	even/even	even/even

Table B.1 Symmetries of computational azimuthal Fourier modes (even modes/odd modes) at the axis for all variables and equations for different azimuthal domain-sizes.

variable	mode k_N	1/2	1/4	1/6	1/8	1/16
$\rho, \rho u, \rho E$	0	non-zero	non-zero	non-zero	non-zero	non-zero
	1	zero	zero	zero	zero	zero
	> 1	zero	zero	zero	zero	zero
$\rho v, \rho w$	0	zero	zero	zero	zero	zero
	1	non-zero	zero	zero	zero	zero
	> 1	zero	zero	zero	zero	zero
$\rho K, \rho \varepsilon$	0	non-zero	non-zero	non-zero	non-zero	non-zero
	1	zero	zero	zero	zero	zero
	> 1	zero	zero	zero	zero	zero

Table B.2 Boundary conditions of computational azimuthal Fourier modes at the axis for all variables for different circumferential domain-sizes.

Appendix C: NUMERICAL DETAILS

C.1 Runge-Kutta Time Integration

Four intermediate time-steps are used, which Tannehill *et al.* (1997) writes as

$$\begin{aligned}
 \phi^1 &= \phi^n + \frac{\Delta t}{2} f(\phi^n) \\
 \phi^2 &= \phi^n + \frac{\Delta t}{2} f(\phi^1) \\
 \phi^3 &= \phi^n + \Delta t f(\phi^2) \\
 \phi^{n+1} &= \phi^n + \frac{\Delta t}{6} [f(\phi^n) + 2f(\phi^1) + 2f(\phi^2) + f(\phi^3)] ,
 \end{aligned} \tag{C.1}$$

where n and $n+1$ denote the old and the new time-level, respectively. This time-integration can be shown to be fourth-order accurate. When formulated as given above, three intermediate levels of variables (ϕ^1, ϕ^2, ϕ^3) are needed. For very large DNS, the required memory can be a limiting factor for performing the calculation on a given computer. It is therefore essential to allocate as few arrays as possible. To that end, the above algorithm is manipulated to a more memory-conserving form, that only requires two intermediate variables:

$$\begin{aligned}
 \phi^1 &= \phi^n + \frac{\Delta t}{2} f(\phi^n) \\
 \phi^2 &= \phi^n + \frac{\Delta t}{2} f(\phi^1) \\
 \phi^1 &= \phi^1 + 2\phi^2 \\
 \phi^2 &= \phi^n + \Delta t f(\phi^2) \\
 \phi^1 &= \frac{1}{3} (-\phi^n + \phi^1 + \phi^2) \\
 \phi^{n+1} &= \phi^1 + \frac{\Delta t}{6} f(\phi^2) .
 \end{aligned} \tag{C.2}$$

C.2 Finite Difference Stencils

Further details concerning grid stretching and the derivation of finite differences for non-uniform grids is given in this section. In the radial direction, three different

options of grid stretching are available:

1. The region behind the base ($0 \leq r \leq 1$) is equidistant and the slope of a 5^{th} -order polynomial for $r \geq 1$ is matched at $r = 1$.
2. The slope of a 5^{th} -order polynomial for the region behind the base ($0 \leq r \leq 1$) is matched at $r = 1$ with the slope of another 5^{th} -order polynomial for $r \geq 1$.
3. A single 5^{th} -order polynomial is used for the full radial extent ($0 \leq r \leq r_{max}$).

For all three cases, the number of radial points in the approach boundary layer, $mr1$, the number of radial points between axis and freestream, $mr2$, the radial extent of the domain, r_{max} , and the slope of the functions at $r = 1$ have to be specified. Enforcing the additional constraints of the first grid-point being zero (at the axis) and the inflection point of the grid-function being at $r = 1$, a linear system can be solved for the coefficients of the polynomials

$$f_r(r) = a_r + b_r r + c_r r^3 + d_r r^5 . \quad (C.3)$$

For the grid in the streamwise direction, the slopes of two separate 5^{th} -order polynomials for the approach boundary layer and the wake-region, are matched at the corner location ($z = 0$). The length of the approach flow (z_a), the length of the wake-region (z_{max}), and the slope of the grid-function at the corner need to be specified. Again, employing the constraint that the grid function has its inflection point at $z = 0$, a linear system can be solved for the coefficients of the polynomials

$$f_z(z) = a_z + b_z z + c_z z^3 + d_z z^5 . \quad (C.4)$$

Typical grids for a base flow calculation at moderate Reynolds number using DNS and a calculations at high Reynolds number, using RANS and FSM, are shown in figure C.1. In both cases, a significant clustering of grid-points in the corner region is realized, which is even more pronounced in figure C.1 (right). The grid for RANS

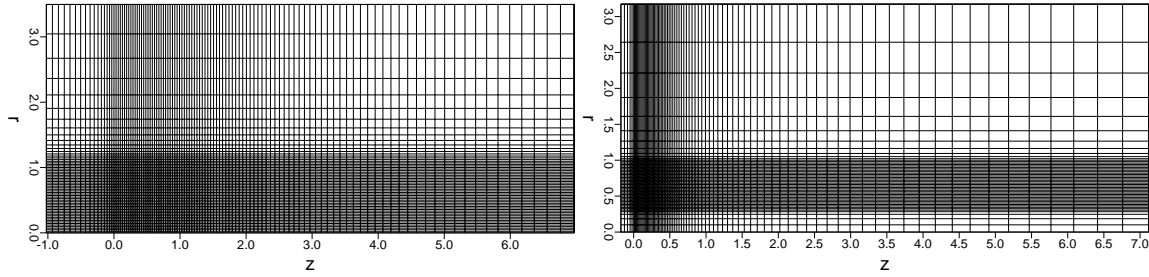


Figure C.1 Typical grid for base flow calculations using DNS (left) or RANS and FSM calculations (right), for clarity only every fourth grid-point in the streamwise direction and every third point in the radial direction are shown.

and FSM calculations used a very fine resolution at the walls which is required for high Reynolds number cases. Note that for boundary layer calculations, only the polynomial for $r \geq 1$ and for $z_a \leq z \leq 0$ need to be specified.

As mentioned in section 3.3, fourth-order split finite-differences were previously used by Tourbier (1996) and Harris (1997). However, they were employed on an equidistant computational grid. For the present code, the derivative stencils are derived for non-equidistant grids. To obtain the split finite-differences for a non-uniform grid, first a central, fourth-order accurate finite difference stencil is derived as follows. Let a, b, c, d, e be the coefficients sought for the finite difference representation of the first derivative of a variable

$$\left. \frac{\partial \phi}{\partial x} \right|_i = a\phi_{i-2} + b\phi_{i-1} + c\phi_i + d\phi_{i+1} + e\phi_{i+2}, \quad (\text{C.5})$$

and let $h(j) = z(j) - z(j-1)$, for $j = -1, \dots, 2$ be the grid-spacing between the five grid-points used for the stencil. Through Taylor series expansion, the coefficients can

be determined as

$$\begin{aligned}
a &= \frac{h(0) \cdot h(1) \cdot [h(1) + h(2)]}{h(-1) \cdot [h(-1) + h(0)] \cdot [h(-1) + h(0) + h(1)] \cdot [h(-1) + h(0) + h(1) + h(2)]} \\
b &= -\frac{[h(-1) + h(0)] \cdot h(1) \cdot [h(1) + h(2)]}{h(-1) \cdot h(0) \cdot [h(0) + h(1)] \cdot [h(0) + h(1) + h(2)]} \\
c &= \frac{h(-1) \cdot \{h(1) \cdot [h(1) + h(2)] - h(0) \cdot [2 \cdot h(1) + h(2)]\}}{h(0) \cdot [h(-1) + h(0)] \cdot h(1) \cdot [h(1) + h(2)]} \\
&\quad + \frac{h(0) \cdot \{2 \cdot h(1) \cdot [h(1) + h(2)] - h(0) \cdot [2 \cdot h(1) + h(2)]\}}{h(0) \cdot [h(-1) + h(0)] \cdot h(1) \cdot [h(1) + h(2)]} \\
d &= \frac{h(0) \cdot [h(-1) + h(0)] \cdot [h(1) + h(2)]}{h(1) \cdot [h(0) + h(1)] \cdot [h(-1) + h(0) + h(1)] \cdot h(2)} \\
e &= -\frac{h(0) \cdot [h(-1) + h(0)] \cdot h(1)}{h(2) \cdot [h(1) + h(2)] \cdot [h(0) + h(1) + h(2)] \cdot [h(-1) + h(0) + h(1) + h(2)]} .
\end{aligned} \tag{C.6}$$

In order to obtain the split differences, let c^+, d^+, e^+ and a^-, b^-, c^- be the coefficients for the forward and backward stencils

$$\begin{aligned}
\left. \frac{\partial \phi^-}{\partial x} \right|_i &= a^- \phi_{i-2} + b^- \phi_{i-1} + c^- \phi_i \\
\left. \frac{\partial \phi^+}{\partial x} \right|_i &= c^+ \phi_i + d^+ \phi_{i+1} + e^+ \phi_{i+2} ,
\end{aligned} \tag{C.7}$$

respectively. The coefficients are determined using the following relationship with the original coefficients given in equation (C.6)

$$\begin{aligned}
a^- &= 2 \cdot a & e^+ &= 2 \cdot e \\
b^- &= 2 \cdot b & d^+ &= 2 \cdot d \\
c^- &= 2 \cdot [c + d + e] & c^+ &= 2 \cdot [a + b + c]
\end{aligned} \tag{C.8}$$

On an equidistant grid with $h(j) = \Delta x$, the central difference takes the familiar form

$$\left. \frac{\partial \phi}{\partial x} \right|_i = \frac{\phi_{i-2} - 8\phi_{i-1} + 8\phi_{i+1} - \phi_{i+2}}{12\Delta x} , \tag{C.9}$$

and the split differences result in

$$\left. \frac{\partial \phi^+}{\partial x} \right|_i = \frac{-7\phi_i + 8\phi_{i+1} - \phi_{i+2}}{6\Delta x} , \quad \left. \frac{\partial \phi^-}{\partial x} \right|_i = \frac{\phi_{i-2} - 8\phi_{i-1} + 7\phi_i}{6\Delta x} . \tag{C.10}$$

The derivation of compact finite difference stencils for non-equidistant grids was conducted by Burke (2001). To obtain the one-sided stencils required for the splitting, the same procedure as shown above for the standard differences was applied.

C.3 Derivation of Parity Conditions

The derivation of the parity conditions at the axis was performed by Burke (2001) and is reproduced in the following. Due to the pseudospectral approach in the azimuthal direction, all variables are given in Fourier modes according to

$$\phi(r, \theta) = \sum_{k=0}^{\infty} \hat{\phi}_k(r) e^{ik\theta}. \quad (\text{C.11})$$

Specify a cartesian coordinate system (x, y) , rotated by an angle κ in the $r - \theta$ plane as shown in figure C.2. On y , the cylindrical coordinates and unit vectors are given

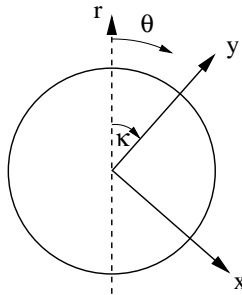


Figure C.2 Cartesian coordinate system rotated by angle κ in the $r - \theta$ plane.

by,

$$r = |y|, \quad \theta = \begin{cases} \kappa, & y > 0 \\ \kappa + \pi, & y < 0 \end{cases} \quad (\text{C.12})$$

$$\frac{d^n}{dy^n} = \text{sgn}^n(y) \frac{d^n}{dr^n}, \quad e^{ik\theta} = \text{sgn}^k(y) e^{ik\kappa} \quad (\text{C.13})$$

Parity conditions for the Fourier modes are derived by requiring the existence of all derivatives on y at the origin. For the scalar case, this is

$$\lim_{y \rightarrow 0^-} \frac{d^n \phi}{dy^n} = \lim_{y \rightarrow 0^+} \frac{d^n \phi}{dy^n} \quad (\text{C.14})$$

Even if ϕ is a smooth function, radial derivatives of ϕ need not be continuous at the origin due to the coordinate singularity. Even so, the Fourier modes of functions that are the radial derivatives of smooth functions have notable parity properties. These

are seen almost by inspection of the Fourier representation, given that $\hat{\phi}_k(r)$ is either even or odd in r . One may note that any odd order of radial differentiation will switch the parity "state" relative to the original function, while an even number will not. Define "even parity" as being an even function in r in the even Fourier modes, while being an odd function in r in the odd modes. "Odd parity" is then being an even function in the odd modes, etc. For functions with even parity,

$$\hat{\phi}_k^{(n)}(r) = \begin{cases} \text{even} & k+n \text{ even} \\ \text{odd} & k+n \text{ odd} \end{cases} \quad (\text{C.15})$$

Functions with odd parity have

$$\hat{\phi}_k^{(n)}(r) = \begin{cases} \text{even} & k+n \text{ odd} \\ \text{odd} & k+n \text{ even} \end{cases} \quad (\text{C.16})$$

Note that derivatives in θ do not change the parity of a function.

C.3.1 Scalars

The Fourier representation of ϕ is

$$\phi(y) = \sum_{k=0}^{\infty} \hat{\phi}_k(|y|) e^{ik\kappa} \text{sgn}^k(y), \quad (\text{C.17})$$

and the n^{th} derivative of ϕ can be written as

$$\phi^{(n)}(y) = \sum_{k=0}^{\infty} \hat{\phi}_k^{(n)}(|y|) e^{ik\kappa} \text{sgn}^k(s) \text{sgn}^n(s). \quad (\text{C.18})$$

Substituting this into equation C.14 results in

$$\sum_{k=0}^{\infty} \hat{\phi}_k^{(n)}(0) e^{ik\kappa} (-1)^{(k+n)} = \sum_{k=0}^{\infty} \hat{\phi}_k^{(n)}(0) e^{ik\kappa}, \quad (\text{C.19})$$

or

$$\sum_{k=0}^{\infty} \hat{\phi}_k^{(n)}(0) e^{ik\kappa} [1 - (-1)^{(k+n)}] = 0, \quad (\text{C.20})$$

or

$$\sum_{k=0, n+k \text{ odd}}^{\infty} 2\hat{\phi}_k^{(n)}(0) e^{ik\kappa} = 0. \quad (\text{C.21})$$

Since this is required for all κ ,

$$\hat{\phi}_k^{(n)}(0) = 0, \quad n + k \text{ odd}, \quad (\text{C.22})$$

that is, scalar functions have even parity.

C.3.2 Vectors

Consider now the velocity vector u_i with the Fourier representation

$$u_i(r, \theta, z) = \sum_{k=0}^{\infty} (\hat{v}_k(r, z)\mathbf{e}_r + \hat{w}_k(r, z)\mathbf{e}_\theta + \hat{u}_k(r, z)\mathbf{e}_z) e^{ik\theta} \quad (\text{C.23})$$

with

$$\mathbf{e}_r = \text{sgn}(y)\mathbf{e}_y \quad (\text{C.24})$$

$$\mathbf{e}_\theta = \text{sgn}(y)\mathbf{e}_x \quad (\text{C.25})$$

On y , u_i is represented by,

$$u_i(s, z) = \sum_{k=0}^{\infty} [(\hat{v}_k(|y|, z)\mathbf{e}_y + \hat{w}_k(|y|, z)\mathbf{e}_x) \text{sgn}(y) + \hat{u}_k(|y|, z)\mathbf{e}_z] e^{ik\kappa} \text{sgn}^k(y) \quad (\text{C.26})$$

Taking the n^{th} derivative in y and taking the two-sided limit as before

$$0 = \sum_{k=0}^{\infty} \left\{ \begin{array}{l} \hat{v}_k^{(n)}(0, z)\mathbf{e}_y [1 - (-1)^{n+k+1}] \\ + \hat{w}_k^{(n)}(0, z)\mathbf{e}_x [1 - (-1)^{n+k+1}] \\ + \hat{u}_k^{(n)}(0, z)\mathbf{e}_z [1 - (-1)^{n+k}] \end{array} \right\} e^{ik\kappa} \quad (\text{C.27})$$

or,

$$0 = \sum_{\substack{k=0 \\ n+k \text{ even}}}^{\infty} 2\hat{v}_k^{(n)}(0, z)\mathbf{e}_y e^{ik\kappa} + \sum_{\substack{k=0 \\ n+k \text{ even}}}^{\infty} 2\hat{w}_k^{(n)}(0, z)\mathbf{e}_x e^{ik\kappa} + \sum_{\substack{k=0 \\ n+k \text{ odd}}}^{\infty} 2\hat{u}_k^{(n)}(0, z)\mathbf{e}_z e^{ik\kappa} \quad (\text{C.28})$$

Again invoking orthogonality,

$$\begin{aligned} \hat{v}_k^{(n)}(0, z) &= 0, \quad n + k \text{ even} \\ \hat{w}_k^{(n)}(0, z) &= 0, \quad n + k \text{ even} \\ \hat{u}_k^{(n)}(0, z) &= 0, \quad n + k \text{ odd}, \end{aligned} \quad (\text{C.29})$$

so the radial and azimuthal vector components have odd parity, while the axial component has even parity. The parity conditions for all cases are listed in table B.1.

C.4 Stability of the Numerical Method

In order to evaluate whether split finite-differences for the spatial discretization in combination with a Runge-Kutta method for the time advancement are suitable for the present research, a von Neumann stability analysis, as described in Tannehill *et al.* (1997), is performed for a simplified model-equation. The compressible Navier-Stokes equations can be classified as hyperbolic partial differential equations (PDE) and, therefore, wave-like solutions are expected. Furthermore, the Reynolds number for the flows of interest in this work is sufficiently high to justify neglecting the viscous term in the stability analysis. In order to conduct the Neumann stability analysis, also known as Fourier stability analysis, the model equation needs to be linear. Thus the one-dimensional, simplified wave-equation

$$\frac{\partial \phi}{\partial t} + c \frac{\partial \phi}{\partial x} = 0 \quad (\text{C.30})$$

was chosen for the stability analysis. Harris (1997) derived the “modified equation” (see, e.g., Tannehill *et al.*, 1997) for the split finite-differences (equation C.10) in combination with the Runge-Kutta method given in equation C.1 applied to the wave-equation (C.30). He found that the method could be considered to be of order $\mathcal{O}(\Delta x^3)$ with the leading error term being an even derivative, thus the major error would be dissipative rather than dispersive.

C.4.1 Low-Order Discretization

For the sake of simplicity, a second-order Runge-Kutta time-discretization will be employed in combination with second-order spatial derivatives for illustrating the advantages of using split finite-differences for hyperbolic problems. The second-order Runge-Kutta method can be written as

$$\begin{aligned} \phi^1 &= \phi^n + \Delta t f(\phi^n) \\ \phi^{n+1} &= \phi^n + \frac{\Delta t}{2} (f(\phi^n) + f(\phi^1)) . \end{aligned} \quad (\text{C.31})$$

Inserting the second-order central difference for an equidistant grid

$$\frac{\partial \phi}{\partial x} = \frac{\phi_{i+1}^n - \phi_{i-1}^n}{2\Delta x} \quad (\text{C.32})$$

into this algorithm, the resulting scheme becomes

$$\phi_i^{n+1} = \phi_i^n - \frac{CFL}{4} (2\phi_{i+1}^n - 2\phi_{i-1}^n) + \frac{CFL^2}{8} (\phi_{i+2}^n - 2\phi_i^n + \phi_{i-2}^n) , \quad (\text{C.33})$$

with $CFL = \frac{c\Delta x}{\Delta t}$.

It is assumed that an infinitesimally small error ϵ_i^n can be written as a Fourier series of the form

$$\epsilon_i^n = \sum_m e^{at} e^{ik_m x} , \quad (\text{C.34})$$

with k_m being the wavenumber of the corresponding Fourier mode. The error must satisfy the same difference equation as the solution, i.e., the error possesses the same growth behavior in time as the solution. Therefore, one term of the series¹ given in equation C.34 can be inserted into the difference equation. Setting $k_m \Delta x = \Theta$ and using the trigonometric relations $e^{i\Theta} + e^{-i\Theta} = 2 \cos \Theta$ and $e^{i\Theta} - e^{-i\Theta} = 2i \sin \Theta$, the amplification factor becomes

$$G = \frac{\epsilon^{n+1}}{\epsilon^n} = e^{a\Delta t} = 1 - \frac{CFL^2}{2} \sin^2 \Theta - iCFL \sin \Theta . \quad (\text{C.35})$$

The absolute value of the complex amplification factor can be written as

$$|G| = \sqrt{1 + \frac{CFL^4}{4} \sin^4 \Theta} . \quad (\text{C.36})$$

The condition for stability ($|G| \leq 1$) can therefore never be satisfied for this method, i.e., the method is unconditionally unstable.

The stability analysis is now repeated using split finite-differences, which approximate the spatial derivative as follows

$$\frac{\partial \phi^+}{\partial x} = \frac{\phi_{i+1}^n - \phi_i^n}{\Delta x} , \quad (\text{C.37})$$

$$\frac{\partial \phi^-}{\partial x} = \frac{\phi_i^n - \phi_{i-1}^n}{\Delta x} , \quad (\text{C.38})$$

¹Due to the linearity of the difference equation, superposition can be used and it suffices to analyze the behavior of a single term of the Fourier series.

for the upwind and downwind differences, respectively. In order to achieve the same spatial order of accuracy as when using a central finite-difference, two full time-steps need to be computed with half the time-step for each. Therefore, the algorithm for the time integration now becomes

$$\begin{aligned}\phi^1 &= \phi^n + \Delta t f^+(\phi^n) \\ \phi^{n+1} &= \phi^n + \frac{\Delta t}{2} (f^+(\phi^n) + f^-(\phi^1))\end{aligned}\tag{C.39}$$

where f^+ denotes an upwind difference stencil and f^- a downwind difference stencil. After one full Runge-Kutta cycle and the time-level Δt , the amplification rate is

$$G = 1 - 2CFL^2 \sin^2 \frac{\Theta}{2} - \mathbf{i}CFL \sin \Theta ,\tag{C.40}$$

with the only difference to the amplification factor of the central difference method (equation C.36) being the factor $\frac{1}{2}$ in the argument of the trigonometric function in the real part. This difference, however, significantly alters the stability behavior, as the method now becomes conditionally stable for $CFL \leq 1$. As can be seen in figure C.3, the method also shows no phase error when $CFL = 1$. For smaller values of CFL, however, the method exhibits significant phase lag and damping.

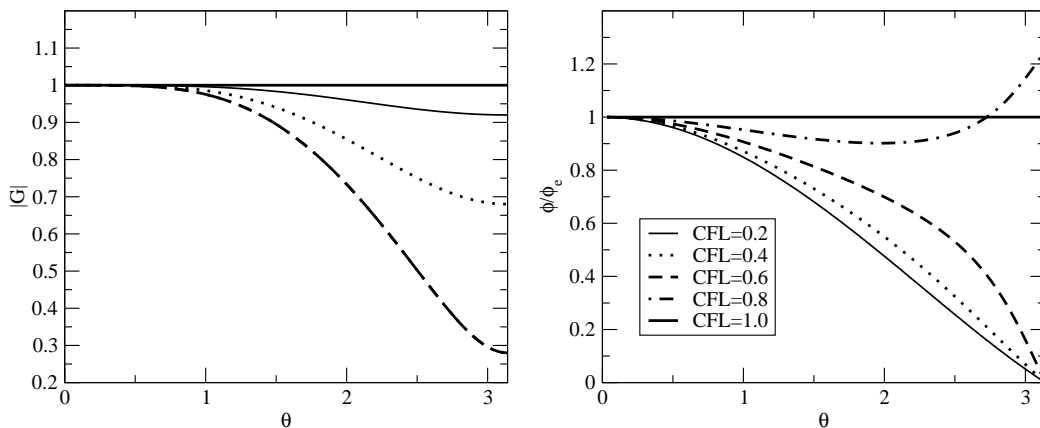


Figure C.3 Amplification factor (left) and phase shift (right) for linearized wave equation using 2^{nd} -order split differences with 2^{nd} -order Runge-Kutta time integration for several values of CFL .

The additional cost associated with splitting (two Runge-Kutta cycles need to be computed) is, therefore, compensated by obtaining a conditionally stable method. Additionally, for higher-order methods, the overhead is reduced by the fact that the split finite-differences become more compact, i.e., they contain less discrete points than the central differences for the same order of accuracy.

C.4.2 High-Order Discretization

The analysis of Appendix C.4.1 was repeated for high-order methods. The stability behavior of the finite-difference stencils derived in section C.2 in combination with the fourth-order accurate Runge-Kutta method presented in section C.1 was tested with the simplified wave equation (equation C.30). Inserting the central finite difference stencil (equation C.9) in the fourth-order Runge-Kutta method yields the amplification factor

$$\begin{aligned}
 G = & 1 - \frac{65}{144}CFL^2 + \frac{13059}{12^5}CFL^4 + \left(\frac{CFL^2}{9} - \frac{4192CFL^4}{12^5}\right)\cos\Theta \\
 & + \left(\frac{4CFL^2}{9} - \frac{16768CFL^4}{12^5}\right)\cos 2\Theta + \left(-\frac{CFL^2}{9} - \frac{6240CFL^4}{12^5}\right)\cos 3\Theta \\
 & + \left(\frac{CFL^2}{144} - \frac{3324CFL^4}{12^5}\right)\cos 4\Theta - \frac{2016CFL^4}{12^5}\cos 5\Theta + \frac{384CFL^4}{12^5}\cos 6\Theta \\
 & - \frac{32CFL^4}{12^5}\cos 7\Theta + \frac{CFL^4}{12^5}\cos 8\Theta \\
 & + i \left[\left(-\frac{4CFL}{3} - \frac{1584CFL^3}{3 \cdot 12^3}\right)\sin\Theta + \left(\frac{CFL}{6} - \frac{387CFL^3}{3 \cdot 12^3}\right)\sin 2\Theta \right. \\
 & \left. - \frac{488CFL^3}{3 \cdot 12^3}\sin 3\Theta + \frac{192CFL^3}{3 \cdot 12^3}\sin 4\Theta - \frac{24CFL^3}{3 \cdot 12^3}\sin 5\Theta + \frac{CFL^3}{3 \cdot 12^3}\sin 6\Theta \right] .
 \end{aligned} \tag{C.41}$$

When plotting the absolute value of the complex amplification factor, shown in figure C.4, it can be seen that in contrast to the low order example given above, the method appears to be stable for values of CFL up to 2.0 (it was iteratively determined that the limit is $CFL = 2.06$). This is in good agreement with the result presented by Hu *et al.* (1996), who state that the fourth-order Runge-Kutta scheme is stable if Δt is

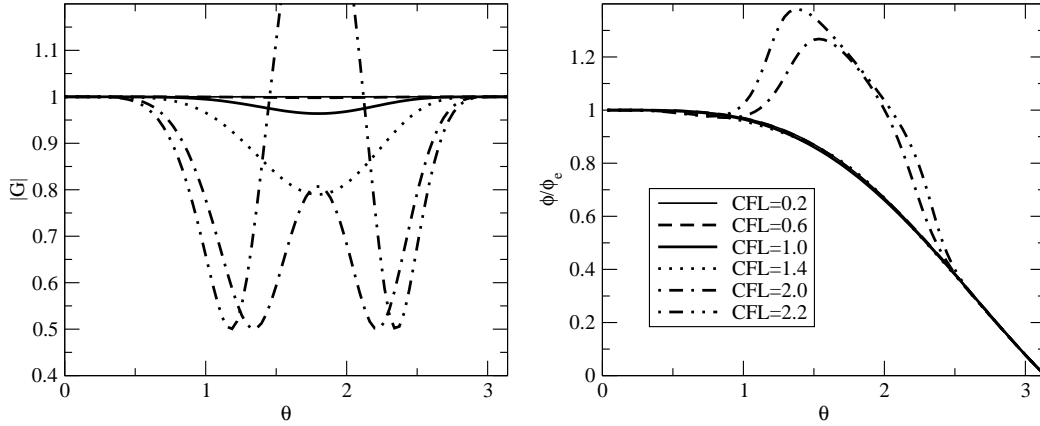


Figure C.4 Amplification factor (left) and phase shift (right) for linearized wave equation using 4th-order central differences with 4th-order Runge-Kutta time integration for several values of CFL .

chosen such that $ck_{max}^* \Delta t \leq 2.83$, where, for a 5-point finite difference for the spatial discretization, $k_{max}^* = \frac{1.4}{\Delta x}$. This results in $CFL = 2.02$. The figure also reveals that this method exhibits considerable amplitude errors for $CFL > 1$. When considering the phase shift, a significant phase lag in all frequencies for $CFL \leq 1.4$ and a leading phase error for the intermediate frequency range for $CFL \geq 1.4$ can be observed.

For the split differences shown in equation C.10, the amplification factor after one Runge-Kutta cycle becomes

$$\begin{aligned}
 G = & 1 - 228 \frac{CFL^2}{12^2} + \frac{42572}{3} \frac{CFL^4}{12^4} + \left(256 \frac{CFL^2}{12^2} - \frac{61952}{3} \frac{CFL^4}{12^4} \right) \cos \Theta \\
 & + \left(-28 \frac{CFL^2}{12^2} + \frac{22768}{3} \frac{CFL^4}{12^4} \right) \cos 2\Theta \\
 & - \frac{3584}{3} \frac{CFL^4}{12^4} \cos 3\Theta + \frac{196}{3} \frac{CFL^4}{12^4} \cos 4\Theta \\
 & + i \left[\left(-16 \frac{CFL}{12} + \frac{3680}{3} \frac{CFL^3}{12^3} \right) \sin \Theta + \left(\frac{CFL}{12} - \frac{2504}{3} \frac{CFL^3}{12^3} \right) \sin 2\Theta \right. \\
 & \left. + 160 \frac{CFL^3}{12^3} \sin 3\Theta - \frac{28}{3} \frac{CFL^3}{12^3} \sin 4\Theta \right]. \quad (C.42)
 \end{aligned}$$

Figure C.5 reveals, that the maximum value of CFL to maintain a stable solution is between 1.2 and 1.4. The limit was found iteratively to be $CFL = 1.298$. In contrast to the case when central differences are employed, the dominant amplitude error

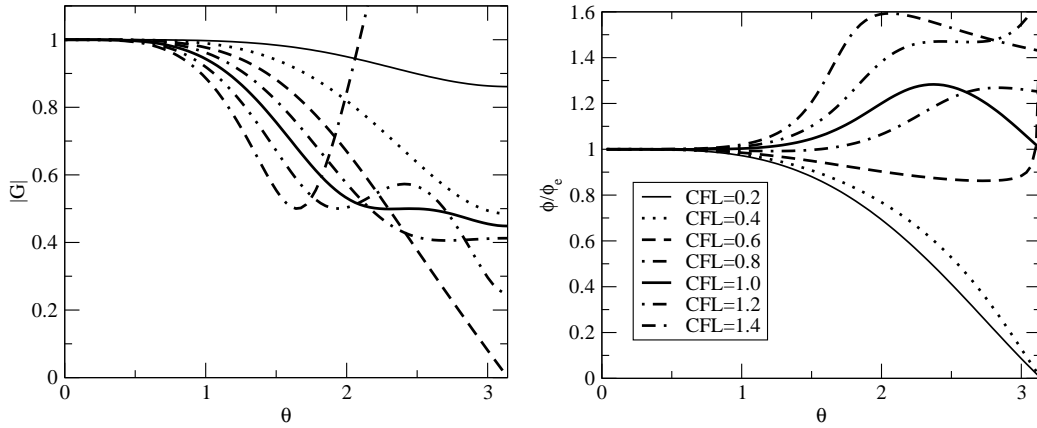


Figure C.5 Amplification factor (left) and phase shift (right) for linearized wave equation using 4th-order split differences with 4th-order Runge-Kutta time integration for several values of CFL .

occurs for the high wavenumber range and the phase lag appears to be considerably reduced for $CFL > 0.4$.

By performing a von Neumann stability analysis using the simplified wave-equation it was shown that using split finite-differences increases dissipation (larger amplitude errors) in the higher wavenumber range and reduces dispersion errors (phase shift) for $CFL > 0.4$. Presumably, for the problems under consideration, amplitude errors are preferred over phase errors because phase errors can influence where and if vortices are generated and affect their interaction whereas the amplitude error will most likely only modify the intensity of the vortices.

The model equation used up to this point is linear and with the results obtained so far, little can be said about how the numerical methods tested above will perform for nonlinear PDEs. Consequently, to investigate the performance of some numerical schemes for a nonlinear problem, several tests were conducted for a nonlinear model problem. Following the same reasoning for dropping the viscous term as above, the inviscid form of Burger's equation

$$\frac{\partial \phi}{\partial t} + \phi \frac{\partial \phi}{\partial x} = 0 \quad (\text{C.43})$$

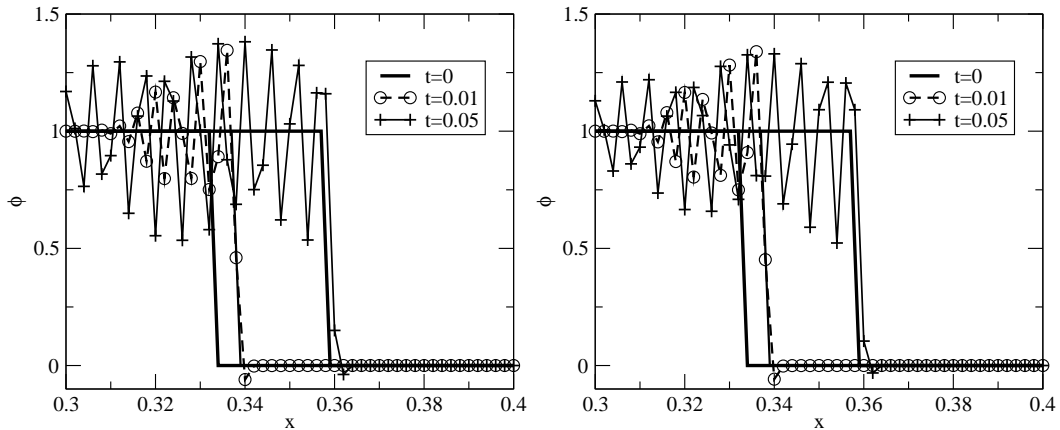


Figure C.6 Calculation of the propagation of a discontinuity using the inviscid Burger's equation; time levels shown $t = 0$, $t = 0.01$ and $t = 0.05$; 4^{th} -order central differences with 4^{th} -order Runge-Kutta time integration for $CFL = 0.2$ (left) and $CFL = 1.0$ (right) with $\Delta x = 0.002$ and $\Delta t = CFL \cdot \Delta x$.

is selected as a test case. Due to the non-linearity of the equation, the von Neumann analysis cannot be repeated for this example because superposition of individual Fourier terms is no longer valid. Instead, the propagation of a discontinuity is examined numerically, a phenomenon that is expected to occur in the calculations of supersonic wake flows (e.g., shocklets caused by large structures that travel with the convection speed of the structure). Figure C.6 shows that using central differences for computing the propagation of a discontinuity, for no value of CFL a stable solution can be obtained.

Switching to the split finite-differences, given in equation (C.10), it can be seen in figure C.7 that the propagation of the discontinuity is properly represented for $CFL = 1.0$. A slight dispersion error (caused by a phase error of the scheme) is visible but appears to not be amplified in time. However, when decreasing the CFL number, the solution deteriorates slightly, and considerable oscillations can be observed for $CFL = 0.2$. This is consistent with the increased phase lag that was found for small values of CFL for the wave equation (see figure C.5). Nevertheless, using the split finite-differences in combination with the fourth-order Runge-Kutta method, a stable

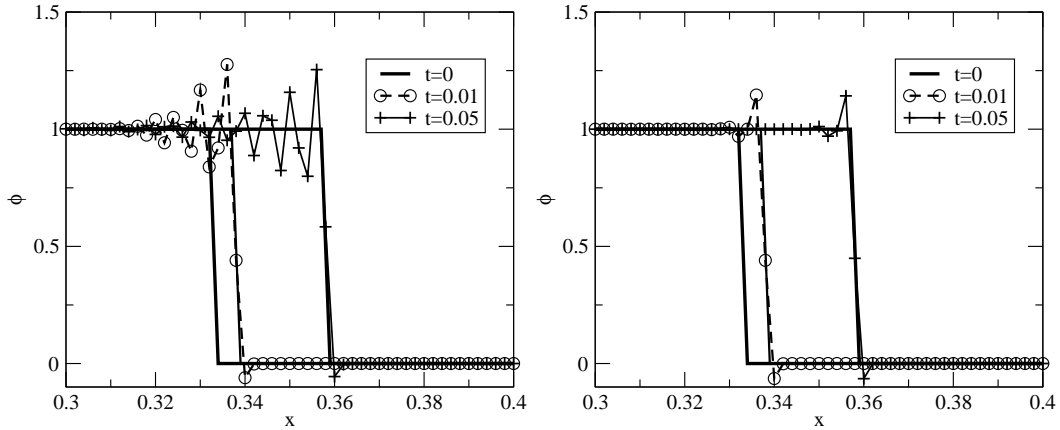


Figure C.7 Calculation of the propagation of a discontinuity using the inviscid Burger's equation; time levels shown $t = 0$, $t = 0.01$ and $t = 0.05$; 4^{th} -order split differences with 4^{th} -order Runge-Kutta time integration for $CFL = 0.2$ (left) and $CFL = 1.0$ (right) with $\Delta x = 0.002$ and $\Delta t = CFL \cdot \Delta x$.

solution is obtained, in contradistinction to the case where central differences were employed.

Following this analysis, it can be concluded that the fourth-order split finite differences in combination with a fourth-order Runge-Kutta method are suitable for the present research. The analysis described above is based on simplified model equations, however, the applicability of the numerical method for the full Navier-Stokes equations is illustrated by several validation cases in section 4.3.

C.5 Filtering

In order to allow for an efficient parallelization of the codes using domain-decomposition, explicit filters for the streamwise direction are derived.

C.5.1 Derivation

The most general form of a filter application utilizing a central stencil is

$$\sum_{j=i-l}^{i+l} \alpha_j \tilde{\phi}_j = \sum_{j=i-l}^{i+l} c_j \phi_j, \quad (C.44)$$

where $\tilde{\phi}_j$ represent the filtered values at the grid-points j and ϕ_j are the function values at the respective nodes. The width of the stencil and thereby the order of the filter operation is specified by l . In this section, only explicit filters are considered, hence $\alpha_i = 1$ and $\alpha_j = 0$ if $j \neq i$.

For the purpose of analyzing the filter operation, an equidistant grid is assumed in order to enable a straight-forward Fourier representation of the function ϕ and the function to be filtered is assumed to be periodic on the interval $[0, L]$. Then ϕ can be represented as

$$\phi_j = \sum_{k=-\frac{N}{2}}^{\frac{N}{2}} A_k \exp\left(\frac{2\pi \mathbf{i} k z_j}{L}\right), \quad (\text{C.45})$$

where N is the number of points in the interval $[0, L]$ and z_j is the streamwise location of the function value. For an equidistant grid, the grid-spacing is defined as $h = \frac{L}{N}$ and a wavenumber and a scaled coordinate are introduced of the form $\Theta = \frac{2\pi k h}{L} = \frac{2\pi k}{N}$, $s_j = \frac{z_j}{h}$, respectively. The Fourier series of equation (C.45) can now be rewritten as

$$\phi_j = \sum_{k=-\frac{N}{2}}^{\frac{N}{2}} A_k \exp(\mathbf{i} \Theta s_j), \quad (\text{C.46})$$

where the wavenumber Θ is in the interval $[0, \pi]$. Substituting the Fourier representation (C.46) into equation (C.44), one obtains the equation

$$\tilde{\phi}_i = \sum_{k=-\frac{N}{2}}^{\frac{N}{2}} \tilde{A}_k \exp(\mathbf{i} \Theta s_i) = \sum_{k=-\frac{N}{2}}^{\frac{N}{2}} \left(\sum_{j=i-l}^{i+l} A_k c_j \exp(\mathbf{i} \Theta s_j) \right). \quad (\text{C.47})$$

Due to the linearity of the Fourier series, an evaluation of every individual mode k is possible. Dividing by $A_k \exp(\mathbf{i} \Theta s_i)$ and using $s_{i+1} = \frac{z_i+h}{h} = s_i + 1$, the transfer function

$$T(\Theta) = \frac{\tilde{A}_k}{A_k} = \sum_{j=i-l}^{i+l} c_j \exp(\mathbf{i} j \Theta) \quad (\text{C.48})$$

is obtained. The transfer function can also be written in the form

$$T(\Theta) = c_0 + 2c_1 \cos \Theta + 2c_2 \cos 2\Theta + 2c_3 \cos 3\Theta \dots \quad (\text{C.49})$$

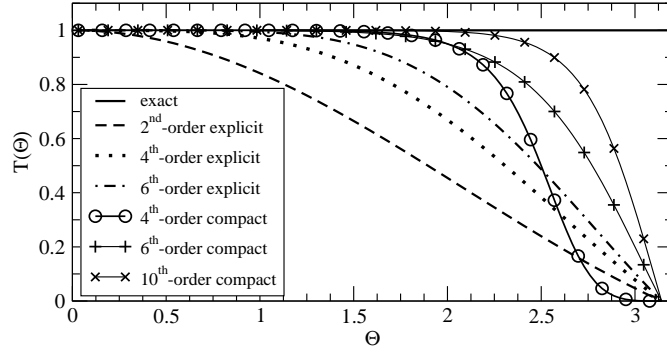


Figure C.8 Transfer functions for explicit and compact filters over scaled wavenumber Θ .

The motivation of the filter was to remove the highest frequencies, to that end it is required that

$$T(\pi) = 0 . \quad (\text{C.50})$$

That leads to the constraint on the coefficients c_j

$$\sum_{j=i-l}^{i+l} c_j \exp(\mathbf{i}j\pi) = \sum_{j=i-l}^{i+l} (-1)^{j-i} c_j = 0 . \quad (\text{C.51})$$

The transfer function for several filters, both explicit and compact are shown in figure C.8. Clearly, for higher-order accurate filters, only the high frequencies are removed whereas the cut-off occurs much earlier for lower-order accurate filters. By using a formally higher-order accurate filter and optimizing the scheme by posing specific conditions on the shape of the transfer function, the location of the cut-off can be adjusted. A 4th-order compact filter, which is optimized such that the cut-off is delayed until $\Theta = 2$ was derived in Lele (1992) and is included in figure C.8. This filter was used in the radial direction in most calculations presented in this research.

In order to derive a filter for a non-equidistant grid, the grid-spacing between the grid-point i and all other nodes used in the filter-stencil ($i-l \leq j \leq i+l$) is denoted by Δ_j . The function values adjacent to node i are expanded in a Taylor series

$$\phi_j = \sum_{k=0}^n \frac{1}{k!} (\Delta_j)^k \phi_i^{(k)} , \quad i-l \leq j \leq i+l . \quad (\text{C.52})$$

The Taylor-series representation of each point $i - l \leq j \leq i + l$ is substituted into equation (C.44) and all terms with the same power $(\Delta_j)^l$ are collected. The first constraint on the coefficients c_j that is imposed is

$$\sum_{j=-l}^l c_j = 1 . \quad (\text{C.53})$$

By requiring a linear combination of coefficients c_j multiplying $(\Delta_j)^k$ to equal zero, the filter becomes $(k + 1)^{th}$ -order accurate. The powers $1 \leq k \leq 2l - 1$ are considered, consequently the truncation error is of $(2l)^{th}$ order. Note that also including a constraint for the $(2l)^{th}$ power results in a degenerate matrix and the trivial solution $\tilde{\phi}_j = \phi_j$ would be obtained. In lack of a better condition, the last constraint that will be used for the system to be solved is the result of equation (C.51), in spite of being derived for an equidistant grid. The effect of this inconsistency will be discussed in section C.5.2.

In summary, equation C.53, the constraint by the transfer function and cancelling out the lower order terms of the Taylor-series result in a linear system of $2l + 1$ equations for the $2l + 1$ unknown coefficients c_j that now can be solved

$$A_{jl} \cdot c_j = s_j . \quad (\text{C.54})$$

The entries of the matrix and the vectors are $A_{jl} =$

$$\begin{pmatrix} (\Delta_{i-l})^{2l-1} & (\Delta_{i-l+1})^{2l-1} & \cdots & 0 & \cdots & (\Delta_{i+l-1})^{2l-1} & (\Delta_{i+l})^{2l-1} \\ (\Delta_{i-l})^{2l-2} & (\Delta_{i-l+1})^{2l-2} & \cdots & 0 & \cdots & (\Delta_{i+l-1})^{2l-2} & (\Delta_{i+l})^{2l-2} \\ \vdots & \vdots & \vdots & \vdots & \vdots & \vdots & \vdots \\ 1 & 1 & \cdots & 1 & \cdots & 1 & 1 \\ (\Delta_{i-l}) & (\Delta_{i-l+1}) & \cdots & 0 & \cdots & (\Delta_{i+l-1}) & (\Delta_{i+l}) \\ \vdots & \vdots & \vdots & \vdots & \vdots & \vdots & \vdots \\ \pm 1 & \cdots & -1 & 1 & -1 & \cdots & \pm 1 \end{pmatrix} \quad (\text{C.55})$$

$$c_j = \begin{pmatrix} c_{i-l} \\ c_{i-l+1} \\ \vdots \\ c_i \\ \vdots \\ c_{i+l-1} \\ c_{i+l} \end{pmatrix} \quad \text{and} \quad s_j = \begin{pmatrix} 1 \\ 0 \\ \vdots \\ 0 \\ \vdots \\ 0 \\ 0 \end{pmatrix} \quad (\text{C.56})$$

The coefficients c_j for every interior grid-point $l \leq i \leq nz1tot + nz2tot - l$ are solved for during initialization of the code, once the grid is known, and stored in a common array.

So far, only central filter-stencils that can be used for interior nodes have been derived. At the boundaries and for the boundary-next points, one-sided or offset stencils are derived. The derivation of these one-sided stencils (offset for the boundary-next points) follows the above derivation, i.e., a Taylor series expansion is employed, the sum of all coefficients needs to equal unity (see equation C.53) and the last equation of the system is chosen to be the transfer function. As an example, all entries for the system $A_{jl} \cdot c_j = s_j$ of the base-next point ($i = 2$) for a 4th-order offset stencil are given

$$\begin{pmatrix} (\Delta_1) & 0 & (\Delta_3) & (\Delta_4) & (\Delta_5) \\ 1 & 1 & 1 & 1 & 1 \\ (\Delta_1)^2 & 0 & (\Delta_3)^2 & (\Delta_4)^2 & (\Delta_5)^2 \\ (\Delta_1)^3 & 0 & (\Delta_3)^3 & (\Delta_4)^3 & (\Delta_5)^3 \\ -1 & 1 & -1 & 1 & -1 \end{pmatrix} \cdot \begin{pmatrix} c_1 \\ c_2 \\ c_3 \\ c_4 \\ c_5 \end{pmatrix} = \begin{pmatrix} 0 \\ 1 \\ 0 \\ 0 \\ 0 \end{pmatrix}. \quad (\text{C.57})$$

C.5.2 Validation and Observations

To ensure a correct implementation of all filter-stencils, first an equidistant grid was generated and the stencils were computed for the interior points and the boundary and boundary-next points. All values of the coefficients (given in table C.1) were found to correspond to the coefficients derived for equidistant grids by Lele (1992). For stretched grids, the accuracy of the derived filters was tested employing analytic test-functions. The filter-stencils were computed for a particular grid and the flow

type	$i - 3$	$i - 2$	$i - 1$	i	$i + 1$	$i + 2$	$i + 3$	$i + 4$	$i + 5$	$i + 6$
6^{th} c	$\frac{1}{64}$	$-\frac{3}{32}$	$\frac{15}{64}$	$\frac{11}{32}$	$\frac{15}{64}$	$-\frac{3}{32}$	$\frac{1}{64}$			
6^{th} b				$\frac{63}{64}$	$\frac{3}{32}$	$-\frac{15}{64}$	$\frac{5}{16}$	$-\frac{15}{64}$	$\frac{3}{32}$	$-\frac{1}{64}$
6^{th} b+1			$\frac{1}{64}$	$\frac{29}{32}$	$\frac{15}{64}$	$-\frac{5}{16}$	$\frac{15}{64}$	$-\frac{3}{32}$	$\frac{1}{64}$	
6^{th} b+2		$-\frac{1}{64}$	$\frac{3}{32}$	$\frac{49}{64}$	$\frac{5}{16}$	$-\frac{15}{64}$	$\frac{3}{32}$	$-\frac{1}{64}$		
4^{th} c		$-\frac{1}{16}$	$\frac{1}{4}$	$\frac{5}{8}$	$\frac{1}{4}$	$-\frac{1}{16}$				
4^{th} b				$\frac{15}{16}$	$\frac{1}{4}$	$-\frac{3}{8}$	$\frac{1}{4}$	$-\frac{1}{16}$		
4^{th} b+1			$\frac{1}{16}$	$\frac{3}{4}$	$\frac{3}{8}$	$-\frac{1}{4}$	$\frac{1}{16}$			
4^{th} b+2		$-\frac{1}{16}$	$\frac{1}{4}$	$\frac{5}{8}$	$\frac{1}{4}$	$-\frac{1}{16}$				

Table C.1 Coefficients of 4^{th} - and 6^{th} -order accurate filter-stencils for an equidistant grid (c=central, b=boundary, b+1=boundary-next, etc.)

field was initialized with a test function Ψ . The test-function was then filtered once and the difference between the original test-function and the filtered function was computed and scaled with the local grid-spacing as

$$\epsilon_{\Delta} = \frac{\tilde{\Psi} - \Psi}{\Delta_{i+1}}. \quad (C.58)$$

The results of that analysis for both 4^{th} -order accurate and 6^{th} -order accurate filters for different grids are shown in figure C.9. The parameters of the grids employed are listed in table C.2. Note that for the exponential grids, the grid-spacing constantly increases whereas for polynomial grids, the grid-function has an inflection point, i.e.,

points	A	b	a_z	b_z	c_z	d_z
50	154.91	1	n/a			
100	41.18	1	n/a			
200	21.05	1	n/a			
400	10.00	1	n/a			
100	n/a		0.61	4.94	21.92	0.55

Table C.2 Parameters for computational grids employed for testing accuracy of filter-operations on stretched grids ($1 \leq z \leq 10$). A and b are the coefficients of the grid-function $f_z(z) = Ae^{bz}$ and a_z, b_z, c_z and d_z are the coefficients for the standard polynomial grid-function given in equation (C.4).

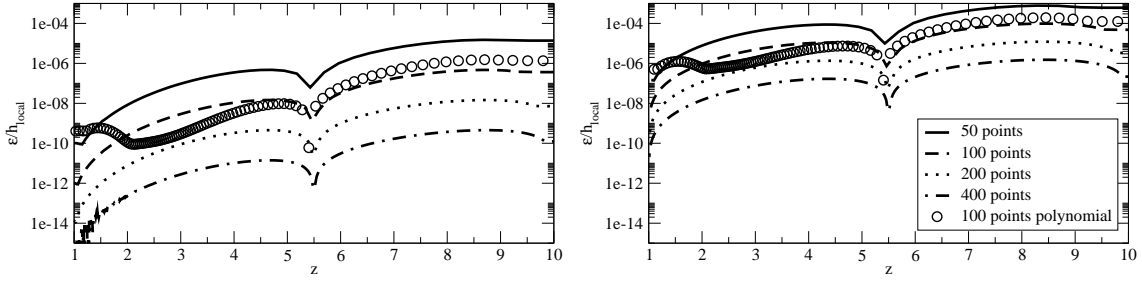


Figure C.9 Errors normalized with the local grid-spacing (Δ_{i+1}) for the explicit filters on stretched grids; 6th-order accurate (left) and 4th-order accurate (right); lines denote exponential grids, symbols denote polynomial grids with an inflection point at $z = 2$.

the grid-spacing first decreases and then increases again as is the case for the grids employed in base flow calculations. For the results shown, a sine-wave was chosen as a test-function. The prominent 'kink' seen in all curves marks the location where the sine-wave changes sign. For all cases employing an exponential grid, the error ϵ_{Δ} increases monotonically with downstream distance (except at the sign change of the test-function). This was expected, because the grid-spacing was increasing. The error can be estimated as

$$\left. \begin{aligned} \epsilon_{\Delta 4} &\approx \frac{\Delta^4}{\Delta_{i+1}} \approx \Delta^3 \\ \epsilon_{\Delta 6} &\approx \frac{\Delta^6}{\Delta_{i+1}} \approx \Delta^5 \end{aligned} \right\} \Rightarrow \epsilon_{\Delta 6} = \mathcal{O}(\Delta^2) \cdot \epsilon_{\Delta 4} . \quad (\text{C.59})$$

This behavior can be observed when comparing the results for the 6th-order accurate filter with the results for the 4th-order accurate filter, shown in figure C.9. Note also, that the order of accuracy ($\mathcal{O}(\Delta^l)$) for the boundary and boundary-next points is preserved. Only the constant multiplying $\mathcal{O}(\Delta^l)$ for the one-sided stencils differs from the constant that would be obtained for the interior central stencil.

In order to study the behavior of the different filters under conditions that were expected to occur for the planned investigation, a test-case was chosen with the following requirements: A thin approach boundary layer so that strong grid-stretching needed to be employed in radial direction to resolve the high gradient at the wall with a small number of radial points. Supersonic flow conditions to generate an expansion

fan emanating from the base. Slow convergence, thus requiring a large number of time-steps and therefore a large number of filter-operations.

The calculations of an axisymmetric wake at $Re_D = 10,000$ and $M = 2.46$ with and approach boundary layer thickness at the separation point of $\delta_c = 0.1$ was determined to satisfy the above characteristics. In order to fully converge the calculations to a steady-state solution, 100,000 time-steps were required. In the radial direction, the 4th-order accurate compact filter, introduced in section C.5.1, was employed. For comparison, 4th- and 6th-order accurate explicit filters, derived following the above described method, were employed in the radial direction. In the streamwise direction, only 4th- and 6th-order accurate explicit filters were used in order to ensure an efficient parallelization. The tests were performed on both an equidistant and a stretched grid.

As figure of merit, contours of ρu were chosen. The contour of $\rho u = 0$ is shown as a dashed line and visualizes the extent of the separation region. Note, that for an equidistant grid, all filters employed are “exact”, i.e. no error is introduced by choosing a transfer function that applies to an equidistant grid. Looking at the results from the calculations on the equidistant grid (not shown here), no differences can be observed in the converged solution when employing either the compact filter or the 6th-order accurate explicit filter in the radial direction. However, when employing the 4th-order accurate explicit filter in the radial direction, the recirculation length slightly decreases compared to the cases employing higher-order filtering in the radial direction, implying that, for the utilized resolution in the radial direction, the filter introduces an unacceptable error.

The picture changes, when all filter combinations are tested on stretched grids (figure C.10). The stretching in the radial direction is significantly stronger than in the streamwise direction. Now, an additional error is introduced when deriving the filter weights by using a transfer function that is applicable for an equidistant grid. The solution obtained when using the compact filter in the radial direction and the 6th-order accurate explicit filter in the streamwise direction reproduces the result of

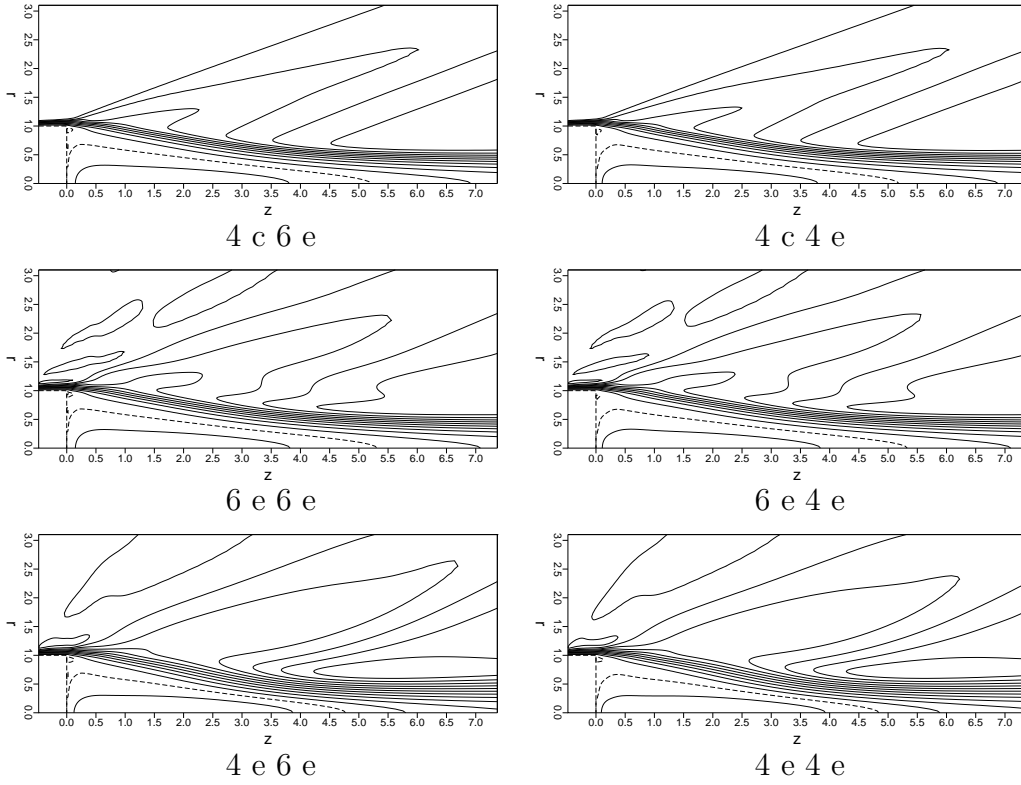


Figure C.10 Converged streamwise velocity field employing different filters; axisymmetric “DNS” on stretched grid; $M = 2.46$ and $Re_D = 10,000$ (first number denotes order of accuracy of filter in radial direction, second number denotes order of accuracy of filter in streamwise direction, c: compact, e: explicit).

the reference calculation on the equidistant grid. This implies that the filters do not deteriorate the solution when employing stretching. However, when employing either the compact or the 6th-order accurate explicit filter in the radial direction, the flow-field shows differences. Using the 6th-order accurate explicit filter in the radial direction, a standing wave can be observed in the radial direction (visible through the interruption of the contours in the expansion fan) that has a wavelength corresponding to the filter-width. That, in combination with an overpredicted recirculation length, renders the solution useless.

The reason for this behavior is assumed to lie in the use of a transfer function for an equidistant grid as a condition for deriving the filter-stencils for stretched grids.

It is speculated that, if a transfer function for a stretched grid could be established, it would most likely possess a value larger than unity for low wavenumbers, leading to the occurrence of the (unphysical) standing wave in the radial direction. The error made by using the “equidistant transfer function” depends on the degree of stretching and also becomes larger, the wider the utilized stencil becomes, because the ratio of the smallest to the largest Δ increases with the stencil-width. The latter can be observed in figure C.10, where the 4th-order accurate explicit filter is used in the radial direction. The amplitudes of the observed standing waves in radial direction are not as large as for the higher-order accurate explicit filter, however, the solution still suffers from the unphysical effects introduced by the filter and shows too small a recirculation length, independent of which filter was chosen in the streamwise direction.

Finally, for the three different options of filtering in the radial direction, it can be observed that no noticeable difference in the converged solution originates from the choice of the streamwise filter. This was to be expected in light of the lack of significant gradients in the streamwise direction. Also, the stretching in the streamwise direction was moderate for most calculations performed in the present investigation. On grids with only moderate stretching in the streamwise direction, both explicit filters could be used. The choice of which one to employ depended solely on the amount of additional dissipation desired for the given calculation. For all calculations denoted by “DNS” in this work, the 6th-order explicit filter was employed.

To conclude, for all calculations presented in this work, the compact filter was chosen for the radial direction. It was determined, that the explicit filters for the streamwise direction, allowing for a significantly more efficient parallelization, were adequate. The results in the validation chapter 4 confirmed that a correct representation of various flow-fields was achieved with the current numerical method, including the above discussed filters.

C.6 Parallelization

C.6.1 Domain Decomposition

As shown in figure 3.1, the computational domain is divided into a boundary layer and a wake region. Each region can be divided into sub-domains. At compile-time, the total number of streamwise points for region 1 ($nz1tot$) and for region 2 ($nz2tot$) and the number of sub-domains desired for each region ($ndom1$ and $ndom2$, respectively) needs to be specified. The streamwise number of points for the sub-domains in region 1 and 2 are given as

$$nz1 = \frac{nz1tot}{ndom1} \quad , \quad nz2 = \frac{nz2tot}{ndom2} \quad , \quad (C.60)$$

with the constraint, that both $nz1$ and $nz2$ need to be integer numbers and larger than the widest derivative- or filter-stencils.

Two different modes of parallelization are possible with the current implementation: Both regions are divided into the same number of sub-domains (as shown in figure C.11). For this approach, first the sub-domains in region 1 and then the sub-domains in region 2 are computed, or vice-versa, depending on the splitting direction. This mode of parallelization has the advantage that the size of the sub-domains in region 1 and 2 ($mr1 \cdot nz1$ and $mr2 \cdot nz2$, respectively) can be highly disparate without causing a reduction in efficiency of the parallelization due to idle-time of individual

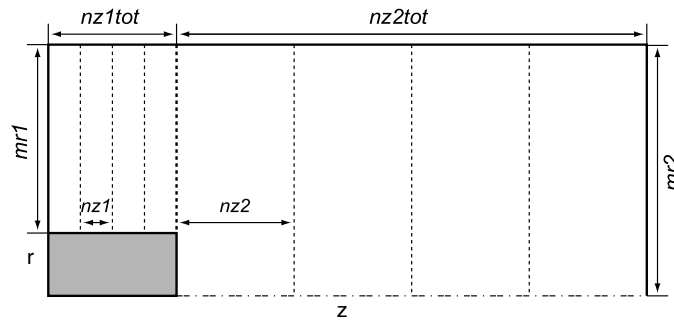


Figure C.11 Domain decomposition for base flow simulations with 4 processors.

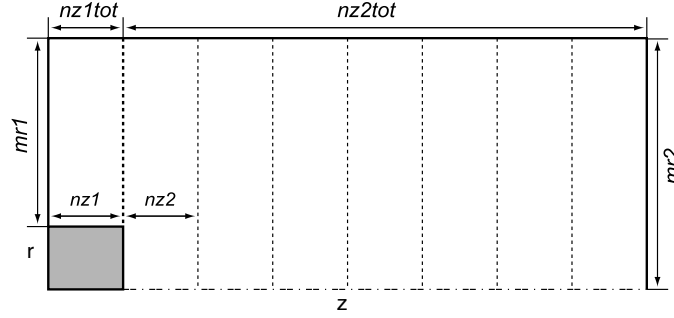


Figure C.12 Domain decomposition for base flow simulations with 8 processors.

CPUs that have a smaller work-load than others. However, this approach is only of practical use for small numbers of CPUs, as the main interest of the present work is on investigating the wake flow and not the incoming boundary layer, hence typically $nz1tot < 100$. Here, the maximum number of CPUs that can be used for the full simulation is restricted by $ndom1$. For this reason, the second approach, where both regions contain a different number of sub-domains (an example for that option is shown in figure C.12) was implemented. The smallest number of sub-domains allowed in this case is one for region 1 and two for region 2. Here, while calling loops over the total number of domains ($1 \leq nd \leq ndom1 + ndom2$), it is distinguished, whether nd corresponds to a sub-domain in region 1 or 2. For this case, it is now crucial that the size of the sub-domains in region 1 and 2 is roughly the same in order to allow for an efficient parallelization

$$mr1 \cdot nz1 \simeq mr2 \cdot nz2. \quad (C.61)$$

Note that for both approaches, the number of utilized CPUs does not necessarily have to correspond to the number of sub-domains. The number of CPUs must be less or equal to the number of sub-domains. To ensure an efficient parallelization in both cases, the following constraints need to be satisfied

$$\frac{ndom1}{CPUs} = \frac{ndom2}{CPUs} = \text{integer} \quad \text{or} \quad \frac{ndom1 + ndom2}{CPUs} = \text{integer}, \quad (C.62)$$

respectively.

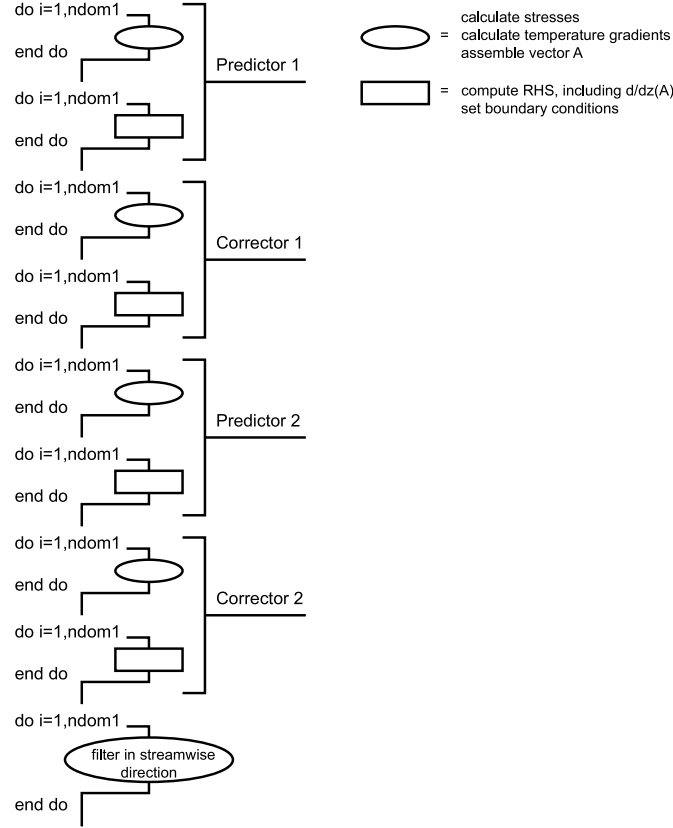


Figure C.13 Flow chart of parallel loops and implicit synchronization contained in one Runge-Kutta cycle for a boundary-layer calculation.

Before calling the subroutines that compute streamwise derivatives, the required number of radial/azimuthal planes² of the neighboring upstream ($nd - 1$) or downstream ($nd + 1$) sub-domain, depending on the splitting direction, is copied into a temporary array that will be passed into the respective subroutine in addition to the function values for the current sub-domain (nd). In the case of streamwise filtering, no passing of extra information is required because the filtering routine accesses a temporary array defined solely for that purpose. This array contains the data to be filtered for all sub-domains (after implicit synchronization, as described below and shown in figure C.13).

²This number depends on the width of the finite-difference stencil and is two for the 4th-order accurate split-differences and one for the low order stencils used for the sub-grid mass-fluxes.

Synchronization is required before information of neighboring domains can be accessed, as described above. The code does not contain explicit synchronization statements, but the fact is exploited that in *Open MP*, at the end of a “do-loop” over the number of sub-domains, all CPUs have to return the result of their respective work before the next operation will be executed, thereby performing an implicit synchronization. To illustrate this method, a flow-chart of the simplest case, a boundary layer calculation, where only region 1 is computed, is given in figure C.13. It can be seen, that before information of a neighboring domain needs to be accessed (streamwise derivatives required for the stress-tensor and temperature gradients, streamwise derivative of vector A of equation 3.1, streamwise filtering, etc.) an implicit synchronization in form of closing the loop over the sub-domains has been executed. The efficiency of the algorithm will be discussed in the next section.

C.6.2 Performance Study

For the present investigation, most large-scale simulations were conducted on *SGI Origin 3k*-type computers. That particular series features R12k or R16k processors with 400 or 700 MHz, respectively, and each processor contains 8 MB cache. Several calculations were also conducted on *HP Alpha* machines. Before conducting large calculations, the efficiency of the code was thoroughly tested for several different problem sizes. As described in Terzi (2004), optimizing the scheduling environment of multi-processor computers on the *SGI Origin* systems can increase efficiency of the parallelization significantly. Therefore the settings found optimal in his work were adapted and used for all test-cases and final simulations. For evaluation of the efficiency of the parallelization, two different quantities are used: the speed-up that is defined as the ratio of the required time for a computation using one processor over the required time using n processors

$$Sp = \frac{t(1)}{t(n)}, \quad (C.63)$$

and the parallel efficiency that is formed by the fraction of speed-up over the number of processors

$$\eta_P = \frac{Sp}{n} . \quad (\text{C.64})$$

According to Amdahl's law

$$Sp = \frac{1}{\frac{fp}{n} + 1 - fp} , \quad (\text{C.65})$$

the speed-up is limited by the parallel fraction fp of the code. Profiling of the code on the *SGI* system revealed that the parallel fraction is approximately $fp = 99\%$, most likely due to communication delays of the hardware.

The parallel performance of the code was tested conducting several calculations with different domain-sizes, i.e., memory requirements. Initially, several calculations were performed where the domain-size was chosen such that the job would be contained fully in cache for a sufficiently large number of CPUs. The number of CPUs needed to contain the entire calculation in cache can be computed as $\frac{\text{job-size}}{8\text{MB}/\text{CPU}} = \text{CPUs}_C$. Table C.3 lists the domain-size, along with the resulting job-size and CPUs_C for the test-calculations.

Figure C.14 illustrates, that for all cases, when the number of utilized processors approaches CPUs_C , the speed-up and therefore the efficiency increases significantly. For the smallest case (squares), the calculation fits into cache for all parallel calculations which results in “super-linear” speed-up, i.e., the efficiency is larger than unity. From the case requiring 155MB , it becomes obvious that even if only a portion of the

<i>mr1</i>	<i>mr2</i>	<i>nz1tot</i>	<i>nz2tot</i>	<i>kh</i>	size (MB)	CPUs_C
50	80	64	448	0	28	4
50	80	64	448	4	155	19
50	80	64	448	8	409	52

Table C.3 Parameters of test-cases conducted for illustration of importance of cache-effects for parallel calculations, CPUs_C denotes the number of CPUs required to fit the entire calculation into cache on an *SGI Origin 3900*.

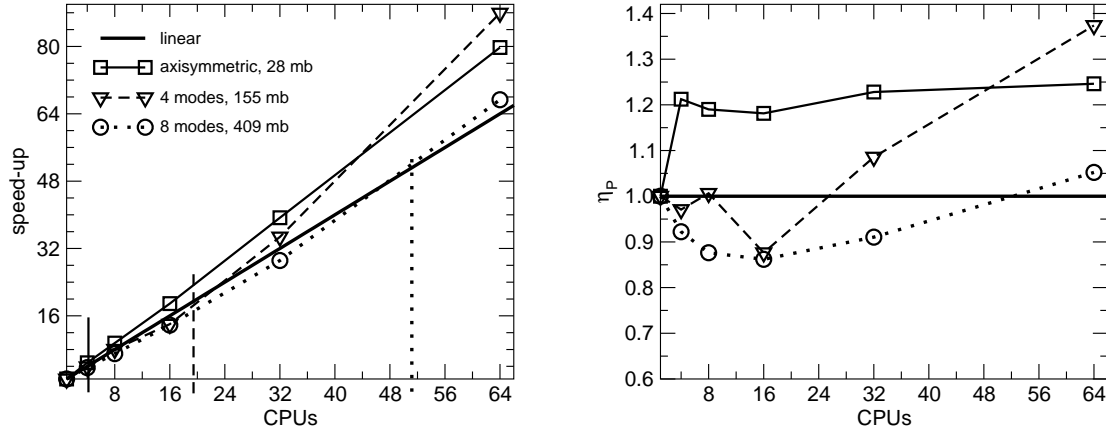


Figure C.14 Speed-up (left) and efficiency (right) over number of CPUs for calculations with different problem-sizes on an *SGI Origin 3900*; vertical bars denote the number of CPUs required to fully fit the respective calculation into cache.

required memory fits into cache, “super-linear” speed up can be achieved, as most of the needed memory is accessible very quickly. The largest case (denoted by circles) initially shows a decrease in efficiency because too small a portion of the memory can be stored in cache. As the number of utilized CPUs increases, the efficiency recovers and for $\text{CPUs} \geq \text{CPUs}_C$, super-linear speed up is achieved again. As a consequence, it is highly desirable to utilize a sufficient number of CPUs to exploit cache-effects as they can achieve considerable savings in computational time.

However, typical DNS of supersonic base flows require an amount of memory significantly exceeding the available cache memory. For that reason, a case with a job size of $4GB$, that would require $\frac{4,000MB}{8MB/CPU} = 500$ CPUs to be fully contained in cache on the *SGI Origin* was conducted on both the *SGI* and the *HP* machines in order to evaluate the performance in absence of cache-effects. The results obtained from the benchmark calculations are shown in figure C.15. Note that on the *HP* machine, each node was configured with 64 CPUs, therefore, the benchmarks could only be completed up to that number. On the *SGI Origin 3900*, the efficiency reaches very low levels for large numbers of CPUs due to the fact that a large amount of memory has to be distributed across the machine. This leads to high communication penalties

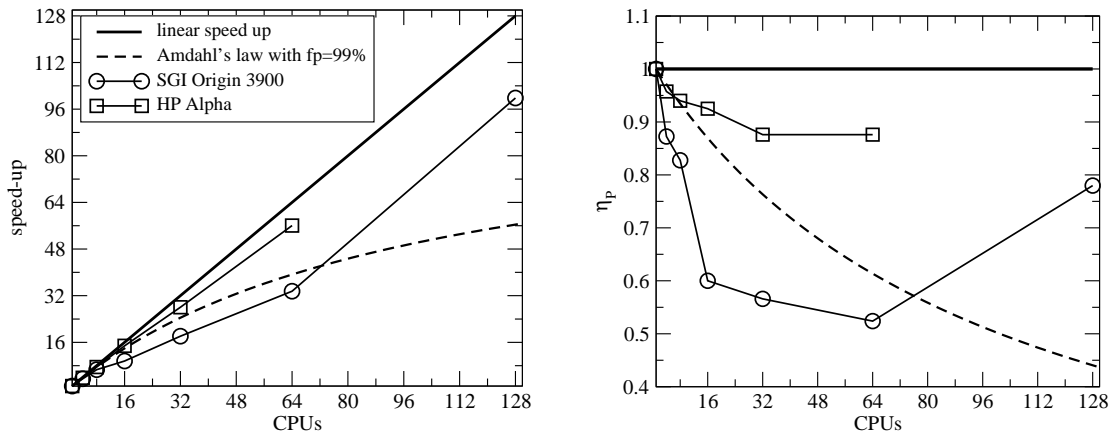


Figure C.15 Speed-up (left) and efficiency (right) over number of CPUs on *SGI Origin 3900* and *HP Alpha* computers; size of calculation was approximately 4GB.

when each CPU needs to retrieve information. However, when the number of CPUs is increased to 128 on the *SGI*, the efficiency significantly improves, suggesting that part of the memory most frequently needed can be placed into cache. The architecture of the *HP Alpha* computer appears to be better suited for the large problem-size tested here. The parallel efficiency does not drop below 85% for all numbers of CPUs tested, well above the values obtained from Amdahl's law using $fp = 99\%$. This indicates that the parallel fraction of the code obtained on the *SGI* system is hardware dependent.

In addition to the parallel efficiency, the number of operations that can be performed per second also determines the wall-time required to conduct a calculation. A profiler was therefore employed to determine the floating-point operations per second (*FLOPS*). Note that the *FLOPS* value obtained by the profiler constitutes a lower bound, as the hardware counter only counts one instruction for a multiply-add, which, strictly speaking, are two floating-point operations. The values obtained for the benchmark computations are included in table C.4. The *MFLOPS*-rate of the *HP* computer is up to four times higher than that of the *SGI* machine. This is in part due to the better parallel efficiency. More important, however, is, that the

CPUs	<i>SGI Origin 3900</i>				<i>HP Alpha</i>			
	$t[s]/\text{step}$	$MFLOPS$	Sp	η_P	$t[s]/\text{step}$	$MFLOPS$	Sp	η_P
1	42.92	147	1	1.00	18.50	341	1	1.00
4	12.29	500	3.49	0.88	4.83	1,273	3.83	0.96
8	6.49	913	6.62	0.83	2.46	2,411	7.52	0.94
16	4.47	1,395	9.6	0.60	1.25	4,979	14.8	0.93
32	2.37	2,599	18.11	0.57	0.66	9,400	28.03	0.88
64	1.28	4,638	33.53	0.52	0.33	17,705	56.06	0.88
128	0.43	10,523	99.81	0.78	N/A	N/A	N/A	N/A

Table C.4 Time in seconds per time-step, $MFLOPS$ -rate, speed up Sp and efficiency η_P for large wake-computation (4,000 MB) on *SGI Origin 3900* with R16k, 700MHz CPUs and *HP Alpha*.

$MFLOPS$ -rate already is a factor of 2.32 larger on a single CPU. The efficiency of the algorithm also was shown to be satisfactory, achieving 147 $MFLOPS$ per CPU on the *SGI Origin 3900* and up to 341 $MFLOPS$ per CPU on the *HP Alpha*. The highest sustained performance achieved with the parallel code was 10.5 $GFLOPS$ and 17.7 $GFLOPS$ on the *SGI Origin 3900* and the *HP Alpha*, respectively.

In conclusion, several benchmark cases with varying job-sizes were conducted on different computer architectures. A high efficiency of the algorithm itself and a good parallel efficiency of the parallel code were established on large shared-memory systems. For cases, where the job-size was small enough to fit into cache memory, super-linear speed-up was achieved. It was demonstrated that even in the absence of cache-effects, the parallel efficiency of the code maintains values exceeding 85% for up to 64 CPUs on an *HP Alpha*.

Appendix D: FLOW PARAMETERS

quantity	TDNS	LNS, COARSE	LNS/DNS, FINE
Re	10,000	100,000	
M	0.25		
Pr	0.71		
γ	1.4		
\mathcal{R}_{Su}/T	0.36866		
$\lambda_z = \frac{2\pi}{\alpha_z}$	2.51327	N/A	
z_0	N/A	0.2583	
Re_{δ_1} at inflow	1,000	280.674	280.677
$mr1$	80	68	88
$nz1/lh$	N/A / 4	288 / N/A	576 / N/A
Δz	N/A	0.0133	0.00665
Δr_{wall}	0.002	$7.94 \cdot 10^{-4}$	$5 \cdot 10^{-4}$
r_{wall}	$1 \cdot 10^3$	$1 \cdot 10^3$	$1 \cdot 10^3$
$r_{max} - r_{wall}$	$3 \cdot \delta$	$5.3198 \cdot 10^{-2}$	$9.75 \cdot 10^{-2}$
A_{dist}	$1 \cdot 10^{-5}$	$1 \cdot 10^{-4}$	$1 \cdot 10^{-4}/2 \cdot 10^{-2}$
$\omega = \frac{\beta}{2\pi}$	N/A	2.228169	2.228169
r_b	N/A	$7.146 \cdot 10^{-3}$	$4.5 \cdot 10^{-3}$
r_e	N/A	$1.2704 \cdot 10^{-3}$	$8 \cdot 10^{-3}$
z_b	N/A	0.3780	0.31815
z_e	N/A	0.4578	0.35805
dt	$5 \cdot 10^{-4}$	$2.805 \cdot 10^{-4}$	$1.496 \cdot 10^{-4}$
CPU hours/period	N/A	0.04298	0.20713

Table D.1 Parameters for 2-D TS wave validation calculations with the DNS, TDNS and the LNS code; CPU time on *HP Alpha* per forcing period.

case	2-D wave		3-D oblique wave		
quantity	LNS	DNS	TDNS	LNS	DNS
Re	100,000		1,578,102		
M	1.6		3		
Pr	0.71		0.71		
γ	1.4		1.4		
\mathcal{R}_{Su}/T	0.36866		1.06757		
λ_z	N/A		0.05194	N/A	
ψ	0		60°		
λ_θ	0		0.02998		
z_0	0.2250		N/A	$1.5917 \cdot 10^{-3}$	
Re_{δ_1} at inflow	438.802		3842.68	274.857	
$mr1$	150		120	130	
$nz1 / lh$	300 / N/A		N/A / 6	280 / N/A	
kh	0		4	1	
Δz	0.03704		N/A	$1.6228 \cdot 10^{-3}$	
Δr_{wall}	$1.25 \cdot 10^{-3}$		$4 \cdot 10^{-5}$	$3.51 \cdot 10^{-5}$	
r_{wall}	$1 \cdot 10^3$		$1 \cdot 10^3$		
$r_{max} - r_{wall}$	3.2283		0.0191	$4.702 \cdot 10^{-2}$	
A_{dist}	$1 \cdot 10^{-4}$	$2 \cdot 10^{-2}$	$5 \cdot 10^{-5}$	1	
$\omega = \frac{\beta}{2\pi}$	0.7961726		N/A	12.558136	
r_b	$5 \cdot 10^{-3}$		N/A	$1.40403 \cdot 10^{-4}$	
r_e	$1.375 \cdot 10^{-2}$		N/A	$3.86378 \cdot 10^{-4}$	
z_b	0.55836		N/A	$2.59337 \cdot 10^{-2}$	
z_e	0.78060		N/A	$3.56705 \cdot 10^{-2}$	
dt	$1.04667 \cdot 10^{-3}$		$5 \cdot 10^{-5}$	$3.3179 \cdot 10^{-5}$	
CPU hours	0.0968		N/A	0.3226	0.4266

Table D.2 Parameters for supersonic TS wave validation calculations with the DNS, TDNS and the LNS code; CPU time on *HP Alpha* per forcing period.

quantity	2-D TS wave	quantity	2-D TS wave
Re	5,000 - 200,000	$mr2$	130
M	2.46	lh	16
Pr	0.71	kh	8
γ	1.4	A_{dist}	$1 \cdot 10^{-8}$
\mathcal{R}_{Su}/T	0.36866	dt	$1 \cdot 10^{-3}$
$\lambda_z = \frac{2\pi}{\alpha_z}$	$2 \cdot \pi$	CPU hours	8.935
$\lambda_\theta = \frac{2\pi}{\alpha_\theta}$	$2 \cdot \pi$		

Table D.3 Parameters for stability investigations using the temporal code; CPU time on *HP Alpha* per forcing period.

Method	DNS				LNS
quantity	COARSE	FINE	3D COARSE	3D FINE	3D COARSE
M	0.25				
Re	500-8,000	500-2,000	500-2,000	2,000	500-2,000
Pr	0.71				
γ	1.4				
\mathcal{R}_{Su}/T	0.36866				
z_a	6				
r_{max}	7.6				
z_{max}	42				
probe (r, z)	(1,1)				
$\Delta r_c = \Delta z_c$	0.01	0.02	0.01	0.02	0.01
$nz1$	80	64	80	64	80
$nz2$	200	660	200	660	200
$mr1$	50	50	50	50	50
$mr2$	90	100	90	100	90
kh	0	0	8	8/16/32	4
dt	$2.897 \cdot 10^{-3}$	$4.0 \cdot 10^{-3}$	$2.897 \cdot 10^{-3}$	$3/2/2 \cdot 10^{-3}$	$1.932 \cdot 10^{-3}$
CPU hours	4.52	4.70*	14.86	61/128/268	3.49

Table D.4 Parameters used for DNS and LNS code validation calculations of subsonic axisymmetric and 3-D wake; CPU time on *HP Alpha* until converged for axisymmetric cases and per flow-trough time for unsteady cases; * using the result from the coarse calculation as initial condition.

Method	temporal RANS				spatial RANS
quantity	EASM	EASM $_{\alpha}$			EASM $_{\alpha}$
M	0.25				2.46
Re_{δ}	1, 700			50, 000	165, 000
Pr, γ	0.71, 1.4				
\mathcal{R}_{Su}/T	0.36866				
z_{max}	N/A				1.73
Δz	N/A				0.02 – 0.07
r_{wall}	$1 \cdot 10^3$				1
$r_{max} - r_{wall}$	2.4				0.56
Δr_{wall}	$4 \cdot 10^{-4}/1 \cdot 10^{-3}$	$2 \cdot 10^{-4}/2 \cdot 10^{-3}$		$2 \cdot 10^{-4}$	$5 \cdot 10^{-5}$
$mr1$	60	80	160	120	80
$nz1 / lh$	N/A / 0				52 / N/A
dt	$1 \cdot 10^{-4}/2.5 \cdot 10^{-3}$	$2.5 \cdot 10^{-5}/4 \cdot 10^{-3}$		$2 \cdot 10^{-5}$	$4 \cdot 10^{-5}$
CPU hours	0.14/0.06	0.74/0.05	1.1/0.07	0.13	2.0*

Table D.5 Parameters for validation calculations of turbulent boundary layers; CPU time until converged on Pentium 4 PC; * CPU time on *SGI Origin 3900*.

quantity	DNS		LNS			
M	2.46					
Re	20,000	$\{5, 10, 20, 200\} \cdot 10^3$	30,000	60,000	100,000	
Pr, γ	0.71, 1.4					
\mathcal{R}_{Su}/T	0.36866					
δ_c, z_a	0.1, 1					
(r_{max}, z_{max})	(6,10)					
probe (r, z)	(0.5,2.5)					
$\Delta r_c = \Delta z_c$	0.008			0.01		0.008
$nz1$	32					
$mr1$	45					
$nz2$	780			420	780	1240
$mr2$	130					160
kh	8				16	8
dt	$2.4 \cdot 10^{-3}$			$3.0 \cdot 10^{-3}$		$2.4 \cdot 10^{-3}$
CPU hours	19.55	9.14		8.49*	44*	53.99*

Table D.6 Parameters used for DNS and LNS calculations of supersonic base flows; CPU time on *HP Alpha* per flow-trough time; * CPU time on *SGI Origin 3900*.

quantity	SDNS1a	SDNS1b	SDNS2	SDNS3
M	2.46			
Re	30,000	30,000	60,000	100,000
$Pr, \gamma, \mathcal{R}_{Su}/T$	0.71, 1.4, 0.36866			
δ_c, z_a, r_{max}	0.1, 1, 6			
z_{max}	12		10	15
probe* (r, z)	(4.82, 0.24)	(4.82, 0.24)	(7.85, 0.465)	(8.27, 0.336)
$\Delta r_c = \Delta z_c$	0.008	0.01	0.01	0.008
$nz1$	64	32	32	32
$nz2$	456	420	780	1240
$mr1$	75	45	45	45
$mr2$	200	130	130	130
kh	64	32	128	128
dt	$1.19 \cdot 10^{-3}$	$1.5 \cdot 10^{-3}$	$1.375 \cdot 10^{-3}$	$8.0 \cdot 10^{-4}$
CPU hours	1,780	104 (<i>HP Alpha</i>)	3,731	19,132

Table D.7 Parameters used for DNS of supersonic base flows; CPU time on *SGI Origin 3900* per flow-trough-time; values for kh and CPU hours for half-cylinder calculations; * for initial growth of higher modes, probe was set at disturbance point (2.5, 0.5) .

quantity	RANS/FSM		RANS/FSM	
			Coarse	Fine
M	2.46			
Re	30,000		60,000	
$Pr, \gamma, \mathcal{R}_{Su}/T$	0.71, 1.4, 0.36866			
$\delta_c, z_a, (r_{max}, z_{max})$	0.1, 1, (6, 12)			
$\Delta r_c = \Delta z_c$	0.01		0.02	0.01
$nz1$	32		32	32
$nz2$	120		130	270
$mr1$	50		45	45
$mr2$	85		90	130
kh	0/4		0/4–16	0/8–32
dt	$\{7, 3^*/2.5\} \cdot 10^{-3}$		$\{7/2.6\} \cdot 10^{-3}$	$\{7/1.54\} \cdot 10^{-3}$
CPU hours	3.6/1.6		4.0/1.9–8.8	24/10.3–76.1
$c_T, c_{\epsilon 1}, c_{\epsilon 2}$	N/A, 1.44, 1.88		4.56, 1.44, 1.88	4.56, 1.44, 1.88

Table D.8 Parameters used for RANS/FSM calculations of transitional supersonic base flows; all values for calculations employing EASM $_{\alpha}$, except when marked with * (EASM model); CPU time on *HP Alpha* until converged for axisymmetric RANS and per flow-trough-time for FSM; values for kh applies to half-cylinder calculations.

quantity	RANS		FSM	
	Coarse	Fine	Coarse	Fine
Re	$3.3 \cdot 10^6$			
M	2.46			
Pr, γ	0.71, 1.4			
\mathcal{R}_{Su}/T	0.816			
δ_c	0.1			
z_a	0.16			
r_{max}	6			
z_{max}	12			
$\Delta r_c = \Delta z_c$	0.005	0.0004	0.005	0.005
$nz1$	16	16	16	16
$nz2$	256	512	256	512
$mr1$	50	50	50	50
$mr2$	220	350	210	210
kh	0	0	16–32	16–32
dt	$4 \cdot 10^{-4}$	$8.45 \cdot 10^{-5}$	$3 \cdot 10^{-4}$	$3 \cdot 10^{-4}$
CPU hours	42*	460*	273	545 – 1200
c_T	4.45	4.45	4.45	4.45
$c_{\epsilon 1}$	1.43/1.44	1.43/1.44	1.43	1.43
$c_{\epsilon 2}$	1.92/1.88	1.92/1.88	1.92	1.92
a_1	0.4866/0.5416	0.4866/0.5416	0.5416	0.5416

Table D.9 Parameters used for RANS/FSM calculations of UIUC case; all values for calculations employing EASM $_{\alpha}$; CPU time on *HP Alpha* until converged for axisymmetric RANS and per flow-trough-time for FSM; * CPU time on *SGI Origin 3900*.

References

- ASCHENBACH, E. 1974 Vortex shedding from spheres. *J. Fluid Mech.* **62**, 209.
- BALZER, W. 2003 Investigation of supersonic wakes using temporal direct numerical simulations. Master's thesis, The University of Arizona.
- BATTEN, P., GOLDBERG, U. & CHAKRAVARTHY, S. 2000 Sub-grid turbulence modelling for unsteady flow with acoustic resonance. *AIAA Paper* **2000-0473**.
- BATTEN, P., GOLDBERG, U. & CHAKRAVARTHY, S. 2002 LNS - an approach towards embedded LES. *AIAA Paper* **2002-0427**.
- BOGDANOFF, D. W. 1983 Compressibility effects in turbulent shear layers. *AIAA J.* **21** (6), 926-927.
- BOURDON, C. J. & DUTTON, J. C. 1998 Planar visualizations of large-scale turbulent structures in axisymmetric supersonic separated flows. *Phys. Fluids* **11**, 201-213.
- BOURDON, C. J. & DUTTON, J. C. 2000 Effects of boattailing on the turbulence structure of a compressible base flow. *AIAA Paper* **2000-2312**.
- BOURDON, C. J. & DUTTON, J. C. 2001 Visualizations and measurements of axisymmetric base flows altered by surface disturbances. *AIAA Paper* **2001-0286**.
- BOURDON, C. J., DUTTON, J. C., SMITH, K. M. & MATHUR, T. 1998 Planar visualizations of large-scale turbulent structures in axisymmetric supersonic base flow. *AIAA Paper* **98-0624**.
- BOUSSINESQ, J. 1877 Théorie de l'écoulement tourbillant. *Mem. Pre. par. div. Sav.* **23**.
- BOWMAN, W. C. & CLAYDEN, W. A. 1968 Boat-tailed afterbodies at $M=2$ with gas ejection. *AIAA J.* **2**, 2029.
- BROWN, G. & ROSHKO, A. 1974 On density effects and large structures in turbulent mixing layers. *J. Fluid Mech.* **64**, 775-781.
- BURKE, C. R. 2001 Private Communication.
- CANNON, S. & CHAMPAGNE, F. H. 1991 Large-scale structures in wakes behind axisymmetric bodies. In *8th Symposium on turbulent shear flows*.
- CHAPMAN, D. R. 1951 An analysis of base pressure at supersonic velocities and comparison with experiments. NACA Rep. 1051. National Advisory Committee for Aeronautics.

- CHILDS, R. E. & CARUSO, S. C. 1987 On the accuracy of turbulent base flow predictions. *AIAA Paper* **87-1439**.
- CHUNG, Y. M. & TUCKER, P. G. 2003 Accuracy of high-order finite difference schemes on nonuniform grids. *AIAA J.* **41** (8), 1609–1611.
- CLAYDEN, W. A. & BOWMAN, W. C. 1968 Cylindrical afterbodies at $M=2$ with hot gas ejection. *AIAA J.* **6**, 2429.
- CORTWRIGHT, E. M. & SCHROEDER, A. H. 1951 Preliminary investigation of effectiveness of base bleed in reducing drag of blunt-base bodies in supersonic stream. NACA Rep. RM E51 A26. National Advisory Committee for Aeronautics.
- CROW, S. C. & CHAMPAGNE, F. H. 1971 Orderly structure in jet turbulence. *J. Fluid Mech.* **48**, 547–591.
- DANBERG, J. & NIETUBICZ, C. 1992 Predicted flight performance of base bleed projectiles. *Journal of Spacecraft and Rockets* **29** (3), 366–372.
- DAYMAN, B. 1963 Support interference effect on the supersonic wake. *AIAA J.* **8**, 1921–1923.
- DEMETRIADES, A. 1968*a* Turbulence front structure of an axisymmetric compressible wake. *J. Fluid Mech.* **34**, 465–480.
- DEMETRIADES, A. 1968*b* Turbulence measurements in an axisymmetric compressible wake. *Phys. Fluids* **11**, 1841–1852.
- DEMETRIADES, A. 1976 Turbulence correlations in a compressible wake. *J. Fluid Mech.* **74**, 251–267.
- DING, Z., CHEN, S., LIU, Y., LUO, R. & LI, J. 1992 Wind tunnel study of aerodynamic characteristics of base combustion. *J. Propulsion and Power* **8**, 630.
- DONALDSON, I. 1955 The effect of sting supports on the base pressure of a blunt-based body in a supersonic stream. *Aeronautical Quarterly* **6**, 221–229.
- DURBIN, P. A. 1993 A Reynolds stress model for near wall turbulence. *J. Fluid Mech.* **249**, 465–498.
- ELLIOTT, G. S., SAMIMY, M. & ARNETTE, S. A. 1995 The characteristics and evolution of large-scale structures in compressible mixing layers. *Phys. Fluids* **7** (4), 864–876.
- FASEL, H. F. 1990 Numerical simulation of instability and transition in boundary layer flows, in Arnal, D. & Michel, R. *Laminar-Turbulent Transition, IUTAM Symposium, Toulouse 1989*. Springer Verlag, Berlin.

- FASEL, H. F. & KONZELMANN, U. 1990 Non-parallel stability of a flat-plate boundary layer using the complete Navier-Stokes equations. *J. Fluid Mech.* **221**, 311–347.
- FASEL, H. F., SEIDEL, J. J. & WERNZ, S. H. 2002 A methodology for simulation of complex turbulent flows. *Journal of Fluids Engineering* **124**, 933–942.
- FASEL, H. F., VON TERZI, D. A. & SANDBERG, R. D. 2006 A methodology for simulating compressible turbulent flows. *Journal of Applied Mechanics* **73**, 405–412.
- FORSYTHE, J. R. & HOFFMANN, K. A. 2000 Detached-eddy simulation of a supersonic axisymmetric base flow with an unstructured solver. *AIAA Paper* **2000-2410**.
- FORSYTHE, J. R., HOFFMANN, K. A. & SQUIRES, K. D. 2002 Detached-eddy simulation with compressibility corrections applied to a supersonic axisymmetric base flow. *AIAA Paper* **02-0586**.
- FUREBY, C. 1999 Large eddy simulation of supersonic baseflow. *AIAA Paper* **99-0426**.
- GASTER, M., KIT, E. & WYGNANSKI, I. 1985 Large-scale structures in a forced turbulent mixing layer. *J. Fluid Mech.* **150**, 23–39.
- GATSKI, T. B. & SPEZIALE, C. G. 1993 On explicit algebraic stress models for complex turbulent flows. *J. Fluid Mech.* **254**, 59–78.
- GAVIGLIO, J., DUSSAUGE, J. P., DEBIEVE, J. F. & FAVRE, A. 1977 Behavior of a turbulent flow, strongly out of equilibrium, at supersonic speeds. *Phys. Fluids* **20** (11), 179–192.
- GUO, Y., ADAMS, N. A. & KLEISER, L. 1996 Comparison of temporal and spatial direct numerical simulation of compressible boundary layer transition. *AIAA J.* **34** (4), 683–690.
- HANNEMANN, K. & OERTEL, H. 1989 Numerical simulation of the absolutely and convectively unstable wake. *J. Fluid Mech.* **199**, 55–88.
- HARRIS, P. J. 1997 Numerical investigation of transitional compressible plane wakes. PhD thesis, The University of Arizona.
- HERBERT, T. 1997 Parabolized stability equations. *Ann. Rev. Fluid Mech.* **29**, 245–283.
- HERRIN, J. L. & DUTTON, J. C. 1989 Supersonic base flow experiments in the near wake of a cylindrical afterbody. *J. Fluid Mech.* **199**, 55–88.

- HERRIN, J. L. & DUTTON, J. C. 1991 An experimental investigation of the supersonic axisymmetric base flow behind a cylindrical afterbody. UILU 91-4004. University of Illinois at Urbana-Champaign.
- HERRIN, J. L. & DUTTON, J. C. 1994 Supersonic base flow experiments in the near wake of a cylindrical afterbody. *AIAA J.* **32** (1), 77.
- HERRIN, J. L. & DUTTON, J. C. 1995 Effect of a rapid expansion on the development of compressible free shear layers. *Phys. Fluids* **7** (1), 159–170.
- HERRIN, J. L. & DUTTON, J. C. 1997 The turbulence structure of a reattaching axisymmetric compressible free shear layer. *Phys. Fluids* **9** (11), 3502–3512.
- HU, F. Q., HUSSAINI, M. Y. & MATHEY, J. L. 1996 Low-dissipation and low-dispersion runge-kutta schemes for computational acoustics. *J. Comp. Phys.* **124**, 177–191.
- HUBBARTT, J. E., STRAHLE, W. C. & NEALE, D. H. 1981 Mach 3 hydrogen external/base burning. *AIAA J.* **19**, 745.
- HUERRE, P. & MONKEWITZ, P. A. 1985 Absolute and convective instabilities in free shear layers. *J. Fluid Mech.* **159**, 151–168.
- HUERRE, P. & MONKEWITZ, P. A. 1990 Local and global instabilities in spatially developing flows. *Ann. Rev. Fluid Mech.* **22**, 473–537.
- HUSMEIER, F. 2002 Stability investigation of a flat plate boundary layer at mach 3. Master's thesis, The University of Arizona.
- HUSSAIN, A. 1986 Coherent structures and turbulence. *J. Fluid Mech.* **173**.
- JIMÉNEZ, J. & MOSER, R. D. 1998 LES: where are we and what can we expect. *AIAA Paper* **98–2891**.
- KRISHNAMURTY, V. S. & SHYY, W. 1997 Study of compressibility modifications to the $k - \epsilon$ turbulence model. *Phys. Fluids* **9**, 2769–2788.
- LAUNDER, B. E., REECE, G. J. & RODI, W. 1975 Progress in the development of a Reynolds-stress turbulence closure. *J. Fluid Mech.* **68** (3), 537–566.
- LAUNDER, B. E. & SHARMA, B. I. 1974 Application of the energy-dissipation model of turbulence to the calculation of flow near a spinning disc. *Letters in Heat and Mass Transfer* **1**, 131–138.
- LAURIEN, E. & KLEISER, L. 1989 Numerical simulation of boundary layer transition and transition control. *J. Fluid Mech.* **199**, 403–440.

- LELE, S. K. 1992 Compact finite difference schemes with spectral-like resolution. *J. Comp. Phys.* **103**, 16–42.
- LELE, S. K. 1994 Compressibility effects on turbulence. *Ann. Rev. Fluid Mech.* **26**, 211–254.
- LESIEUR, M. & METAIS, O. 1996 New trends in large-eddy simulations of turbulence. *Ann. Rev. Fluid Mech.* **28**, 45–82.
- MARASLI, B., CHAMPAGNE, F. H. & WYGNANSKI, I. 1989 Modal decomposition of velocity signals in a plane, turbulent wake. *J. Fluid Mech.* **198**, 255.
- MATHUR, T. & DUTTON, C. 1996*a* Base-bleed experiments with a cylindrical afterbody in supersonic flow. *Journal of Spacecraft and Rockets* **33**, 30.
- MATHUR, T. & DUTTON, C. 1996*b* Velocity and turbulence measurements in a supersonic base flow with mass bleed. *AIAA J.* **34**, 1153.
- MEITZ, H. & FASEL, H. F. 2000 A compact-difference scheme for the Navier-Stokes equations in vorticity-velocity formulation. *J. Comp. Phys.* **157**, 371–403.
- MENTER, F. R. 1994 Two-equation eddy-viscosity turbulence models for engineering applications. *AIAA J.* **32** (8), 1598–1605.
- MONKEWITZ, P. 1988 A note on vortex shedding from axisymmetric bluff bodies. *J. Fluid Mech.* **192**, 561–575.
- MORKOVIN, M. V. 1968 Mécanique de la turbulence. In *Centre de la Recherche Scientifique, Paris*, p. 367.
- NIETUBICZ, C. & GIBELING, H. 1993 Navier-Stokes computations for a reacting, M864 base bleed projectile. *AIAA Paper* **93-0504**.
- OERTEL, H. 1979 Mach wave radiation of hot supersonic jets investigated by means of the shock tube and new optical techniques. Proc. 12th Int. Symp. on shock tubes and waves. Jerusalem.
- OERTEL, H. 1990 Wakes behind blunt bodies. *Ann. Rev. Fluid Mech.* **22**, 539–564.
- PAPAMOSCHOU, D. & BUNYAJITRADULYA, A. 1996 Evolution of large eddies in compressible shear layers. *Phys. Fluids* **9** (3), 756–765.
- PAPAMOSCHOU, D. & ROSHKO, A. 1988 The compressible turbulent shear layer: An experimental study. *J. Fluid Mech.* **197**, 453–477.
- PAPP, J., KENZAKOWSKI, D. & DASH, S. 2002 Calibration and validation of EASM turbulence model for jet flowfields. *AIAA Paper* **2002-0855**.

- PETRIE, H. L. & WALKER, B. J. 1985 Comparison of experiment and computations for a missile base region flow field with a centered propulsive jet. *AIAA Paper* **85-1618**.
- REID, J. & HASTINGS, R. C. 1959 The effect of a central jet on the base pressure of a cylindrical afterbody in a supersonic stream. Reports and Memoranda 3224. Aeronautical Research Council, Great Britain.
- ROLLSTIN, L. 1987 Measurement of inflight base-pressure on an artillery-fired projectile. *AIAA Paper* **87-2427**.
- RUMSEY, C. L. & GATSKI, T. B. 2001 Recent turbulence model advances applied to multielement airfoil computations. *Journal of Aircraft* **38** (5).
- RUMSEY, C. L., GATSKI, T. B. & MORRISON, J. H. 2000 Turbulence model predictions of strongly curved flow in a u-duct. *AIAA J.* **38** (8).
- SAHU, J. & HEAVEY, K. R. 1995 Numerical investigation of supersonic base flow with base bleed. *AIAA Paper* **95-3459**.
- SAHU, J., NIETUBICZ, C. & STEGER, J. 1985 Navier-Stokes computations of projectile base flow with and without mass injection. *AIAA J.* **23** (9), 1348–1355.
- SANDBERG, R. D. 1999 Investigation of turbulence models for boundary layer flows using temporal numerical simulations. Master's thesis, The University of Arizona.
- SANDBERG, R. D. & FASEL, H. 2003 A flow simulation methodology for compressible turbulent axisymmetric wakes. *AIAA Paper* **2003-0267**.
- SANDBERG, R. D. & FASEL, H. 2004 Instability mechanisms in supersonic base flows. *AIAA Paper* **2004-0593**, 42nd Aerospace sciences meeting and exhibit, Reno / Jan 2004.
- SANDBERG, R. D. & FASEL, H. F. 2006a Direct numerical simulations of transitional supersonic base flows. *AIAA J.* **44** (4), 848–858.
- SANDBERG, R. D. & FASEL, H. F. 2006b Numerical investigation of transitional supersonic axisymmetric wakes. *J. Fluid Mech.* **563**, 1–41.
- SARKAR, S. 1992 The pressure-dilatation correlation in compressible flows. *Phys. Fluids A* **4** (12), 2674–2682.
- SARKAR, S. 1995 The stabilizing effect of compressibility in turbulent shear flow. *J. Fluid Mech.* **282**, 163–186.

- SARKAR, S., ERLEBACHER, G., HUSSAINI, M. Y. & KREISS, H. O. 1991 The analysis and modelling of dilatational terms in compressible turbulence. *J. Fluid Mech.* **227**, 473–493.
- SCHLICHTING, H. 1979 *Boundary Layer Theory*, 7th edn. McGraw-Hill.
- SCHWARZ, V. 1996 Numerische Untersuchungen zur Instabilität der Nachlaufströmung eines rotationssymmetrischen Körpers mit stumpfen Heck. PhD thesis, Universität Stuttgart.
- SCHWARZ, V., BESTEK, H. & FASEL, H. F. 1994 Numerical simulation of nonlinear waves in the wake of an axisymmetric bluff body. *AIAA-Paper* **94-2285**.
- SEIDEL, J. 2000 Numerical investigations of laminar and turbulent wall jets over a heated surface. PhD thesis, The University of Arizona.
- SIEGEL, S. G. 1999 Experimental investigation of the wake behind an axisymmetric body. PhD thesis, The University of Arizona.
- SMAGORINSKY, J. 1963 General circulation experiments with the primitive equations. I. The basic experiment. *Mon. Weather Rev.* **91**, 99–164.
- SPALART, P. R., W.-H., J., STRELETS, M. & ALLMARAS, S. R. 1997 Comments on the feasibility of LES for wings, and on a hybrid RANS/LES approach. In *Advances in DNS/LES, 1st AFOSR Int. Conf. on DNS/LES, Aug 4-8, 1997*. Greyden Press, Columbus, OH.
- SPEZIALE, C. G. 1995 A review of Reynolds stress models for turbulent shear flows. ICASE Report 95-15. ICASE, also NASA CR195054.
- SPEZIALE, C. G. 1996 Modeling of turbulent transport equations. In *Simulation and Modeling of Turbulent Shear Flows*. Oxford University Press, New York.
- SPEZIALE, C. G. 1997 A combined large-eddy simulation and time-dependent RANS capability for high-speed compressible flows. *Tech. Rep.* AM-97-022. Boston University.
- SPEZIALE, C. G. 1998a A combined large-eddy simulation and time-dependent RANS capability for high-speed compressible flows. *Journal of Scientific Computing* **13** (3), 253–74.
- SPEZIALE, C. G. 1998b Turbulence modeling for time-dependent RANS and VLES: A review. *AIAA J.* **36**, **2**, 173–184.
- SPEZIALE, C. G. & SO, R. M. C. 1996 Turbulence modeling and simulation. Handbook of Fluid Dynamics Ch. 9. Boston University.

- TANNEHILL, J. C., ANDERSON, D. A. & PLETCHER, R. H. 1997 *Computational Fluid Mechanics and Heat Transfer*, 2nd edn. Taylor & Francis.
- TERZI, D. A. v. 2004 Numerical investigation of transitional and turbulent backward-facing step flows. PhD thesis, The University of Arizona.
- TERZI, D. A. v. & FASEL, H. F. 2002 A new flow simulation methodology applied to the turbulent backward-facing step. *AIAA Paper* **2002-0429**.
- TERZI, D. A. v., SANDBERG, R. D. & FASEL, H. F. 2006 Identification of large coherent structures in compressible wake flows. Submitted to Journal of Fluid Mechanics.
- THEOFILIS, V. 2003 Advances in global linear instability analysis of nonparallel and three-dimensional flows. *Progress in Aerospace Sciences* **39**, 249–315.
- THUMM, A. 1991 Numerische untersuchungen zum laminar-turbulenten strömungsumschlag in transsonischen grenzschichtströmungen. PhD thesis, Universität Stuttgart.
- TOURBIER, D. 1996 Numerical investigation of transitional and turbulent axisymmetric wakes at supersonic speeds. PhD thesis, The University of Arizona.
- TUCKER, P. & SHYY, W. 1993 A numerical analysis of supersonic flow over an axisymmetric afterbody. *AIAA Paper* **93-2347**.
- VALENTINE, D. & PRZIREMBEL, C. 1970 Turbulent axisymmetric near-wake at Mach four with base injection. *AIAA J.* **8** (12), 2279–2280.
- WERNZ, S. 2001 Numerical investigation of forced transitional and turbulent wall jets. PhD thesis, The University of Arizona.
- WHITE, F. M. 1991 *Viscous Fluid Flow*. McGraw Hill.
- WILCOX, D. C. 1998 *Turbulence Modeling for CFD*, 2nd edn. DCW Industries.
- WYGNANSKI, I., CHAMPAGNE, F. H. & MARASLI, B. 1986 On large-scale coherent structures in two-dimensional, turbulent wakes. *J. Fluid Mech.* **168**, 31.